# Investigation of Shear Induced Clot Formation in Extracorporeal Membrane Oxygenation: Computer Based Flow and Clot Evaluation



Dissertation
zur Erlangung des Doktorgrades
der Humanwissenschaften
(Dr. sc. hum.)

der
Fakultät für Medizin
der Universität Regensburg

vorgelegt von
Michael Kranz, M.Sc.
aus
Regensburg

im Jahr
2025

# Investigation of Shear Induced Clot Formation in Extracorporeal Membrane Oxygenation: Computer Based Flow and Clot Evaluation



Dissertation
in order to obtain the doctoral degree
in Human Sciences
(Dr. sc. hum.)

of the
Faculty of Medicine
University of Regensburg

submitted by
Michael Kranz, M.Sc.
born in
Regensburg

in
2025

| | |
|---|---|
| Dean: | Prof. Dr. med. Dirk Hellwig |
| Supervisor: | Prof. Dr. -Ing. Lars Krenkel |
| | |
| Date of Defense: | 24th February 2026 |

# Zusammenfassung

Die extrakorporale Membranoxygenierung (ECMO) ist mit hämostatischen Komplikationen verbunden. Die zugrundeliegenden Gerinnungsmechanismen sind jedoch noch nicht vollumfänglich verstanden, um die Gerinnselbildung in der Praxis zu verhindern. Ziel dieser Arbeit war es, tiefere Einblicke in die komplexen Gerinnungsphänomene zu gewinnen. Die Gerinnsel innerhalb sieben klinisch verwendeter Membranlungen (MLs) wurden evaluiert, numerische Strömungsberechnung (CFD) von realistischen Fasermattenstapeln durchgeführt und experimentelle Strömungsdaten aus ECMO-Pumpen erhoben. Es wurde ein Verfahren zur Polymereinbettung entwickelt, um fasermattenübergreifende immunologische Ablagerungen innerhalb von MLs und ECMO-Pumpen zu analysieren. Ein signifikant höheres Gerinnselvolumen wurde in der ersten Kammer aller MLs beobachtet. Die Gerinnselablagerung war hierbei entlang der Fasermatten konstant. Jedoch in der Nähe von strukturellen Veränderungen (z. B. der Trennwand) wurde ein unregelmäßiges Gerinnselvolumen beobachtet. CFD-Ergebnisse belegen, dass die asymmetrische Anordnung der Hohlfasern die lokalen Strömungsregime deutlich beeinflusst. Ein pathologischer Fluss im Sinne einer Elongation des von Willebrand Faktors (vWF) wurde jedoch nicht festgestellt. Im Gegensatz dazu wurde gezeigt, dass turbulente Strömungsbedingungen innerhalb der Pumpe bestehen. Es scheint wahrscheinlich, dass die Pumpe ein Hauptauslöser der Gerinnselbildung ist. Erhöhte Wandscherraten aufgrund des asymmetrischen Strömungsfelds im ML waren erkennbar, jedoch überstiegen diese nicht den in der Litarature als kritisch

definierten Schwellenwert. Dennoch könnte die strömungsinduzierte Gerinnung in der Nähe der strukturellen Veränderungen im Inneren der ML vorherrschen.

# Abstract

Extracorporeal membrane oxygenation (ECMO) is associated with hemostatic complications, posing great risk on the patients. However, the underlying clotting mechanisms are not yet fully understood to sufficiently prevent clotting in clinical practice. Aim of this work was to gain deeper insights into the complex clotting phenomena. Clotting was investigated with state-of-the-art visualization protocols for seven clinically used membrane lungs (MLs), CFD of realistic fiber mat stacks, and non-invasive flow measurements within ECMO pumps. A polymer embedding procedure was established to analyze fiber mat spanning immunological deposits inside MLs and ECMO pumps, expanding the histological repertoire. A significant higher clot volume was observed in the first chamber of all MLs. Clot deposition was constant along the fiber mats. However, in vicinity of structural changes (e.g. dividing wall) an irregular clot volume was observed. CFD results proved that the asymmetrical hollow-fiber arrangement clearly affects the local flow regimes. Yet, pathological flow, in terms of vWF elongation was not found. In contrast, the pump was associated with a turbulent flow regime. In conclusion, intra-device clot formation remains a complex phenomenon. It seems likely that the pump is a main trigger of clot formation. The local flow regimes close to the hollow-fibers result in elevated shear stress but not above the critical threshold defined in the literature. However, flow induced clotting might still be prevailing close to structural changes inside the ML.

# Table of Contents

**Page**

**Nomenclature** **viii**

**Acronyms** **x**

**1 Introduction** **1**
1.1 Theoretical Background . . . 2
1.1.1 Extracorporeal Membrane Oxygenation . . . 2
1.1.2 Human Blood . . . 9
1.2 Current State of Research . . . 13
1.2.1 Visualization of Clot Structures in Membrane Lungs . . . 13
1.2.2 Histological Investigation of Hollow-Fibers . . . 14
1.2.3 Numerical Flow Investigations within ECMO . . . 14
1.3 Critical Analysis . . . 15
1.3.1 Clot Detection . . . 15
1.3.2 Histological Investigations of Hollow-Fibers . . . 15
1.3.3 Numerical Flow Investigations in ECMO . . . 16
1.4 Relevant Theories and Models . . . 17
1.5 Summary and Outlook . . . 17
1.6 Aim of This Work . . . 18
1.7 Hypothesis . . . 18

**2 Visualization and Evaluation of Blood Clots in Membrane Lungs** **19**
2.1 Introduction . . . 20
2.2 Materials and Methods . . . 20
2.2.1 Investigated Membrane Lungs . . . 21
2.2.2 Evaluation Sectors . . . 21
2.2.3 Preparation of MLs for Imaging . . . 22
2.2.4 Multidetector Computed Tomography . . . 22
2.2.5 Microcomputed Tomography . . . 23
2.2.6 Fiber Mat Imaging . . . 23

2.2.7 Statistical Methods and Data Visualization . . . 26
2.2.8 Volume Correction for MDCT Imaging . . . 27
2.2.9 Measurement of ML Blood Volume . . . 32
2.3 Results . . . 35
2.3.1 Total Clot Volume . . . 37
2.3.2 Mean Absolute Clot Volume per Sector . . . 38
2.3.3 Mean Relative Clot Volume per Sector . . . 40
2.3.4 Absolute Clot Load in ML Chambers . . . 42
2.3.5 Clot Volume per Fiber Mat . . . 43
2.3.6 Clot Progression throughout the ML . . . 47
2.3.7 Comparison of VV and VA ECMO . . . 48
2.3.8 Clot Distribution and Clotting Patterns . . . 48
2.4 Discussion . . . 52
2.4.1 Clot Formation Depending on the Used Polymer . . . 53
2.4.2 Advantages and Disadvantages of Used Imaging Modalities . . . 54
2.4.3 Limitations . . . 57
2.5 Conclusion . . . 57

**3 Large Scale Polymer Embedding of Membrane Lungs 59**
3.1 Introduction . . . 62
3.2 Materials and Equipment . . . 62
3.3 Methods . . . 65
3.3.1 Preparation . . . 65
3.3.2 ML Preparation for Embedding . . . 66
3.3.3 Embedding . . . 68
3.3.4 Creation of Specimen . . . 69
3.3.5 Microtome Sectioning . . . 73
3.3.6 Histology Protocols . . . 74
3.3.7 Microscopic Imaging . . . 84
3.4 Results . . . 87
3.4.1 Embedding Quality . . . 87
3.4.2 Visualized Structures . . . 89
3.4.3 Trouble Shooting . . . 92
3.5 Discussion . . . 96
3.5.1 Significance of Methodology . . . 96
3.5.2 Quality of Embedding and Specimen Extraction . . . 97
3.5.3 Histological Staining . . . 97
3.5.4 Alternative Embedding Approaches . . . 98
3.5.5 Limitations . . . 99
3.6 Conclusion . . . 100

**4 Computational Fluid Dynamics in Membrane Lungs 101**
4.1 Introduction . . . 102
4.2 Materials and Methods . . . 103
4.2.1 Geometry . . . 104
4.2.2 Mesh . . . 107
4.2.3 Numerical Calculation . . . 108
4.3 Results . . . 109
4.3.1 Generic Model . . . 109
4.3.2 Native Model . . . 110
4.4 Discussion . . . 111
4.4.1 Flow Regime . . . 111
4.4.2 Model Practicability . . . 113
4.4.3 Limitations . . . 114
4.5 Conclusion . . . 115

**5 Flow Dynamics in ECMO Pumps 116**
5.1 Introduction . . . 116
5.2 Materials and Methods . . . 117
5.2.1 Fluid Geometry Reconstruction . . . 118
5.2.2 Pump Drive . . . 125
5.2.3 Measurement Setup . . . 126
5.2.4 Reynolds Scaling . . . 132
5.2.5 Calculation of the Turbulence Intensity . . . 133
5.2.6 Pumping Performance . . . 134
5.2.7 Data Processing . . . 135
5.3 Results . . . 135
5.3.1 Velocity and Turbulence Intensity . . . 135
5.3.2 Quality of Pump Reconstruction . . . 138
5.3.3 Refractive Index Matching . . . 138
5.4 Discussion . . . 139
5.4.1 Velocity and Turbulence Intensity . . . 139
5.4.2 Reconstruction of Pump Replica . . . 140
5.4.3 Refractive Index Matching . . . 140
5.4.4 Performance Comparability . . . 141
5.4.5 Experimental Setup . . . 142
5.5 Conclusion . . . 143

**6 Polymer Embedding of ECMO Pump Heads 145**
6.1 Introduction . . . 146
6.2 Materials and Methods . . . 146
6.2.1 Preparation of Pump Heads . . . 146
6.2.2 Pre-Infiltration . . . 147

6.2.3 Embedding . . . 147
6.2.4 Creation of Specimen . . . 147
6.2.5 Microtome Sectioning . . . 150
6.2.6 Microscopy . . . 151
6.3 Results . . . 152
6.4 Discussion . . . 153
6.5 Conclusion . . . 154

**7 Computer Based NETosis Detection 156**
7.1 Introduction . . . 157
7.2 Experimental Setup . . . 157
7.3 Function of Software . . . 158
7.3.1 Importing Images . . . 160
7.3.2 Processing Calibration Image . . . 160
7.3.3 Evaluation of Deposits Area and Count . . . 161
7.3.4 Evaluation of Filaments Area . . . 164
7.3.5 Evaluation of Filaments Length . . . 165
7.3.6 Export Results . . . 166
7.3.7 Export Contour Data for Deep Learning . . . 167
7.3.8 Validation . . . 167
7.4 Results . . . 167
7.4.1 NET Filaments . . . 167
7.4.2 NET Deposits . . . 168
7.5 Discussion . . . 169
7.5.1 Evaluation Performance . . . 170
7.5.2 Usability . . . 170
7.5.3 Limitations . . . 170
7.6 Conclusion . . . 171

**8 Conclusion and Outlook 173**
8.1 Clot Formation is Location-Dependent . . . 174
8.2 Cross-Sectional ML Investigations as New Standard . . . 174
8.3 No vWF Elongation Due to Irregular Fiber Arrangement . . . 175
8.4 Successful Development of Realistic Pump Model for Non-Invasive Optical Flow Investigations . . . 175
8.5 NETosis as Possible Clotting Pathway . . . 176
8.6 Summary . . . 176

**Bibliography I**

**List of Figures XXI**

**List of Tables** **XXIV**

**Acknowledgments** **XXV**

**Selbstständigkeitserklärung/Affidavit** **XXVII**

# Nomenclature

## Latin Letters

| | |
|---|---|
| $A$ | Area |
| $c$ | Concentration, correction factor |
| $ci$ | Confidence interval |
| $d$ | Diameter |
| $F$ | Filter matrix |
| $f$ | Number of fiber mat |
| $h$ | Height |
| $I$ | Image |
| $L$ | Focal length of laser |
| $l$ | Length |
| $m$ | Mass |
| $\bar{m}$ | Mean mass |
| $n$ | Amount, refractive index |
| $p$ | p-value, probability |
| $r$ | Radius |
| $Re$ | Reynolds number |
| $u$ | Velocity in $x$-direction |
| $\bar{u}$ | Mean velocity in $x$-direction |
| $u'$ | Root-mean-square of velocity fluctuations in $x$-direction |
| $V$ | Volume |
| $\bar{V}$ | Mean volume |
| $\dot{V}$ | Volume flow |

| | |
|---|---|
| $v$ | Velocity in $z$-direction |
| $\bar{v}$ | Mean velocity in $z$-direction |
| $v'$ | Root-mean-square of velocity fluctuations in $z$-direction |
| $w$ | Width |
| $v$ | Velocity in $y$-direction |
| $Y$ | y-position of laser intersecting point |

## Greek Letters

| | |
|---|---|
| $\Delta$ | Difference, deviation |
| $\eta$ | Dynamic viscosity |
| $\dot{\gamma}$ | Shear rate |
| $\rho$ | Density |
| $\tau$ | Wall shear stress |
| $\theta$ | Angle |

## Miscellaneous

| | |
|---|---|
| $\circ$ | Opening |
| $\ominus$ | Erosion |
| $\oplus$ | Dilation |

# Acronyms

| | |
|---|---|
| **ABC** | avidin-biotin complex |
| **ARDS** | acute respiratory distress syndrome |
| **BayWISS** | Bavarian Academic Forum (Bayerisches Wissenschaftsforum) |
| **BC** | boundary condition |
| **BSA** | bovine serum albumin |
| **CAD** | computer aided design |
| **CESAR** | Conventional ventilation or ECMO for Severe Adult Respiratory failure |
| **CFD** | Computational Fluid Dynamics |
| **COCO** | Common Object in Context |
| **COVID-19** | corona virus disease 19 |
| **$CO_2$** | carbon dioxide |
| **CVAT** | Computer Vision Annotation Tool |
| **DAB** | 3,3-diaminobenzidine |
| **DAPI** | 4,6-diamidino-2-phenylindole |
| **DC** | direct current |
| **DFG** | German Research Foundation (Deutsche Forschungsgemeinschaft) |
| **DGLR** | German Society for Aeronautics and Astronautics (Deutsche Gesellschaft für Luft- und Raumfahrt) |
| **DL** | Deep Learning |
| **DNA** | desoxyribonucleid acid |
| **ECMO** | extracorporeal membrane oxygenation |
| **EDoF** | extended depth of field |
| **EFDC1** | 1$^{st}$ European Fluid Dynamics Conference |
| **ELSO** | Extracorporeal Life Support Organization |

| | |
|---|---|
| **FIM** | Fluorescence Intensity Manager |
| **FITC** | fluorescein isothiocyanate |
| **FLE** | Fåhræus-Lindqvist effect |
| **FMI** | fiber mat images |
| **FR** | far red |
| **GUI** | graphical user interface |
| **HE** | hematoxylin eosin |
| **HLM** | heart-lung-machine |
| **HSV** | hue-saturation-value |
| **IHC** | immunohistochemistry |
| **IHF** | immunohistofluorescence |
| **IQR** | interquartile range |
| **LDA** | laser-doppler-anemometry |
| **LED** | light emitting diode |
| **LL** | lower left sector |
| **LR** | lower right sector |
| **MDCT** | multidetector computed tomography |
| **MPO** | myeloperoxidase |
| **µCT** | microcomputed tomography |
| **ML** | membrane lung |
| **NDS** | normal donkey serum |
| **NET** | neutrophil extracellular traps |
| **NGS** | normal goat serum |
| **OTH** | Technical University of Applied Sciences (Ostbayerische Technische Hochschule) |
| **$O_2$** | oxygen |
| **PBS** | phosphate buffered saline |
| **PC** | polycarbonate |
| **PDMS** | polydimethylsiloxane |
| **PET** | Polyethyleneterephtalate |
| **PLS** | Permanent Life Support |
| **PMP** | polymethylpentene |
| **PVA** | polyvinylalcohol |
| **RBC** | red blood cell |

| | |
|---|---|
| **RCBE** | Regensburg Center of Biomedical Engineering |
| **RCHST** | Regensburg Center of Health Sciences and Technology |
| **RGB** | red-green-blue |
| **RIM** | refractive index matched |
| **RMS** | root-mean-square |
| **ROI** | region of interest |
| **RT** | room temperature |
| **SD** | standard deviation |
| **SLA** | stereolithography |
| **STAB** | Fluid Mechanics Working Group (Strömungsmechanische Arbeitsgemeinschaft) |
| **STL** | Standard Tesselation Language |
| **TBS** | tris buffered saline |
| **TI** | turbulence intensity |
| **tomo-PIV** | tomographic particle image velocimetry |
| **TPU** | thermoplastic polyurethane |
| **TRITC** | tetramethylrhodamine isothiocyanate |
| **UL** | upper left sector |
| **UKR** | University Hospital Regensburg (Universitätsklimikum Regensburg) |
| **UR** | upper right sector |
| **VA ECMO** | venoarterial ECMO |
| **VV ECMO** | venovenous ECMO |
| **vWF** | von Willebrand factor |
| **WSS** | wall shear stress |

# 1. Introduction

Extracorporeal membrane oxygenation (ECMO) is often the last option in the clinical treatment for adults, infants, and neonates with severe cardiac and/or respiratory failure [1–3]. With this technique, the circulatory function of the heart and/or the gas exchange of the patient's lungs is temporarily supported or completely taken over so that the affected organs can recover. Moreover, ECMO can also be used as a bridge to transplant, providing time until a donor organ is available.

However, this life saving medical device is also associated with serious hemostatic complications. Anticoagulation is often required for safe ECMO operation which significantly increases the risk of hemorrhaging. Despite that, the formation of blood clots within the ECMO pump or the membrane lung (ML) can still be observed in about 30 % of its applications [4, 5]. Clot formation can lead to thromboembolic events in the patient's vascular system or in worsening gas transfer of the ML. This situation requires an immediate ECMO system replacement which is a major challenge for the clinical staff and of high risk for the already ill patient.

Currently, the underlying coagulation pathways in ECMO have not yet been sufficiently elucidated, meaning that the formation of blood clots within the device cannot be effectively prevented in clinical practice. This work is intended to provide further

insights to understand the complex clotting phenomena within device components of the ECMO system.

This research is part of the priority program SPP 2014 "Towards an Implantable Lung" funded by the German Research Foundation (DFG, project no. 447721607). It was conducted in close cooperation between the Department of Biofluid Mechanics of the Technical University of Applied Sciences (OTH) Regensburg, the Department of Cardiothoracic Surgery, and the Department of Internal Medicine II of the University Hospital Regensburg (UKR). Investigation of clinically used MLs for this work was prior approved by the University Regensburg Ethics Committee (vote no. 20-2051-104).

## 1.1 Theoretical Background

This sections defines the basic concepts and provides an overview of the historical development of the field of research.

### 1.1.1 Extracorporeal Membrane Oxygenation

#### History of ECMO

The year 1953 represents an important milestone in the development of ECMO, when the surgeon J. Gibbon successfully treated a septal defect in the heart of an 18-year-old female patient for the first time using the heart-lung-machine (HLM) he had developed [6, 7].

Gibbon's HLM consisted of two main components: A rotary pump and a bubble oxygenator [8]. The rotary pump overtook the heart's circulatory function and the bubble oxygenator replaced the lungs' gas exchange function. The bubble oxygenator infused oxygen ($O_2$) into the patient's blood. The direct exposure of blood to $O_2$ proved

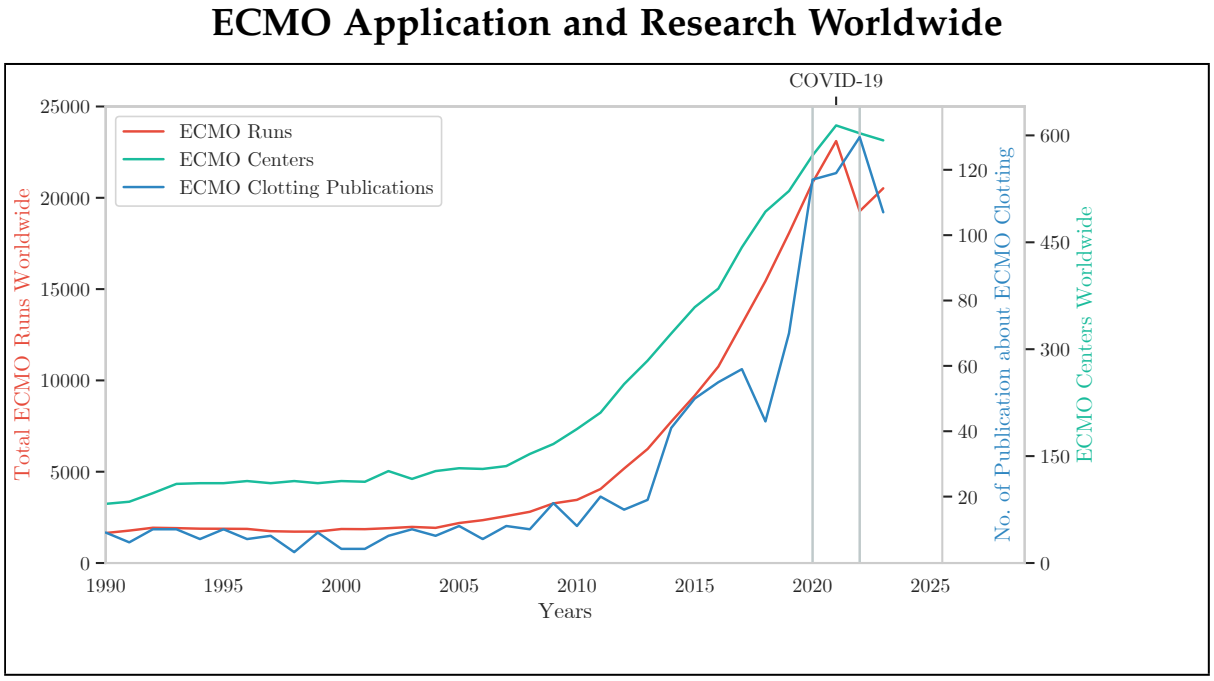


**Figure 1.1: Relevance of ECMO application and research worldwide.** Red: Number of ECMO runs; green: ECMO centers worldwide according to the ELSO registry report [10]. Blue: Number of scientific publications about clotting phenomena during ECMO runs worldwide, accessible on PubMed [11].

to be critical as the blood was severely damaged, thus limiting the duration time to less than 1 h [8, 9].

This has been significantly improved by using oxygenators with semi-permeable membranes to separate the blood from the gas, the so called "membrane oxygenators" [9]. Further optimizations to the membranes in the late 1960s and early 1970s first allowed for an extended application of the HLM [9]. The system was subsequently referred as "extracorporeal membrane oxygenation" (ECMO) since its clinical application shifted from short application during thoracic surgery (few hours) to prolonged treatment (days/weeks).

The second milestone was the first ever reported successful treatment of acute respiratory distress syndrome (ARDS) (formerly known as "shock-lung syndrome") with a venovenous ECMO (VV ECMO) performed by J. D. Hill in 1972 [12]. In the same year

R. Bartlett published a case report on the first successful treatment of postcardiotomy failure, the first application of the venoarterial ECMO (VA ECMO) [9].

In the 1980s R. Bartlett reported the first promising patients' outcomes after neonatal ECMO treatment [9]. During that time only a few specialized medical centers in the USA and Europe were capable of providing adequate ECMO treatment. In order to share their experience the Extracorporeal Life Support Organization (ELSO) was founded in 1988.

In 1991 a randomized clinical trial proved the clear advantage of centrifugal pumps over the state-of-the-art rotary pumps [13]. With significantly less blood trauma and less emissions of plastic particles compared to rotary pumps [8]. These new pumps became the new gold standard in ECMO pumps.

The third milestone was the Conventional ventilation or ECMO for Severe Adult Respiratory failure (CESAR) study, the first mutlicenter randomized controlled trial. It proved the beneficial effects of the ECMO treatment [14, 15].

Since no standardized ECMO terminology had been defined, multiple notions had established over time (e.g. "membrane oxygenator" and "membrane lung" (ML)). Consequently, the ELSO Maastricht Treaty solved that by providing ECMO guidelines [16]. For this reason, this thesis uses the agreed term "membrane lung" for the gas exchanging device.

During the corona virus disease 19 (COVID-19) pandemic ECMO stood out as the last resort for many severely ill patients [15, 17, 18], resulting in a rapid incline in ECMO applications worldwide (Figure 1.1) [19]. However, COVID-19 patients showed an extraordinary high risk of intra-device clot formation especially in the early stages of the pandemic [19–22].

**Principles of ECMO**

Today ECMO still consists of two key components: A centrifugal pump and a ML (Figure 1.2). The pump transports blood from the patient's venous system, pumps it though the ML, and returns it in the vascular system subsequently. The ML oxygenates and decarboxylates the blood. The system is connected to the vascular system via cannulas and silicone tubing (Figure 1.3).

The centrifugal pump comprises of a magnetic rotor and a transparent housing. Blood is aspirated on the top of the housing, accelerated, and ejected through a lateral outlet port. The pump is operated by an electric motor that transmits torque to the rotor via magnets.

The ML is the central gas exchanging device of ECMO. It is comprised of numerous semi-permeable polymethylpentene (PMP) hollow-fibers that are flushed with an $O_2$-rich and carbon dioxide ($CO_2$)-poor gas mixture. The $O_2$-poor and $CO_2$-rich patient's venous blood flows around the hollow-fibers. Consequently, a concentration gradient forms between the gas phase and the blood phase that leads to a gas exchange, similar to the gas exchange within the human alveoli. The gas mixture is composed of pure medical oxygen and compressed air. This composition is defined by the medical staff depending on the patient's condition. For example, by increasing the $O_2$ content within the mixture, the $O_2$ concentration gradient is increased, thus promoting the diffusion of $O_2$ into the patient's blood. By increasing the total gas flow (sweep gas), the $CO_2$ content in the hollow-fibers is reduced, which increases $CO_2$ elimination from the patient's blood.

Besides the gas exchange, the ML can additionally be used for blood tempering. Non-permeable hollow-fibers are located within the ML. Tempered water flows within to control the blood temperature. Various ML and pump designs with different

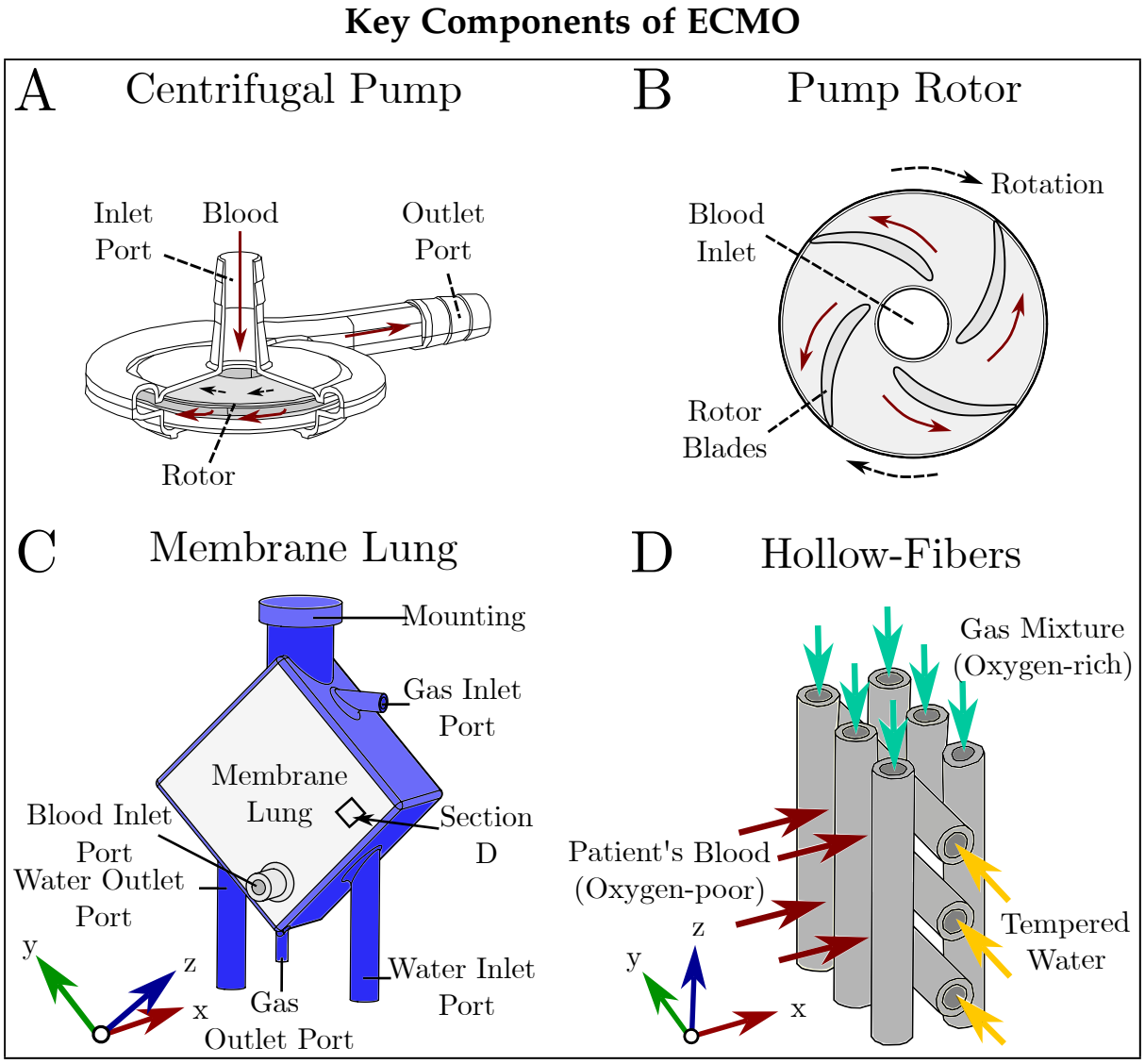


**Figure 1.2: Overview of ECMO components.** (**A**) Drawing of Rotaflow centrifugal pump. Blood is drawn inside via an inlet port and accelerated with a rotor. A lateral channel collects the blood and guides it to the outlet port. From there it flows through a silicone tube into the ML. (**B**) Magnification of the rotor. Blood enters in the center. Rotor blades apply torque to transport the blood. (**C**) Macroscopic overview of the Permanent Life Support (PLS) ML with all relevant ports. (**D**) Visualization of a section of the hollow-fibers with the flow direction of blood, gas, and tempered water. Subfigures C and D were adapted from Kranz et al. [23] reproduced with permission from Springer Nature.

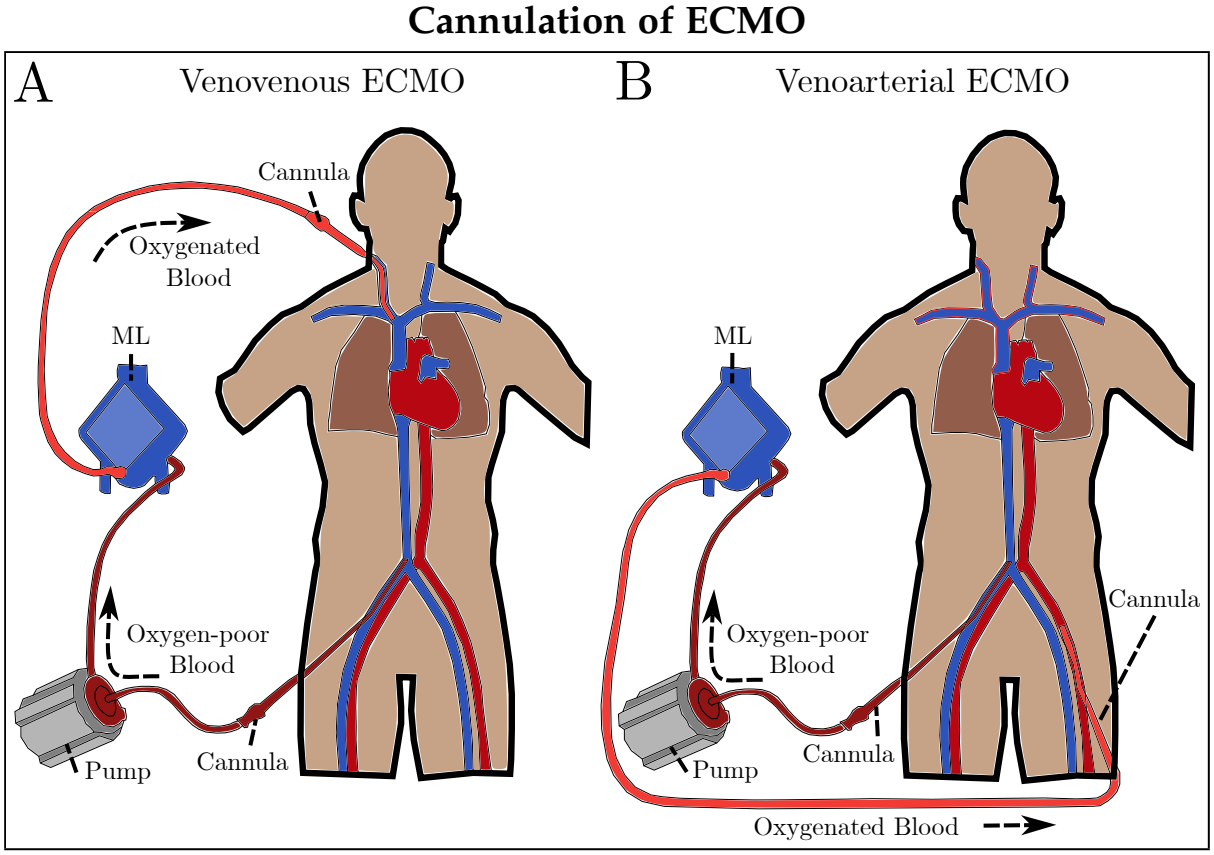


**Figure 1.3: Cannulation of VV ECMO and VA ECMO.** Blood is actively drained from the patient's venous vascular system by the centrifugal pump and transported to the ML. The ML oxygenates and decarboxylates the blood. The oxygenated blood is then returned to the (**A**) venous or (**B**) arterial vascular system, depending on the required support. VV ECMO in general acts as lung support while VA ECMO is considered as heat support. Adapted from [24].

**Table 1.1: Commonly used ML designs and specifications.** Information according to [25] and the manufacturers data sheets.

| ML Type | Manufacturer | Surface Area | Surface Coating | Heat Exchange Material | Priming Volume |
|---|---|---|---|---|---|
| PLS | Getinge, Rastatt, Germany | 1.8 $m^2$ | Bioline® | TPU | 275 ml [26] |
| Hilite 700 LT | Xenios, Heilbronn, Germany | 1.9 $m^2$ | X.ELLENCE | PET | 270 ml [27] |
| Nautilus | Medtronic, Minneapolis, MN, USA | 1.8 $m^2$ | Balance | PET | 226 ml [28] |
| EOS | LivaNova, Munich, Germany | 1.2 $m^2$ | PH.I.S.I.O. | Stainless steel | 150 ml [29] |

**Table 1.2: Commonly used ECMO pumps and specifications.** Information according to [30].

| Pump Type | Manufacturer | Priming Volume |
|---|---|---|
| Rotaflow RF32 | Getinge, Rastatt, Germany | 32 ml |
| Deltastream DP3 | Xenios, Heilbronn, Germany | 16 ml |
| CentriMag | Abbott, Abbott Park, IL, USA | 31 ml |
| Revolution | Sorin, Milan, Italy | 57 ml |

specifications are currently used in the clinical practice. The most commonly used designs are presented in Tables 1.1, 1.2. All MLs consist of PMP hollow-fibers for the gas exchange. However, different materials are used for heat exchange.

In this work, all studies conducted focused only on the PLS ML and the Rotaflow pump.

Despite the benefits provided by ECMO, it still bears a variety of risks and possible complication which may be life-threatening. Blood shows a variety of critical interactions during ECMO operation: Inflammatory reactions induced by the contact with artificial surfaces, hemostatis, hemolysis or the formation of neutrophil extracellular traps (NETosis) [25, 31, 32].

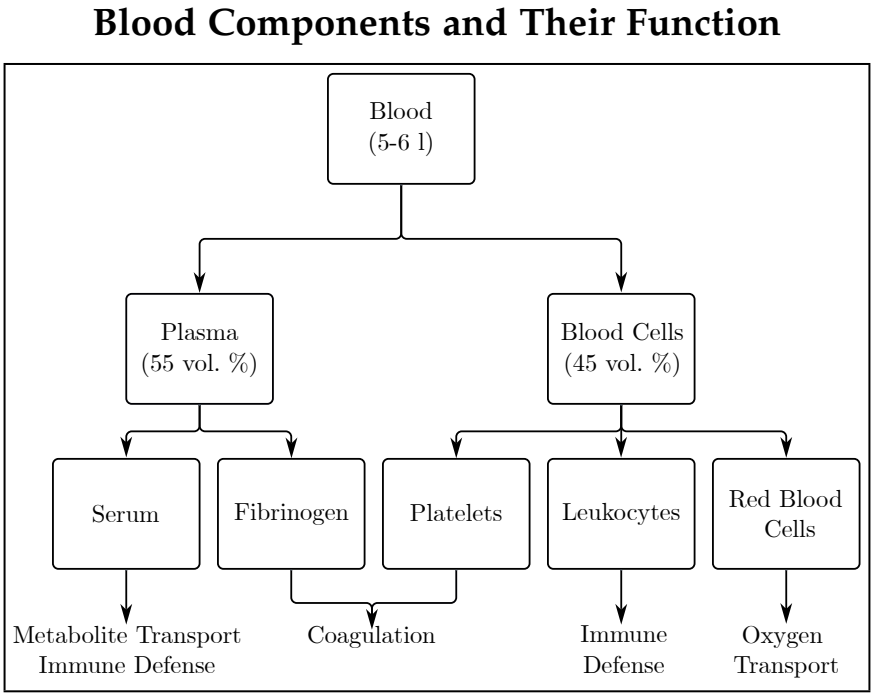


**Figure 1.4: Overview of the central blood components and their function in the circulation.** Adapted from [33].

### 1.1.2 Human Blood

The human blood is essential for numerous functions of the body. A healthy person has $5 - 6$ l of blood circulating through the blood vessels, driven by the heart [33, 37]. It consists of cellular, mainly red blood cells (RBCs), and liquid components, like the serum, creating a vital fluid with complex fluid mechanical properties.

The functions of the main components of the human blood are illustrated in Figure 1.4. The primary tasks of the blood are the transport of nutrients and oxygen, as well as the immune defense and the blood coagulation.

In a general perspective, blood is assumed to be a non-newtonian fluid [34]. This means that with increasing exposure to shear stress, the viscosity declines, illustrated in Figure 1.5 (a). The non-linear shear-thinning effect is a result of the dispersion of the RBCs. With lower shear stress, the RBCs are stacked in the so called Rouleaux-

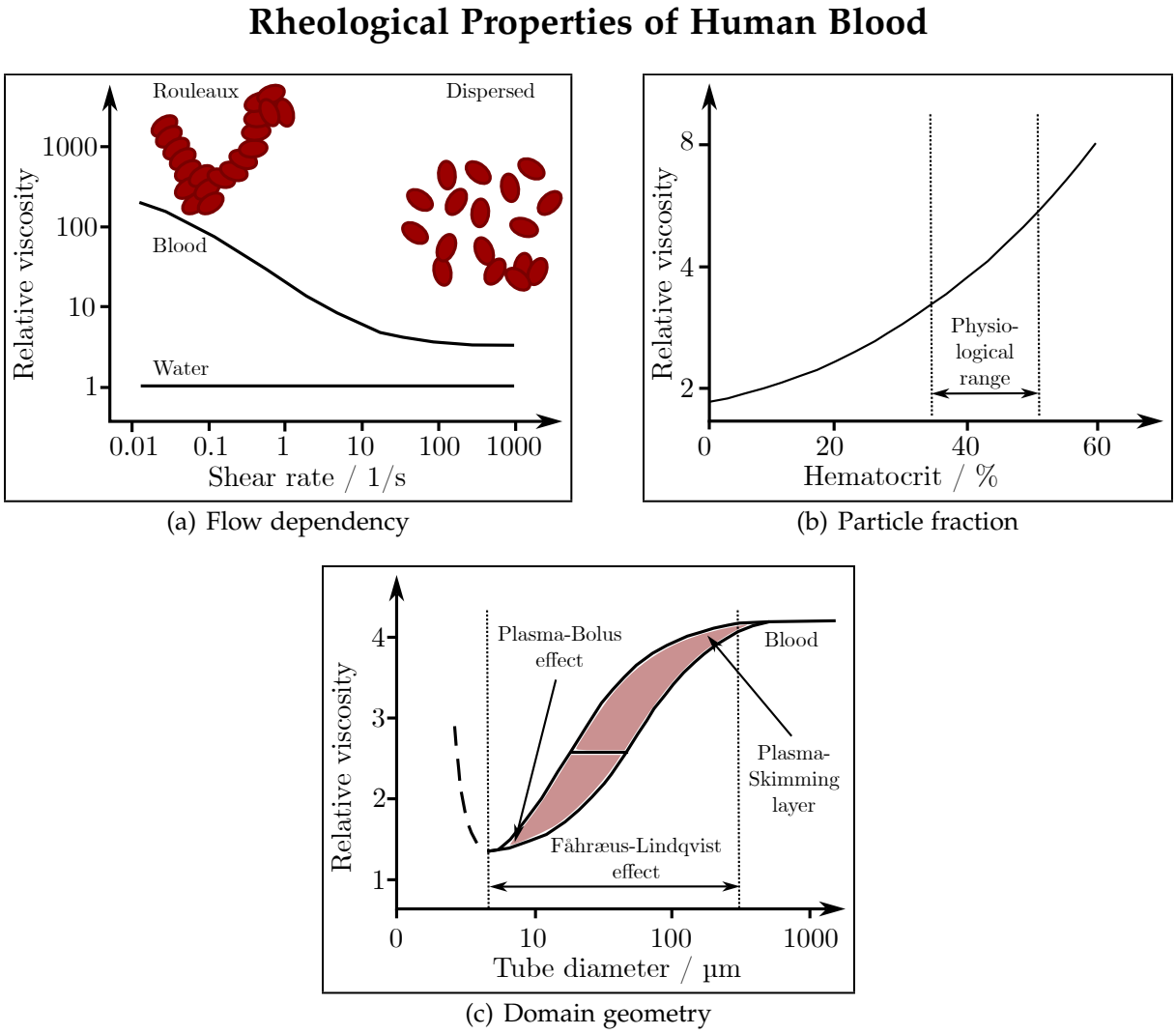


(a) Flow dependency

(b) Particle fraction

(c) Domain geometry

**Figure 1.5: Rheological properties of human blood.** (**a**) Blood is a non-newtonian fluid in general. Shear stress resolves the Rouleaux-formation of RBCs which results in a non-linear decrease of the relative viscosity; adapted from [34, 35]. (**b**) The particle fraction (hematocrit) affects the relative viscosity with a non-linear relation; adapted from [36]. (**c**) It was shown for cylindrical flow geometries that its diameter significantly influences the relative viscosity. Between 3 µm and 300 µm tube diameter the Fåhræus-Lindqvist effect (FLE) occurs; adapted from [34].

formation which is dissolved through elevated shear stress [35]. However, the particle fraction (hematocrit) also affects the viscosity of the blood [36]. By increasing the proportion of cells in the blood, the viscosity increases in a non-linear manner.

In addition, it was observed that the vessel geometry significantly affects the viscosity of the blood [34, 38]. In cylindrical vessels with a diameter between 3 µm and 300 µm, e.g. capillaries, the FLE occurs [34, 38, 39]. The FLE is characterized by the fact that the cellular blood components migrate to the center of the vessel resulting in a high-viscous phase. Moreover, the formation of a plasma skimming layer leads to a viscosity reduction of the blood in those vessels [39]. As plasma layer forms on the vessel wall, this creates a multiphase flow situation [34]. However, the FLE is only applicable for straight cylindrical vessels. Recently C. Birkenmaier proved that a non-uniform multiphase flow occurs due to the moment of inertia even in the non-cylindrical interspace of ML hollow-fibers for a two-dimensional case [40].

**Von Willebrand Factor**

The von Willebrand Factor (vWF) is a multimeric glycoprotein plays an important role in the thrombosis and hemostasis during ECMO operation [41–46]. It is a co-factor within the coagulation cascade that mediates platelet adhesion and aggregation [42, 43, 45, 47–49], as illustrated in Figure 1.6. The exposure to elevated shear stress leads to a change of the spatial arrangement of the vWF protein from a coiled to a chain-like formation oriented in the direction of the flow stress field [50–52], illustrated in Figure 1.7.

This effect of vWF elongation was previously investigated and discussed with in-vitro studies [53] and inside clinically used MLs [31, 54].

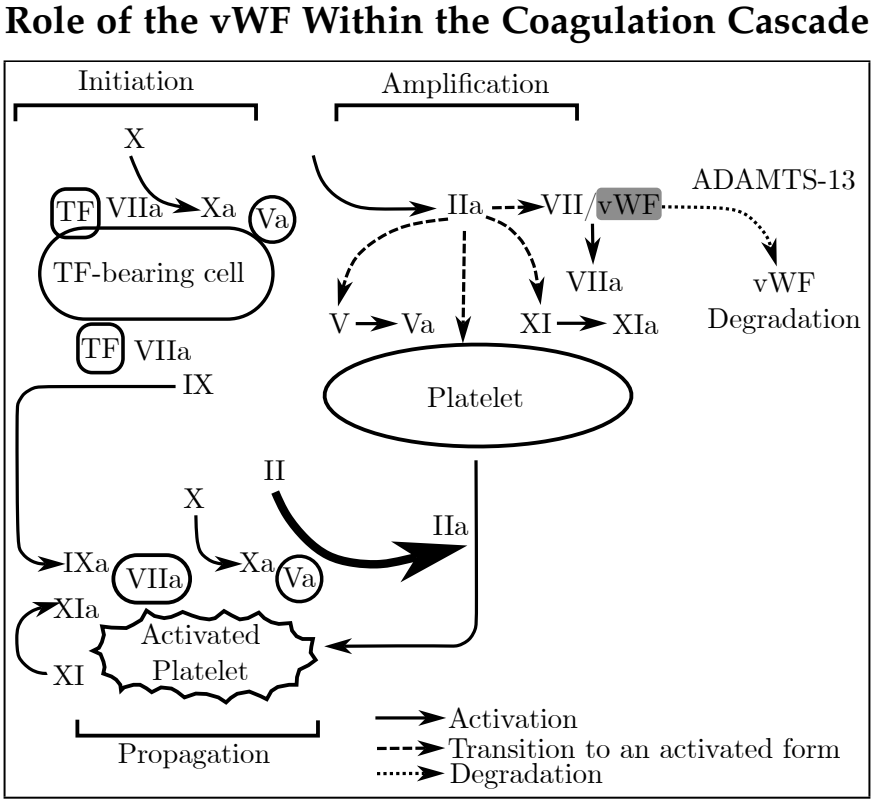


**Figure 1.6: Role of the vWF as co-factor within the coagulation cascade.** Adapted from [47].

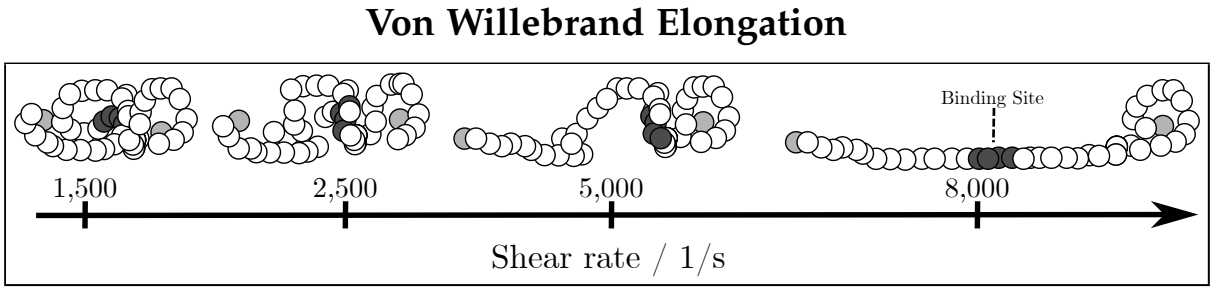


**Figure 1.7: Configuration of the von Willebrand protein after exposure to shear stress.** With unphysiological shear stress ($\dot{\gamma} > 5{,}000\ 1/s$) the vWF unfolds and elongates from a coil to a chain-like structure, making binding sites accessible for triggering clot formation; adapted from [41].

## 1.2 Current State of Research

This section provides an overview of the most important studies as well as their results. Furthermore, the applied methods and approaches used in the literature are presented and critically discussed.

### 1.2.1 Visualization of Clot Structures in Membrane Lungs

Different methods for detection of blood clots within ECMO MLs have been developed in the recent years. Particularly noteworthy here is the multidetector computed tomography (MDCT). First published by Dornia et al. [55] in 2013. They used clinical MDCT to visualize clot structures in ML after clinical application. Their work acted as basis for further investigations by Panigada et al. [56] in 2015 and for Birkenmaier et al. [57] in 2020. Birkenmaier et al. [57] optimized Dornia's protocol by adapting the MDCT scanning parameters. This significantly improved the detection quality.

Moreover, Birkenmaier et al. [57] introduced microcomputed tomography (µCT) as an alternative imaging modality for clot detection. A µCT is an industrial scanning device that features a higher radiation dosage, allowing a distinctly higher spatial resolution. As a result, minuscule clot structures were detectable that could not be captured by the MDCT.

An alternative method was introduced by Wagner and Kranz et al. [31] in 2024. They used systematic photography of clot structures adherent to ML fiber mats and applied a self developed image processing algorithm to detect and evaluate the clot burden.

### 1.2.2 Histological Investigation of Hollow-Fibers

The application of histological methods to investigate immunological interactions of human blood in contact with ML hollow-fibers has been described by few specialized research groups [58]. Two main approaches can be identified, the in-vitro examination in laboratory tests and the ex-vivo examination after clinical ECMO application [58]. The latter approach is of particular interest for this work.

The histological examination of ML hollow-fibers after clinical application was introduced by Lehle et al. [59] in 2008. Since then, her research group continued investigations of clinically used MLs hollow-fibers [31, 54, 60–62] up to the present. All studies followed a similar procedure: First, the ML was collected after the termination of ECMO support or after an ECMO system replacement. Residual blood was drained and deposed structures were fixed with formol solution [61, 62]. The ML was cut open and the gas exchanging hollow-fiber mats were removed. Sections of these fiber mats were then histologically stained and examined using a fluorescence microscope with a top view perspective.

### 1.2.3 Numerical Flow Investigations within ECMO

The ECMO ML was subject to numerous in-silico investigations using CFD [63–74]. They all applied different CFD approaches towards a variety of fluid mechanical effects inside the ML. The studies presented and discussed the performance of the gas exchange [64, 65, 72, 74], the pressure drop along the ML [68, 74], the residence time of blood in certain ML regions [63] or insights into the hemodynamic assessment of ECMO [67]. All studies found laminar flow conditions inside the ML.

Furthermore, the application of numerical flow calculations was also conducted with ECMO pump models in the past [75–79]. These studies compared the influence of

different ECMO pump models used in the clinical practice with regard to unphysiological shear stress promoting hemolysis [75, 78], the vorticity and its relation to platelet activation [77] or the investigation of elevated shear stress leading to vWF elongation and hemolysis [78]. In contrast to the laminar flow regime inside the ML, turbulent flow prevailed inside the pumps.

## 1.3 Critical Analysis

This section presents information on identified research gaps and open questions which were the foundation for this research project.

### 1.3.1 Clot Detection

Different methods for clot detection in clinically used MLs have been presented. However, the results were heterogeneous. Wagner and Kranz et al. [31] developed a systematic protocol for detection of the clot volume and the distribution of deposed clots considering important contributions to increase the detection accuracy by Birkenmaier et al [57]. Based on their strategy, clot investigations with multiple MLs is proposed to gain important information on clotting behavior.

### 1.3.2 Histological Investigations of Hollow-Fibers

Histological investigation of hollow-fibers already gave important insights in limiting gas transfer efficiency due to deposition of cellular structures [59]. Subsequent studies followed a similar approach. Hollow-fiber segments were histologically stained and immunological deposits were visualized with transmitting light and fluorescence microscopy. This method, however, is limited to regions of the hollow-fibers with only a low amount of single-layered deposits since its lack in depth information. Fiber mat

spanning structures and multi-layered cell accumulation were disrupted during the retrieval of the fiber mats. Hence, investigating them was not possible.

However, a relation of the flow regime and the spatial arrangement of the immunological deposits which is proposed in the hypothesis strictly requires a cross-sectional (crossing hollow-fibers) view to sufficiently yield data on the elongated vWF. Furthermore, cross-sectional ML specimens would allow for examinations of fiber-mat spanning structures and multi-layered cell structures. This ultimately circumvents the main limitation of top view microscopy and expands the repertoire of histological examinations methods.

### 1.3.3 Numerical Flow Investigations in ECMO

Numerical flow calculations were applied to a variety of different fluid mechanical research questions in ECMO. However, the question whether the flow regime in the vicinity of the hollow-fibers leads to an elongation of the vWF and thus triggering local clot formation cannot be answered with the presented results. This was due to the holistic view of the ML, which did not consider the hollow-fiber geometry at all or only had a comparatively low spatial discretization around the hollow-fibers.

Furthermore, modeling was conducted in generic flow domains designed with computer aided design (CAD) tools. With regard to the seemingly random clot distribution pattern presented in the literature [31, 55, 56, 80], the symmetrical flow fields derived from published CFD results seem not intuitive. Wagner and Kranz et al. [31] observed a non-uniform fiber mat shift towards the blood flow direction which was considered an indicator for an asymmetrical flow domain. This asymmetrical flow domain might significantly affect the flow field, which is particularly important when investigating the local flow regimes close to the hollow-fibers.

Additionally, studies assume blood as an in-compressible newtonian fluid [66, 81]. The FLE and the distortion of the RBCs in small vessels were not considered [67, 82]. The extent to which blood rheology influences the flow field here is not yet known. However, a non-uniform multiphase flow regime in a generic two-dimensional ML model was observed by C. Birkenmaier [83] which seems likely to play a role in clotting phenomena.

## 1.4 Relevant Theories and Models

Intra-device clot formation in ECMO is accompanied with two theories: First, the ML is the actual effector point of clot formation or, secondly, the ML acts as a sieve, trapping e.g. elongated vWF or platelets that were activated upstream in the ECMO pump or result from activated endothelial cells from the patient's vessels. However, literature was not capable to prove or refute any of the theories. Still, a combination of both theories might apply.

## 1.5 Summary and Outlook

In summary, ECMO is a lifesaving treatment which is associated with thrombotic and hemostatic complications [4, 84–87]. The underlying clotting mechanisms are not yet sufficiently understood for tackling these issues in the clinical practice. The use of histological examination of ML hollow-fiber cross-sections coupled with high-resolution CFD has great potential to achieve a profound understanding of the underlying clotting phenomena.

## 1.6 Aim of This Work

Aim of this work is to gain deeper insights into shear-induced clot formation within the ECMO device and its relation to the vWF. This knowledge will help to prevent severe clotting in the clinical practice and increase patient's safety.

## 1.7 Hypothesis

Figure 1.8 illustrates the hypothesis of this work.

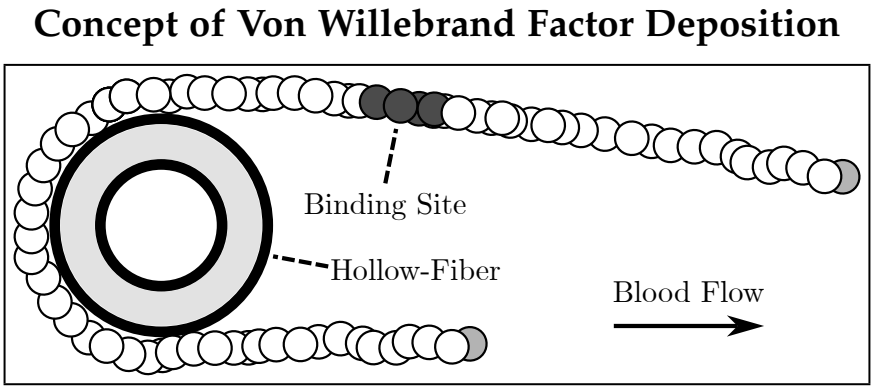


**Figure 1.8: Concept of vWF deposition as initiator for clotting.** The protein deposes on the hollow-fiber surface due to the blood flow after elongation. This makes binding sites accessible for later intra-device clot formation.

It is proposed that un-physiological shear stress induces an elongation of the vWF which adheres to the hollow-fibers of the ML. In this state, the vWF can reach a length in the small millimeter scale and interior binding sites are accessible initiating intra-device clot formation [41, 48].

# 2. Visualization and Evaluation of Blood Clots in Membrane Lungs

Clotting structures in MLs pose a high risk for the patients during ECMO operation [4, 5, 59]. These can result in decreased blood flow and gas transfer efficiency, necessitating an overall system replacement. In the following chapter three different methods for visualization and calculation of clot volume with their individual advantages and disadvantages are described and discussed.

Following chapter is partly presented in the first section of *Computer Based Visualization of Clot Structures in Extracorporeal Membrane Oxygenation and Histological Clot Investigations for Understanding Thrombosis in Membrane Lungs* [31] first published in *Frontiers in Medicine* in June 2024 under Creative Commons Attribution License (CC-BY). Furthermore, these findings were presented at the 11$^{th}$ EuroELSO Congress in Lisbon, Portugal in April 2023 in the session "Optimizing ECMO technology" [88].

## 2.1 Introduction

Clot deposition occurs regularly during ECMO treatment posing a great risk for patients [4, 5, 89]. Previous studies utilized different detection methods and parameters. However, they agreed on a heterogeneous clot distribution which did not allow for a general statement on ML regions prone to clot deposition [31, 55–57]. By using a sequence of different imaging modalities published by Wagner and Kranz et al. [31], the individual strengths of non-invasive and invasive clot detection were utilized to obtain high quality data on clot volume and distribution. This enables statements to be made about regions with particularly high clot volumes. Different imaging methods are used for visualization of clot distribution within seven clinically used MLs: Clinically used MDCT, an industrial µCT, and evaluation of fiber mat images (FMI). The procedure for visualization and the required data as well as the process-specific clot images and calculated volumes are presented below.

## 2.2 Materials and Methods

Clot visualizing and volume calculation was carried out using MDCT based an Dornia et al. [55] with the optimizations from Birkenmaier et al. [57], µCT according to Birkenmaier et al. [57] and an in-house developed method of evaluating fiber mat images (FMI) first published by Wagner and Kranz et al. [31]. The ML was virtually divided into four sectors and investigated independently, illustrated in Figure 2.1. FMI in contrast requires two-dimensional images taken of the front and rear side of each fiber mat. A developed Python 3.12 algorithm calculates the total clot volume by evaluating pixel values of the individual fiber mat images.

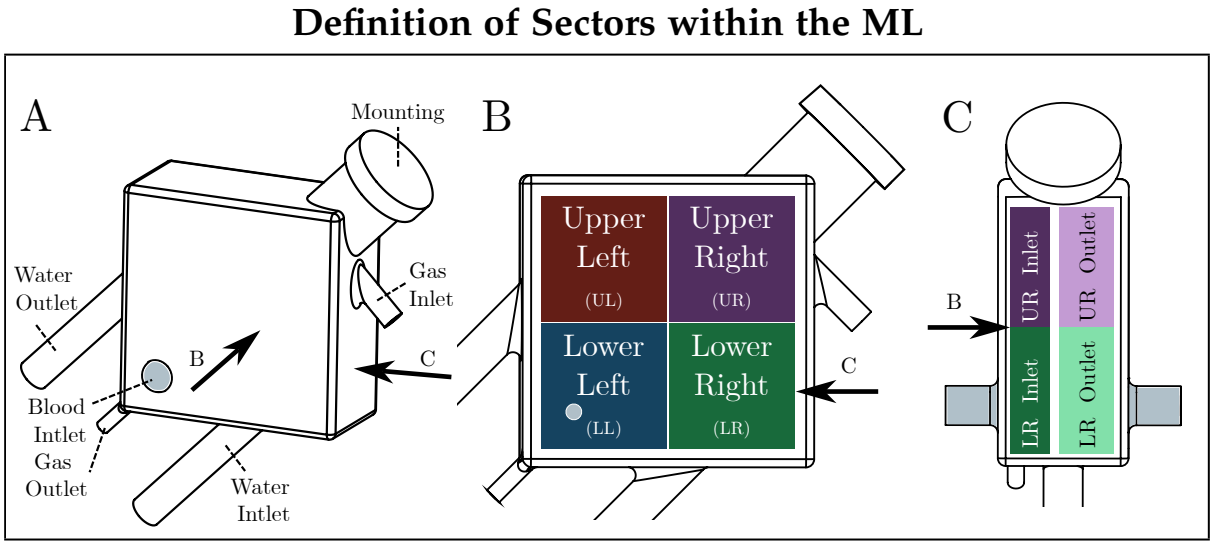


**Figure 2.1: Definition of region of interest (ROI) for clot calculation.** (**A**) Overview of ML housing. (**B**) Front view showing the four defined sectors: Upper Left (UL), Upper Right (UR), Lower Left (LL), and Lower Right (LR). (**C**) Displaying the lateral view of the ML with the inlet and outlet chamber. These are separated by a dividing wall. Gray circle/cylinder indicating position of blood inlet and outlet ports.

### 2.2.1 Investigated Membrane Lungs

Seven randomly collected clinically used PLS MLs (Getinge/Maquet, Rastatt, Germany) were subject for this study. These were retrieved after termination of ECMO support or after an ECMO system exchange. More details are presented in Table 2.1.

### 2.2.2 Evaluation Sectors

The MLs were virtually divided in four evaluation sectors: The upper left sector (UL), the upper right sector (UR), the lower left sector (LL), and the lower right sector (LR), depicted in Figure 2.1. Every sector is subdivided by the ML's dividing wall. The clotting volume was detected within these certain sectors by accumulation of all contained clotting structures.

**Table 2.1: Operation data of the seven investigated MLs.**

| **ML No. for Investigation** | **Median** | **Mean ± SD** | **1** | **2** | **3** | **4** | **5** | **6** | **7** |
|---|---|---|---|---|---|---|---|---|---|
| **Cannulation** | - | - | VV | VV | VV | VA | VA | VA | VA |
| **ML Type** | - | - | End | End | End | End | Ex-change | End | Ex-change |
| **ML Duration** / days | 8.0 | 12.1 ± 9.2 | 7 | 19 | 32 | 8 | 4 | 9 | 6 |
| **Total Time on ECMO** / days | 14.0 | 21.3 ± 21.5 | 14 | 19 | 73 | 8 | 11 | 7 | 17 |
| **No. ECMO System** | - | - | 2 | 1 | 4 | 1 | 1 | 2 | 2 |
| **Total ECMO Systems** | 2.0 | 2.7 ± 1.5 | 2 | 1 | 4 | 1 | 4 | 2 | 4 |
| **Gender** | - | - | male | female | female | male | male | male | male |
| **Age** / years | 59.0 | 59.9 ± 5.3 | 54 | 62 | 59 | 56 | 54 | 65 | 69 |

### 2.2.3 Preparation of MLs for Imaging

ML preparation was conducted directly after clinical use following state-of-the-art protocols [31, 54, 61, 62]. In summary, the ML was rinsed with 10 l of saline solution to remove blood residuals from the device. The deposed clot structures were fixed with paraformaldehyde (4 %, in 0.1 M phosphate buffer, pH 7.2 + 10 % methanol, 1 l) and stored at a temperature of 4 °C until imaging.

Prior to the imaging, the fixative solution was removed and the ML was rinsed with 2 l of isotonic saline solution. Pressurized air was used to dry the ML (1 l/min for 15 min). To reduce scanning artifacts, all metal parts (one screw and one spring) were removed.

### 2.2.4 Multidetector Computed Tomography

MDCT imaging was conducted at the UKR, Department of Radiology using a Somatom Definition Flash Scanner (Siemens Healthineers, Erlangen, Germany) according to Wagner and Kranz et al. [31]. Briefly, the image acquisition was based on the protocol of Dornia et al. [55] with the revised settings of Birkenmaier et al. [57]. Clot detection was implemented with VGStudio Max 2022.2 software (Volume Graphics, Heidelberg,

Germany) using a porosity analysis within the predefined sectors (Figure 2.1). The 'Only Threshold' algorithm was chosen with 'Inclusion' as analysis mode (settings: minimal grayscale iclusion: -470.00, probability threshold: 0.30, max. diameter size: 159.00 mm) [31].

### 2.2.5 Microcomputed Tomography

µCT scanning followed the protocol of Wagner and Kranz et al. [31] with the scanning parameters published by Birkenmaier et al. [57]. Prior to the µCT scan, the water connectors of the ML were cut off to fit inside the scanner [31]. A Phoenix v|tome|xs 240/180 µCT scanner (Baker Hughes Digital Solutions, Hürth, Germany) was used. Subsequent clot volume detection was conducted analogously to the MDCT except for the minimal grayscale inclusion of 0.0148 [31].

### 2.2.6 Fiber Mat Imaging

FMI was first introduced by Wagner and Kranz et al. [31] as an alternative method for clot detection within clinically used MLs. It utilizes camera images of ML fiber mats which are automatically evaluated by a computer algorithm. In contrast to MDCT and µCT, FMI is a simple and cost efficient imaging modality that does only require a digital camera and a computer.

#### Retrieval of Fiber Mats

In order to retrieve the fiber mats, the ML housing was cut open using a band saw (TC-SB 305 U, Einhell, Landau, Germany). The entire fiber mat stack was then removed from the housing and a small part of the UL corner was cut off to maintain the orientation of the fiber mats, illustrated in Figure 2.2. The fiber mat stack was stored in a lockable plastic container until image acquisition.

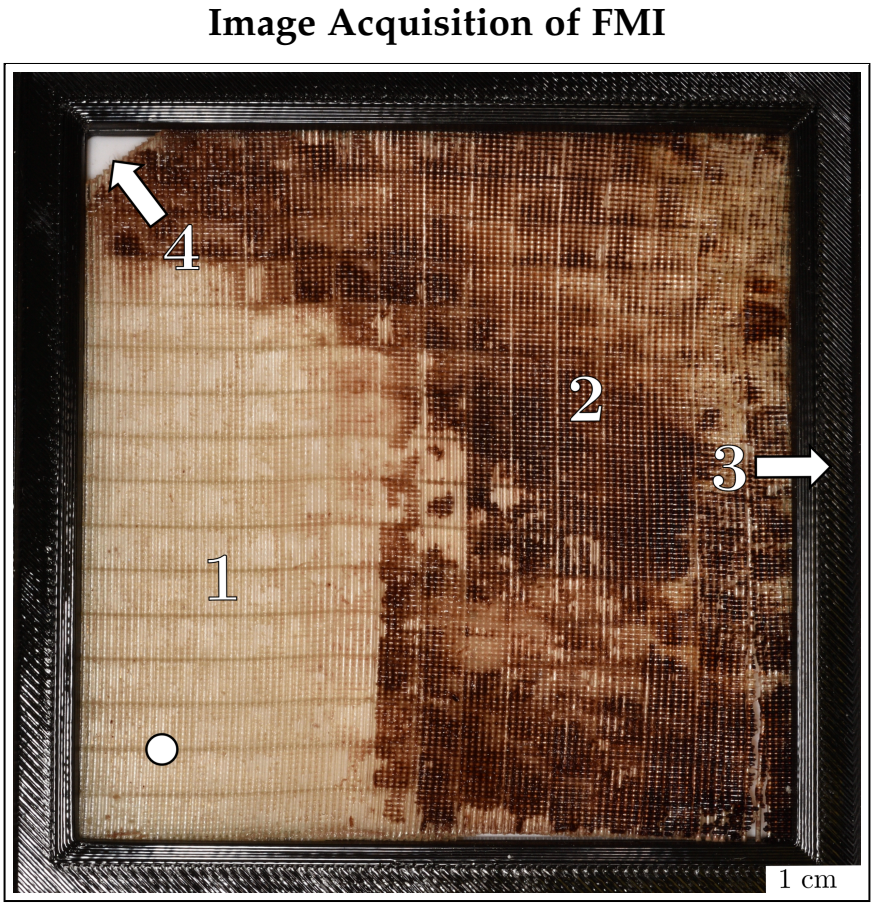


**Figure 2.2: Setup for image acquisition of FMI.** (1) Visually clot-free and (2) visually clotted areas as defined by Wagner and Kranz et al. [31]. (3) 3D-printed stabilization frame securely fixing the hollow-fiber mat in place during photography. (4) Upper left corner cut off to maintain the orientation of the hollow-fiber mat. White circle indicating the location of the inlet port.

### Photography

The first fiber mat was taken and clamped into a 3D-printed stabilization frame with the side pointing to the inlet connector facing upwards. For a secure hold of the fiber mat, the frame covered the outer 5 mm of the fiber mat. A D3400 camera (Nikon, Shiyoda, Tokyo, Japan) supplemented by a ring flash (Walimex pro TTL MACRO Ringblitz, Altena, Germany) were used with a distance to the fiber mat of 25 cm, a focal length of 24 mm, a shutter speed of 1/160, an aperture of 16, a photo sensitivity of ISO 400, and a resolution of 6000 by 4000 pixels. The ring flash was set to 'Multimode',

power control of 1/64, and a frequency of 2 Hz. Then, the stabilization frame was flipped horizontally and an image of the rear side was taken. These steps were repeated for all other 118 fiber mats. [31]

**Image Processing**

All images were converted from the native NEF format to an 8-bit TIF file using Capture NX-D software (Nikon, Shiyoda, Tokyo, Japan). A developed Python 3.12 algorithm automatically detected and evaluated the clot volume deposed on the fiber mats. It first used edge detection to find the coordinates of the inner perimeter of the stabilization frame. If the camera image is slightly rotated, an automatic correction is conducted. The image is then cropped to the relevant size (only fiber mat, no stabilization frame) and binarized with a threshold of 160. Black pixels then represent clotted and white pixels represent clot-free areas. To determine the clot volume per image, the proportion of black pixels was multiplied by the area of the fiber mat and half the fiber diameter. This process was repeated for both the front and back sides of the fiber mat layers. The total clot volume was then calculated by summing the clots from each individual fiber mat. During preparation, when the fiber mats were removed, large portions of the clots remained on the front side of the underlying fiber mat. Unlike the gas fibers, the heat exchange fibers were more transparent, which allowed clot structures on the front side to be visible on the back side in photographs. For three randomly selected heat exchange fiber mats, the reverse side was visually inspected for clotting structures, leading to the determination of a correction factor of 0.01. This indicates that only one percent of the black pixels detected on the reverse side were evaluated as blood clots. [31]

### 2.2.7 Statistical Methods and Data Visualization

The statistical analysis was carried out using a Python 3.12 script that automatically processed and analyzed the data. Essential packages were `SciPy` for performing statistical tests and `Matplotlib` as well as `Seaborn` for data visualization. In addition, an automatic selection of the required statistical test according to Figure 2.3 was established.

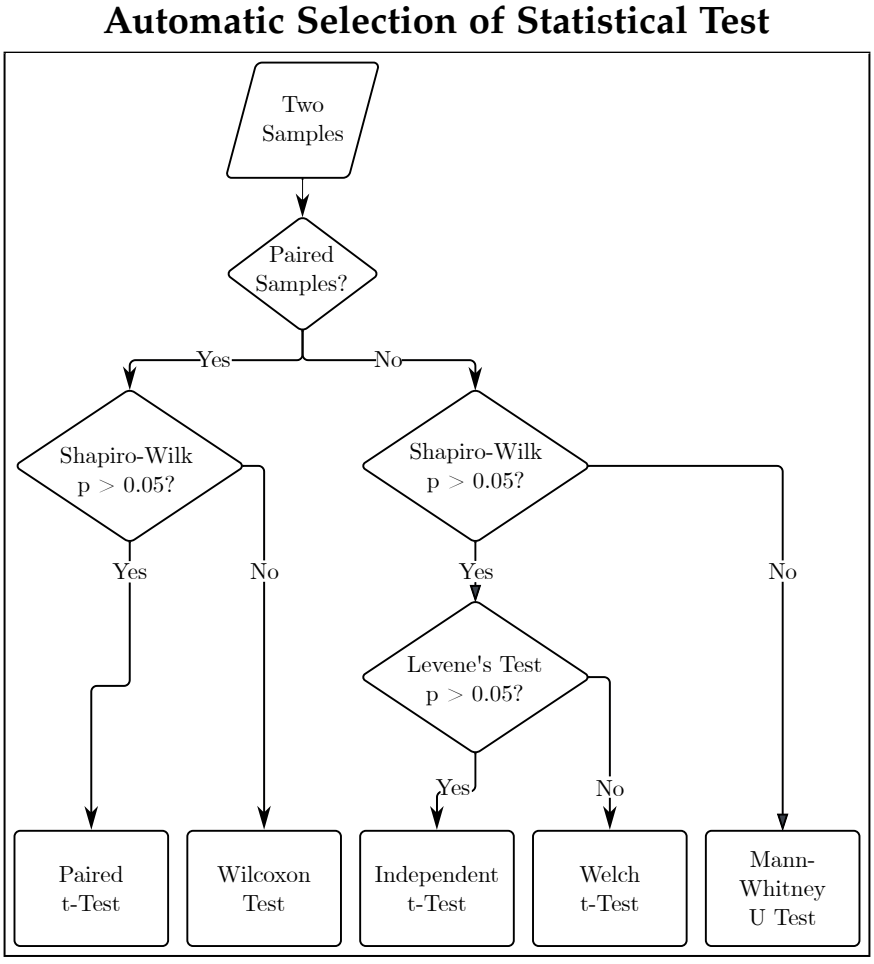


**Figure 2.3: Automatic selection of statistical test during the data processing.** Two samples are put into a Python 3.12 script that performs the specifically required tests. First, the user must provide information on the dependency of the two samples. Second, it is checked for Gaussian distribution using the Shapiro-Wilk test. If the samples are independent and showed Gaussian distribution, the Levene's test checks for equal variances. In case of small sample sizes, the correct test settings are automatically applied allowing valid results. For example, the Mann-Whitney U test is still reliable for sample size of $n = 7$.

### 2.2.8 Volume Correction for MDCT Imaging

Since MDCT also detects the hollow-fibers included in the clots, the measured clot volume overestimates the actual clotting situation, as shown in Figure 2.4. Consequently, correction factors were introduced for the inlet and the outlet chamber.

Since the hollow-fibers were not visible in the MDCT scans, a direct observation of the exact clot-hollow-fiber ratio was not possible. Instead, a geometrical approach was then chosen. The idea was to determine the ratio of blood filled volume (Figure 2.5) in the chamber versus the volume of the chamber without the hollow-fibers as an approximation of the clot-hollow-fiber ratio within the clots. Figures 2.4 and 2.6 provide a graphical explanation of the concept behind the correction factors.

Derived from the concept of Figure 2.6 Equations (2.1) and (2.2) were formulated.

$$c_{Inlet\,Chamber} = \frac{V_{Blood_{Inlet\,Chamber}}}{V_{Inlet\,Chamber}} \approx \frac{V_{Clot_{excluding\,Fibers}}}{V_{Clot_{including\,Fibers}}} \tag{2.1}$$

$$c_{Outlet\,Chamber} = \frac{V_{Blood_{Outlet\,Chamber}}}{V_{Outlet\,Chamber}} \approx \frac{V_{Clot_{excluding\,Fibers}}}{V_{Clot_{including\,Fibers}}} \tag{2.2}$$

Basis for following calculations were measurements taken from a cut-open ML that was not clinically used. To determine correction factors for the MDCT imaging, the total volumes of the inlet and the outlet chamber must be known. Their volumes were calculated according to Equations (2.3) and (2.4). With $l_{ML}$ being the length and $w_{ML}$ being the width of the chamber. The heights of the chamber were defined as $h_{Inlet\,Chamber} = 18$ mm and $h_{Outlet\,Chamber} = 26$ mm. To reduce the complexity of the underlying calculations, symmetrical hollow-fiber arrangement without deformation of the hollow-fibers was assumed. A possible swelling of the hollow-fibers as an interaction with water in the subsequent volume measurements was not considered.

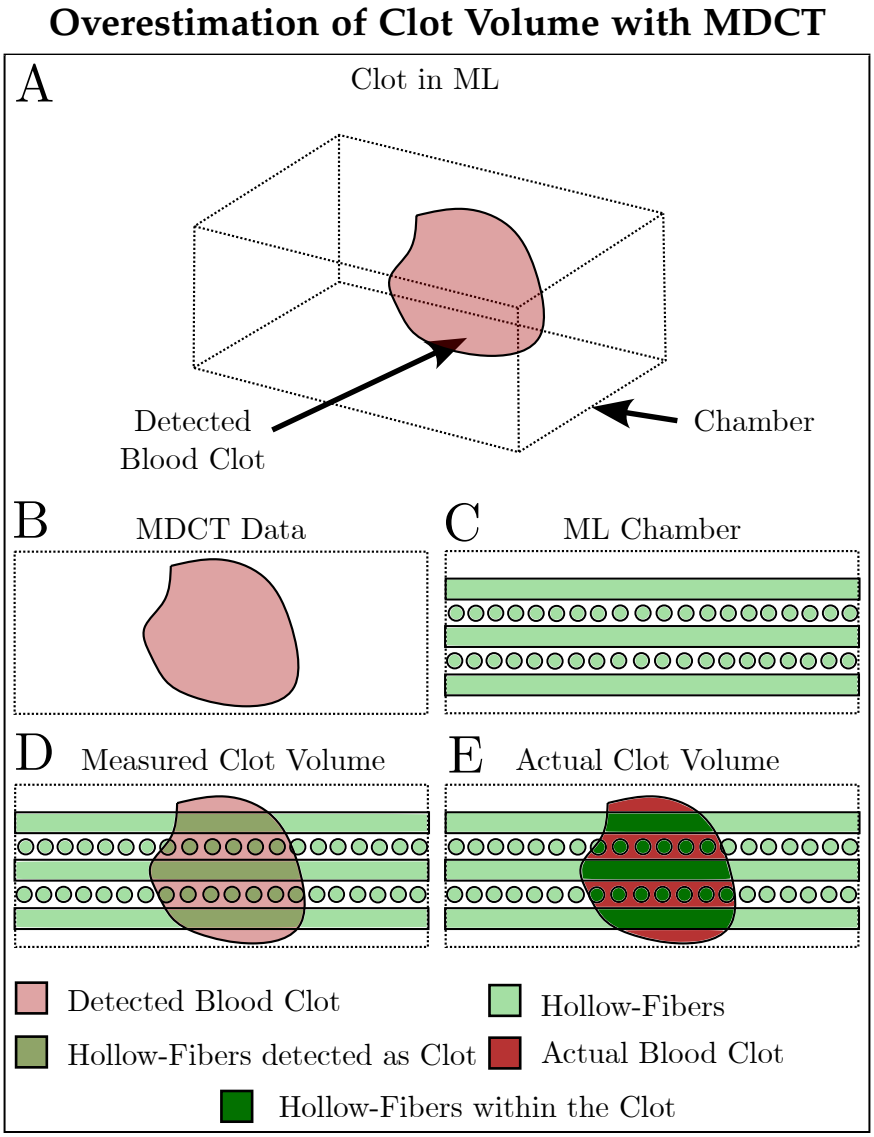


**Figure 2.4: Explanation of wrongfully detected clot volume with MDCT.** (**A,B**) Representation of a three-dimensional blood clot detected by MDCT. This imaging modality only detects the clot but not the hollow-fibers of the ML. (**C**) Display of the actual hollow-fibers of the ML without a blood clot. (**D**) Visualization of the wrongfully detection of hollow-fibers inside the blood clot as a result of the similar attenuation coefficients. (**E**) Actual clot volume depicted as dark red.

Calculation of the inlet chamber volume $V_{Inlet\,Chamber}$:

$$\begin{aligned} V_{Inlet\,Chamber} &= l_{ML} \times w_{ML} \times h_{Inlet\,Chamber} \\ &= 90\ \text{mm} \times 90\ \text{mm} \times 18\ \text{mm} \\ &= 145,800\ \text{mm}^3 \equiv \boxed{145.8\ \text{ml}} \end{aligned} \tag{2.3}$$

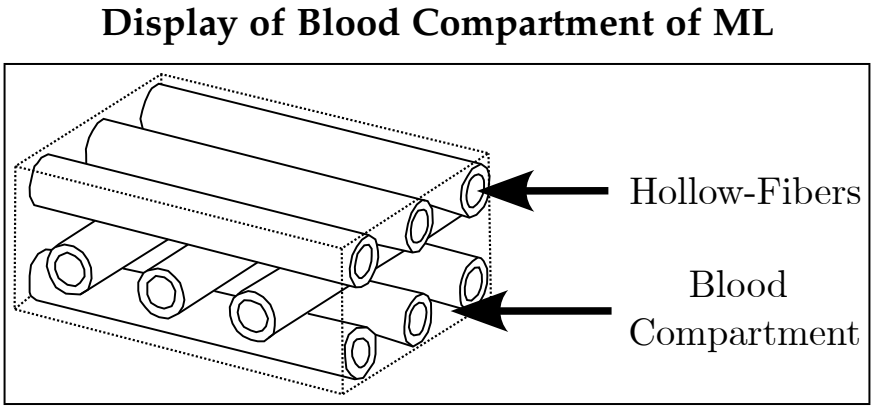


**Figure 2.5: Display of the blood compartment inside the ML.**

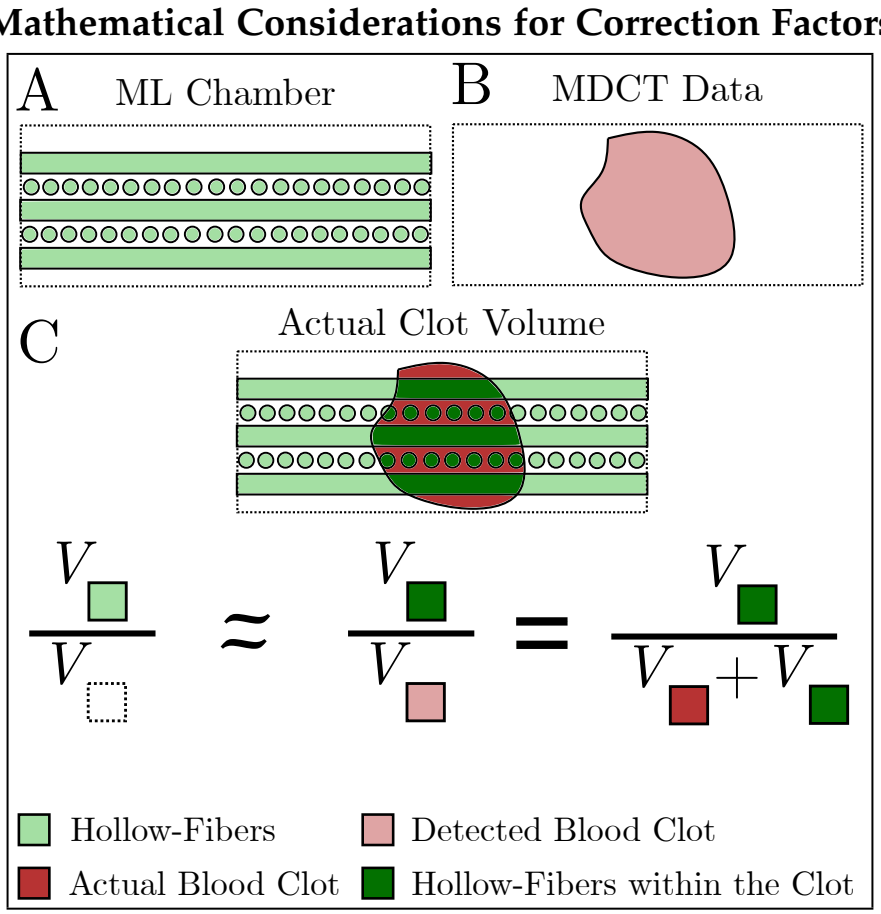


**Figure 2.6: Concept of correction factor for MDCT clot calculation.** (**A**) Illustration of ML hollow-fibers without clot deposition. (**B**) Clot volume derived from MDCT. (**C**) Overestimation of clot volume. The volume of the hollow-fibers surrounded by clots (dark green) was detected as clot volume. Actual clot volume depicted in dark red.

The calculation of the outlet chamber volume $V_{Outlet\,Chamber}$ was performed analogously:

$$\begin{aligned} V_{Outlet\,Chamber} &= l_{ML} \times w_{ML} \times h_{Outlet\,Chamber} \\ &= 90\text{ mm} \times 90\text{ mm} \times 26\text{ mm} \\ &= 210,600\text{ mm}^3 \equiv \boxed{210.6\ \text{ml}} \end{aligned} \tag{2.4}$$

In the next step, the total number of fiber mats for each chamber ($n_{Fibers\,Inlet}$ and $n_{Fibers\,Outlet}$) was calculated according to Equations (2.5) and (2.6). with the number of hollow-fibers in a single fiber mat $n_{Fibers\,per\,Mat} = 160$ and $f$ as the number of fiber mats in the chambers ($f_{Inlet} = 45$ and $f_{Outlet} = 74$).

Calculation of the total number of hollow-fibers in the inlet chamber ($n_{Fibers\,Inlet}$):

$$\begin{aligned} n_{Fibers\,Inlet} &= n_{Fibers\,per\,Mat} \times f_{Inlet} \\ &= 160 \times 45 = \boxed{7{,}200} \end{aligned} \tag{2.5}$$

Calculation of the total number of hollow-fibers in the outlet chamber ($n_{Fibers\,Outlet}$):

$$\begin{aligned} n_{Fibers\,Outlet} &= n_{Fibers\,per\,Mat} \times f_{Outlet} \\ &= 160 \times 74 = \boxed{11{,}840} \end{aligned} \tag{2.6}$$

Furthermore, the volume occupied by a single hollow-fiber $V_{Single\,Hollow-Fiber}$ was calculated according to Equation (2.7). With $d = 0.38$ mm as the diameter and

$l_{Hollow-Fiber} = 90$ mm as the length of the hollow-fiber.

$$\begin{aligned} V_{Single\,Hollow-Fiber} &= \frac{d^2}{4} \times \pi \times l_{Hollow-Fiber} \\ &= \frac{(0.38\text{ mm})^2}{4} \times \pi \times 90\text{ mm} \\ &= 10.21\text{ mm}^3 \equiv \boxed{0.01021\text{ ml}} \end{aligned} \tag{2.7}$$

With this information, the volume of the chambers which are filled with blood was determined with Equations (2.8) and (2.9):

$$\begin{aligned} V_{Blood_{Inlet\,Chamber}} &= V_{Inlet\,Chamber} - V_{Single\,Hollow-Fiber} \times n_{Fibers\,Inlet} \\ &= 145.8\text{ ml} - 0.01021\text{ ml} \times 7,200 \\ &= 145.8\text{ ml} - 73.5\text{ ml} = \boxed{72.3\text{ ml}} \end{aligned} \tag{2.8}$$

$$\begin{aligned} V_{Blood_{Outlet\,Chamber}} &= V_{Outlet\,Chamber} - V_{Single\,Hollow-Fiber} \times n_{Fibers\,Outlet} \\ &= 210.6\text{ ml} - 0.01021\text{ ml} \times 11,840 \\ &= 210.6\text{ ml} - 120.9\text{ ml} = \boxed{89.7\text{ ml}} \end{aligned} \tag{2.9}$$

Based on these calculations, the correction factors can be derived with Equations (2.10) and (2.11):

$$c_{Inlet\,Chamber} = \frac{V_{Blood_{Inlet\,Chamber}}}{V_{Inlet\,Chamber}} = \frac{72.3\text{ ml}}{145.8\text{ ml}} = \boxed{0.496} \tag{2.10}$$

$$c_{Outlet\,Chamber} = \frac{V_{Blood_{Outlet\,Chamber}}}{V_{Outlet\,Chamber}} = \frac{89.7\text{ ml}}{210.6\text{ ml}} = \boxed{0.426} \tag{2.11}$$

### 2.2.9 Measurement of ML Blood Volume

In order to relate the detected clot volume with the total volume of the blood compartment (Figure 2.5), its volume was measured.

Figure 2.7 depicts the measurement setup. A non-clinically used PLS ML was fixed to a mounting in a horizontal position with the inlet connector pointing downwards. Via a syringe pump (AL-1000, World Precision Instruments, Sarasota, FL, USA) equipped with a 50 ml syringe distilled water was filled in a controlled manner.

First, the syringe was filled with water by opening a three-way valve that allow aspirating water from a glass container (filled with 500 ml of distilled water). The valve was then switched to allow the water to flow inside the ML. The entire silicone tubing was filled prior to the measurements.

#### Volume of the Inlet Connector

The syringe pump set to a flow rate of 500 ml/h and water filled the inlet connector as well as the area of the distributor plate. The pump was stopped when the all holes of

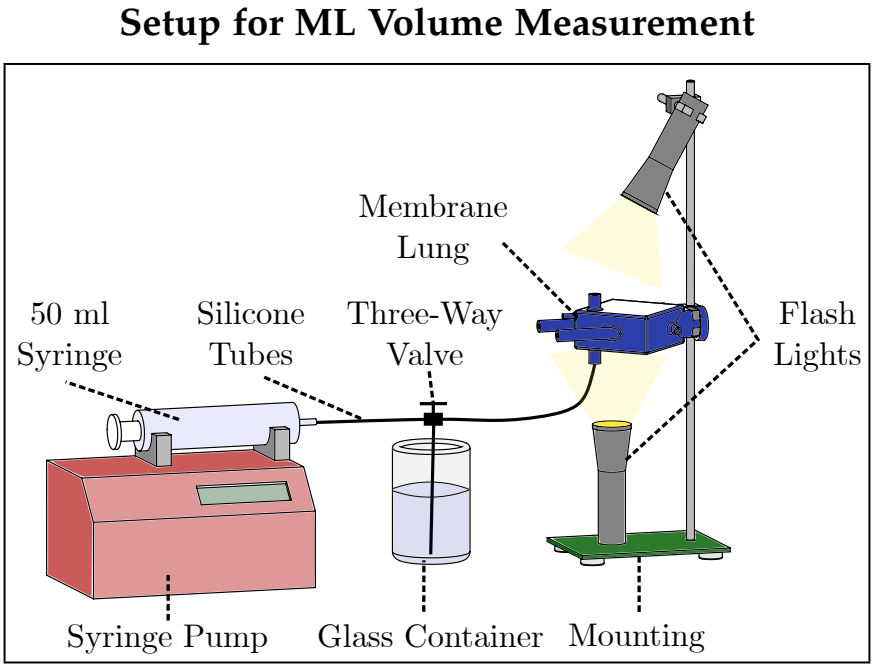


**Figure 2.7: Setup for measuring blood filled volume of ML.** The setup consists of three central components: A syringe pump (left), a container filled with 500 ml of distilled water (middle), and a vertical mounting with the ML fixed in a horizontal position illuminated from the bottom and the top using two torch lights (right). Water is infused into the ML via silicone tubes while the syringe pumps documents the introduced volume. In order to refill the syringe without impacting the already infused volume, a three-way valve is utilized. Depending on its configuration, the water can be aspirated from the glass container or infused into the ML. The torch lights facilitated the observation of the rising water level. Finally, the total infused volume was read from the syringe pump.

the distributor plate were filled with water. This moment was determined by visual inspection, flash lights facilitated the visibility of the water. The total infused volume of water was then taken from the syringe pump. At the end, the water was completely drained from the ML. The measurement was repeated four more times.

### Volume of the Outlet Connector

The ML was rotated 180° so that the outlet connector was facing downwards. The measurement was conducted analogously to the inlet connector volume.

### Volume of Entire ML

The water was filled in with a flow rate of 999.9 ml/h (max. flow rate of syringe pump) until it reached the top of the upper connector. The syringe had to be refilled during the measurement. This was carried out by pausing the pump and switching the three-way valve. The syringe was then filled with water from the glass container. After switching the back the three-way valve, the filling was continued. The refilling process was required for another four times. After the measurement was complete, the water was drained and the ML was dried with pressurized air for 15 minutes. This measurement was then also repeated for another four times.

### Volume of the Dividing Wall

The volume of the dividing wall was determined by removing it from another non-clinically used ML that was cut open (Section 2.2.8). The entire dividing wall was weighed with a high-precision scale (ABJ-NM/ABS-N, Kern & Sohn, Balingen-Frommern, Germany). With a density of $\rho = 1.24\ \mathrm{g/cm^3}$ of polycarbonate (PC), the volume of the dividing wall was calculated according to Equation (2.12).

$$\begin{aligned} V_{DW_{Grid}} &= \frac{\bar{m}_{DW}\ \mathrm{g}}{1.24\ \mathrm{g/cm^3}} \\ &= \frac{11.19\ \mathrm{g}}{1.24\ \mathrm{g/cm^3}} = 9.02\ \mathrm{cm^3} \equiv \boxed{9.02\ \mathrm{ml}} \end{aligned} \tag{2.12}$$

In order to receive the free space (blood volume) within the dividing wall, its volume was subtracted from a cuboid with the dividing wall's outer dimensions, as shown in Equation (2.13).

**Table 2.2: Blood volume of ML subsections.** Data given as mean ± standard deviation; *: Calculated value.

| Structure | Inlet Port | Dividing Wall | Outlet Port | Blood Comp. | Total |
|---|---|---|---|---|---|
| **Blood Volume / ml** | 24.13 ± 1.14 | 15.28 ± 0.00 | 24.13 ± 1.14 | 165.34 * | 228.88 ± 0.93 |

$$
\begin{aligned}
V_{DW_{Blood\ Volume}} &= l_{DW} \times w_{DW} \times h_{DW} - V_{DW_{Grid}} \\
&= 90\ \text{mm} \times 90\ \text{mm} \times 3\ \text{mm} - 9.02\ \text{ml} \\
&= 24,3000\ \text{mm}^3 - 9.02\ \text{ml} \\
&\equiv 24.30\ \text{ml} - 9.02\ \text{ml} = \boxed{15.28\ \text{ml}}
\end{aligned}
\tag{2.13}
$$

**Volume of the Blood Compartment**

The resulting volume data are presented in Table 2.2. Specifically relevant was the volume of the blood compartment ($V_{Blood\,Compartment} = 165.34$ ml) for later categorization of the clot volume. It was received by subtracting the individual volumes of the inlet port, the dividing wall, and the outlet port from the total priming volume of the ML.

## 2.3 Results

Following section presents the calculated clot volumes derived from MDCT, µCT, and FMI data. First, an macroscopic overview clot volume in the entire is provided follow by detailed information on clot load on individual fiber mats. The results are presented as mean values with their corresponding 95 % confidence interval.

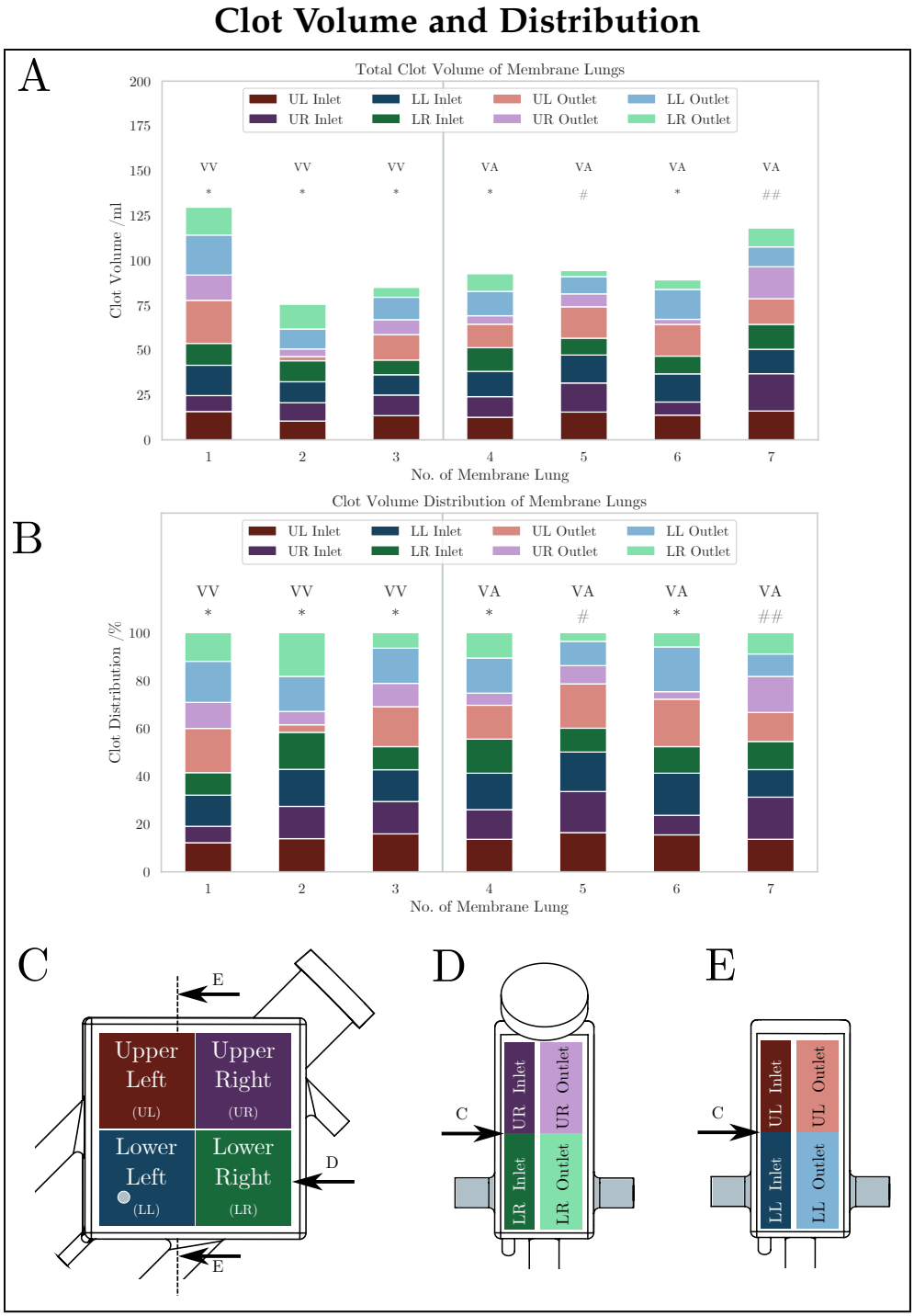


**Figure 2.8: Total clot volume of seven investigated MLs with µCT.** (**A**) Total clot load of each sector in all investigated MLs. (**B**) Clot volume distribution depending on the ML sector. (**C-E**) Display of each sector inside the ML. *: End-of-therapy ML; #: First exchange ML; ##: Second exchange ML. VV: VV ECMO; VA: VA ECMO.

### 2.3.1 Total Clot Volume

Figure 2.8 depicts to total clot volume found with µCT as well as their distribution across the predefined sectors within the seven investigated MLs. It can be observed that clot volumes ranged between $V_{total_{min}} = 75$ ml ($\approx 45$ % of ML blood volume) and $V_{total_{max}} = 129$ ml ($\approx 78$ % of ML volume). MLs #2-#6 show similar clot volume ($V_{total} = 75 - 94$ ml; $\approx\ 45 - 57$ % ML volume). However, MLs #1 and #7 are distinguished by a considerably higher clot volume ($V_{total} = 118 - 129$ ml; $\approx\ 71 - 78$ % ML volume). In order to identify certain sectors of high clot volume, a normalization was conducted. All measured clot volumes of each sector were divided by the total ML blood volume ($V_{ML_{Blood}} = 165.34$ ml) from Table 2.2. The clot volume distribution indicates a similar clot volume in the inlet chamber and the outlet chamber, except for ML #1 which is characterized by a clearly higher clot volume in the outlet chamber. Clot formation focuses especially on the UL, the UR, and LL sectors of the inlet chamber as well as on the UL and LL sectors of the outlet chamber.

A comparison of the total clot volume detected with the three given imaging modalities is presented in Figure 2.9 (a). Each boxplot presents the total measured clot volume of all seven MLs. It can be observed that all three imaging modalities yield different results.

µCT shows the highest total clot volume with a mean volume of $\bar{V}_{total_{\mu CT}} = 98$ ml ($ci_{total_{\mu CT}} = 84 - 111$ ml). MDCT data detects slightly less clot volume with a mean volume of $\bar{V}_{total_{MDCT}} = 70$ ml ($ci_{total_{MDCT}} = 50 - 90$ ml). However, both imaging modalities showed no significant difference ($p > 0.05$). In contrast, FMI showed significant lower total clot volume ($p \leq 0.05$) compared to both other imaging modalities. FMI detected a mean clot volume of $\bar{V}_{total_{FMI}} = 32$ ml ($ci_{total_{FMI}} = 7 - 57$ ml).

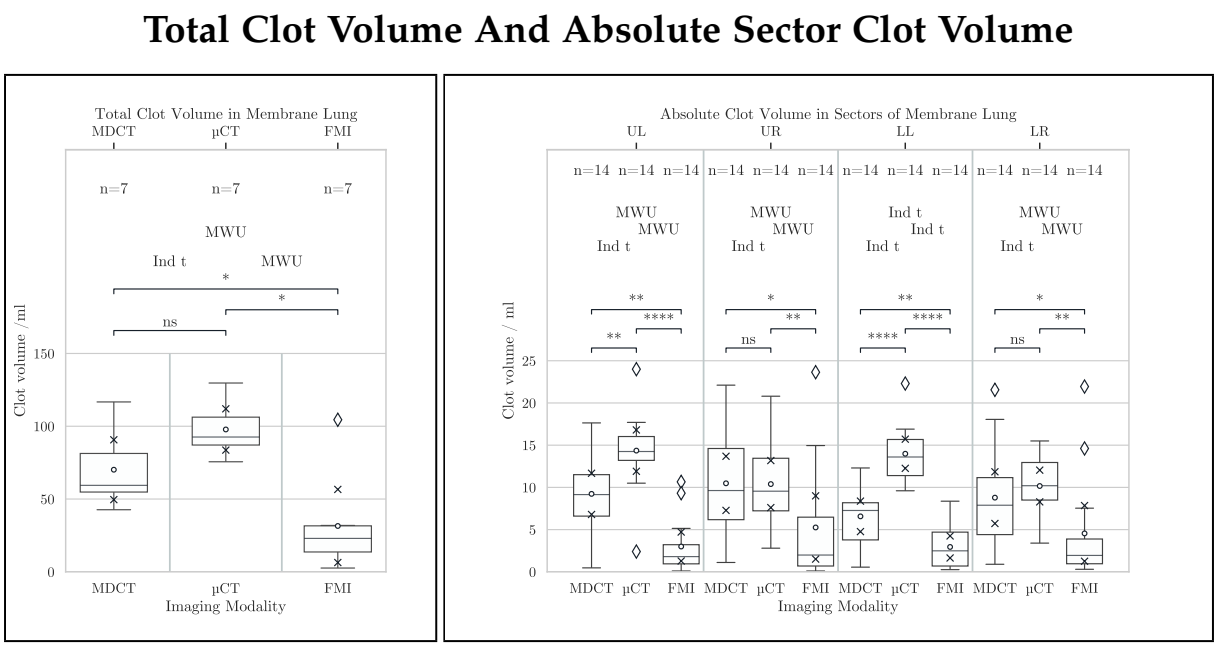


(a) Total clot volume in MLs. (b) Absolute clot volume per sector.

**Figure 2.9: Total clot volume inside the seven analyzed MLs investigated with MDCT, µCT, and FMI.**
(**a**) Display of total clot load detected in all seven MLs. (**b**) Absolute clot load in all four previously defined sectors; both chambers combined. $n$: Number of data points in the boxplot; $f$: Number of fiber mats in chamber. Whisker bars: 1.5 × IQR; box: ranging from the 1st quartile to the 3rd quartile; horizontal line: median; circle: mean; crosses: 95 % confidence interval, diamonds: outliers. UL: upper left sector; UR: upper right sector; LL: lower left sector; LR: lower right sector. VV: VV ECMO; VA: VA ECMO. Statistical tests: MWU: Mann-Whitney U test; Welch t: Welch t-test, Ind t: Independent t-test, Wilcoxon: Wilcoxon test; Paired t: Paired t-test. ns: not significant $0.05 < p \leq 1.00$; *: $0.01 < p \leq 0.05$; **: $0.001 < p \leq 0.01$; ***: $0.0001 < p \leq 0.001$; ****: $p \leq 0.0001$.

### 2.3.2 Mean Absolute Clot Volume per Sector

Figure 2.9 (b) presents the clot volume in each individual sector (both chambers). Every boxplot is composed of 14 data points since both the inlet part and the outlet part of the sector are considered.

#### Upper Left and Lower Left Sector

It can be observed that the UL and the LL sectors show similar clot load, independent from the imaging modality. Again, µCT shows the highest clot volume with a mean

clot volume per sector of $\bar{V}_{abs_{UL_{\mu CT}}} = 17$ ml ($ci_{abs_{UL_{\mu CT}}} = 12 - 17$ ml) for the UL sector and $\bar{V}_{abs_{LL_{\mu CT}}} = 16$ ml ($ci_{abs_{LL_{\mu CT}}} = 12 - 16$ ml).

MDCT detects significantly less clot volume in those two sectors compared to the µCT (UL: $p \leq 0.001$ and LL: $p \leq 0.0001$). Still, the clot volumes within the UL and the LL sectors are similar. MDCT shows a mean clot volume per sector of $\bar{V}_{abs_{UL_{MDCT}}} = 9$ ml ($ci_{abs_{UL_{MDCT}}} = 7 - 12$ ml) for the UL sector and $\bar{V}_{abs_{LL_{MDCT}}} = 7$ ml ($ci_{abs_{LL_{MDCT}}} = 5 - 8$ ml) for the LL sector.

FMI shows again the lowest clot volume with a mean clot volume per sector of $\bar{V}_{abs_{UL_{FMI}}} = 3$ ml ($ciabs_{UL_{FMI}} = 1 - 3$ ml) for the UL sector and $\bar{V}_{abs_{LL_{FMI}}} = 3$ ml ($ci_{abs_{LL_{FMI}}} = 2 - 3$ ml) for the LL sector. A significant difference between FMI and µCT ($p \leq 0.0001$) as well as between FMI and MDCT ($p \leq 0.001$) was detected for both sectors ($p \leq 0.0001$).

**Upper Right and Lower Right Sector**

Contrary to the UL and LL sectors, µCT and MDCT show no significant difference ($p > 0.05$) in clot volume for both, the UR and LR sector.

A mean clot volume for the UR sector was detected with $\bar{V}_{abs_{UR_{\mu CT}}} = 10$ ml ($ci_{abs_{UR_{\mu CT}}} = 8 - 13$ ml) using µCT and $\bar{V}_{abs_{UR_{MDCT}}} = 10$ ml ($ci_{abs_{UR_{MDCT}}} = 7 - 14$ ml) using MDCT.

In the LR sector, µCT yields a higher, still not significant ($p > 0.05$), clot volume compared to the MDCT. µCT shows a mean clot volume of $\bar{V}_{abs_{LR_{\mu CT}}} = 10$ ml ($ci_{abs_{LR_{\mu CT}}} = 8 - 12$ ml). However, MDCT detects $\bar{V}_{LR_{MDCT}} = 9$ ml ($ci_{abs_{LR_{MDCT}}} = 6 - 12$ ml).

Again, FMI yields the lowest mean clot volume with $\bar{V}_{abs_{UR_{FMI}}} = 5$ ml ($ci_{abs_{UR_{FMI}}} = 2 - 9$ ml) for the UR sector and $\bar{V}_{abs_{LR_{FMI}}} = 5$ ml ($ci_{abs_{LR_{FMI}}} = 1 - 8$ ml) for the LR sector.

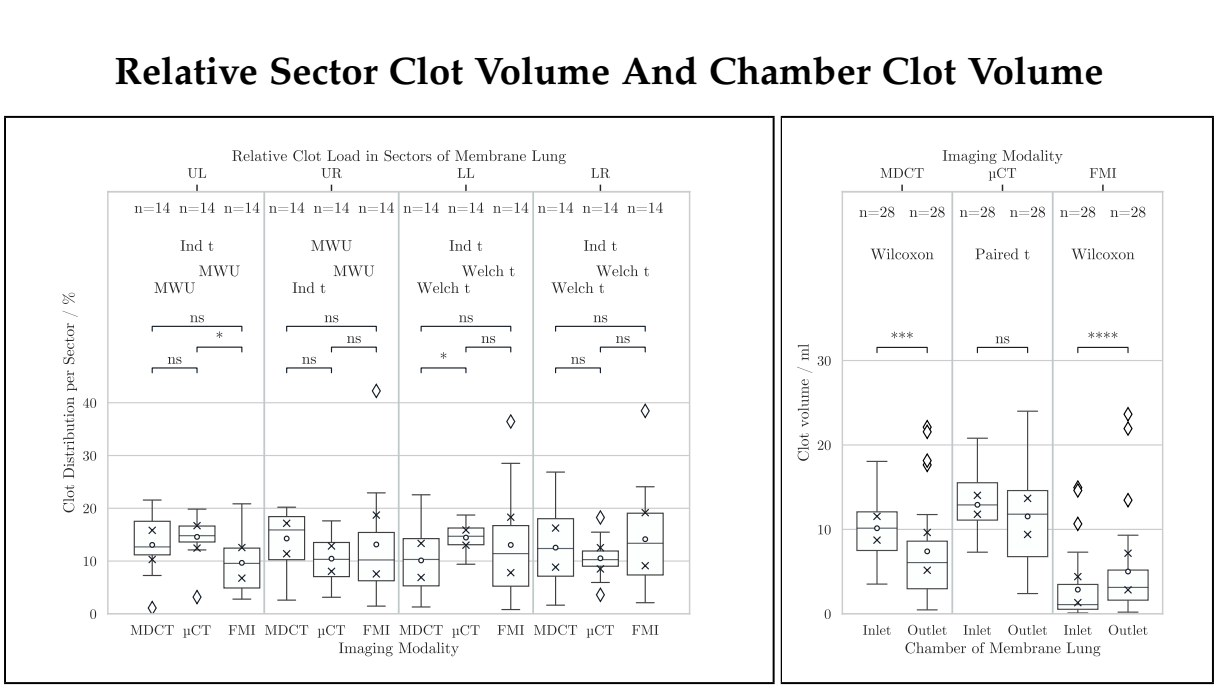


(a) Relative clot volume per sector. (b) Absolute clot vol. per chamber.

**Figure 2.10: Clot volume inside the seven analyzed MLs investigated with MDCT, µCT, and FMI.** (**a**) Relative clot load in all four previously defined sectors. Both chambers combined; normalized to the volume of the sector. (**b**) Comparison of all sectors in the inlet chamber to all sectors of the outlet chamber. $n$: Number of data points in the boxplot; $f$: Number of fiber mats in chamber. Whisker bars: 1.5 × IQR; box: ranging from the 1st quartile to the 3rd quartile; horizontal line: median; circle: mean; crosses: 95 % confidence interval, diamonds: outliers. UL: upper left sector; UR: upper right sector; LL: lower left sector; LR: lower right sector. VV: VV ECMO; VA: VA ECMO. Statistical tests: MWU: Mann-Whitney U test; Welch t: Welch t-test, Ind t: Independent t-test, Wilcoxon: Wilcoxon test; Paired t: Paired t-test. ns: not significant $0.05 < p \leq 1.00$; *: $0.01 < p \leq 0.05$; **: $0.001 < p \leq 0.01$; ***: $0.0001 < p \leq 0.001$; ****: $p \leq 0.0001$.

### 2.3.3 Mean Relative Clot Volume per Sector

The relative clot volume was calculated by dividing the individual clot volume per sector by the measured total clot volume of the entire ML. These results are presented in Figure 2.10 (a). Every boxplot is composed of 14 data points since both the inlet part and the outlet part of the sector are considered.

In general, this illustration shows that the relative clot volume is similar across all sectors, regardless of imaging modality.

### Upper Left Sector

The mean relative clot volume in the UL sector amounts to $\bar{V}_{rel_{UL_{\mu CT}}} = 15$ % and a confidence interval of $ci_{rel_{UL_{\mu CT}}} = 13 - 17$ % using µCT, $\bar{V}_{rel_{UL_{MDCT}}} = 13$ % and a confidence interval of $ci_{rel_{UL_{MDCT}}} = 10 - 16$ % using MDCT, and $\bar{V}_{rel_{UL_{FMI}}} = 10$ % and a confidence interval of $ci_{rel_{UL_{\mu CT}}} = 6 - 13$ % using FMI. Only a significant difference between the µCT and the FMI data sets ($p \leq 0.05$) was detectable. The MDCT and the µCT data sets as well as MDCT and FMI data sets showed no significant difference ($p > 0.05$).

### Upper Right Sector

The mean relative clot volume in the UR sector amounts to $\bar{V}_{rel_{UR_{\mu CT}}} = 10$ % and a confidence interval of $ci_{rel_{UR_{\mu CT}}} = 8 - 13$ % using µCT, $\bar{V}_{rel_{UR_{MDCT}}} = 15$ % and a confidence interval of $ci_{rel_{UR_{MDCT}}} = 11 - 18$ % using MDCT, and $\bar{V}_{rel_{UR_{FMI}}} = 14$ % and a confidence interval of $ci_{rel_{UR_{\mu CT}}} = 7 - 18$ % using FMI. All three data sets showed no significant differences ($p > 0.05$).

### Lower Left Sector

The mean relative clot volume in the LL sector amounts to $\bar{V}_{rel_{LL_{\mu CT}}} = 14$ % and a confidence interval of $ci_{rel_{LL_{\mu CT}}} = 12 - 16$ % using µCT, $\bar{V}_{rel_{LL_{MDCT}}} = 10$ % and a confidence interval of $ci_{rel_{LL_{MDCT}}} = 7 - 13$ % using MDCT, and $\bar{V}_{rel_{LL_{FMI}}} = 13$ % and a confidence interval of $ci_{rel_{LL_{\mu CT}}} = 8 - 18$ % using FMI. The µCT data showed a significant difference ($p \leq 0.05$) compared to the MDCT data. All other data sets showed no significant difference ($p > 0.05$).

#### Lower Right Sector

The mean relative clot volume in the UL sector amounts to $\bar{V}_{rel_{LR_{\mu CT}}} = 11$ % and a confidence interval of $ci_{rel_{LR_{\mu CT}}} = 8 - 13$ % using µCT, $\bar{V}_{rel_{LR_{MDCT}}} = 13$ % and a confidence interval of $ci_{rel_{LR_{MDCT}}} = 9 - 13$ % using MDCT, and $\bar{V}_{rel_{LR_{FMI}}} = 14$ % and a confidence interval of $ci_{rel_{LR_{\mu CT}}} = 9 - 18$ % using FMI. All three data sets showed no significant differences ($p > 0.05$).

### 2.3.4 Absolute Clot Load in ML Chambers

A second division of the total ML volume was carried out by using the structural separation in the inlet and the outlet chamber. In Figure 2.10 (b) the clot volume located in the inlet chamber (UL inlet, UR inlet, LL inlet, and LR inlet) is compared to the clot volume in the outlet chamber (UL outlet, UR outlet, LL outlet, and LR outlet). Every boxplot is composed of 28 data points (four sectors per chamber for each of the seven MLs). It was checked for significant differences in clot volume per chamber. Each imaging modality detected different clot volumes.

#### µCT Data

The µCT again resulted in the highest mean clot volume per chamber with $\bar{V}_{abs_{Inlet_{\mu CT}}} = 13$ ml ($ci_{abs_{Inlet_{\mu CT}}} = 12 - 14$ ml) for the inlet chamber and $\bar{V}_{abs_{Outlet_{\mu CT}}} = 11$ ml ($ci_{abs_{Inlet_{\mu CT}}} = 10 - 14$ ml) for the outlet chamber. No significant differences ($p > 0.05$) between the inlet and the outlet chamber was found.

#### MDCT Data

The MDCT shows slightly less clot volume in both chambers compared to the µCT. A mean clot volume per chamber of $\bar{V}_{abs_{Inlet_{MDCT}}} = 10$ ml ($ci_{abs_{Inlet_{MDCT}}} = 9 - 12$ ml) was

detected for the inlet chamber and $\bar{V}_{abs_{Outlet_{MDCT}}} = 8$ ml ($ci_{abs_{Inlet_{\mu CT}}} = 5 - 10$ ml) was detected for the outlet chamber. A highly significant difference ($p \leq 0.001$) between the inlet and the outlet chamber was found.

**FMI Data**

Similar to previous results, FMI yields less clot volume. FMI detected a mean clot volume per chamber of $\bar{V}_{abs_{Inlet_{FMI}}} = 3$ ml ($ci_{abs_{Inlet_{FMI}}} = 1 - 5$ ml) inside the inlet chamber and a volume of $\bar{V}_{abs_{Outlet_{FMI}}} = 5$ ml ($ci_{abs_{Inlet_{\mu CT}}} = 3 - 7$ ml) for the outlet chamber. Furthermore, a highly significant difference ($p \leq 0.0001$) between the inlet and the outlet chamber was found.

### 2.3.5 Clot Volume per Fiber Mat

Observing the absolute clot volume per chamber does not consider the difference in size of the chambers. As illustrated in Figure 2.1 the inlet chamber is distinctly smaller than the outlet chamber. It only comprises of 45 fiber mats compared to the 74 fiber mats of the outlet chamber. Under the consideration of the different chamber sizes, a normalization of the data was chosen. The data was divided by the individual number of fiber mats to yield the mean clot volume per fiber mat, shown in Figure 2.11.

The MDCT and µCT data in Figure 2.11 indicate a significantly higher clot volume per fiber mat in the inlet chamber compared to the outlet chamber for all sectors. In contrast, FMI shows no significant difference between the clot volume per fiber mat in the inlet and the outlet chamber ($p > 0.05$).

**µCT Data**

Again, µCT shows the highest clot volume per fiber mat with a mean of $\bar{V}_{UL-Inlet_{\mu CT}} = 0.31$ ml ($ci_{UL-Inlet_{\mu CT}} = 0.27 - 0.34$ ml) for the inlet chamber and a mean of $\bar{V}_{UL-Outlet_{\mu CT}} =$

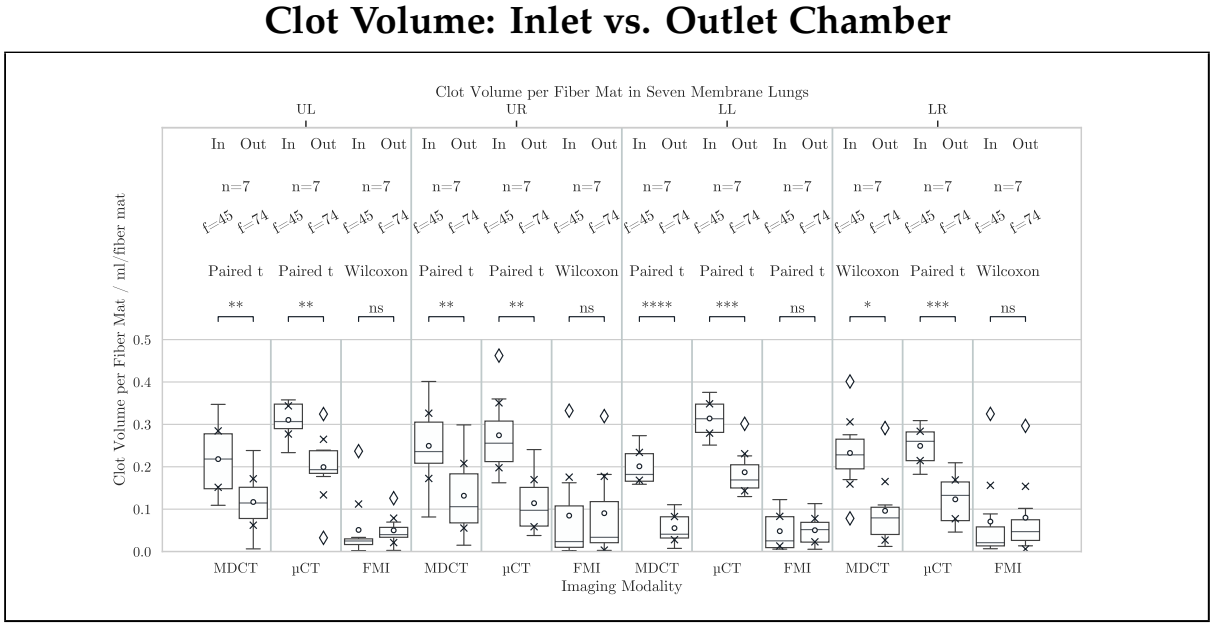


**Figure 2.11: Clot volume per fiber mat in seven investigated MLs**. Comparison of the clot volume per fiber mat in the inlet chamber and the outlet chamber for all sectors. To allow this comparison, a normalization was carried out by division of the total clot load in each sector by the number of fiber mats ($f$) within the chamber.
In: Inlet chamber; Out: Outlet chamber. $n$: Number of data points in the boxplot; $f$: Number of fiber mats in chamber. UL: Upper left sector; UR: upper right sector; LL: lower left sector; LR: lower right sector. Whisker bars: 1.5 × IQR; box: ranging from the 1$^{st}$ quartile to the 3$^{rd}$ quartile; horizontal line: median; circle: mean; crosses: 95 % confidence interval, diamonds: outliers. Statistical tests: Wilcoxon: Wilcoxon test; Paired t: Paired t-test. ns: not significant $0.05 < p \leq 1.00$; *: $0.01 < p \leq 0.05$; **: $0.001 < p \leq 0.01$; ***: $0.0001 < p \leq 0.001$; ****: $p \leq 0.0001$.

0.19 ml ($ci_{UL-Inlet_{\mu CT}} = 0.13 - 0.26$ ml) for the outlet chamber within the UL sector. The fiber mats of the inlet chamber contain significantly more ($p \leq 0.01$) clot volume per fiber mat compared to those inside the outlet chamber.

Inside the UR sector a mean clot volume per fiber mat of $\bar{V}_{UR-Inlet_{\mu CT}} = 0.27$ ml ($ci_{UR-Inlet_{\mu CT}} = 0.19 - 0.35$ ml) for the inlet chamber and a mean of $\bar{V}_{UR-Outlet_{\mu CT}} = 0.11$ ml ($ci_{UR-Inlet_{\mu CT}} = 0.06 - 0.17$ ml) for the outlet chamber was detected. Also in this sector, the fiber mats of the inlet chamber contain significantly more ($p \leq 0.001$) clot volume per fiber mat compared to those inside the outlet chamber.

Inside the LL sector a mean clot volume per fiber mat of $\bar{V}_{LL-Inlet_{\mu CT}} = 0.31$ ml ($ci_{UR-Inlet_{\mu CT}} = 0.28 - 0.35$ ml) for the inlet chamber and a mean of $\bar{V}_{LL-Outlet_{\mu CT}} = 0.19$ ml ($ci_{LL-Inlet_{\mu CT}} = 0.14 - 0.23$ ml) for the outlet chamber was detected. A significantly higher ($p \leq 0.001$) clot volume per fiber mat inside the inlet chamber compared to the outlet chamber was found.

The LR sector shows a mean clot volume per fiber mat of $\bar{V}_{LR-Inlet_{\mu CT}} = 0.25$ ml ($ci_{LR-Inlet_{\mu CT}} = 0.21 - 0.29$ ml) for the inlet chamber and a mean of $\bar{V}_{LR-Outlet_{\mu CT}} = 0.12$ ml ($ci_{LR-Inlet_{\mu CT}} = 0.08 - 0.17$ ml) for the outlet chamber was detected. A significantly higher ($p \leq 0.001$) clot volume per fiber mat inside the inlet chamber compared to the outlet chamber was found.

**MDCT Data**

The MDCT detects slightly less clot volume per fiber mat than the µCT with a mean of $\bar{V}_{UL-Inlet_{MDCT}} = 0.22$ ml ($ci_{UL-Inlet_{MDCT}} = 0.15 - 0.28$ ml) for the inlet chamber and a mean of $\bar{V}_{UL-Outlet_{MDCT}} = 0.19$ ml ($ci_{UL-Inlet_{MDCT}} = 0.06 - 0.17$ ml) for the outlet chamber within the UL sector. The fiber mats of the inlet chamber contain significantly more ($p \leq 0.01$) clot volume per fiber mat compared to those inside the outlet chamber.

Inside the UR sector a mean clot volume per fiber mat of $\bar{V}_{UR-Inlet_{MDCT}} = 0.25$ ml ($ci_{UR-Inlet_{MDCT}} = 0.17 - 0.33$ ml) for the inlet chamber and a mean of $\bar{V}_{UR-Outlet_{MDCT}} = 0.13$ ml ($ci_{UR-Inlet_{MDCT}} = 0.06 - 0.21$ ml) for the outlet chamber was detected. Also in this sector, the fiber mats of the inlet chamber contain significantly more ($p \leq 0.001$) clot volume per fiber mat compared to those inside the outlet chamber.

Inside the LL sector a mean clot volume per fiber mat of $\bar{V}_{LL-Inlet_{MDCT}} = 0.20$ ml ($ci_{LL-Inlet_{MDCT}} = 0.17 - 0.23$ ml) for the inlet chamber and a mean of $\bar{V}_{LL-Outlet_{MDCT}} = 0.06$ ml ($ci_{LL-Inlet_{MDCT}} = 0.03 - 0.08$ ml) for the outlet chamber was detected. A

significantly higher ($p \leq 0.0001$) clot volume per fiber mat inside the inlet chamber compared to the outlet chamber was found.

The LR sector shows a mean clot volume per fiber mat of $\bar{V}_{LR-Inlet_{MDCT}} = 0.23$ ml ($ci_{LR-Inlet_{MDCT}} = 0.16 - 0.30$ ml) for the inlet chamber and a mean of $\bar{V}_{LR-Outlet_{MDCT}} = 0.09$ ml ($ci_{LR-Inlet_{MDCT}} = 0.03 - 0.16$ ml) for the outlet chamber was detected. A significantly higher ($p \leq 0.05$) clot volume per fiber mat inside the inlet chamber compared to the outlet chamber was found.

**FMI Data**

In contrast to µCT and MDCT, FMI shows distinctly less clot volume per fiber. Furthermore, no significant difference ($p > 0.05$) between the two chambers regarding the clot volume per fiber mat was found in any sector. In addition, every sector contains a similar clot volume per fiber mat.

The FMI detects a mean clot volume per fiber mat of $\bar{V}_{UL-Inlet_{FMI}} = 0.05$ ml ($ci_{UL-Inlet_{FMI}} = 0.01 - 0.11$ ml) for the inlet chamber and a mean of $\bar{V}_{UL-Outlet_{FMI}} = 0.05$ ml ($ci_{UL-Inlet_{FMI}} = 0.02 - 0.08$ ml) for the outlet chamber within the UL sector.

Inside the UR sector a mean clot volume per fiber mat of $\bar{V}_{UR-Inlet_{FMI}} = 0.09$ ml ($ci_{UR-Inlet_{FMI}} = 0.00 - 0.18$ ml) for the inlet chamber and a mean of $\bar{V}_{UR-Outlet_{FMI}} = 0.05$ ml ($ci_{UR-Inlet_{FMI}} = 0.01 - 0.08$ ml) for the outlet chamber was detected.

Inside the LL sector a mean clot volume per fiber mat of $\bar{V}_{LL-Inlet_{FMI}} = 0.05$ ml ($ci_{LL-Inlet_{FMI}} = 0.01 - 0.08$ ml) for the inlet chamber and a mean of $\bar{V}_{LL-Outlet_{FMI}} = 0.05$ ml ($ci_{LL-Inlet_{FMI}} = 0.01 - 0.08$ ml) for the outlet chamber was detected.

The LR sector shows a mean clot volume per fiber mat of $\bar{V}_{LR-Inlet_{MDCT}} = 0.07$ ml ($ci_{LR-Inlet_{FMI}} = 0.00 - 0.15$ ml) for the inlet chamber and a mean of $\bar{V}_{LR-Outlet_{FMI}} = 0.08$ ml ($ci_{LR-Inlet_{FMI}} = 0.00 - 0.15$ ml) for the outlet chamber was detected.

### 2.3.6 Clot Progression throughout the ML

FMI stands out as an imaging modality that allows the detection of the clot volume deposed on each individual fiber mat. While µCT and MDCT detect the clot volume within in a pre-defined region, a direct observation of the clot volume per fiber mat cannot be performed, only a mean clot volume can be calculated.

By this, FMI provides information on the clot progression throughout the entire ML, as depicted in Figure 2.12. Every boxplot consists of seven data points. For better readability, only the results of every second fiber mat are illustrated (only PMP fiber mats) and the median of all seven data points is plotted. Furthermore, when retrieving the TPU fiber mats, the clot were mainly torn and remained on the underlying PMP fiber mat which would have caused artifacts in the data. Therefore, clot may A) have a high affinity to adhere to PMP or A) have a low affinity to adhere to TPU, or both simultaneously.

The course of the graph marks six relevant subsections:

**I** The first layers of the fiber mat in the vicinity of the perforated distributor plate with a rapid decrease in clot volume

**II** A relative constant deposition between fiber mats #7 and #35 (only PMP and TPU fibers)

**III** An increase in clot volume prior to the dividing wall

**IV** A rapid drop of the clot volume after the dividing wall

**V** A second constant clot deposition between fiber mats #53 and #111 (only PMP fibers) with is significantly (Wilcoxon test: $p < 0.0001$) lower clot load compared to the subsection II

**VI** A steep increase in clot volume when approaching the perforated collector plate

### 2.3.7 Comparison of VV and VA ECMO

Unblinding of the data revealed that the MLs of 3 VV ECMO and 4 VA ECMO patients were analyzed. These were compared graphically in Figure 2.13. Statistical analysis was not performed due to the small sample size.

The µCT and the MDCT data of the three investigated MLs from VV ECMO support and the four MLs from VA ECMO support show similar distribution in total clot volume, depicted in Figure 2.13. µCT suggests the highest mean values of $\bar{V}_{total_{VV_{\mu CT}}} =$ 97 ml (min: 76 ml and max: 129 ml) for VV ECMO MLs and $\bar{V}_{total_{VA_{\mu CT}}} = 99$ ml (min: 89 ml and max: 118 ml) for VA ECMO MLs.

MDCT detects less total clot volume with a mean of $\bar{V}_{total_{VV_{MDCT}}} = 73$ ml (min: 43 ml and max: 116 ml) for VV ECMO MLs and $\bar{V}_{total_{VA_{MDCT}}} = 68$ ml (min: 54 ml and max: 102 ml) for VA ECMO MLs.

FMI shows the least total clot volume with a mean of $\bar{V}_{total_{VV_{FMI}}} = 41$ ml (min: 3 ml and max: 104 ml) for VV ECMO MLs and $\bar{V}_{total_{VA_{FMI}}} = 24$ ml (min: 10 ml and max: 32 ml) for VA ECMO MLs.

### 2.3.8 Clot Distribution and Clotting Patterns

Figure 2.14 depicts the raw data derived MDCT (prior to applying the correction factors). It becomes evident that a highly heterogeneous clot distribution is predominant. A clotting pattern can hardly be identified. However, the corner regions of the MLs show a higher affinity to clot deposition.

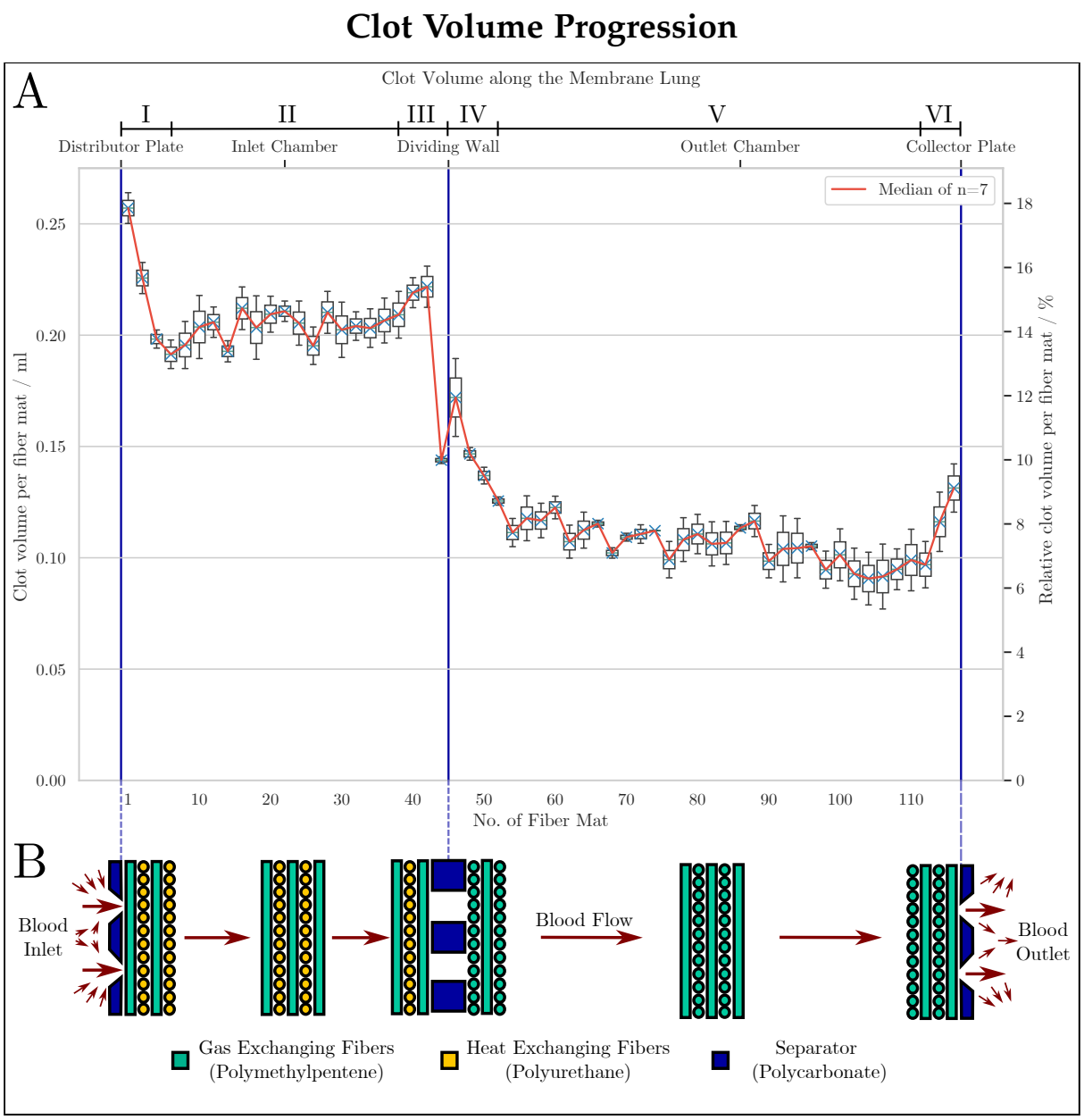


**Figure 2.12: Clot progression along the ML detected with FMI.** (**A**) FMI shows high clot loads especially in the vicinity of both the distributor and the collector plate as well as near the dividing wall. For better readability, only every second data point is presented. (**B**) Display of the relevant interior ML structures for orientation. Whisker bars: 1.5 × IQR; box: ranging from the 1st quartile to the 3rd quartile; green horizontal line: median; blue cross: mean; red line: median across all values. Each boxplot consists of $n = 7$ data points.

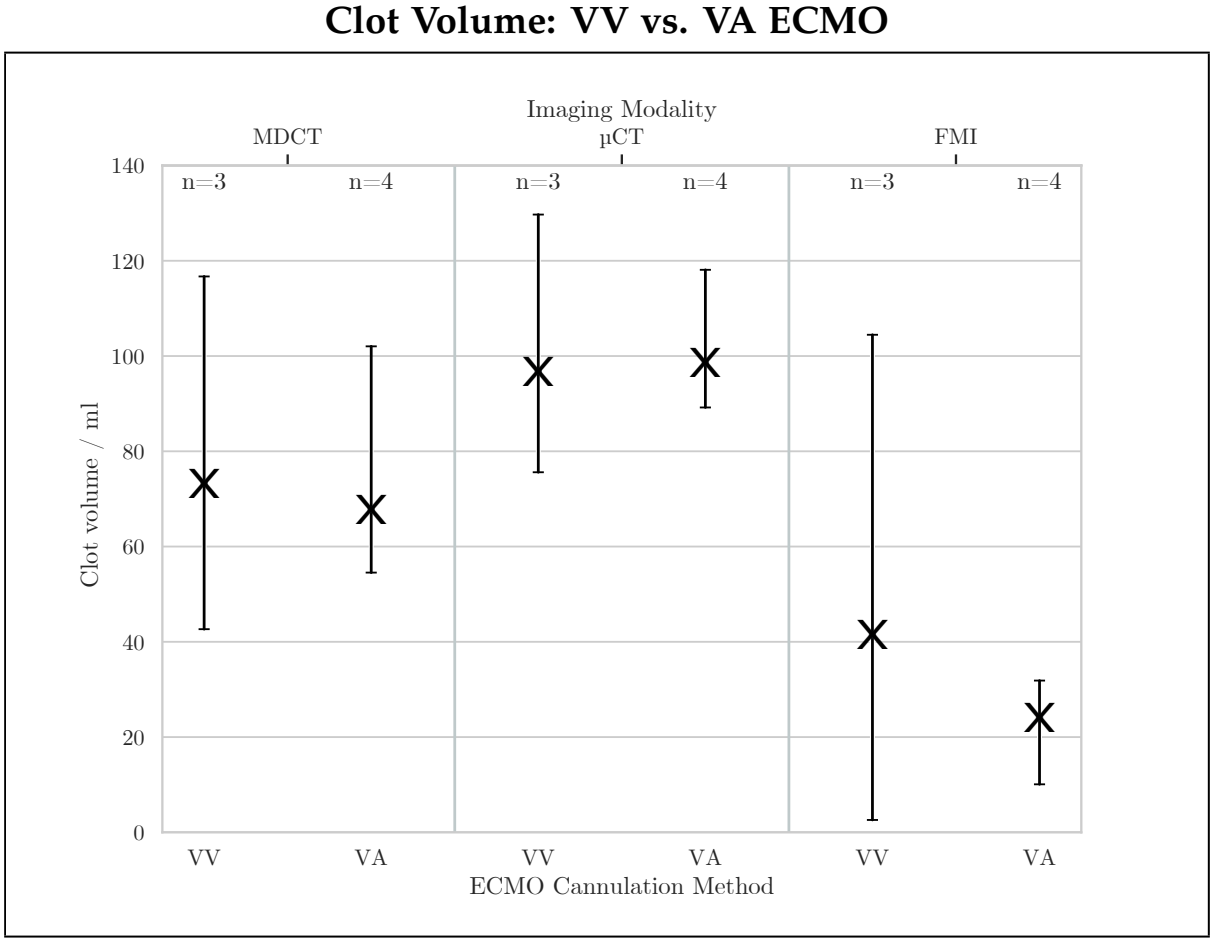


**Figure 2.13: Comparison of clot volume in VV ECMO and VA ECMO using different imaging modalities.** Cross: Mean of sample; Horizontal line: maximum and minimum value of sample.

In addition, special geometrical clot structure were observed, displayed in Figures 2.14 (E4, E5) and 2.15. These structures consist of a large clot structure within the coarse lattice of the dividing wall and a tail-like structure that forms downstream within the hollow-fibers of th outlet chamber. Due to the geometrical shape of the clot structure, these formations were referred as 'comets'. These structures were observed in five of the seven MLs.

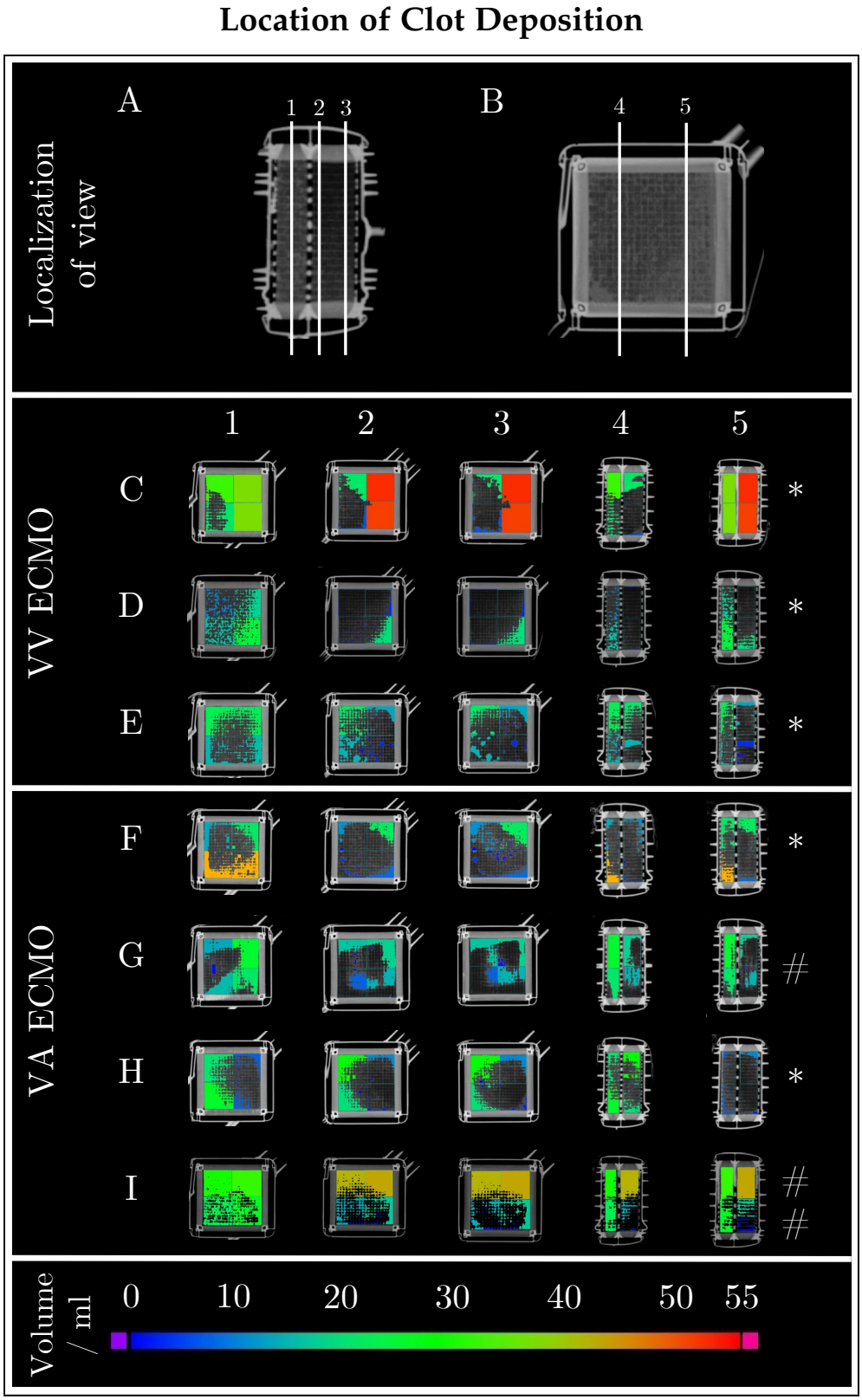


**Figure 2.14: Clot volume in seven investigated MLs using MDCT.** * End-of-therapy MLs, # 1st exchange ML, ## 2nd exchange ML.

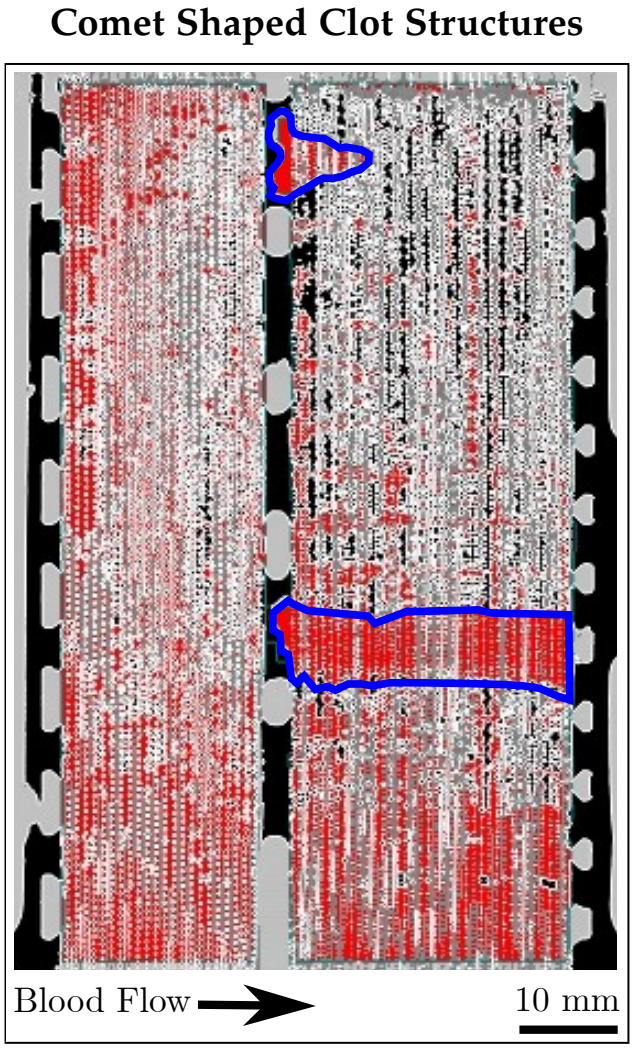


**Figure 2.15: Comet shaped clot structures visualized with µCT**. Blue: Comet structures with a larger clot formation in the coarse lattice of the dividing wall and a tail-like shaped clot structure reaching in the fiber mats of the outlet chamber.

## 2.4 Discussion

This chapter presented three state-of-the-art imaging modalities to detect and evaluate blood clots inside seven clinically used MLs. The MLs were retrieved after clinical ECMO application and imaging was conducted subsequently. Two of the three imaging modalities (µCT and MDCT) are based on computed tomography featuring differently high spatial resolution. A method of improving the data processing of MDCT imaging

was established in this work. In contrast, FMI differs significantly regarding the data acquisition. FMI uses photography of extracted hollow-fiber mats from disassembled and cut-open MLs.

### 2.4.1 Clot Formation Depending on the Used Polymer

As shown by the results, the total clot volume between the investigated MLs differs substantially, making systematic statements hardly possible. However, the data suggest that clots depose especially in the left sectors of the MLs (Figures 2.8 and 2.9 (b, c)).

The total clot volume inside of both chambers seems similar in the first place (Figure 2.9 (d)). However, the inlet chamber is distinctly smaller than the outlet chamber. To allow a better comparison, a normalization to the number of hollow-fiber mats in each chamber was introduced (Figure 2.11).

With this normalization, µCT and MDCT prove a significant higher clot volume per fiber mat within the inlet chamber compared to the outlet chamber. However, FMI does not indicate any difference between both chambers, but it detects significantly less clot volume in general. The representation of the clot volume in Figure 2.11 accumulates the clot volumes of each fiber mat and applies the mean to it. For this reason, the significant difference in clot volume between both chamber is not visible.

However, FMI acquires clot volume data of each individual fiber mat which allows the representation of the clot progression along the MLs, as depicted in Figure 2.12. This representation shows a significant difference between clot volume in the inlet and the outlet chamber (II and V). Furthermore, it allows for the visualization of the clot volume deposed on each individual fiber mat for the first time. It can be observed that the clot deposition is clearly higher in proximity to the PC structures (distributor plate (I), the dividing wall (II and IV), and the collector plate (VI)). Since,

with increasing distance to the PC parts, the clot volume remains constant, the effect of those is expected to be negligible. The structural difference between the inlet chamber and the outlet chamber is the presence of the TPU hollow-fibers. While the inlet chamber contains an alternating arrangement of PMP and TPU hollow-fibers, the outlet chamber does only contain PMP hollow-fibers. This indicates a pro-thrombotic influence of the TPU hollow-fibers as an explanation of the significantly higher clot volume inside the inlet chamber. Recent histological studies from Lehle et al. [59], Wilm et al. [61], Steiger et al. [54], Dropco et al. [62], and Wagner and Kranz et al. [31] excluded the TPU hollow-fibers due to their transparency in the fluorescence microscopy that severely aggravated histological examinations.

A second explanation might be that the fiber mat packaging densities significantly impact the clot depositions. It was shown by the derivation of the corrections factors that the inlet chamber is less densely packed. This additional space might allow a higher clot volume due to its reduced geometrical limitations. Also this concept has not been further discussed in the literature.

Since all three state-of-the-art imaging modalities suggest significantly higher clot volume in areas with TPU hollow-fibers and no dedicated data about their influence inside MLs is currently available, histological examinations of those could provide important insights in the future.

### 2.4.2 Advantages and Disadvantages of Used Imaging Modalities

Successfully detecting clot structures inside clinically used MLs using MDCT was first introduced by Dornia et al. [55]. Since then, Birkenmaier et al. [57] optimized Dornia's protocol to improve the detection quality. Furthermore, Birkenmaier et al. established a protocol for clot detection using high-resolution industrial µCT. However, Wagner and

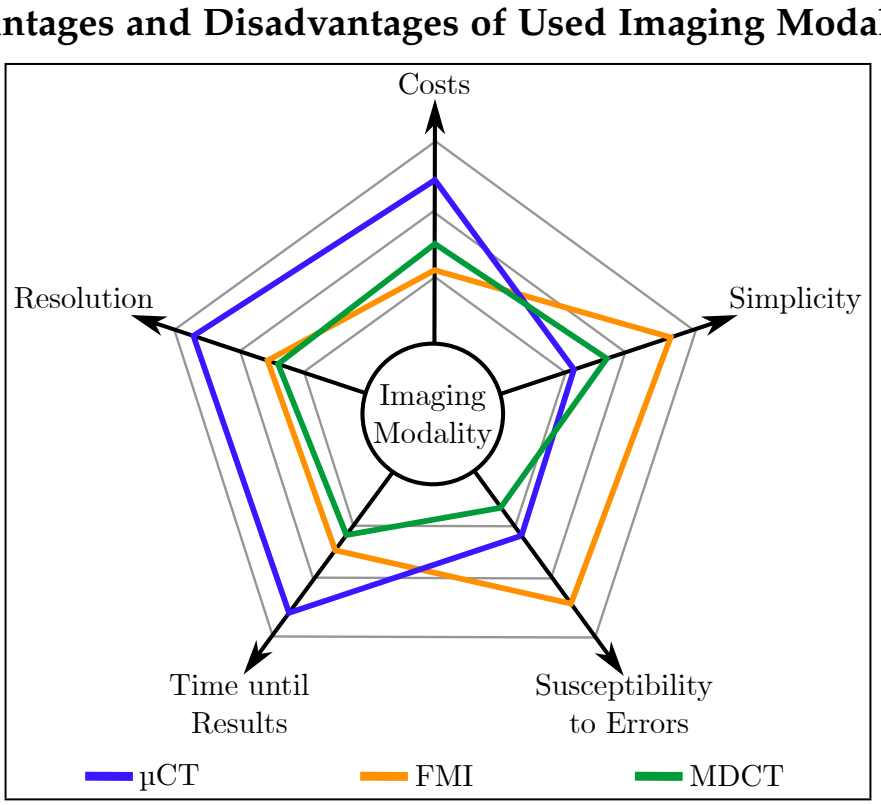


**Figure 2.16: Qualitative display of key criteria of used imaging modalities.** Every imaging modality showed its individual advantages and disadvantages.

Kranz et al. [31] observed an overestimation of clot volume when using MDCT, since the discrimination of hollow-fibers inside of clot structures is technically not possible. This study introduced correction factors based on mathematical approximations that aim to provide more realistic MDCT data. FMI was established as an alternative to exiting imaging modalities by Wagner and Kranz et al. [31] using a fundamentally different data acquisition.

Those three imaging modalities were used and evaluated for this study. As proposed by Wagner and Kranz et al. [31] µCT is considered as gold standard in terms of data quality. However, this goes along with high costs and an extended time for image acquisition.

The MDCT with Birkenmaier's revised settings and the introduced correction factors provides an adequate alternative to µCT. In fact, MDCT detects a little less clots but no significant difference ($p > 0.05$) can be seen compared to the gold standard µCT (Figure 2.9 (a)). This is due to the limited detection of very small structures that results in an overall lower clot volume. Still, it proves reliable data quality and requires a significantly reduced scanning time (MDCT: 5 s vs. µCT: 40 h), allowing rapid clot volume estimations.

It could be seen that FMI detects significantly less ($p \leq 0.05$) clot volume (Figure 2.9 (a)). FMI is only capable of detection clots that are not covered by the stabilization frame. Therefore, only a portion of $\approx 79$ % of the fiber mat area can be evaluated. In addition, the results indicate that the mathematical assumptions and approximations might underestimate the actual clot volume. This impairs the validity of the overall clot volume calculation. Statements of total clot volume should therefore not be made solely on FMI data. However, the relative clot volume (Figure 2.10 (a)) is reliable and (except for the UL sector) no significant differences to the gold standard µCT were found. This is expected to be an artifact from the cut off corner that was cut off to maintain the orientation of the fiber mats. As this corner has been cut off and therefore no data is available there, the algorithm evaluates this as clot-free. This generally reduces the clot volume in the UL sector.

The biggest advantage of FMI is the detection of clot volume on every single hollow-fiber mat. Therefore, FMI is the only used imaging modality that allows the investigation of the clot progression along the ML. With this data, a reasonable explanation of why the clot volume is significantly higher inside the inlet chamber than in the outlet chamber could be made. Furthermore, the visualization of blood clots in proximity to

the distributor plate, the dividing wall, and the collector plate (Figure 2.12, areas I, III, IV, and VI) is possible [31].

The imaging modalities used showed all their individual advantages and disadvantages during the study. Wagner and Kranz et al. [31] provided their experience with the mentioned imaging modalities after the investigation of one ML. With the examination of seven clinically used MLs, their evaluation was reasonable. The strengths and weaknesses of the imaging modalities used are summarized according to objective and subjective evaluation in Figure 2.16.

### 2.4.3 Limitations

This study presented advantages and disadvantages of three imaging modalities for clot detection in clinically used MLs. Data was derived from seven clinically used MLs after termination of ECMO support or after system replacement. However, the sample size of $n = 7$ MLs and the heterogeneity of the patient cohort providing the MLs may limit the transfer of the results towards general statements. Yet, the sample size was considered in the statistical tests and all three imaging modalities yielded congruent results.

## 2.5 Conclusion

The total clot volume ranged between 75 ml to 129 ml with clot deposed predominantly in the inlet chamber of the ML. Along the fiber mats, a relatively constant clot volume was observed. This indicates that clot formation is location-dependent, as a result of the different fiber mat packaging densities inside the inlet and outlet chamber. In clear contrast, however, structural changes inside the ML like the transition from the

distributor plate to the fiber mat stack resulted in a significant deviation in clot volume. This suggests that these structural changes influence clot deposition in their vicinity.

All three imaging modalities provided sufficient data on clot distribution. Based on presented results, µCT continues to be the gold standard due to its high detection quality. MDCT detected only larger clot structures and overestimated the total clot volume. However, the presented clot volume correction factors allow for an adequate estimation while benefiting from the short scanning time of MDCT. FMI gave new important insights into the clot progression throughout the ML which were not detectable with µCT or MDCT.

# 3. Large Scale Polymer Embedding of Membrane Lungs

Histological examination of immunological deposits within clinically used MLs provides important information on interactions between the device and the human blood. Currently, state-of-the-art methods extract single fiber mats from the ML which are then histologically stained. By using an inverse fluorescence microscope with a top view perspective, the composition of these immunological deposits can be examined (Figure 3.1) [31, 54, 61, 62].

However, since the vWF is expected to align with the blood flow (Figure 1.8), top view microscopy is not suitable, as it does not provide sufficient depth information. Consequently, the spatial arrangement of immunological deposits cannot be investigated either. As a solution, performing examinations on hollow-fiber cross-sections is proposed. Preliminary tests proved the porosity of the hollow-fibers and the clots which prohibited reliable microtome sections. By using an embedding procedure, the ML interior and deposed clots are mechanically stabilized allowing microtome cross-sectioning and subsequent histological analysis. This concept was prior tested with paraffin by Steiger et al. [54]. Paraffin embedding was feasible for a small exemplary section of the ML, yet the high viscosity and the low hardness of paraffin prevented

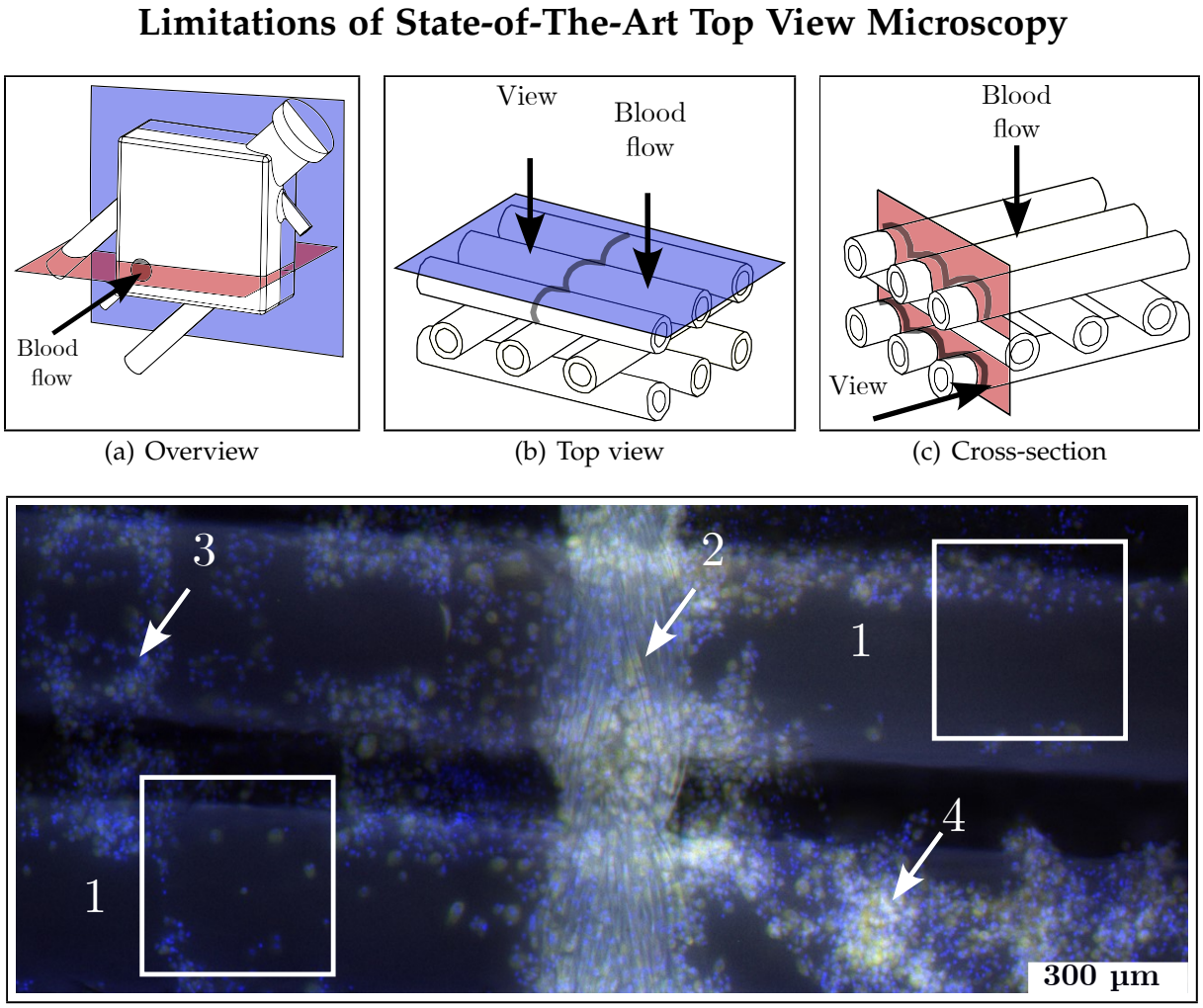


(a) Overview (b) Top view (c) Cross-section

(d) Top view microscopic image

**Figure 3.1: Limitations of top view microscopy and concept of cross-sections.** (**a**) Overview of viewing planes in ML. (**b**) Top view perspective with blood flow parallel to the direction of view. (**c**) Cross-sectional view with blood flowing orthogonally to the direction of view. (**d**) Display of the examination capability of the state-of-the-art top view microscopy. Only the areas within the white squares can be examined; (1) hollow-fiber; (2) warp thread; (3) multi-layerd cell structure at hollow-fiber crossing point; (4) multi-layerd clot structure. All subfigures are excerpts from Kranz et al. [90].

sufficient filling of the ML and resulted in disruption of the immunological deposits. Therefore, a systematic large scale study was not possible with paraffin embedding.

A liquid embedding solution was aimed for with a low viscosity in its liquid state and a hardness similar to the hollow-fibers in its hardened state.

## Preliminary Experiments with Technovit® 9100

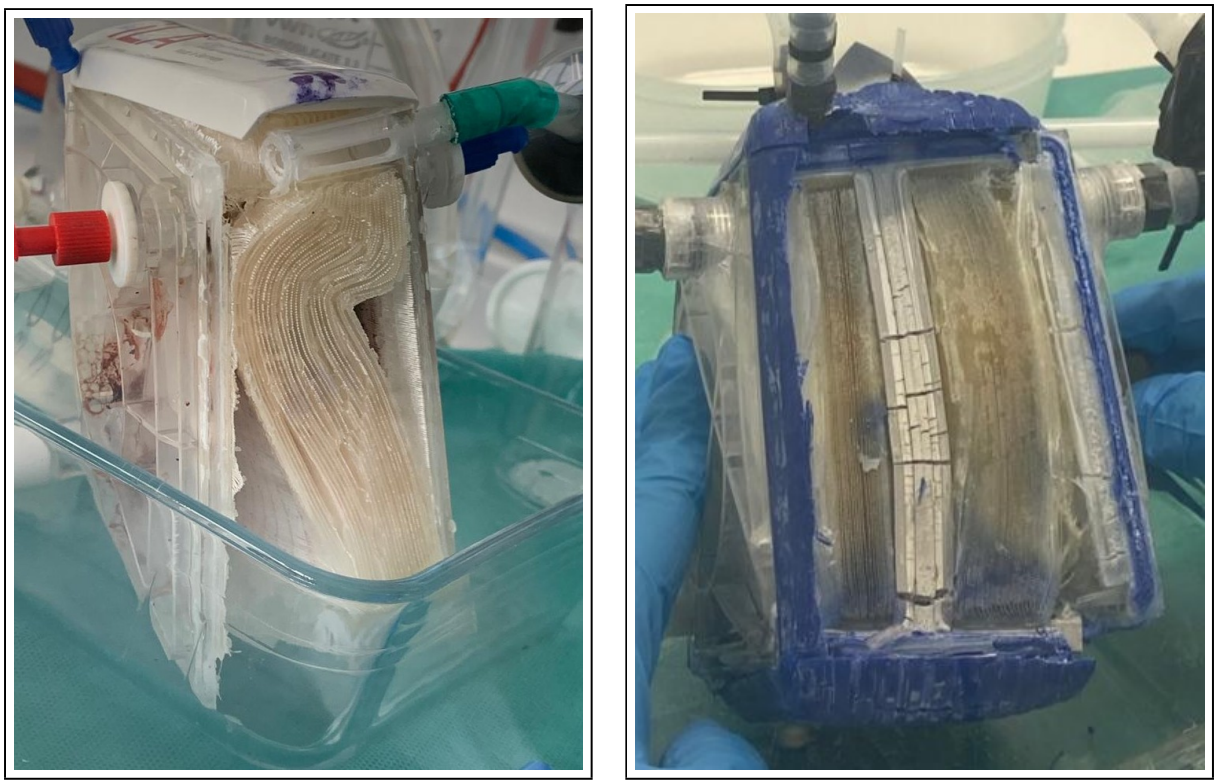

(a) iLA® ML (b) PLS ML

**Figure 3.2: Preliminary embedding tests with Technovit® 9100.** An elongation of the PMP hollow-fibers was observed as an interaction with the polymer solution in an (**a**) iLA® (Xenios, Heilbronn, Germany) ML and in a (**b**) PLS ML. Furthermore, the housings of both MLs became brittle. Additionally, in (**b**) the blue colorant of the PC housing was dissolved out and deposited within the hollow-fibers.

Technovit® 9100 (Morphisto, Offenbach, Germany) was tested as it is one of the most commonly used polymers in histology. However, the xylene required for the dehydration of the immunological deposits severely damaged the PC housing of the MLs (Figure 3.2). In addition, an elongation of the PMP hollow-fibers of approximately 10 % was observed. These issues were circumvented by using HistoCURE 8100 (Morphisto, Offenbach, Germany).

Following methodology is presented in *Polymer embedding of membrane lungs for histological investigations of intra-device clot formation* [90] first published in *Frontiers in*

*Cardiovascular Medicine* in February 2026 under Creative Commons Attribution License (CC-BY). In addition, the embedding protocol was presented at the 12$^{th}$ EuroELSO Congress in Krakow, Poland in April 2024 [91].

## 3.1 Introduction

Histological examinations of fiber mats captured from top view already provided important insights in ongoing immunological reactions inside MLs [31, 54, 61, 62]. However, to investigate the initially postulated hypothesis that the vWF is elongated by unphysiological shear stress thus triggering intra-device clot formation, it was important to incorporate the blood flow direction into the histological imaging. Since the top view microscopy lacks in depth information, it was aimed for an orthogonal visualization of clot structures. This can be done by investigating cross-sections of ML fibers. By this, the structures aligned with the blood flow can be examined. The major challenge is not to break the porous fibers nor the fragile clot structures during microtome sectioning. Performing those sections was accomplished by embedding the clinically used ML after termination of ECMO support.

The exact workflow from the embedding process to histological examinations is presented in the following chapter.

## 3.2 Materials and Equipment

Information on used equipment, tools, and reagents are listed in Tables 3.1 and 3.2.

**Table 3.1: Required equipment and tools. The table is an excerpt from Kranz et al. [90].**

| # | Item | QTY | Desciption | Supplier |
|---|---|---|---|---|
| **Polymer Embedding and Specimen Extraction** | | | | |
| **1** | PLS ML | 1 | Embedded and examined ML | Getinge, Rastatt, Germany |
| **2** | Technovit® embedding mold with hexagonal inserts | 18 | Embedding mold for specimen stabilization | Morphisto, Offenbach, Germany |
| **3** | Micro V G222E $O_2$ monitor | 1 | Monitoring $O_2$ during $CO_2$ application | GfG, Dortmund, Germany |
| **4** | MH 20 magnetic stirrer | 1 | Stirring of polymer solution | Carl Roth, Karlsruhe, Germany |
| **5** | Testo 835-T1 infra-red thermometer | 1 | Monitoring polymerization temperature | Testo, Titisee-Neustadt, Germany |
| **6** | Dremel 4000 | 1 | Cutting off connector ports of ML | Dremel, Racine, WI, USA |
| **7** | TC-SB 305 U band saw | 1 | Cutting out specimens from embedded ML | Einhell, Landau, Germany |
| **Microtome Sectioning** | | | | |
| **8** | HM355S rotary microtome | 1 | Microtome sectioning of embedded ML specimens | Thermo Fisher, Waltham, MA, USA |
| **9** | R16D Tungsten-carbide D-knife 16 cm | 1 | | Gigatome, Roggenburg, Germany |
| **10** | Cylindrical microtome mounting with fixation for 25 mm diameter specimens | 1 | | OTH Regensburg, Regensburg, Germany |
| **11** | Superfrost Ultra Plus® glass slides | 1 | Glass slides | Thermo Fisher, Waltham, MA, USA |
| **Image Acquisition and Processing** | | | | |
| **12** | DMi8 inverse microscope with a LED 5 light source | 1 | Imaging of specimens from embedded ML | Leica Microsystems, Wetzlar, Germany |
| **13** | K3C RGB camera | 1 | Transmitting lights microscopy | |
| **14** | K5 grayscale camera | 1 | Fluorescence microscopy | |
| **15** | DFT51011 filter cube | 1 | Optical filter for fluorescence microscopy | |
| **16** | DFT5 filter wheel | 1 | | |
| **167** | LAS X 3.10 software | 1 | Control software for DMi8 microscope | |
| **18** | Adobe Photoshop CS5 64 bit | 1 | Imaging software to reduce background | Adobe, San José, CA, USA |

**Table 3.2: Required reagents. The table is an excerpt from Kranz et al. [90].**

| # | Reagent | Article # and Supplier |
|---|---|---|
| | **Embedding Polymers** | |
| **19** | HistoCURE 8100 set 500 ml (2 sets) | 12226.K0500, Morphisto, Offenbach, Germany |
| **20** | Technovit® 3040 set | 12226.K0180, Morphisto, Offenbach, Germany |
| | **Fixative and Buffer Solutions** | |
| **21** | NaCl 0.9 % | 1310181, Fresenius-Kabi, Bad Homburg, Germany |
| **22** | Paraformaldehyde | 104005, Merck, Darmstadt, Germany |
| **23** | Methanol | 4627, Carl Roth, Karlsruhe, Germany |
| **24** | NaOH flakes | LC4994.1, LaboChem, Ruse, Bulgaria |
| **25** | $Na_2HPO_4$ (PBS) | 106579, Merck, Darmstadt, Germany |
| **26** | KCl | HN02.2, Carl Roth, Karlsruhe, Germany |
| **27** | $KH_2PO_4$ | 104873, Merck, Darmstadt, Germany |
| **28** | NaCl | 1ß06400, Merck, Darmstadt, Germany |
| **29** | Tris-Base | T1503-1kg, Sigma-Aldrich, Steinheim, Germany |
| **30** | Tris-HCl | 9090.2, Carl Roth, Karlsruhe, Germany |
| **31** | Bovine serum albumin (BSA), Frakt. V | 8076.2, Carl Roth, Karlsruhe, Germany |
| **32** | Gelatin from cold fish skin | G-7765, Sigma-Aldrich, Steinheim, Germany |
| **33** | Normal goat serum (NGS) | G-9023, Sigma-Aldrich, Steinheim, Germany |
| **34** | Normal donkey serum (NDS) | D-9663, Sigma-Aldrich, Steinheim, Germany |
| | **Histological Staining Solutions** | |
| **35** | Mayer's hemalum solution | 1.09249.0500, Sigma-Aldrich, Steinheim, Germany |
| **36** | Eosin | 15935, Merck, Darmstadt, Germany |
| **37** | May-Grunwald stain | 63595, Sigma-Aldrich, Steinheim, Germany |
| **38** | Giemsa stain | 48900, Sigma-Aldrich, Steinheim, Germany |
| | **Antibodies** | |
| **39** | Rabbit, anti human, anti-myeloperoxidase (MPO) | A0398, DAKO Cytomation, Wiesentheid, Germany |
| **40** | Rabbit, anti vWF | A0082, DAKO Cytomation, Wiesentheid, Germany |
| **41** | Rabbit, anti human, isotype control antibody | 31235, Invitrogen, Waltham, MA, USA |
| **42** | Goat, anti rabbit, biotinylated antibody | BA-1000, Vector, Newark, CA, USA |
| **43** | Donkey, anti rabbit, AlexaFluor 647 | A-31573, Invitrogen, Waltham, MA, USA |
| | **Agents and Stains for immunohistochemistry (IHC) and for immunohistofluorescence (IHF)** | |
| **44** | Vectastain® Elite® ABC Kit, Peroxydase (Standard) | PK-6100, Vector Laboratories, Newark, CA, USA |
| **45** | Histogreen | E109, Linaris/Biozol Diagnostica, Eching, Germany |
| **46** | DAB-Liquid | K3468, Dako/Agilent, Santa Clara, CA, USA |
| **47** | SYTOX™-Green | S-7020, Thermo Fisher, Waltham, MA, USA |
| | **Mounting Agents** | |
| **48** | Entellan™ | 1.07961.0500, Merck, Darmstadt, Germany |
| **49** | VectaMount® AQ | H-5501, Vector Laboratories, Newark, CA, USA |
| **50** | Fouromount-G™ | 00-4958-02, Thermo Fisher, Waltham, MA, USA |
| **51** | Fluoromount-G™ 4,6-diamidino-2-phenylindole (DAPI) | 00-4959-52, Thermo Fisher, Waltham, MA, USA |
| | **Miscellaneous Reagents** | |
| **52** | Ethanol absolute | 107017, Merck, Darmstadt, Germany |
| **53** | HCl | 1.00317.0510, Merck, Darmstadt, Germany |
| **54** | Acetic acid 100 % | 1.00063.1011, Merck, Darmstadt, Germany |
| **55** | Xylene (mixture of isomers) $\leq$ 98 % | 28973.363, VWR, Radnor, PA, USA |
| **56** | $H_2O_2$ | 3867909, Merck, Darmstadt, Germany |
| **57** | Trypsin-EDTA | T4174, Sigma-Aldrich, Steinheim, Germany |
| **58** | $CaCl_2$ (1M) | 21114, Honeywell Fluka, Sleeze, Germany |
| **59** | Citric buffer (pH 6) | ZUC 028-500, Zytomed, Berlin, Germany |
| **60** | Glycerol $>$ 99 % | SHBL3980, Sigma-Aldrich, Steinheim, Germany |

## 3.3 Methods

Clinically used end-of-therapy PLS MLs (Table 3.1, item #1) were embedded according to the following protocol. In brief, the MLs were collected post-ECMO therapy and filled with HistoCURE 8100 (Table 3.2, item #19). Once the polymer had fully hardened, the ML housing was opened. ROIs were excised and placed in embedding molds (Table 3.1, item #2) to generate standardized specimen blocks using a mixture of HistoCURE 8100 and Technovit® 3040 (Table 3.2, item #20). Microtome sections, each 10 µm thick, were then prepared and subjected to various histological staining procedures. The entire embedding process for one ML took approximately 96 h, with an effective working time of 8 h for two individuals. The detailed process, from retrieving the ML post-clinical use to microscopic image acquisition, is described below, with a visual summary provided in Figure 3.3.

### 3.3.1 Preparation

All MLs necessary for establishing this protocol were collected at the University Hospital Regensburg following the termination of ECMO support. To eliminate residual, non-adherent blood components, the MLs were rinsed with 10 l of isotonic saline solution (Table 3.2, item #21). The adherent deposits were then fixed using a formol solution (4 % m/v paraformaldehyde in 0.1 M PBS (1.15 % m/v $Na_2HPO_4$, 0.20 % m/v KCl, 0.20 % m/v $KH_2PO_4$, 8 % m/v NaCl in distilled water), pH 7.3, + 10 % v/v methanol, 1 l, Table 3.2, items #22-28) for at least one week. Whether an influence on the staining quality due to long exposure to formol exists, is currently not yet known. After fixation, the MLs were stored at 4 °C until further processing [31, 61, 62].

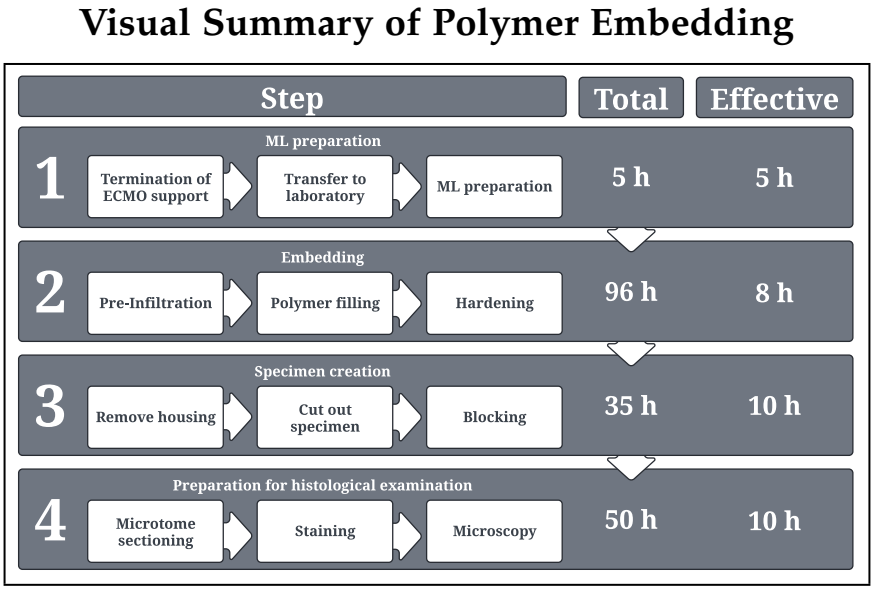


**Figure 3.3: Visual summary of embedding process from retrieval after clinical use to microscopic imaging.** The entire process is structured in four main steps: (1) The preparation after terminations of ECMO support or system exchange and transport to the laboratory; (2) the embedding process including the pre-infiltration of the clot structures; (3) the creation of standardized specimen blocks that allow microtome sectioning and (4) the microtome sectioning, histological staining and microscope imaging. The figure is an excerpt from Kranz et al. [90].

### 3.3.2 ML Preparation for Embedding

To prevent excessive heat generation from the exothermic polymerization, the ML, along with all necessary components and tools, were cooled to 4 °C. Additionally, the draining of the fixative solution, preparation of the ML, embedding, and hardening were all conducted in a well-ventilated room maintained at 4 °C. After removing the formol fixative, 25 cm long silicone tubes (10 mm diameter for the blood and heat exchanging compartments, and 6 mm for the gas compartment) were attached to the ML ports, connecting the inlet and outlet of each compartment. This facilitated the subsequent preparation steps (Figure 3.4). Cable ties were used to secure the tubes and prevent leaks. The ML was then rinsed with 2 l of isotonic saline solution through the blood, gas, and water inlets. At this stage, it is important to check the tightness of the tube connections. If any leaks are detected, additional cable ties can be used to

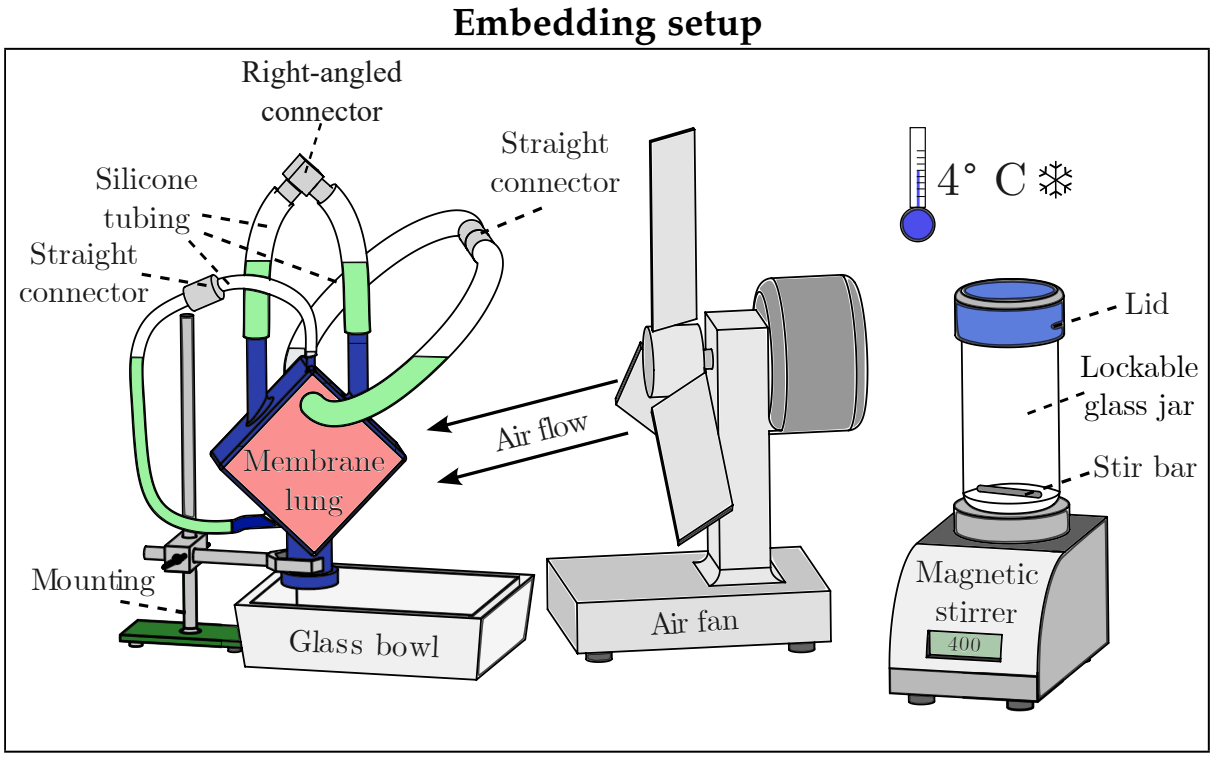


**Figure 3.4: Setup for embedding a PLS ML with HistoCURE 8100.** Left: Clinically used ML with tubes connecting individual compartments of the device; polymer filled in all compartments of the ML and in the silicone tubes (green). Middle: Cooling fan for heat removal during curing process. Right: Magnetic stirrer with lockable glass jar for preparation of polymer mixture. The figure is an excerpt from Kranz et al. [90].

resolve the issue. The ML was then dried with compressed air until no water residues remained, with pivoting the ML aiding in the drainage process. Next, the ML was filled with 500 ml of ethanol (Table 3.2, item #52) using a sterile 100 ml syringe. To avoid rinsing out clot structures, the multi-step dehydration process recommended by the manufacturer was replaced with a single step using 99.97 % ethanol, followed by draining after 7 min. Since $O_2$ inhibits the polymer hardening reaction, each compartment of the ML was flushed with $CO_2$ for 30 s. For safety, it is recommended to use an $O_2$ monitoring device (Table 3.1, item #3) during this step.

### 3.3.3 Embedding

The MLs were embedded using liquid HistoCURE 8100 polymer solution, a glycol methacrylate acetate specifically developed to enhance the mechanical stability of biological specimens for microtome sectioning [92]. Another benefit of HistoCURE 8100 is its suitability for immunohistochemical analysis [92, 93]. The embedding procedure followed the manufacturer's guidelines. Since previous studies only described the use of HistoCURE 8100 in specimens up to a volume of 2 $cm^3$ [94], the manufacturer's protocol was adapted to accommodate the required volume of 400 ml of polymer. The embedding setup is illustrated in Figure 3.4.

To prepare the embedding solution, 300 ml of HistoCURE 8100 base solution and 1.8 g of hardener 1 were added to a 1 l lockable glass jar. The mixture was stirred for 30 min at 400 RPM using a magnetic stirrer (Table 3.1, item #4) and a 2 cm long stir bar. This mixed solution was then introduced into the blood compartment to pre-infiltrate the clots for 72 h, ensuring better binding with the subsequent hardening solution. After pre-infiltration, 500 ml of HistoCURE 8100 base solution and 3 g of hardener 1 were stirred for 30 min as previously described. Then, 34 ml of hardener 2 were added using a 20 ml syringe. $CO_2$ was flushed into the jar for 10 s to remove any $O_2$ before sealing. The substances were stirred for about 7 min until a green discoloration appeared. This mixture was used to harden all ML compartments. It was introduced into the ML through the connected silicone tubing using a sterile 100 ml syringe, displacing the pre-infiltration solution from the opposite side. The compartments were filled 50 mm above the connectors to ensure the hardening solution remained in the tubing to compensate for any polymer shrinkage during hardening. Before sealing, $CO_2$ was flushed into the silicone tubes to prevent any contact with $O_2$. Heat removal during the exothermic polymerization reaction was facilitated by a cooling

fan. Regular temperature monitoring of the front and back of the ML was performed with an infrared thermometer (Table 3.1, item #5) until the main reaction concluded after 4 h. If non-uniform temperature rise was detected, the fan position was adjusted. The maximum temperature (approximately 30 °C at the ML housing) was observed after about 3 h. After 24 h in a cooling room at 4 °C, the ML was fully hardened, and specimens were cut out.

### 3.3.4 Creation of Specimen

To create specimens from the ML, the lateral housing needed to be removed. Initially, all connectors were cut off using a Dremel 4000 (Table 3.1, item #6). This step facilitated the subsequent removal of the outer housing with a band saw (Table 3.1, item #7). Depending on the intended application, maintaining the initial orientation of the specimen might be crucial. This was achieved by employing a coordinate system that assigned location numbers to each specimen (Figure 3.5 (A)). To prevent contamination of the hardened fiber mat stack, it was wrapped in adhesive tape. A printed cutting template was attached on top to aid the sawing process. The specimens were then cut out as shown in Figures 3.5 (A, B). After removing the surrounding tape, the specimens were immediately placed into a cylindrical embedding mold with a hexagonal insert (Figures 3.5 (C, D)). Arrows were attached to the embedding molds to indicate the coordinate axes (Figure 3.5 (C)). It is crucial to place the cut-out specimens in the exact orientation indicated on the embedding mold, as any error at this stage may not be detectable later.

The location number was also incorporated into a barcode labeled on each embedding mold to identify individual specimens (Figure 3.5 (C)) and link them to a database documenting specific properties (e.g., date of embedding, clot burden, specimen quality, cutting behavior, etc.). The embedded specimens were placed in embedding molds

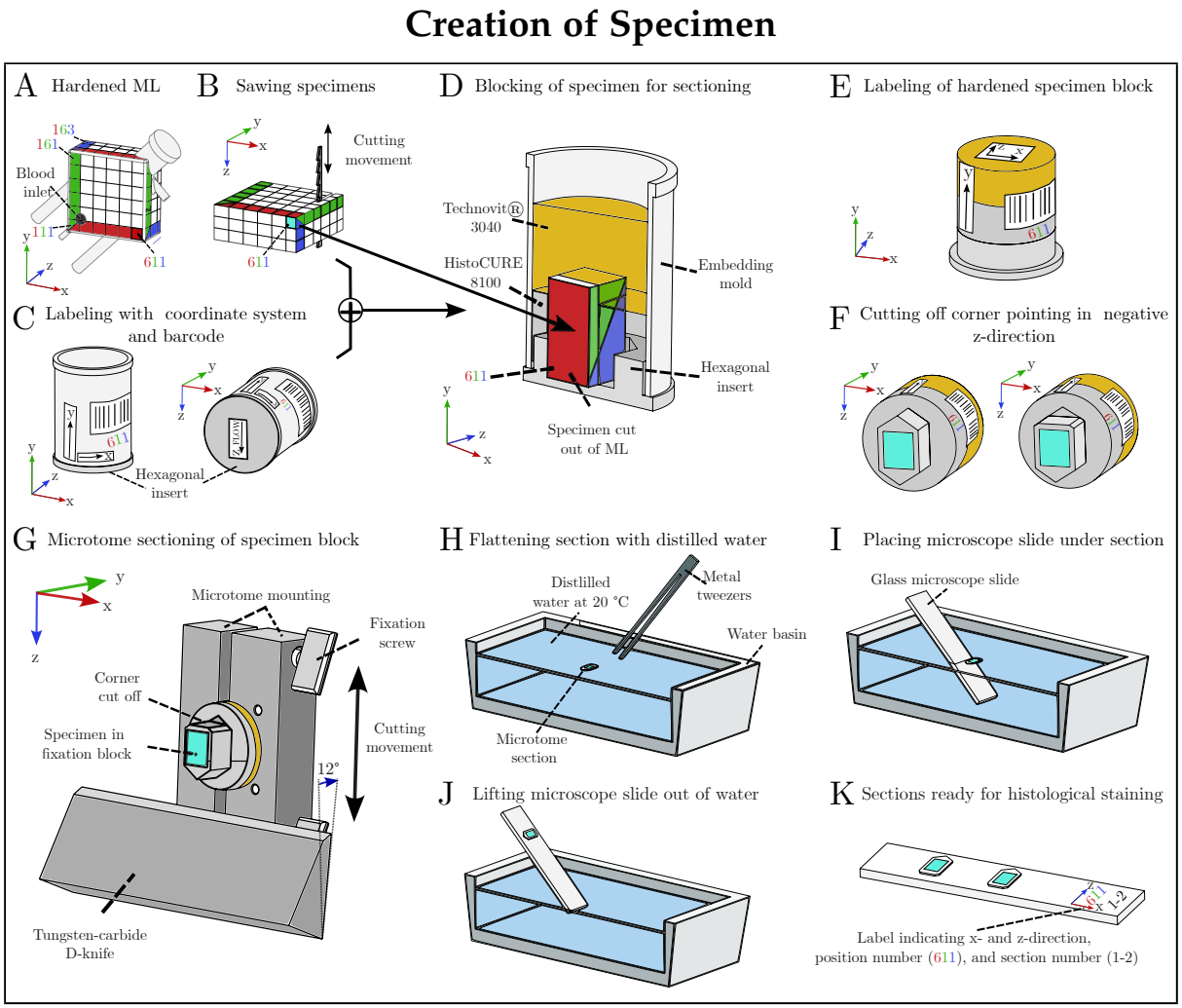


**Figure 3.5: Creation of specimen from embedded MLs.** (**A**) Defining a coordinate system to ensure consistent orientation of each specimen. (**B**) Cutting the individual specimens using a band saw. (**C**) Marking the embedding mold with coordinate indicators. (**D**) Embedding the specimen in a block made from e mixture of HistoCURE 8100 and Technovit® 3040. (**E**) Removing the specimen from the mold, leaving the hexagonal insert attached to preserve the z-axis orientation. (**F**) Trimming off the corner facing in the negative z-direction to maintain the correct z-orientation during microtomy. (**G**) Sectioning the specimen with a cylindrical mounting and a tungsten-carbide D-knife, ensuring the lower corner points towards the positive- z-direction; transferring each section into a water bath using metal tweezers. (**H**) Flattening the section by gently placing it on the surface of the temperature-controlled (20 °C) distilled water. (**I**) Sliding a glass microscope slide diagonally underneath the flattened surface. (**J**) Lifting the slide so that the section adheres to its surface. (**K**) Multiple sections may be mounted on a single slide for a subsequent histological staining. The figure is an excerpt from Kranz et al. [90].

(Table 3.1 item #2) and encapsulated with additional polymer to form specimen blocks (Figure 3.5 (D)), which is later cut using a microtome (Figure 3.5 (G)). This process is known as "blocking". It is not necessary to saw out and block all 108 specimens immediately after embedding. Instead, specimens that have not been sawed out can be stored at 4 °C and blocked later. It was observed that even after more than one and a half years post-embedding, the samples could still be processed and analyzed without any restrictions.

In this step, 18 specimens were processed simultaneously, as this was found to be the optimal quantity to handle at once. The embedding molds were placed in a shallow, sealable glass container with the cut-out specimens positioned in the center of the hexagonal mold insert (Figure 3.5 (D)). The glass container was then placed in a cooling room at 4 °C for 3 h before block preparation. The subsequent blocking procedure was performed similarly to the ML embedding at an ambient temperature of 4 °C (with specimens and materials previously tempered to 4 °C).

Each embedding mold was filled with 5 ml of HistoCURE 8100 hardening solution (total: 100 ml base solution + 1 package of hardener 1 + 7 ml of hardener 2, processed as previously described; 18 specimens require 90 ml, with 10 ml included as a reserve). Any displacement of the specimen due to polymer pouring should be manually corrected using a glass bar, for example. Care must be taken to prevent the formation of air bubbles under or next to the cut-out specimen, as this would result in insufficient hardening and render the block unusable. $CO_2$ was again used in the HistoCURE 8100 hardening process to remove $O_2$ by flushing the container for 30 s before sealing it with a lid. After 24 h, the HistoCURE 8100 had fully hardened. The embedding molds were then removed from the container and placed in a laboratory fume hood at room temperature (RT, $\approx$ 20 °C).

The following steps were conducted at RT. Once the molds reached RT, each was filled with Technovit® 3040 hardening solution up to just below the upper edge of the mold. This solution was prepared with a mixing ratio of 2 parts powder to 1 part liquid (10 ml powder and 5 ml liquid per embedding mold, 180 ml powder and 90 ml liquid in total). These components were mixed in a disposable cup and stirred with a glass bar until no lumps were visible (about 10 s). The solution was immediately poured into the embedding molds. After 30 min, the Technovit® 3040 had completely hardened. The specimen blocks were removed from the molds and labeled according to the labeling on the outside of the mold (Figure 3.5 (E)). The corresponding barcode sticker was then placed on the side of the specimen (Figure 3.5 (E)).

To identify the z-direction after microtome sectioning, the corner of the specimen pointing in the negative z-direction was removed with a handsaw (Figure 3.5 (F)). The remaining corner thus points like an arrow in the z-direction (Figure 3.5 (F). The specimens were stored at RT until microtome sectioning. It is recommended to store them in a well-ventilated room, as the polymer emits chemical vapors within the first few weeks after blocking. Storing at 4 °C was also tested, but no advantage for sample quality was determined. When performing microtome sectioning, it is important to ensure that the specimens reach RT first, as the polymer is significantly more brittle when cold.

Using a combination of two polymers for specimen blocking offered distinct advantages. HistoCURE 8100, used in the cutting area of the specimens, improved cutting behavior due to its lower hardness. Conversely, Technovit® 3040, which has higher hardness, was easier to handle and more cost-effective. Therefore, Technovit® 3040 was used in the area of the specimen block that would later be clamped in the microtome mounting. Additionally, pouring two thinner layers of HistoCURE 8100 and Technovit® 3040,

rather than a single thicker layer of HistoCURE 8100, enhanced heat removal and reduced the formation of air bubbles within the polymer. These air bubbles could negatively impact sectioning properties due to their differing hardness.

### 3.3.5 Microtome Sectioning

A rotary microtome (Table 3.1, item #8) equipped with a tungsten-carbide D-knife (Table 3.1, item #9) was used for sectioning. The sectioning was performed using an in-house designed microtome mounting with a fixture (Table 3.1, item #10) for cylindrical specimen blocks with a diameter of 25 mm (Figures 3.5 (G), 3.6). The knife was tilted 12° towards the microtome mounting. Before cutting analyzable sections, the upper layer of the specimen block was trimmed until the hollow fibers were exposed, creating an even surface for the actual sections.

Great care was taken during this step to prevent breaking the blocks. The best trimming results were achieved with a section thickness of 4 µm. Trimming and sectioning were carried out using the microtome's manual drive at a high cutting speed (comparable to 80 m/s in motor-driven mode). The actual sectioning was performed with 5 µm and 10 µm thickness, with the latter providing better handling in subsequent histological staining.

After that, the sections were carefully picked up with pointed metal tweezers and placed on the surface of a water basin filled with distilled water at RT (Figure 3.5 (H)). The sections then rolled out flat. A microscope slide (Table 3.1, item #11) was positioned diagonally under the section (Figure 3.5 (I)). By lifting the slide, the section adhered to it (Figure 3.5 (J)). To maintain the orientation of the sections, each slide was labeled with the corresponding location number (Figure 3.5 (K)) and an x-z-coordinate system. Sections were set to dry for at least 5 h at RT or 2 h at 37 °C and stored at 4 °C

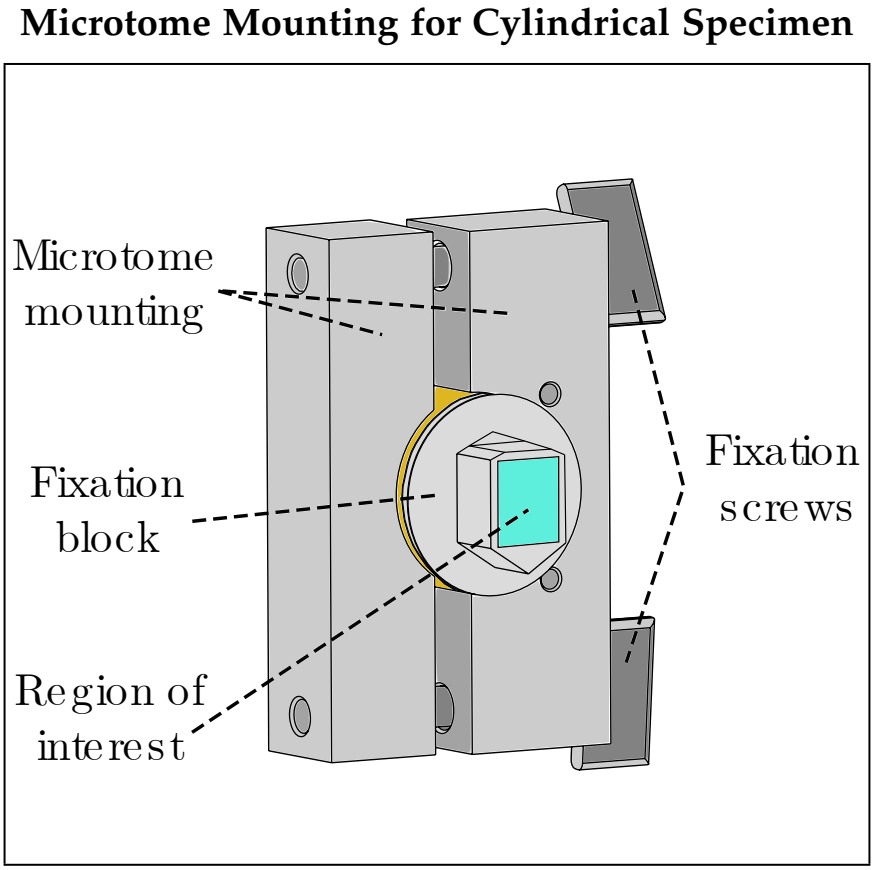


**Figure 3.6: Microtome mounting for cylindrical specimen specifically designed for Thermo Fisher HM25S rotary microtomes.**

for a maximum of 10 days for histological staining and a maximum of 5 days before immunohistochemistry (IHC) or immunohistofluorescence (IHF).

### 3.3.6 Histology Protocols

Staining procedures for embedded specimens were developed based on the state-of-the-art protocol for paraffin-embedded tissues and non-embedded MLs [31], incorporating protocols from Malik et al. [93], De Jonge et al. [94], and Ponsioen et al. [95]. The final protocols are detailed below, with examples shown in Figures 3.7 (a, b, e, f), 3.8 (a, b, e, f) 3.9 (transmitting light microscopy) and Figures 3.7 (c, d, g, h), 3.8 (c, d, g, h), 3.10 (fluorescence microscopy). One significant adaptation compared to existing protocols

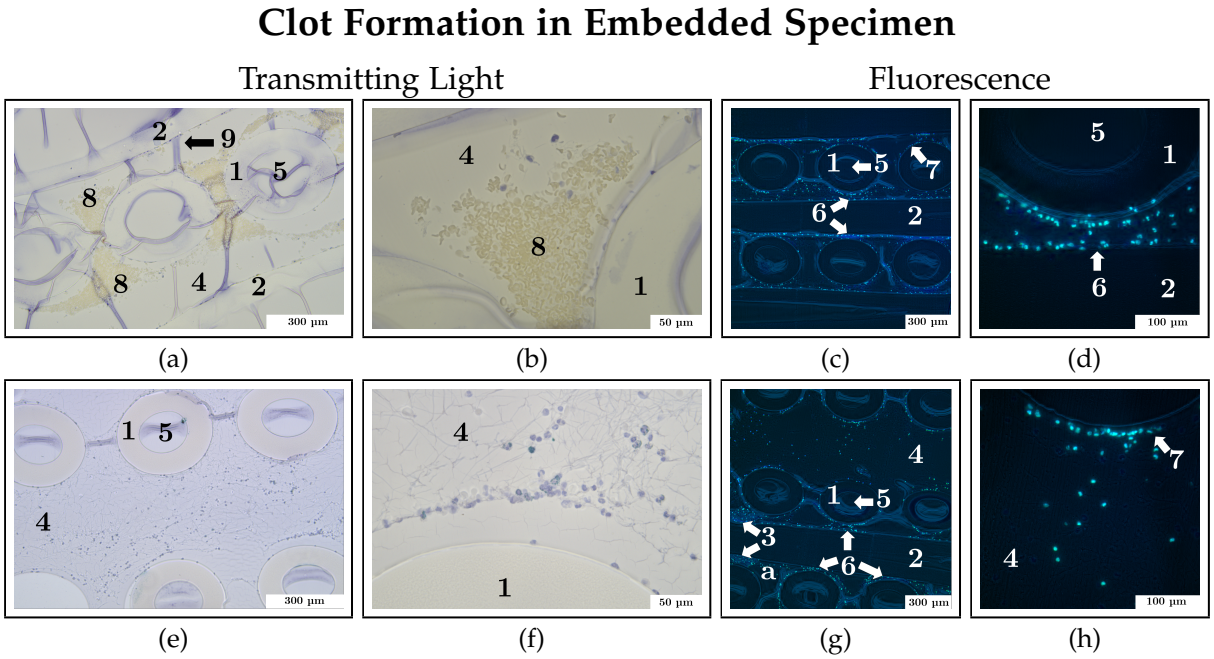


**Figure 3.7: Clot structures in sections from embedding MLs visualized with transmitting light ( 1st and 2nd column) and fluorescence microscopy (3rd and 4th column).** 1st and 3rd column at 100 fold magnification; 2nd and 4th column at 400 fold magnification. After polymer embedding, the sections display (1) cross-sections and (2) longitudinal section of PMP fibers, as shown in the overview images (**a**, **c**, **e**, and **g**; 100 fold magnification). The fibers are interwoven into mats by (3) a warp thread. Both the (4) blood compartment and (5) the lumina of the the hollow-fibers are filled with HistoCURE 8100. In particular, (6) intersections of two PMP hollow-fibers as wells as (7) the surfaces of hollow-fibers and the warp threads (3a) represent sites susceptible to the accumulation of nuclear deposits and the formation of (8) clots. In all images, blood flow is directed downward.
Detailed views (**b**, **d**, **f**, and **h**; 400 fold magnification) provide a closer examination of the biological deposits. Blood flow within the ML proceeds from the top to bottom within these sections.
Biological deposits in the blood compartment are stained using (1st and 2nd column) Hemalum (highlighting nucleated cells in blue) combined with anti-MPO (green, visualized with Histogreen), and (3rd and 4th column) DAPI and SYTOX™ Green for nuclear visualization (DAPI in blue, SYTOX™ Green in green), together with fluorescence phase contrast (turquoise) for hollow-fiber visualization. Except for (**a**) and (**b**), which are cut at 5 µm thickness, all sections are 10 µm thick an exhibit (9) typical folds. All subfigures are excerpts from Kranz et al. [90].

is the use of higher dye concentrations since no deplastification of the polymer was conducted. Consequently, a limited access to binding site was prominent. By increasing the dye concentration, a proper occupation of the accessible binding sites was achieved. Still, with following protocols, sufficient and reproducible results were achieved.

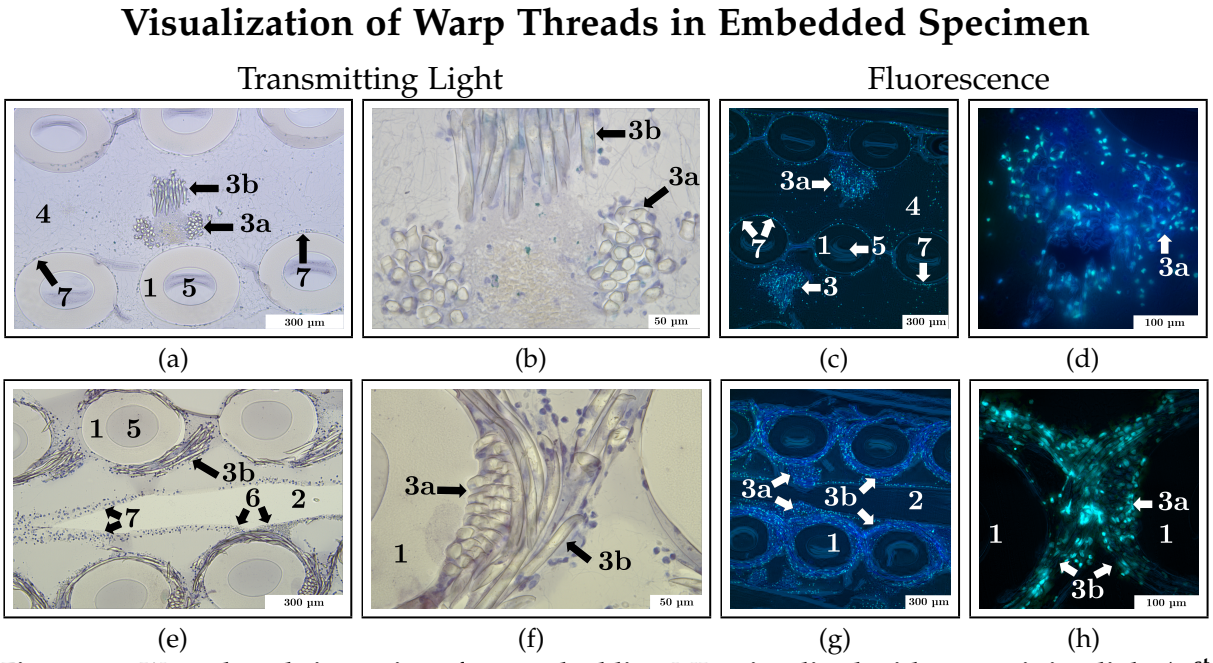


**Figure 3.8: Warp threads in sections from embedding MLs visualized with transmitting light ( 1st and 2nd column) and fluorescence microscopy (3rd and 4th column).** 1st and 3rd column at 100 fold magnification; 2nd and 4th column at 400 fold magnification. After polymer embedding, the sections display (1) cross-sections and (2) longitudinal section of PMP fibers, as shown in the overview images (**a**, **c**, **e**, and **g**; 100 fold magnification). The fibers are interwoven into mats by (3) a warp thread. Both the (4) blood compartment and (5) the lumina of the the hollow-fibers are filled with HistoCURE 8100. In particular, (6) intersections of two PMP hollow-fibers as wells as (7) the surfaces of hollow-fibers and the warp threads ((3a) cross-section, (3b) longitudinal section) represent sites susceptible to the accumulation of nuclear deposits and the formation of clots. In all images, blood flow is directed downward.
Detailed views (**b**, **d**, **f**, and **h**; 400 fold magnification) provide a closer examination of the biological deposits within the warp threads.
Biological deposits in the blood compartment are stained using (1st and 2nd column) hemalum (highlighting nucleated cells in blue) combined with anti-MPO (green, visualized with Histogreen), and (3rd and 4th column) DAPI and SYTOX™ Green for nuclear visualization (DAPI in blue, SYTOX™ Green in green), together with fluorescence phase contrast (turquoise) for warp thread visualization. All subfigures are excerpts from Kranz et al. [90].

### Positive and Negative Controls

To generate positive tissue controls, paraffin-embedded human tonsils and arteries were stained using the original protocol for paraffin-embedded tissues. Furthermore, also the use of positive controls embedded with HistoCURE 8100 was successfully tested, with pre-infiltration analogously to the ML embedding. These tissue samples

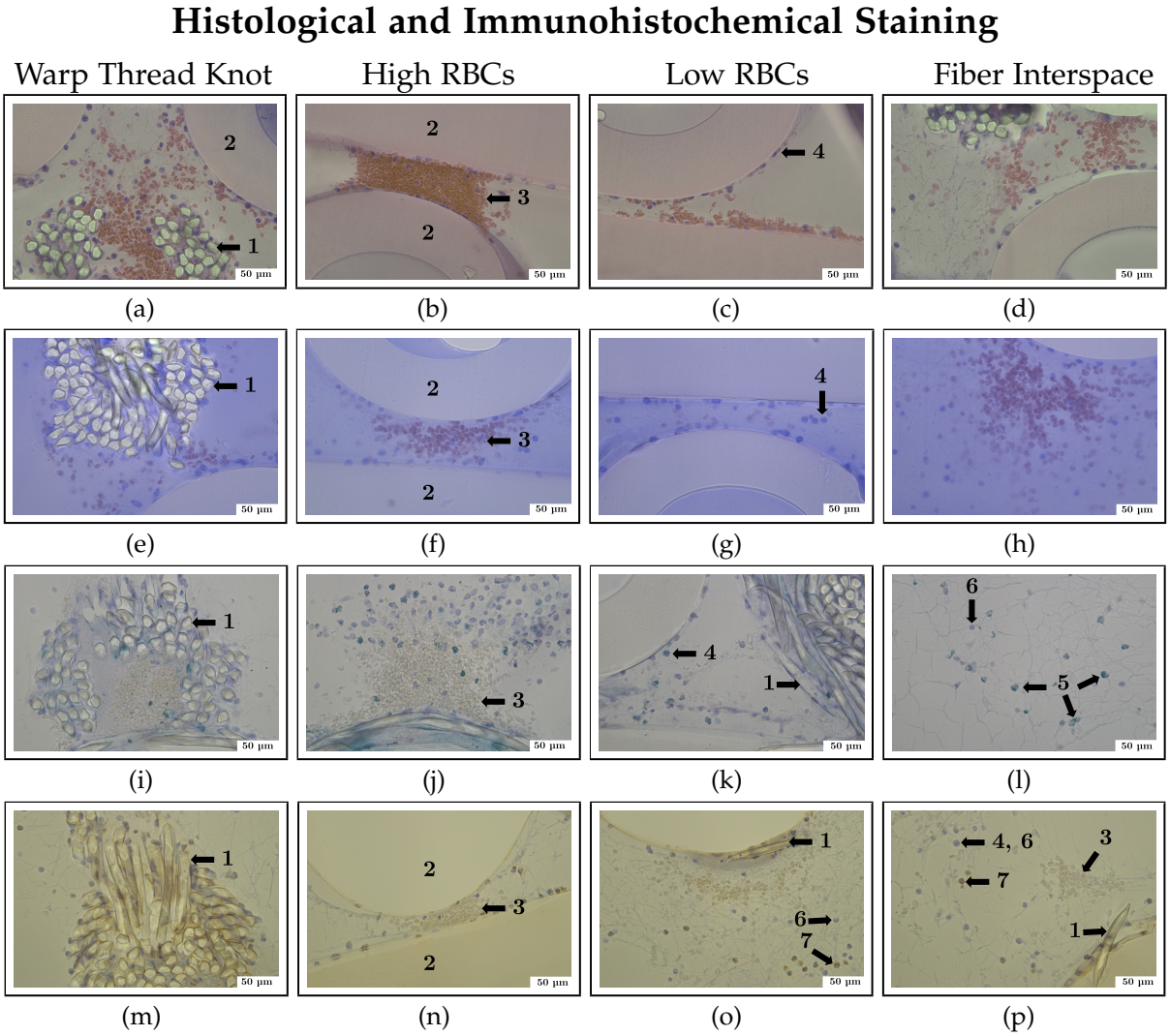


**Figure 3.9: Established histological and IHC stainings for transmitting light microscopy.** Images show (left to right) deposits within or around the warp thread, crossing points with high and low load of RBCs and the interspace of the blood compartment; blood flow from top to bottom. Optimal staining results were performed using (**a-d**) hematoxylin eosin (HE) staining with 1.0 % eosin (RBCs pink-red) and 6 min Hemalum (nucleated cells blue) incubation mounted with VectaMount®; (**a-d**) Pappenheim staining using 3 min May-Grunwald (staining nucleated cells blue) followed by Giemsa (staining RBCs pink), and sections were mounted with Fluoromount-G™. For IHC, anti-MPO antibody was applied at a 1:1,000 dilution, with visualization using either (**i–l**) Histogreen (MPO in green) or (**m–p**) DAB (MPO in brown). Both IHC stainings were counterstained with hemalum (nuclei blue) mounted with Entellan™. The stains caused slight alternations in the appearance of the polymer components: (**a–d**) Eosin in combination with VectaMount® AQ induced a subtle rose coloration of the PMP fibers. (**a–d**, **i–l**) Hemalum produced a faint gray-blue tint in the HistoCURE 8100. (**a–d**) Pappenheim staining mounted with Fluoromount-G™ colored HistoCURE 8100 light blue and the PMP fibers light purple. (**m–p**) DAB imparted a light yellow-brown hue to all plastic components. All subfigures are excerpts from Kranz et al. [90].

were provided by the PD Dr. K. Evert from the Department of Pathology at the University Hospital Regensburg.

Negative controls for testing specific antibody binding consisted of naïve embedded sections. For antibody staining, negative controls were performed by either A) omitting primary and secondary antibodies, B) using only the secondary antibody, or C) using an isotype control antibody (Table 3.2, item #40) at a dilution matching the primary antibody concentration.

**Histological Staining of Polymer Embedded Specimen**

Protocols for HE and Pappenheim staining were established. These are presented in this section. For HE staining, dried sections were equilibrated with deionized water for 2 min at RT and then incubated with Mayer's hemalum solution (Table 3.2, item #35) for 6 min at RT. They were quickly rinsed with deionized water for 10 s at RT, followed by 0.1 % HCl in distilled water (Table 3.2, item #53) for 10 a at RT, and then rinsed again with deionized water.

To enable the color shift to blue, sections were incubated with tempered tap water (20 °C) twice for 3 min each and rinsed with deionized water. Subsequently, sections were stained with 1 % eosin (Table 3.2, item #36) for 30 s at RT in distilled water, acidified with 1 drop of acetic acid per 100 ml (Table 3.2, item #54), and rinsed with deionized water. Sections were dehydrated by dipping in ethanol (3 × at 100 %; Table 3.2, item #52) and xylene (2 ×; Table 3.2, item #55) before mounting with Entellan™ (Table 3.2, item #48) and a cover slide (polymerization for 24 h at 4 °C). This protocol provided the best staining results with minimal staining of the polymer background or fibers (Figures 3.9 (a-d)). Alternatively, sections were dehydrated by dipping in ethanol (2 × at 70 %, 2 × at 96 %, and 2 × at 100 %) and xylene (2 ×) before mounting

with Entellan™ or directly with VectaMount® AQ (Table 3.2, item #49). Staining with 0.1 % eosin for 30 **s** at RT was tested but resulted in unsatisfactory staining of RBCs despite similar background staining.

For Pappenheim staining, air-dried sections were incubated with freshly filtered May-Grunwald solution (Table 3.2, item #37) for 3 min at RT and rinsed with distilled water for 3 min. Giemsa staining (Table 3.2, item #38) was performed at a 1:20 dilution in distilled water for 15 min at RT. Finally, samples were rinsed with distilled water and mounted with FluoromountG™ (Table 3.2, item #50) and a cover slide (polymerization for 24 h at 4 °C; Figures 3.9 (e-h)).

Other methods for mounting the slides, such as air drying with or without adding a coverslip (with a drop of distilled water) just before microscopy, or direct mounting with VectaMount® AQ and a cover slide (polymerization for 24 h at 4 °C), were tested but resulted in stronger background staining and overall inferior staining quality. A shorter incubation with May-Grunwald stain (1 min at RT) was also tested to reduce background staining, but it led to unsatisfactory staining of nucleated cells despite similar background intensity.

**Immunohistochemical Staining of Polymer Embedded Specimen**

An IHC staining protocol was established using an antibody against MPO. Variations of the protocol during development are listed below.

To prevent dispersion of the liquid staining solution, the dried sections were framed with a lipophilic marker and set to dry for 30 min at RT. They were then equilibrated with deionized water for 5 min at RT. Endogenous peroxidase was blocked using 3 % $H_2O_2$ (Table 3.2, item #56) in deionized water (2 $\times$ 5 min at RT) following our laboratory's protocol [31]. Samples were washed with deionized water (2 $\times$ 5 min at

RT) and 0.1 M TBS (0.424 % m/v Tris Base, 2.6 % m/v Tris-HCl, 8.76 % m/v NaCl; Table 3.2, items #28-30) in distilled water, pH 7.4, for 5 min at RT before antigen retrieval with 0.05 % trypsin (Table 3.2, item #57) and 0.1 % $CaCl_2$ (Table 3.2, item #58) in 0.1 M Tris-HCl buffer (2.12 % m/v Tris Base, 13 % m/v Tris-HCl in distilled water, pH 7.8; Table 3.2, items #29-30) for 30 min at 37 °C in a humid compartment [95]. Sections were washed with TBS (3 × 5 min at RT) and incubated for 30 min at RT in a humid compartment in blocking buffer (1 % m/v BSA + 0.2 % m/v gelatin from cold water fish skin; Table 3.2, items #31-32) in TBS + 10 % NGS (Table 3.2, item #33).

Sections were incubated with the primary antibody against MPO (dilution 1:100; Table 3.2, item #39) or isotype control antibody (Table 3.2, item #40) in blocking buffer + 2 % NGS for 18 h at RT in a humid compartment. Samples were washed with TBS (2 × 5 min at RT) and PBS (5 min at RT) before incubation with biotinylated secondary antibody (Table 3.2, item #41), diluted 1:100 in PBS + 2 % NGS for 1 h at RT in a humid compartment. Sections were washed with PBS (3 × 5 min at RT) and primed with avidin-biotin complex (ABC, Table 3.2, item #43) for 1 h at RT in a humid compartment, then washed again with PBS (3 × 5 min at RT). To visualize the bound secondary antibody, sections were incubated with either A) Histogreen (pre-incubation with substrate + buffer for 10 min at RT in a humid compartment; incubation with substrate + buffer + $H_2O_2$ for 3-4 min at RT in a humid compartment; Table 3.2, item #45; Figures 3.9 (i-l)) or B) DAB-Liquid (pre-incubation with DAB + PBS for 10 min at RT in a humid compartment; incubation with DAB + buffer for 3-4 min at RT in a humid compartment; Table 3.2, item #46; Figures 3.9 (m-p)). Sections were then rinsed with deionized water (3 × 5 min at RT) and counterstained with Mayer's hemalum for 30 s. Sections were rinsed with deionized water, tempered tap water (20 °C), and again deionized water before dehydration by dipping in 100 % ethanol (3 ×) and

xylene (2 ×). Sections were mounted with Entellan™ and covered with a cover slide (polymerization for 24 h at 4 °C).

During protocol development, several variations were tested: Blocking endogenous peroxidase with 0.06 % $H_2O_2$ showed non-specific positivity in negative controls and was discarded. The primary MPO antibody was tested at dilutions of 1:50, 1:300, and 1:600, all of which showed inferior staining results. Incubation temperatures of the primary antibody were varied to A) 4 °C for 18 h [31], resulting in reduced staining intensity, or B) 1 h at 37 °C followed by 17 h at RT [94], which provided similar results to the final protocol. Mayer's hemalum counterstaining was initially performed by dipping (2x) during method establishment. Subsequently, counterstaining with Mayer's hemalum was tested for 5 s, 30 s, 60 s, 5 min, and 10 min, with 30 s providing the best results for visualizing nuclei (Mayer's hemalum, blue) combined with MPO (Histogreen, green or DAB, brown).

Paraffin-embedded human tonsils served as positive controls for the staining results. Briefly, paraffin was removed from the 5 µm sections by incubation with xylene (2 × 10 min at RT), 100% ethanol (2 × 5 min at RT), 96 % ethanol (2 × 5 min at RT), 70 % ethanol (1 × 5 min at RT), and deionized water (2 × 5 min at RT). Endogenous peroxidase was blocked with 3 % $H_2O_2$ in deionized water (2 × 5 min at RT), then sections were washed with deionized water. For antigen retrieval, sections were incubated in citric buffer (pH 6; refer to Table 3.2, item #57; dilution 1:10 in distilled water) in a water bath at 97.7–98.4 °C for 1 h and washed with deionized water after a 20-min cooling period. The samples were dried, framed with a lipophilic marker, and set to dry for 30 min at RT. Sections were equilibrated in deionized water (2 × 5 min at RT), washed in PBS (3 × 5 min), and incubated in blocking buffer + 10 % NGS for 30 min at RT in a humid compartment before incubation with the primary

anti-MPO antibody at dilution 1:600 in PBS + 5 % NGS for 18 h at 4 °C in a humid compartment. Samples were then tempered for 1 h at RT, washed with PBS (3 × 5 min), and incubated with biotinylated secondary antibody at dilution 1:300 in PBS + 5 % NGS for 1 h at RT in a humid compartment. Sections were washed in PBS (3 × 5 min), incubated with ABC for 1 h at RT in a humid compartment, and washed again in PBS (3 × 5 min). Visualization of the bound antibody was performed with Histogreen or DAB-Liquid (pre-incubation for 10 min at RT; incubation for 3-4 min at RT). As soon as staining was visible, the incubation was stopped by rinsing with deionized water (3 × 5 min at RT). For counterstaining, samples were dipped (2 ×) in Mayer's hemalum at a dilution of 1:2 with distilled water, then rinsed with deionized water, tempered tap water (20 °C), and again deionized water. For dehydration, samples were dipped in 100 % ethanol (3 ×) and xylene (2 ×). Sections were mounted with Entellan™ under a cover slide (polymerization for 24 h at 4 °C).

**Fluorescence and Immunofluorescence Staining of Polymer Embedded Specimen**

Fluorescence staining protocols using DAPI, SYTOX™ Green, and IHF with antibodies targeting MPO and vWF were successfully established. Variations tested during protocol optimization are detailed below. Once fluorescent dyes were introduced, all tissue sections were protected from light exposure.

To visualize nucleated cells, the fluorescent desoxyribonucleid acid (DNA) stains DAPI and SYTOX™ Green were employed. Dried tissue sections, outlined with a lipophilic marker, were first equilibrated in deionized water for 5 min at RT. They were then stained with SYTOX™ Green (Table 3.2, item #47) at a 1:500 dilution in TBS for 30 min at RT. Following staining, sections were washed in TBS (3 × for 5 min each at RT) and mounted using Fluoromount-G™ DAPI (Table 3.2, item #51) with a coverslip. Polymerization was carried out for 24 h at 4 °C (Figure 3.10).

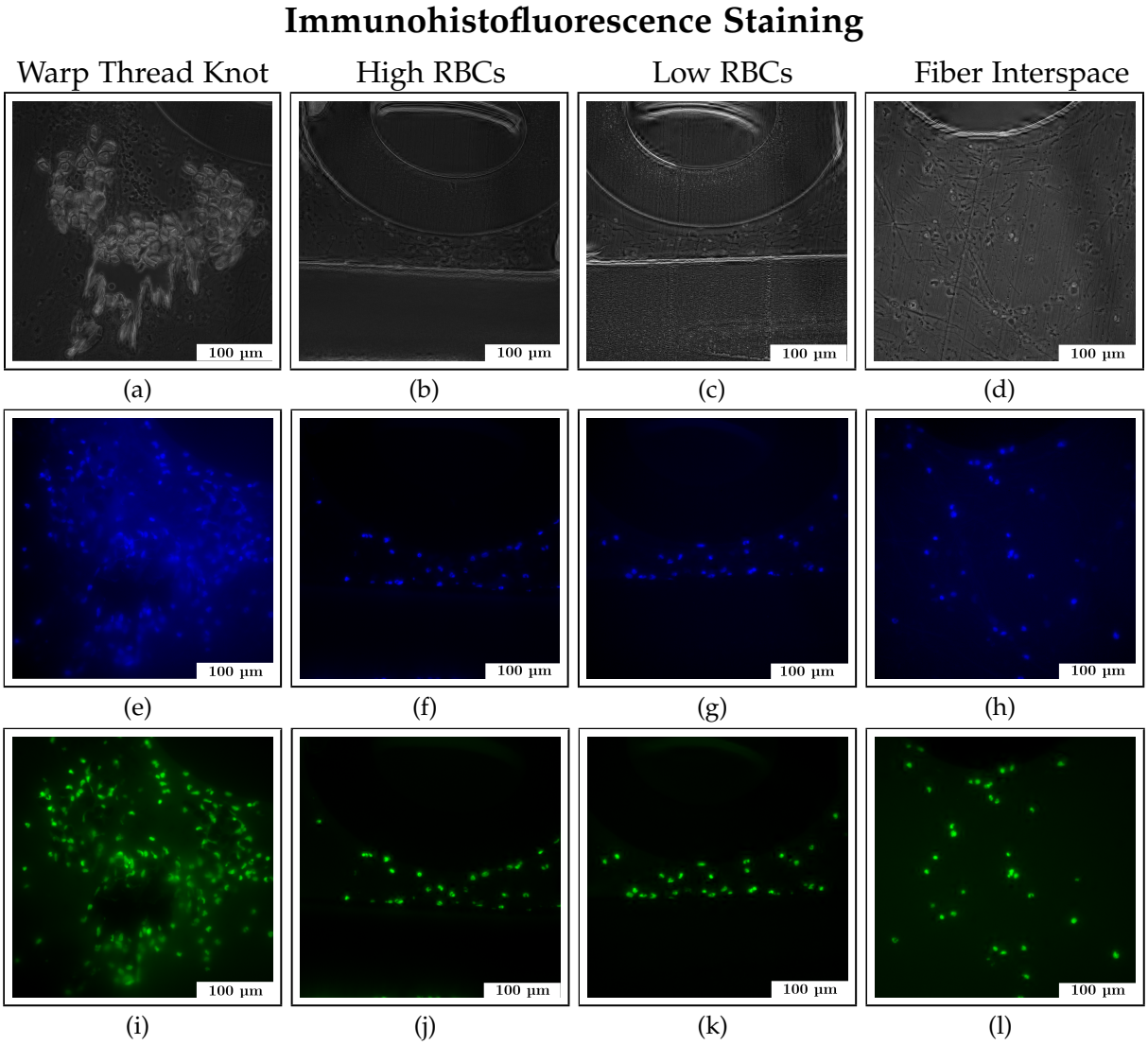


**Figure 3.10: Established IHF protocols.** The images illustrate, from left to right, deposits located within or adjacent to the warp thread, deposits at crossing points with both high and low RBC loads, and deposits in the interspace of the blood compartment; blood flow is oriented from top to bottom. (**a**–**d**) Fluorescence phase contrast images provide structural context. Fluorescence staining results are shown using (**e**–**h**) DAPI (DNA in blue) and (**i**–**l**) SYTOX™ Green (DNA in green). All subfigures are excerpts from Kranz et al. [90].

During protocol development, antigen retrieval using 0.05% trypsin and 0.1 % $CaCl_2$ in Tris-HCl buffer (30 min, 37 °C, humid compartment) was tested prior to SYTOX™ Green (5 mmol) staining but did not yield significant improvements. Additionally, SYTOX™ Green was evaluated at dilutions of 1:500, 1:750, and 1:1000 in TBS (30 min, RT), with 1:500 providing the most effective results. For IHF staining, dried sections framed with a lipophilic marker were rehydrated in deionized water (5 min, RT). Antigen retrieval was performed using 0.05 % trypsin and 0.1 % $CaCl_2$ in Tris-HCl buffer (2.12 % w/v Tris Base, 13 % w/v Tris-HCl, pH 7.8; 30 min, 37 °C, humid compartment). Sections were then washed in TBS (3 × 5 min, RT) and blocked using a buffer containing 1 % w/v BSA, 0.2 % w/v cold water fish skin gelatin in TBS, and 10 % NDS (Table 3.2, item #34) for 30 min at RT in a humid compartment.

Next, sections were incubated overnight (18 h, RT, humid compartment) with primary antibodies against MPO or vWF (both at 1:100 dilution; vWF: Table 3.2, item #40), or with an isotype control antibody, all diluted in blocking buffer supplemented with 2 % NDS. After washing with TBS (3 × 5 min, RT), sections were incubated with a fluorophore-conjugated secondary antibody (Table 3.2 , item #43) at a 1:500 dilution in TBS + 2 % NDS for 1 h at RT in a humid chamber. Finally, sections were washed again (3 × 5 min, RT), mounted with Fluoromount-G™ DAPI for nuclear counterstaining, and covered with a coverslip (polymerization: 24 h at 4 °C; Figure 3.10).

### 3.3.7 Microscopic Imaging

Imaging was performed using a DMi8 microscope (Table 3.1, item #12), equipped with a K3C RGB camera (Table 3.1, item #13) for transmitted light microscopy, and a K5 grayscale camera (Table 3.1, item #14) paired with optical filters (Table 3.1, items #15–16) for fluorescence microscopy. The system was operated via LAS X software (Table 3.1, item #17) and enclosed in a dark housing to minimize fluorophore photobleaching.

At 400 fold magnification, slight unevenness in the tissue sections was observed. To address the limited depth of field and ensure image sharpness, a series of consecutive images at varying focal planes (z-stacks) were captured. These z-stacks were then merged using the LAS X software to produce extended depth of field (EDoF) images.

Overview images were acquired at 25 fold magnification to assess sectioning quality and fiber arrangement. For detailed analysis of staining results, images were taken at 100 fold, and 400 fold magnifications. At 100 fold, z-stacks were collected up to a depth of 45 µm with a system-optimized z-step size of 3.80 µm. At 400 fold, the z-stack depth ranged from 5 to 35 µm, with a z-step size of 0.29 µm. Flatter regions required smaller z-depths (5–20 µm), while imaging of warp threads necessitated greater depths (up to 35 µm).

Detailed protocols for transmitting light (Figure 3.9) and fluorescence microscopy (Figure 3.10) are provided in the following sections. When needed, image post-processing, such as background reduction, was performed using Adobe Photoshop CS5 (Table 3.1, item #18).

**Transmitting Light Microscopy**

For transmitting light microscopy (image format: 3:2 ratio, resolution: 3,072 $\times$ 2,048 pixels), a single channel was used, and colors were displayed using the split RGB channel in color mode. The full pixel value range (0–4,095) was applied throughout.

Across all magnifications, the Fluorescence Intensity Manager (FIM) was utilized, and the camera captured 100 % of the available light. The exposure time was consistently set to 85 ms with a gain of 1.

Lighting conditions varied by magnification: 25 fold magnification: Light intensity at 50 %, aperture set to 3, and light-field value of 26. 100 fold magnification: Light

intensity at 30 %, aperture set to 10, and light-field value of 37. 400 fold magnification: Light intensity at 50 %, aperture set to 21, and light-field value of 28.

**Fluorescence Microscopy**

For fluorescence microscopy (square format, 2,048 × 2,048 pixels), each color channel was imaged separately using illumination wavelengths matched to the excitation spectra of the respective fluorophores.

DAPI was visualized in blue using an excitation wavelength of 390 nm (LED intensity: 58 %, filter: 420–460 nm) with an exposure time of 250 ms. SYTOX™ Green was imaged in the fluorescein isothiocyanate (FITC) channel (green) with excitation at 475 nm (LED intensity: 30 %, filter: 500–540 nm) and an exposure time of 10 ms. MPO was visualized in red using the far red (FR) channel, excited at 635 nm (LED intensity: 58 %, filter: 662–738 nm) with an exposure time of 800 ms.

For all three channels, the FIM was set to 100 %, the illumination field was configured to 6, and 100 % of the light was directed to the camera.

To enhance visualization of co-localization between stained biological deposits and structural elements of the ML (e.g., hollow-fibers, warp threads), fluorescence phase contrast imaging was added. This was performed using 390 nm excitation (LED intensity: 58 %, 100 % filter transmission), with a 25 ms exposure time. For overlay visualization, the RGB color settings were adjusted to 0-50-80.

DAPI and SYTOX™ Green channels were displayed using automated grayscale adjustment. For IHF, the grayscale range for the FR channel was manually set to 350–1,200 to visualize MPO and vWF. A composite overlay image combining all channels was generated. Additionally, raw images were exported using the full grayscale range (65,535 values).

## 3.4 Results

This chapter presents a protocol for polymer embedding of entire MLs using a combination of HistoCURE 8100 and Technovit® 3040 resins. The embedded fiber mats were generally well stabilized within the polymer matrix and remained intact during microtome sectioning. Occasionally, individual dislocated hollow fibers were observed during sectioning (Figure 3.11 (a)). However, the rigid polymer scaffold effectively supported both the hollow fibers and the multi-layered biological deposits, preserving their native positions.

### 3.4.1 Embedding Quality

Unlike Technovit® 9100, no elongation of PMP hollow-fibers or formation of air bubbles within the polymer was detected. Sections as thin as 5 µm were achievable (Figures 3.7 (a-d), though a thickness of 10 µm was preferred for easier handling and flatter sections (Figures 3.7 (e-h), 3.8, 3.9–3.11). HistoCURE 8100 proved effective in securing biological deposits in both clotted (Figures 3.7 (a-d)) and non-clotted (Figures 3.7 (e-g)) regions. This enabled visualization of large deposits adhering to fiber surfaces and forming structures that spanned between fibers. Clots within the warp thread were also well preserved (Figures 3.8 (a-d)). Both PMP hollow-fibers and warp threads could be sectioned longitudinally and in cross-section (Figure 3.8).It was also possible to cut the TPU hollow-fibers within the inlet chamber. However, these showed a deformation which had to be prominent prior to the hardening, as illustrated in Figure 3.12. Still, it was possible to perform microtome sectioning and histological staining.

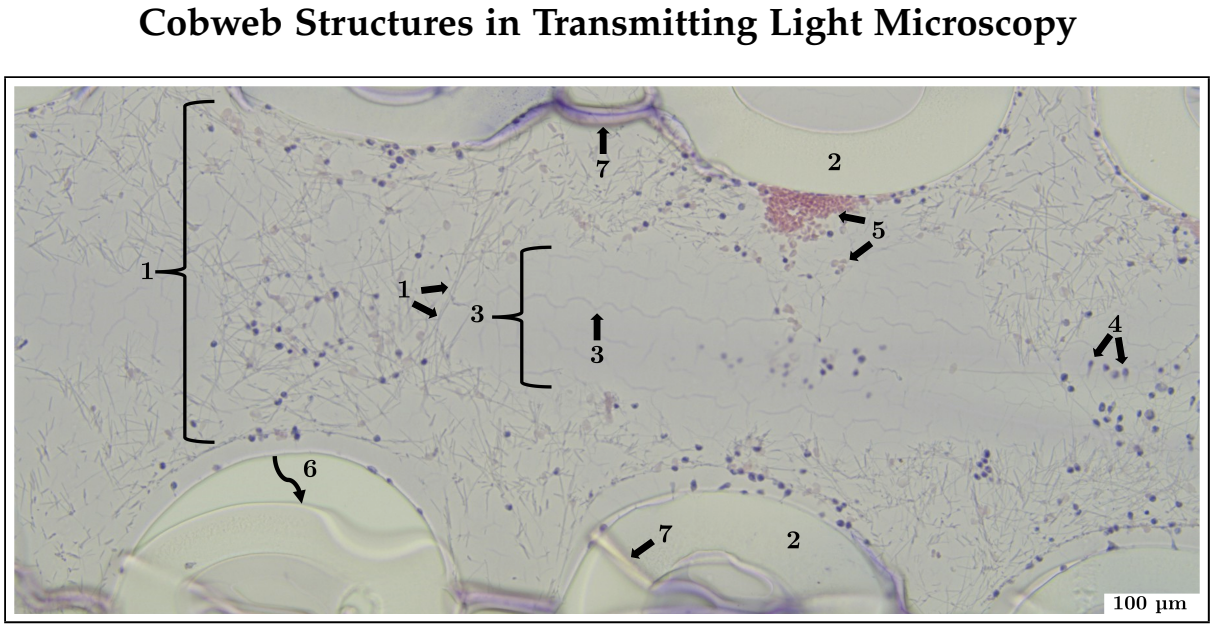


(a)

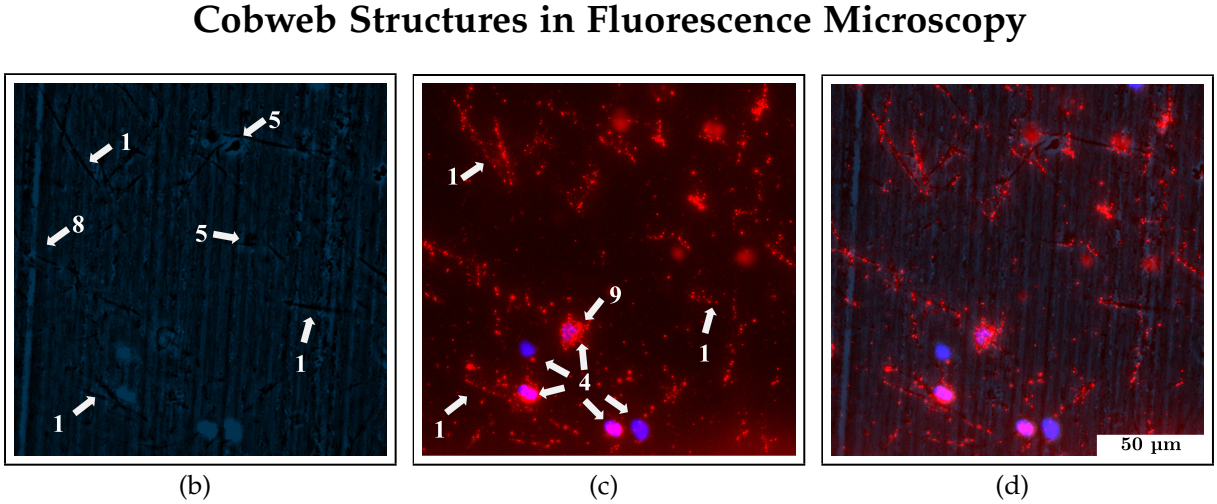


(b) (c) (d)

**Figure 3.11: Identification of distinct biological clot components.** The images distinguish between (1) biological cobweb-like networks spanning between the (2) gas-exchange fibers and (3) geometric cracks in the HistoCURE 8100, which are visible in cobweb-free regions of the blood compartment. Blood flow is oriented from top to bottom. (**a**) HE staining differentiates (4) nucleated cells (blue), (5) RBCs (pink), and fibrin fibers within the cobweb (light purple). Cellular deposits were observed either on the surfaces of the gas-exchange fibers or embedded within the cobweb structure, but were absent in cobweb-free areas. (6) Displacement of gas-exchange fibers during microtomy did not affect the position of deposits, which were fixed in place by the HistoCURE 8100. (7) Artifact folds are present. (**b–d**) Detection of vWF using IHF. (**b**) Fluorescence phase contrast highlights surface structures, including (1) the cobweb formations and an (8) artifact caused by sectioning. (**c**) IHF staining visualizes nucleated cells (DAPI, blue) and vWF (red). vWF appears either (1) dispersed as bead-like dots along strands or (9) localized near nucleated cells as granules. (**d**) The overlay confirms that the vWF-positive strands align precisely with the cobweb structures observed in the phase contrast image. All subfigures are excerpts from Kranz et al. [90].

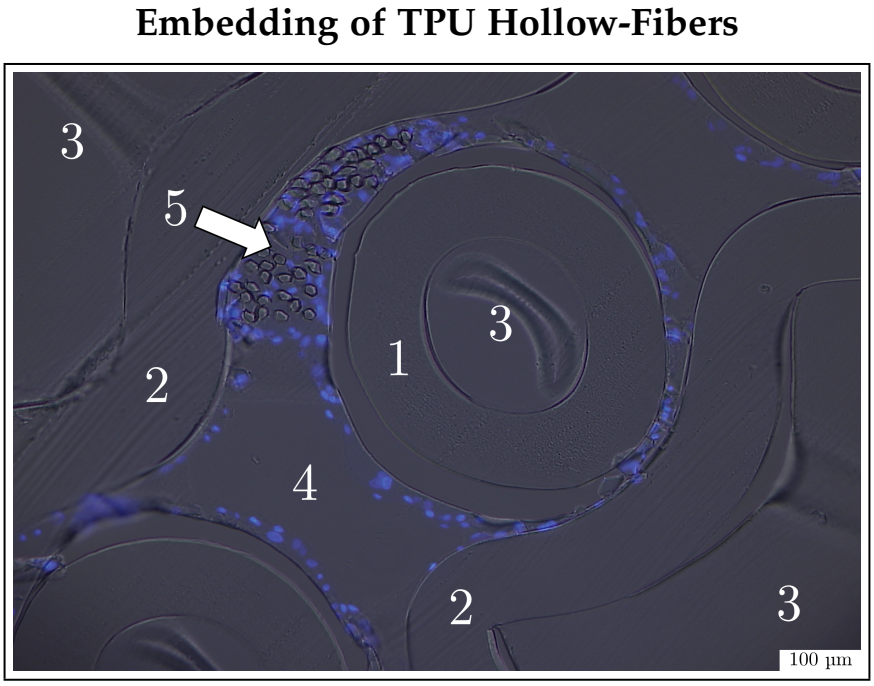


**Figure 3.12: Embedding of PMP and TPU hollow-fibers in the inlet chamber.** Overlay of bright field and DAPI images. (1) Transversely cut PMP and (2) longitudinally cut TPU hollow-fiber. The TPU hollow-fibers show a deformation before the polymer was fully hardened. (3) Interior of hollow-fibers stabilized with polymer. (4) Hollow-fiber interspace with leukocytes (DAPI: blue). (5) Transversely cut warp thread with deposed leukocytes.

### 3.4.2 Visualized Structures

Histological stains (HE, Pappenheim, Mayer's Hemalum; Figures 3.7–3.9, 3.11 (a)) revealed a high density of leukocytes and RBCs, primarily attached to fiber surfaces, within the warp thread, or entangled in cobweb-like structures across the fiber mat. Further cellular and protein differentiation within the deposits was achieved using IHC (Figures 3.9 (i-p)) and IHF (Figures 3.10, 3.13, 3.11 (b)). Occasionally, thin geometric cracks appeared in the HistoCURE 8100 matrix (Figure 3.11 (a)), distinguishable from biological cobwebs. These cracks likely resulted from interactions between the polymer and solvents used prior to mounting.

Observed vWF structures appeared either as spaced beaded dots or as granules near nucleated cells. In overlay images, these beaded dots aligned with cobweb-like

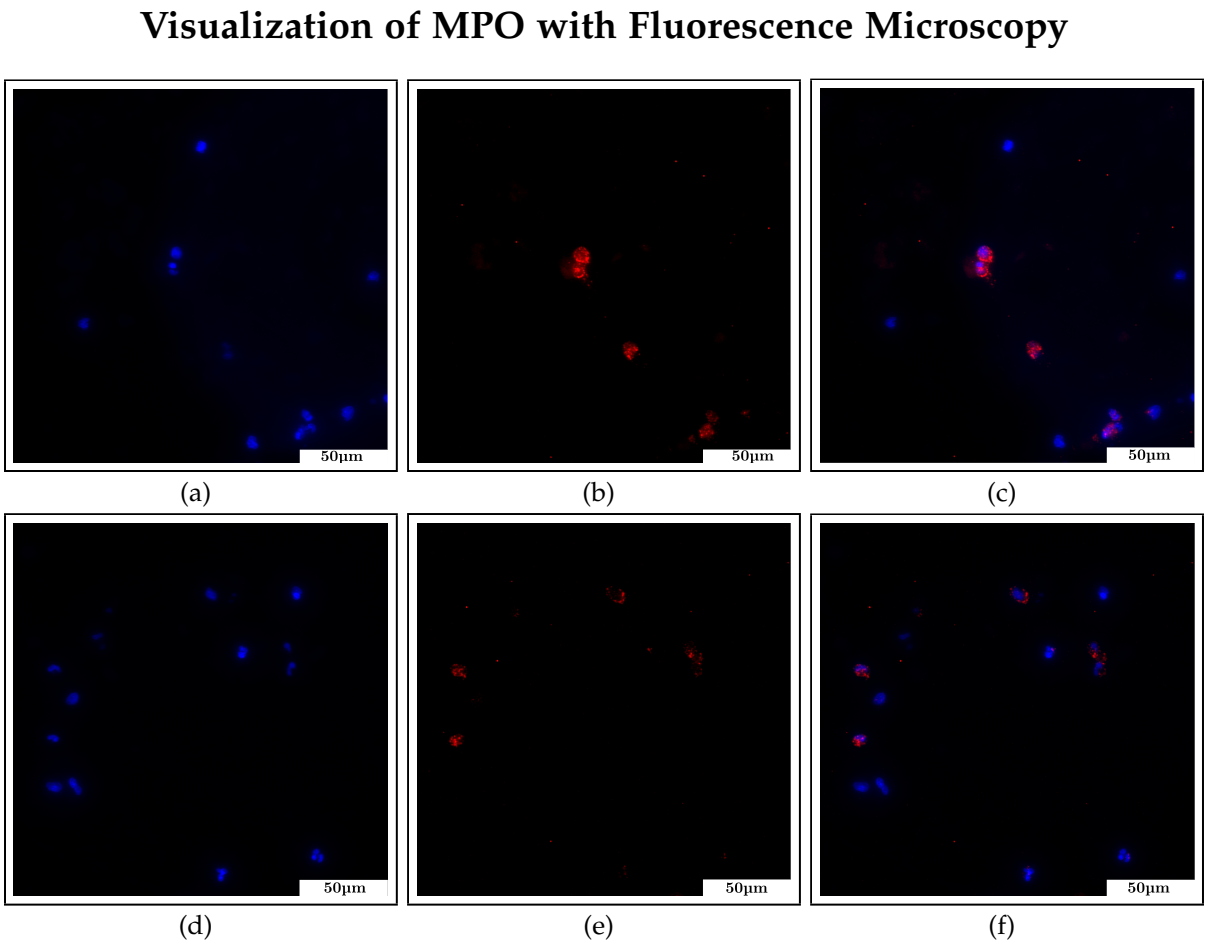


**Figure 3.13: Visualization of cytoplasm with MPO using IHF.** Images were taken at two representative locations, both within the interspace of the blood compartment, with blood flow oriented from top to bottom. (**a**, **d**) DAPI staining highlights nuclei in blue. (**b**, **e**) IHF staining against MPO is shown in red. (**c**, **f**) Overlay images demonstrate MPO signals closely associated with the nuclei. All subfigures are excerpts from Kranz et al. [90].

structures seen in fluorescence phase contrast (Figure 3.11 (d)). These biological cobwebs are three-dimensional, meaning only strands aligned with the sectioning plane were visible in IHF. Strands crossing the plane appeared as dots in IHF but were clearly visible in fluorescence phase contrast (Figure 3.11 (b)) and transmitted light microscopy (Figure 3.11 (a)). Based on these observations, vWF is proposed as a key component of the cobweb structures (Figure 3.11 (b-d)).

Previously, the three-dimensional nature of warp threads hindered top-view imaging and limited access to the dense cellular content interwoven among the strands (Figure 3.1). Embedding with HistoCURE 8100 enabled both cross-sectional (Figures 3.8 (a-d)) and longitudinal (Figure 3.8 (e-h)) sectioning of warp threads. Histological and IHC staining provided detailed insights into cells adhered to the warp thread strands (Figures 3.8 (a, b, e, f)). However, fluorescence signals in IHF were limited by light refraction on the transparent warp thread strands (Figures 3.8 (c, d, g, h)). While fluorescence area measurements may indicate deposit density, cell differentiation via IHF is more effective in regions outside the warp thread strands.

IHC proved to be a robust, reproducible method for detecting biological proteins, with the added benefit of being resistant to light exposure, unlike IHF. Both Histogreen and DAB staining enabled grading of MPO expression in nucleated cells (Figures 3.14 (a, b)). Notably, Histogreen staining provided clear differentiation between strongly MPO-positive cells and those with only faint granular MPO signals (light green). Furthermore, in some cases an unspecific staining of DAB was observed due to hemosiderin deposition inside the ML.

### 3.4.3 Trouble Shooting

Pre-infiltration was essential to ensure effective binding of HistoCURE 8100 to clots. The lower-viscosity pre-infiltration solution was absorbed by the clots, allowing internal hardening. Without this step, clots were merely encapsulated by the polymer without internal stabilization, resulting in uneven specimen hardness that prevented successful microtome sectioning. Therefore, pre-infiltration is particularly critical for MLs with a high clot burden.

Although HistoCURE 8100 does not support deplastification, histological and fluorescence stains could still access all deposits within the sections due to the small molecular size of the dyes. However, antibody-based staining (IHC and IHF) was limited to the section surface. This surface-only accessibility could result in low antigen detection, especially for intracellular targets like MPO, if the nucleus was sectioned through and the antigen was located just beneath the surface (Figures 3.14 (a, b)). Consequently, higher antibody concentrations were required compared to paraffin-embedded sections when optimizing staining protocols for HistoCURE 8100.

Fluorescence staining and IHF successfully enabled visualization of structures across different channels. Nuclei were clearly visible in the DAPI channel, while MPO and vWF were detected in red, allowing both individual analysis and co-localization in merged images (Figures 3.13, 3.11 (b-d)).

During protocol development, MPO and vWF were visualized using a state-of-the-art secondary antibody (Donkey anti-rabbit AlexaFluor 594, 711-585-152, Dianova, Hamburg, Germany) in the TRITC channel, following Wagner and Kranz et al. [31]. Excitation was performed at 560 nm (58 % LED intensity, filter: 565–615 nm) with a 60 ms exposure time (Figures 3.14 (c, d), 3.10, 3.15 (a)). To reduce autofluorescence,

## Trouble Shooting

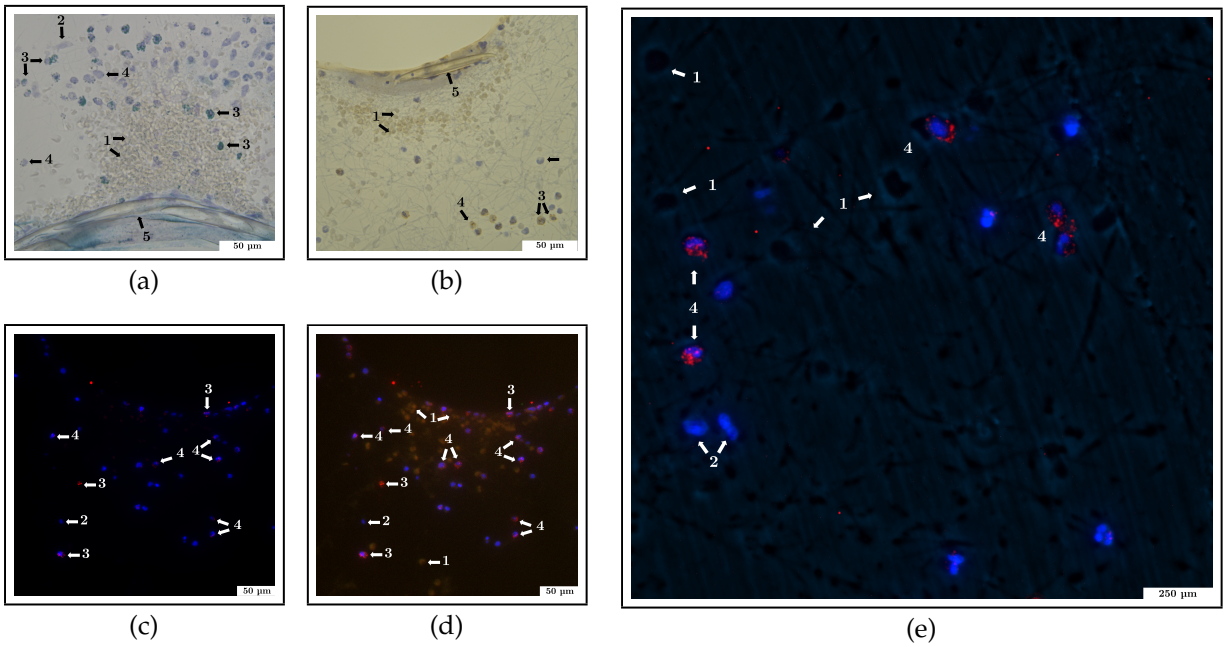


**Figure 3.14: Differentiation of MPO signal intensity in IHC and IHF stainings.** IHC staining with anti-MPO was visualized using (**a**) Histogreen (MPO in green) and (**b**) DAB (MPO in brown), with hemalum counterstaining for nuclei (blue). Blood flow is oriented from top to bottom. The cellular deposits primarily consisted of RBCs (1, unstained) and nucleated cells (blue), which were present either (2) without or (3–4) with MPO expression, typically appearing as granular structures. Both staining approaches enabled distinction between cells containing (3) high levels and (4) lower levels of MPO antigen, although Histogreen provided more distinct visual contrast. The depicted cells are located adjacent to (5) a warp thread. (**c**–**e**) IHF offered an alternative method capable of visualizing even small amounts of MPO (red) in spatial proximity to DAPI-stained nuclei (blue) and supports automated detection using separated channels. As part of protocol development, MPO visualization was evaluated in both the tetramethylrhodamine isothiocyanate (TRITC) and FR channels. (**c**, **d**) Overlay images show MPO in the TRITC channel at different gray-value thresholds, combined with DAPI. The gray-value settings applied for the TRITC channel (MPO) and the FITC channel (empty control) were (**c**) 150–250 and (**d**) 100–250. Lower threshold values improved visibility of fine granular MPO, but simultaneously increased detection of autofluorescent RBCs (1). Autofluorescence of RBCs was suppressed at threshold values above 150 in both the FITC and TRITC channels. (**e**) Overlay of fluorescence phase-contrast imaging with MPO detection in the FR channel and DAPI. Using a secondary antibody with excitation in the FR channel reduced interference from RBC autofluorescence. Under these conditions, RBC silhouettes were visible only in the fluorescence phase-contrast image (1). All subfigures are excerpts from Kranz et al. [90].

TRITC channel gray values were adjusted to 150–250, though small granules were best seen at 100–250. Non-stained RBCs within the 10 µm sections, visible in fluorescence phase contrast, exhibited autofluorescence in both FITC and TRITC channels at these gray values (Figure 3.14 (d)). These RBCs appeared as diffuse, cloud-like structures. When clustered in clots, they formed larger autofluorescent areas. Despite this, the strong MPO staining (limited to the section surface) produced signal intensities that exceeded those of RBC autofluorescence, allowing clear visualization of MPO granules. While setting gray values to 150–250 suppressed RBC autofluorescence, it also reduced visibility of smaller MPO granules (Figure 3.14 (c)). Introducing the secondary antibody in the FR channel significantly reduced autofluorescence, leaving only structural silhouettes visible in fluorescence phase contrast (Figure 3.14 (e)).

Similarly, vWF visualization in the TRITC channel required short exposure times to minimize autofluorescence (Figure 3.15 (a)). However, the vWF signal was relatively weak. To enhance it, a control image was acquired in the FITC channel and digitally subtracted from the TRITC image. This grayscale subtraction isolated the vWF signal (Figure 3.15 (b)), which was then added to the original overlay to produce an enhanced composite image (Figure 3.15 (c)). Still, using the secondary antibody in the FR channel provided superior signal quality (Figures 3.11 (b-d)).

Occasionally, non-specific antibody accumulation was observed in deep microtome knife marks caused by the polymer's hardness. This issue was significantly reduced by regularly adjusting the knife position. Minor knife artifacts, however, did not show any antibody accumulation (Figure 3.11 (b)).

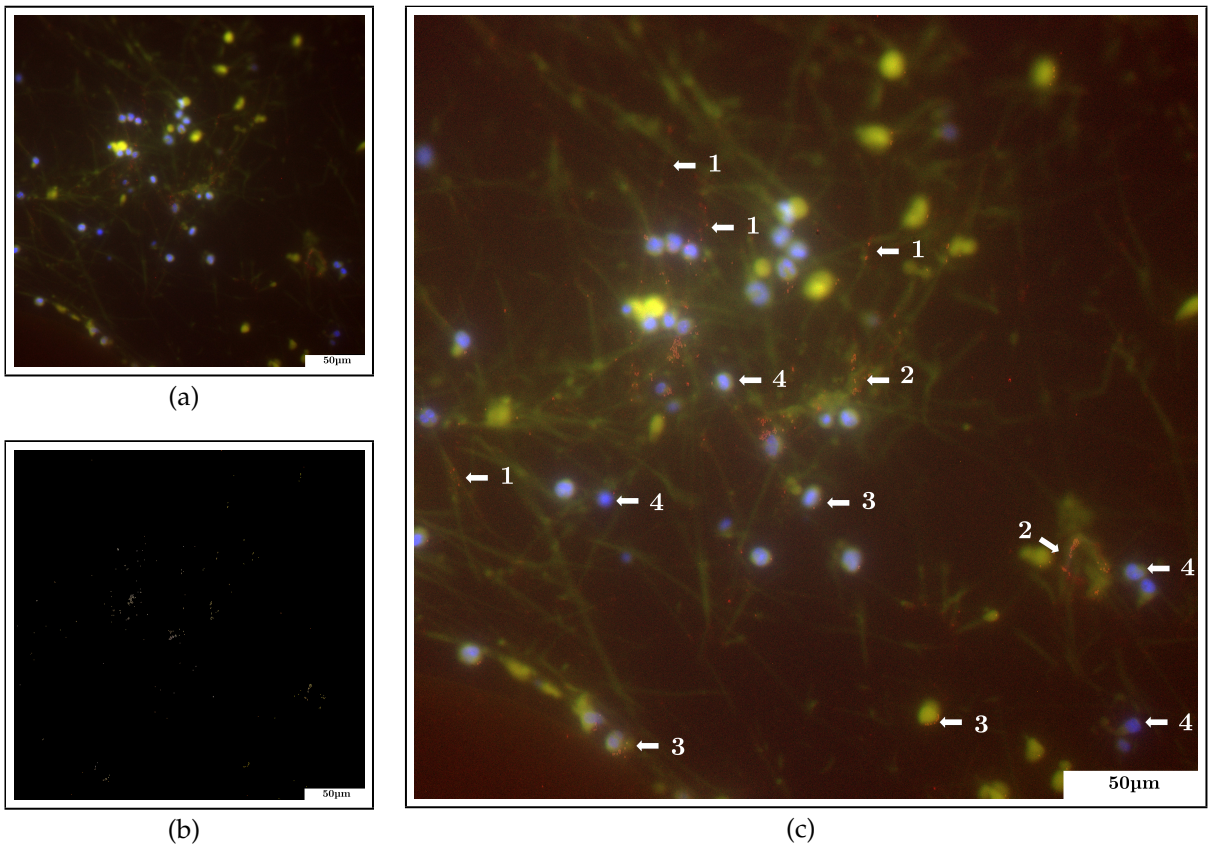


**Figure 3.15: Visualization of vWF structures using the TRITC-channel and digital image subtraction**. The image was captured within the interspace of the blood compartment, with blood flow directed from top to bottom. (**a**) Overlay of vWF (red) detected in the TRITC channel together with DAPI-stained nuclei (blue). Because vWF structures were accessible to staining only on the section surface, the resulting signal was reduced and required the use of a low gray-value threshold. Under these conditions, autofluorescent structures located deeper within the 10 µm-thick section interfered with the vWF signal. To account for this, the FITC channel (empty control) was acquired specifically to detect autofluorescence (visualized as yellow in the overlay). Gray-value thresholds for both the FITC and TRITC channels were set to 100–250 to enable detection of small vWF structures. (**b**) To isolate the vWF signal, digital grayscale subtraction was performed between the TRITC and FITC channels. (**c**) Enhanced overlay in which the isolated vWF signal from (**b**, shown in red) is added back onto the original image in (**a**). This visualization highlights vWF located on top of autofluorescent structures within the section. vWF was detected along (1) strand-like structures, (2) areas with accumulated autofluorescence, and (3) in close proximity to (4) DAPI-stained nuclei. All subfigures are excerpts from Kranz et al. [90].

## 3.5 Discussion

This protocol offers a reliable and reproducible method for polymer embedding of an entire clinically used ML. It meets the key objective of significantly enhancing the mechanical stability of both the ML structure and the associated cellular and extracellular deposits, thereby enabling high-quality histological analysis of the resulting sections.

### 3.5.1 Significance of Methodology

Polymer embedding of MLs presents an innovative technique for preserving delicate clot structures, enabling histological analysis in regions that were previously inaccessible. This method allows for the examination of deposits surrounding the entire circumference of hollow-fibers, within warp threads, and across fiber mats, all in their native positions without visible distortion as it was the case with paraffin embedding [54]. The resulting stabilization of clot structures supports reliable cross-sectioning and histological staining.

Preliminary findings demonstrate clear advantages over conventional top view fluorescence microscopy of fiber mats, which is limited to visually clot-free regions on individual fibers [31, 54]. This embedding approach offers a promising avenue for studying intra-device clot formation, significantly broadening the scope of histological analysis and contributing to a deeper understanding of the complex, multifactorial coagulation processes within MLs.

In previous publications HistoCURE 8100 was used for investigation of tissue specimens [94, 95] or of stented arteries [92, 93]. However, the large-scale application of this polymer in medical devices has not yet been carried out. Moreover, the method's applicability may extend beyond ECMO. As it involves embedding large-volume

samples (up to 400 ml) in polymer for histological staining and analysis, it could be adapted for use with other blood-contacting medical devices, such as ECMO blood pumps or dialysis filters. These potential applications highlight the broader relevance of this technique in medical research and device evaluation.

### 3.5.2 Quality of Embedding and Specimen Extraction

Following embedding, the ML was sufficiently stabilized to allow microtome sectioning at thicknesses of 5–10 µm without introducing optical artifacts. A section thickness of 10 µm was found to offer optimal handling characteristics. These sections preserved membrane morphology and were compatible with standard histological, IHC, and IHF staining techniques. The warp thread encasing individual hollow-fibers remained intact, enabling detailed histological analysis of associated deposits.

This protocol enables investigations of immunological processes surrounding hollow-fibers that are not feasible with conventional paraffin embedding.

As such, polymer embedding represents a promising methodological advancement, laying the groundwork for new insights into the complex mechanisms of intra-device clot formation.

### 3.5.3 Histological Staining

Polymer embedding enables reproducible serial cross-sections of both hollow-fibers and biological material in clot-rich and clot-free regions. These regions can be precisely localized prior to specimen extraction using MDCT. Importantly, this method allows for the investigation of deposits along the direction of blood flow, an analytical dimension that was previously inaccessible in top-view studies of ML hollow-fibers

[31, 54]. This advancement opens the possibility of correlating flow dynamics with clotting mechanisms.

Thin serial sections facilitate detailed analysis of various components of the coagulation cascade through (immuno-)histological staining. This approach supports the reconstruction and interpretation of three-dimensional structures within the ML, particularly in relation to blood flow direction.

Staining polymer-embedded samples poses a significant challenge due to the physical properties of many polymers. After evaluating multiple approaches, optimized protocols were successfully established for standard histological stains (e.g., HE, Pappenheim) as well as for IHC and IHF techniques. Protocols were adapted from state-of-the-art protocols for paraffin embedding and from published protocols from Malik et al. [93], De Jonge et al. [94], and Ponsioen et al. [95]. These include DNA stains such as DAPI and SYTOX™ Green, and antibody-based detection of MPO and vWF. The protocols were validated using both positive and negative controls, yielding consistent and reproducible results. Depending on specific research needs, these protocols can be further refined and expanded to include additional antibodies. Due to the staining with the polymer in place, fewer binding sites were accessible for antibody-staining. This was circumvented by increasing the antibody concentration. Other staining agents as HE for example showed the capability of penetrating through the polymer, allowing for high quality staining.

### 3.5.4 Alternative Embedding Approaches

Identifying a suitable embedding polymer posed a significant challenge. To support other research groups facing similar difficulties, this section presents experiences with alternative plastics that were evaluated but ultimately excluded from the final protocol.

Technovit® 2000 LC (with curing agent) was tested in preliminary experiments (unpublished) and demonstrated excellent mechanical stability and ease of handling. It proved suitable for light microscopy. However, according to the manufacturer, it was not developed for histological analyses and therefore discarded.

As described above, Technovit® 9100 was also tested due to its compatibility with IHC and IHF staining and its advertised ability to undergo deplastification after sectioning. However, an interaction between the base solution and the hollow-fibers led to an approximate 10 % elongation of the hollow-fibers, compromising structural integrity. Additionally, the use of xylene, recommended by the manufacturer for sample preparation, was problematic. Xylene dissolved plasticizers in the ML housing, rendering it brittle, and also caused the housing's dye to leach, resulting in an unintended blue discoloration of the hollow-fibers (Figure 3.2).

### 3.5.5 Limitations

This method has shown promising results for PMP gas exchange hollow-fibers. However, heat exchange hollow-fibers, which are made of TPU, are more prone to softening and deformation. In preliminary tests without pre-infiltration, deformation of TPU hollow-fibers was observed. While examination of TPU hollow-fibers is still feasible, potential dislocation of the hollow-fibers must be taken into account.

HistoCURE 8100 does not support deplastification [92], meaning that all staining procedures must be performed with the polymer in place. As a result, antibody staining is limited to the two-dimensional surface of the microtome sections, whereas histological dyes can penetrate deeper into the section. Therefore, the accessibility of binding sites for antibodies is reduced and a background staining of the polymer can possibly limit the significance of certain staining methods.

Nevertheless, this protocol enables the production of thin microtome sections, allowing for the reconstruction of large three-dimensional structures by analyzing a series of consecutive closely spaced two-dimensional sections.

## 3.6 Conclusion

In summary, the methodology presented offers a robust and reproducible approach to enhancing the mechanical stability of ML hollow-fibers and associated biological deposits. This advancement enables histological analysis of previously inaccessible regions within membrane layers, particularly clots and deposits aligned with the direction of blood flow. As a result, it opens new avenues for scientific exploration and contributes to a deeper understanding of the complex, multifactorial clotting mechanisms involved in ECMO MLs.

# 4. Computational Fluid Dynamics in Membrane Lungs

The influence of unphysiological shear stress (i.e. $\dot{\gamma} > 5000\ 1/s$ according to Colace et al. [96]) on the vWF has been subject to various studies. The presence of elongated vWF in cobweb structures within clinically used MLs was proven in previous studies [31, 54]. Consequently, elongated vWF is considered a biomarker for elevated shear rates. However, whether the flow conditions inside MLs actually induce an elongation of the vWF is not yet known and, in specific, which regions are critical for intra-device clot formation. Despite the evidence of the presence of elongated vWF, exposure to elevated shear stress could still occur elsewhere, e.g. in the upstream ECMO pump (sieve theory).

This chapter provides deeper insights into the local flow regimes in the vicinity of the hollow-fibers. Using a generic model featuring parallel and equidistant hollow-fiber arrangement, similar to recent studies, and a native model with a flow domain directly derived from a non-clinically used ML to investigate the influence of irregular hollow-fiber arrangement which was prior observed by Wagner and Kranz et al. [31].

Parts of this chapter were accepted for publication in *High-Resolution Flow Investigations in Membrane Lungs for Understanding Shear-Induced Blood Clot Formation* as contribu-

tion to the series *Notes on Numerical Fluid Mechanics and Multidisciplinary Design* [23]. The content and illustrations in this chapter were reproduced with permission from Springer Nature.

Moreover, first results were presented at 1st European Fluid Dynamics Conference (EFDC1) in Aachen, Germany in September 2024 as well as at 24th symposium of the Fluid Mechanics Working Group (Strömungsmechanische Arbeitsgemeinschaft) (STAB) of the German Society for Aeronautics and Astronautics (Deutsche Gesellschaft für Luft- und Raumfahrt) (DGLR) in Regensburg, Germany in November 2024 [23, 97].

## 4.1 Introduction

As described above, clotting in MLs is expected to be an interplay of inflammatory reaction due to foreign body interaction, blood stasis because of stagnant blood flow, and vWF activation caused by elevated shear stress. Latter is of particular interest for this work.

Since non-invasive optical blood flow measurements inside MLs is limited due to the restricted accessibility and limitation of the application of blood as test fluid, a computer based blood flow model was chosen. However, modeling blood flow in MLs is a major challenge. Mainly because of the complex geometry of the fluid domain. But also the rheological properties of human blood must be considered.

Previously published CFD studies of ML blood flow investigated blood distribution and the location-dependent residence time of blood. To investigate this, the research groups looked at the device as a whole. In their work, Fu et al. [63] considered the fiber mats as a porosity boundary condition and did not model hollow fibers, but only the macroscopic geometry of the ML. They compared five different types of MLs

from different manufacturers (also PLS ML) and discussed the global flow velocity and the residence time of the blood to identify local stasis effects. Dipresa et al. [67], on the other hand, also modeled the hollow fibers, but a different type of ML with a significantly different structure was chosen as the basis for the study, which is why comparability with the PLS model is limited.

Consequently, these certain studies mostly did not represent the resolution required for the detection of local shear stress in the vicinity of the ML hollow-fibers.

Aim was the development of a realistic PLS ML model for performing highly resolved CFD in order to detect regions of unphysiological shear stress.

## 4.2 Materials and Methods

As found out in preliminary studies (unpublished), a realistic model with sufficient resolution would require an estimate of 1 billion nodes. Since this would result in enormous computational costs, only a section of the entire ML was modeled.

A dual model approach was chosen for the study. First, a generic model based on the manufacturer's data sheet. The hollow-fibers were implemented as straight cylinders with a diameter of $d = 380$ µm with parallel and equidistant arrangement. Every second fiber mat was arranged perpendicularly. The distance between the hollow-fibers was set to $l = 120$ µm.

However, the results in Chapter 2 prove a heterogeneous clot volume distribution which seems counter-intuitive to the concept of a symmetrical fluid domain. Furthermore, observed Wagner and Kranz et al. [31] that a fiber mat shift in flow direction is possible, resulting in an irregular hollow-fiber arrangement. To address these facts in the study,

a second step with native ML model was included in order to quantify the influence of the hollow-fiber arrangement.

It was intended to only investigate the local flow regime in the vicinity of the hollow-fibers and no side-effects induced by the distributor plate, the dividing wall, the collector plate, and the edges of the ML. For this reason, the two models only represented a central section of the ML comprising only of hollow-fibers.

### 4.2.1 Geometry

#### Generic Model

The generic model represented the 'ideal' case of the ML with a symmetrical fluid domain. Due to its symmetry, a so called basic element (Figure 4.1) was designed. It allows meshing and subsequent cloning and stacking which significantly reduced the modeling effort.

The generic model consisted of 125 (5 $\times$ 5 $\times$ 5) basic elements. In total, it had a size of 3.8 mm $\times$ 2.5 mm $\times$ 2.5 mm and represented approximately 0.007 % of the entire ML geometry. Modeling was conducted with Argon® 12 (Ashlar-Vellum, Austin, TX, USA). A special focus had to be placed on the numerical discretization problems that arise when dealing with exceedingly small numerical scales in the design of the generic model due to the CAD tolerance of $10^{-7}$. This was circumvented by scaling up the CAD model by $10^3$ and later down scaling prior to the mesh generation.

Tangential flow was prevented by implementing an overlap of $l = 10$ µm at the fiber crossing points. In addition, the crossing points were chamfered with a radius of $r = 5$ µm to avoid exceedingly small elements. Chamfering was conducted with FreeCAD 0.21 software. Fixing the model's edges with CADfix 13 (International

TechneGroup, Cambridge, United Kingdom) was required to receive a valid geometry. Then, the model was inverted to receive to fluid geometry for the study (Figure 4.1).

**Native Model**

The creation of the native model was based on a highly-resolved µCT scan and a specifically developed protocol. A non-clinically used PLS ML was subject foundation for the study. All metal parts (one screw and one spring) were removed and the ML was filled with barium chloride (concentration $c = 250$ g/l) prior to µCT scanning. Like in Chapter 2, a phoenix v|tome|xs 240/180 µCT (Baker Hughes Digital Solutions, Hürth, Germany) was used with folloging settings: voltage 180 kV, current: 190 µA, voxel size: 34.5 µm, timing 1,000 ms, average: 5, skip: 1, images 10,000, scanning time 17 h. To increase the scan quality, low energy radiation was reduced by a 0.5 mm and two 0.1 mm copper filters.

Since the contrast agent showed a distinct higher attenuation coefficient than the PMP of the hollow-fibers, a discrimination was possible. On this basis, the geometry of the contrast agent was extracted as Standard Tesselation Language (STL) model and used as the foundation for the native fluid domain. This process was carried out with VGSTUDIO Max 2022.2 software (Volume Graphics, Heidelberg, Germany). A section of approximately 2 mm $\times$ 3 mm $\times$ 3 mm was cut out of the center of the fluid domain using Meshmixer 3.5 (Autodesk, Mill Valley, CA, USA). This represented 0.006 % of the entire ML geometry.

This approach intended to use of the STL tessellation as initial surface discretization. However, this was not possible at this stage due to tessellation errors. The use of automated STL fixing proved to be insufficient, meaning that a manually conducted

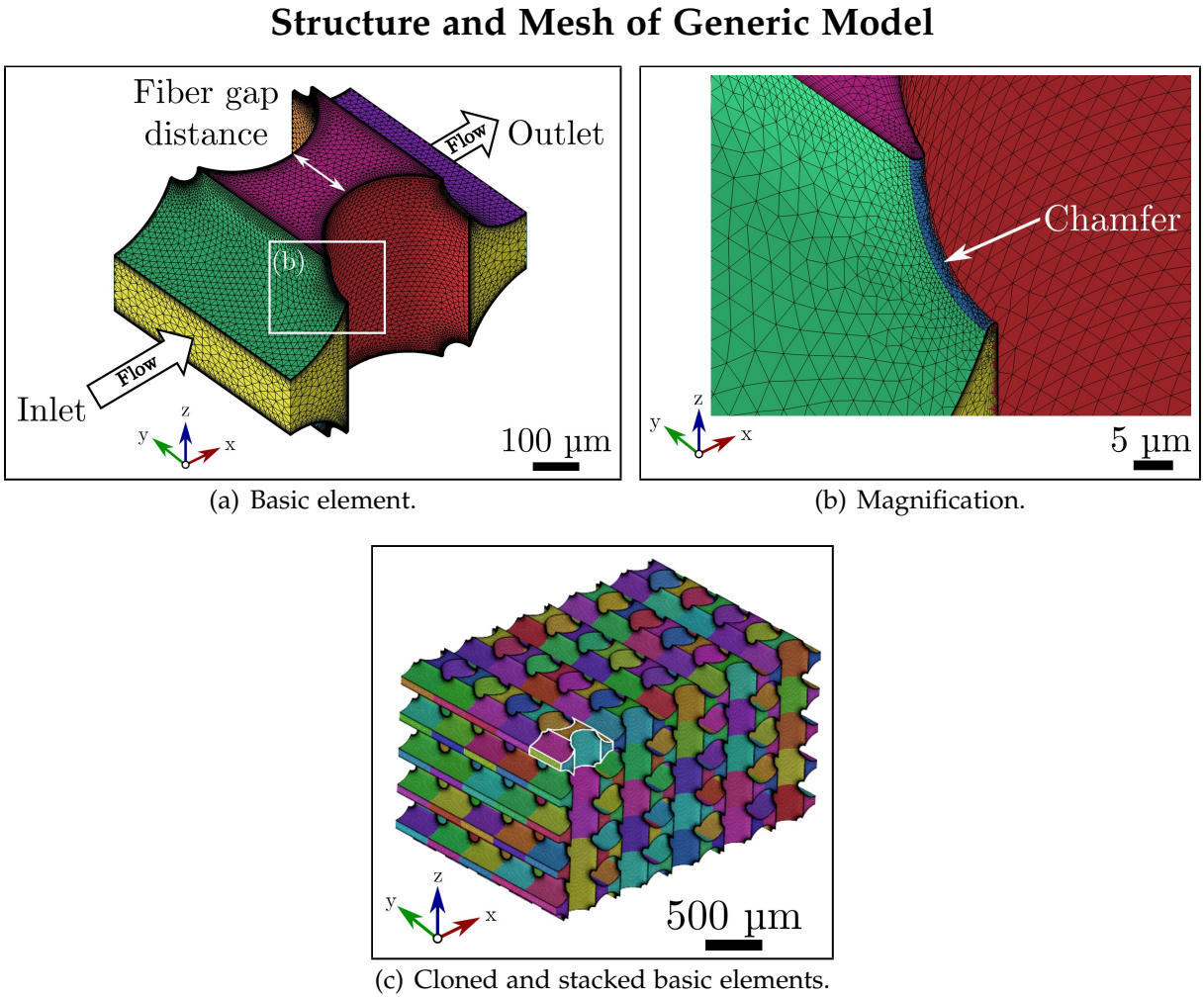


(a) Basic element.

(b) Magnification.

(c) Cloned and stacked basic elements.

**Figure 4.1: Generic ML model used for CFD calculations.** The basic element was developed as symmetrical geometry that was cloned after meshing and stacked to the generic CFD model. (**a**) Basic element with indicated flow direction (positive x-direction). (**b**) Magnification of chamber at the hollow-fiber crossing points. (**c**) Generic model consisting of cloned and stacked basic elements. One basic element highlights as an example. All subfigures are excerpts from Kranz et al. [23]

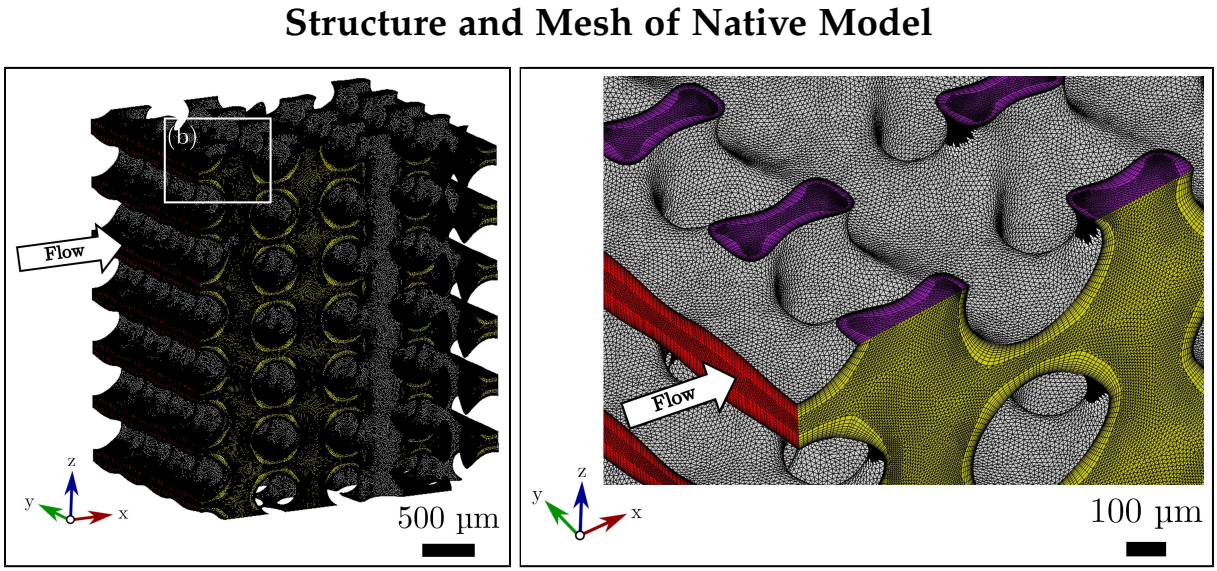


(a) Mesh of native ML model. (b) Magnification of top region.

**Figure 4.2: Geometry of and mesh native ML for CFD reconstructed from µCT scan.** (**a**) Overview of geometry. (**b**) Magnification of top region. Display of prism layers and tetrahedrals in the vicinity of the hollow-fibers. Blood flow in CFD calculation in positive x-direction. The figure is an excerpt from Kranz et al. [23].

repair was necessary. For this small exemplary section of the ML, an enormous STL fixing effort of 17 weeks for one person was required.

### 4.2.2 Mesh

#### Generic Model

The mesh was generated with CENTAUR 18 (Centaursoft, Austin, TX, USA). A pseudo-structured mesh approach was mainly used except for the vicinity of the hollow-fibers. These featured ten prism layers. The basic element consisted of approximately 145,000 nodes (194,000 tetrahedra and 201,000 prisms; 18,125,000 nodes with 125 basic elements). Mesh dependency studies with up to 2,000,000 elements were conducted prior to the study. Threshold were defined for the mesh generation in order to limit the total number of elements to approximately 800,000. The surface length scale

was defined as 0.003 mm for the chamfers and the length scale constraint was set to 0.016 mm for the remaining groups. To prevent collapsing points that were close to each other, the CAD tolerance was scaled by $10^3$ within CENTAUR 18. Subsequently, the model was scaled back to its initial µm scale by multiplication with a transformational matrix with $10^{-3}$ in its main diagonal.

**Native Model**

The mesh generation was also conducted with CENTAUR 18. Similar to the generic model, it also comprised of 17,700,000 nodes, mainly tetrahedral structures with ten prism layers in the vicinity of the hollow-fibers. Following settings were used for the surface mesh: Stretching ratio: 1.8, scaling factor: 1, maximum length scale (wall faces): 1.198 mm, minimum length scale: 0.025 mm, factor for curvature clustering: 48, factor for proximity clustering: 2, and factor for CAD clustering: 2. The settings for the prism layers were defined as: First layer thickness: 0.001 mm, stretching ratio: 1.2, ramp angle: 20°, minimum thickness of first layer: 0.002 mm.

### 4.2.3 Numerical Calculation

The numerical calculations were conducted with an in-compressible newtonian blood model with a density of $\rho = 1060$ kg/m$^3$ [82] and a dynamic viscosity of $\eta = 0.0035$ Pas [98]. The volume flow of approximately $\dot{V} = 5$ l/min is commonly used in the clinical practice. On this basis, a corresponding velocity of $u = 8$ mm/s was derived that was assigned to a velocity inlet boundary condition (BC). Fluent 2023 R2 software (Ansys, Canonsburg, PA, USA) was used running on a Linux cluster with 256 cores. A laminar solver with a steady solution was used applied for both models. After 5,000 iterations, the residuals for the generic model amounted to $< 4 \times 10^{-7}$ for continuity and $< 2 \times 10^{-11}$ for for x-, y-, and z-velocity. In contrast, after 5,000

iterations, the residuals for the native model amounted to $< 9 \times 10^{-3}$ for continuity and $< 3 \times 10^{-5}$ for for x-, y-, and z-velocity.

## 4.3 Results

The results from both models are presented in the following section. Of particular interest were the flow regime, the flow velocity, the wall shear stress (WSS), and the shear rate.

### 4.3.1 Generic Model

The calculated velocity magnitude and the WSS are depicted in Figure 4.3. Throughout the entire fluid domain a symmetrical flow field was observed, with the highest velocity magnitude in the widest domain regions. The flow remained in the same hollow-fiber gap. This means that a migration into the neighboring hollow-fiber gaps was not apparent. Flow velocities ranged between $u = 0$ mm/s at the boundaries and $u = 14$ mm/s at the center of the hollow-fiber gap (Figure 4.3 (a)). A laminar flow prevailed in the entire fluid domain with a Reynolds number of $Re < 1$.

The found WSS ranged between $\tau = 0$ Pa and $\tau = 0.6$ Pa. The WSS peaked at lateral areas of the hollow-fibers, depicted in Figure 4.3 (b). However, the crossing points did not show any relevant WSS. For a newtonian fluid, as it was used in this study, the shear rate $\dot{\gamma}$ is directly proportional to the WSS $\tau$ with the dynamic viscosity $\eta$ as the constant of proportionality, as shown in Equation (4.1).

$$\dot{\gamma} = \frac{\tau}{\eta} \tag{4.1}$$

Derived from the maximum occurring WSS, corresponds a shear rate of $\dot{\gamma} \approx 171\ 1/\text{s}$.

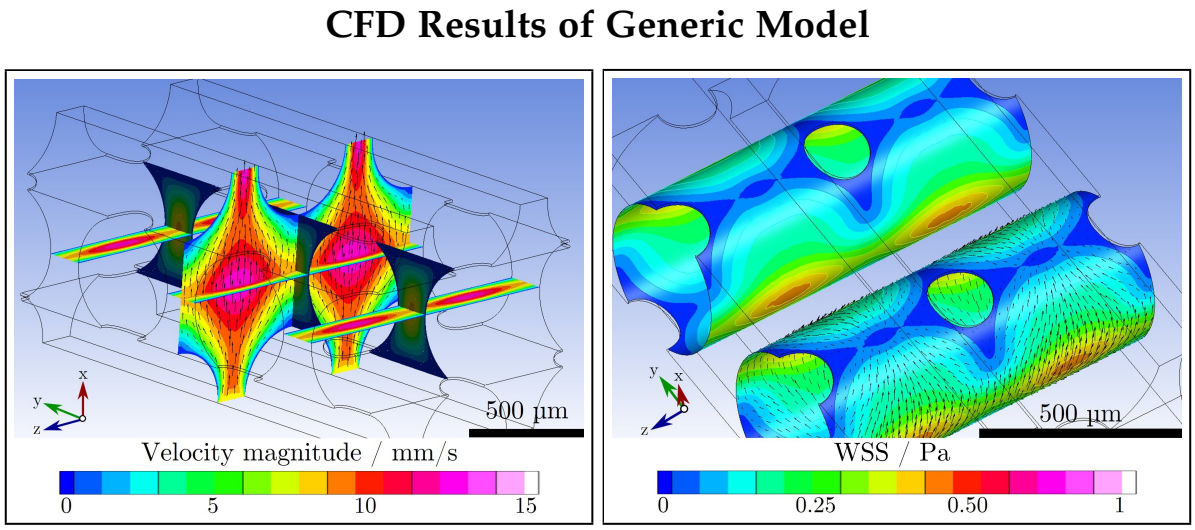


(a) Velocity magnitude (b) WSS within the generic model

**Figure 4.3: Velocity magnitude and WSS within the generic model.** The figure is an excerpt from Kranz et al. [23].

### 4.3.2 Native Model

The numerical results from the native model are illustrated in Figure 4.4. Like in the generic model, a laminar flow regime also prevailed in the native model with a Reynolds number of $Re < 1$. However, a significant difference regarding the model's topology was observed. This effect is depicted in Figures 4.2 and 4.3. An irregular hollow-fiber arrangement was observed. These were not in a perpendicular arrangement and thus showed deformation in some places. Moreover, a direct contact at the crossing point was not always present, like it was in the generic model.

Consequently, a heterogeneous velocity distribution prevailed in the native model with flow velocities in the range between $u = 0$ mm/s and $u = 22$ mm/s which is approximately 1.6 times higher compared to the peak velocity in the generic model. It became evident, that the flow velocity and thus also the WSS were location-dependent (Figures 4.3 (a, b)).

The WSS was in the range between $\tau = 0$ Pa at the hollow-fiber crossing points and $\tau = 3.8$ Pa at the lateral areas of the hollow-fibers, which was similar to the generic model (Figure 4.3 (c)). Still, the maximum WSS in the native model was about 6.3 times higher. This means that the maximum shear rate was also about 6.3 times higher in the native model with $\dot{\gamma} \approx 1080\ 1/s$.

## 4.4 Discussion

In this chapter, highly resolved numerical studies with a generic and a native ML model have been conducted. Two methods of approach were chosen: First, a generic model created with conventional CAD and predefined geometrical properties that were based on the manufacturer's data sheet and second, a native model derived from a high-resolution µCT scan following a specifically developed scanning protocol.

Challenges arose especially with the numerical discretization errors in the generic model and with the numerous tessellation errors from the µCT reconstruction. Still, it was shown that both models were valid and suitable for CFD. Despite the fact that both models only depict a small section of the entire ML domain, they were associated with a considerable modeling time and effort.

### 4.4.1 Flow Regime

The flow pattern of both model were significantly different. A symmetrical flow regime prevailed throughout the generic model while the native model stood out with its heterogeneity and irregular topology. As a result, the flow velocities differed depending on the location within the native model. The generic model was characterized by the equidistant and perpendicular hollow-fiber arrangement which resulted in a symmetrical flow field.

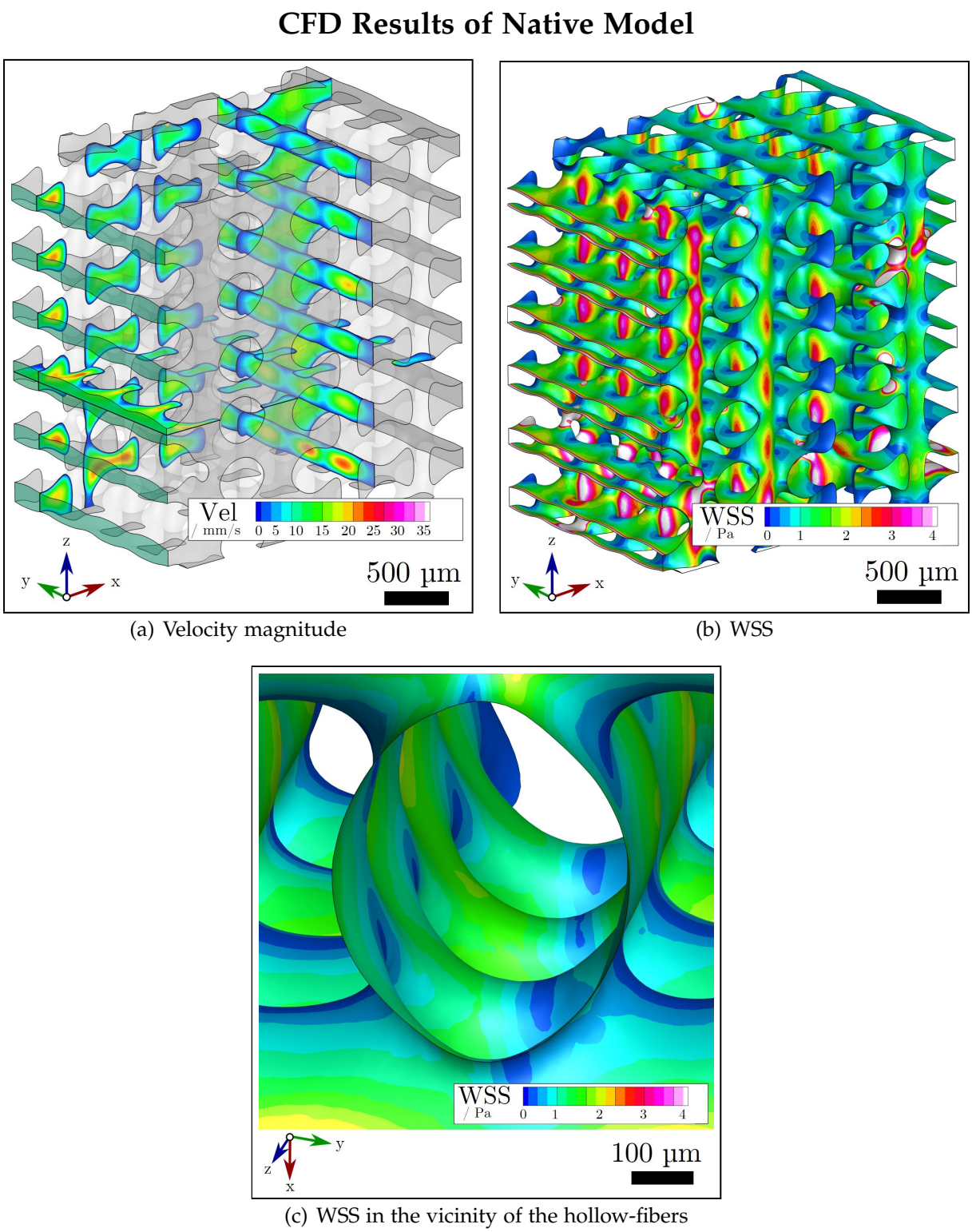


(a) Velocity magnitude

(b) WSS

(c) WSS in the vicinity of the hollow-fibers

**Figure 4.4: Velocity magnitude and WSS within the native model.** The figure is an excerpt from Kranz et al. [23].

In this study, the critical shear rate threshold of $\dot{\gamma} = 5000\ 1/s$ published by Colace et al. [96] was not reached (generic model: 171 1/s and native model: 1080 1/s). Which indicated that no pathological flow regime which could induce an elongation of the vWF is prominent in both models.

The asymmetrical hollow-fiber arrangement clearly increases the shear stress within the ML. Yet, this study indicates that solely the irregular fiber arrangement was insufficient for vWF elongation. Still, the influence of structural changes within the ML was not considered. In Chapter 2, a relation of those structures changes and the clot deposition nearby was observed. Consequently, a vWF elongation might take place in those areas.

Moreover, the future investigation of NET formation is also endorsed since Yu et al. [99] found that the formation of NETs already begins at shear rates of $\dot{\gamma} = 1000\ 1/s$. NETosis is currently discussed as a potential trigger for clot formation in ECMO and could be an alternative shear induced clotting pathway [100].

### 4.4.2 Model Practicability

This work proved the feasibility of performing CFD on a µCT reconstructed fluid domain. However, this came along with an enormous time and effort. Furthermore, the two models differed significantly with their capability of mesh optimizations. While the generic model based on CAD allowed for continuous mesh refinement and mesh dependency studies, the native model did not allow for meaningful mesh optimizations as the underlying geometry was defined by the resolution of the µCT scanner.

The use of smoothing filters can still optimize the mesh. In this study, the scanner's maximum resolution (voxel size 34.5 µm) was utilized. Comparatively, the mesh of the native model is coarser than that of the generic model, but it strikes the best balance

between accuracy and computational effort. Despite the availability of a native model, the future use of enhanced generic models appears more promising. This is because the ML manufacturing process results in tiny differences in fiber arrangement for each ML. Therefore, retrieving a native fluid domain only represents one specific ML geometry, making general statements difficult. Additionally, modeling a clot burden inside the ML is a major challenge. While generic models allow for the later integration of three-dimensional clot structures, µCT scanning can only be performed with MLs that are either not intended for clinical use (no clot structures) or collected after clinical use (with clot structures). Since each ML has a slightly different fiber arrangement, comparing these two geometries provides limited information.

### 4.4.3 Limitations

The study focuses on a section of the entire ML. Assuming the fluid domain is symmetrical, this approach would be efficient. However, the native model revealed an asymmetrical hollow-fiber arrangement. Only a small portion of the domain was considered. Extrapolating these small models to the entire ML may not yield reliable data. A section-wise procedure could be a viable solution, accounting for the complexity of individual regions while reducing calculation effort. Considering the raw tessellation from the µCT scan, this approach allows for realistic modeling, but the STL tessellation used has limitations, particularly in approximating curvature. In this study, blood is assumed to be a newtonian single-phase fluid. Further adapting fluid modeling with more blood attributes would provide detailed information regarding rheological behavior and cell-fluid interaction.

## 4.5 Conclusion

In conclusion, the CFD calculation did not indicate any critical WSS in either model. However, it was observed that the hollow-fibers in native MLs were arranged asymmetrically. The flow velocity was 1.6 times higher and the WSS was 6.3 times higher in the native model. This suggests that the asymmetrical fiber arrangement significantly impacts the local flow regime. Future studies should incorporate the geometry variations observed in the native model into the generic model to account for hollow-fiber irregularities and assess their influence on the flow field. Additionally, the integration of a multi-phase fluid model, such as an Euler-Euler approach with adjustable viscosity, is proposed to adequately depict the FLE effect and the formation of plasma-skimming layers.

# 5. Flow Dynamics in ECMO Pumps

The centrifugal pump is the second key component of ECMO. It consists of a sterile, single-use pump head which is in direct contact with the patient's blood and a reusable pump drive unit. Via magnetic coupling, torque is induced from the pump drive unit to the rotor within the pump head, transporting the blood.

However, the deposition of blood clots within the pump head is a common technical problem during its operation [4]. This is expected to be a consequence of the high rotational speeds of the rotor that are required for establishing a sufficient pump flow.

Aim of this work was to provide experimental data to substantiate the existing numerical results. An experimental setup was developed and tested that allowed for non-invasive optical flow measurements within a Rotaflow ECMO pump. The development process, the setup, as well as flow measurement results are described in the following.

## 5.1 Introduction

Various numerical studies conducted flow investigations within ECMO pumps [75–79], searching for triggers of hemolysis and vWF elongation or compare the pumping performance of different pump models. They observed a turbulent flow regime with

areas of high ($> 10,000$ 1/s) and low shear rates ($< 100$ 1/s) with extended exposure time [77]. With this data, it seems reasonable that the pump is a main cause for clot formation. However, all results are based on numerical data which are heavily depending on the used settings and parameters.

The experimental setup for a laser-doppler-anemometry (LDA) had to meet numerous requirements. Especially when investigating an interior flow regime, the LDA lasers had to be introduced into the pump head without light refraction.

LDA uses two intersecting laser beams directed at a working fluid that is mixed with reflective particles. A velocity vector is determined at the laser beam intersecting point. The back scattered interference pattern from the moving particles is captured by the LDA and the velocity is calculated using the Doppler effect. Modern LDA systems comprise of at least two separate laser systems with different wave lengths to capture two (or three) orthogonal velocity vectors.

## 5.2 Materials and Methods

For measurement of the flow dynamics within a Rotaflow ECMO pump, a test rig for non-invasive optical flow investigations was developed. The original pump head consisted of PC components that were glued together. However, due to the relatively high refractive index of PC with $n \approx 1.585$ [101], the repertoire of existing techniques of non-invasive optical flow measurements was significantly limited. Consequently, the use of the original pump head was discarded and a realistic silicone replica was developed. The development of the replica pump model, the measurement setup using LDA as well as the conduction of the measurements is described below.

### 5.2.1 Fluid Geometry Reconstruction

It was essential to develop a realistic fluid geometry for the measurements. The fluid geometry defines the blood filled volume of the ECMO pump in the clinical use.

#### Capturing of Native Pump Geometry

In order to capture it, a high resolution µCT scan was conducted with a phoenix v|tome|xs 240/180 µCT (Baker Hughes Digital Solutions, Hürth, Germany). Barium chloride (concentration $c = 250$ g/l) was filled into the pump head prior to the scan as a contrast agent. Following settings were used: Voltage: 220 kV, current: 430 µA, voxel size: 95 µm, timing 1,000 ms, fast scan, images 2,000, scanning time 33 min, with two 0.5 mm tin filters.

Segmentation of the fluid geometry was then conducted with VGSTUDIO Max 2022.2 software (Volume Graphics, Heidelberg, Germany). However, the neodymium magnets within the pump rotor caused scanning artifacts resulting in invalid sections of the STL geometry. Subsequently, a valid geometry was generated from the contours of the valid sections of the STL model using CAD (NX, Siemens Digital Industries Software, Plano, TX, USA). The model was sliced horizontally into two parts which was required to insert the rotor afterwards.

#### 3D Printing of Soluble Geometry

The valid geometry was then 3D-printed using a water soluble material as previously published by Tauwald et al. [102] (zp 131 calcium sulfate powder and zb 60 binder, Z Corporation, Burlington, SC, USA; printed by ZPrinter 660Pro, 3D Systems, SC, USA; 3D-printing carried out by 3d-Printwerk, Fürth, Germany). Water solubility was important for the demolding process, as the 3D-printed parts had several undercuts.

However, calcium sulfate proved to have a rough surface and visible layers due to the printing process. In addition, the silicone used later could penetrate the parts, preventing the silicone from curing and causing air bubbles to rise from the parts into the silicone. All these problems have to be overcome for the measurements. As a solution, a water soluble polyvinylalcohol (PVA) coating was applied.

**Surface Coating**

PVA coating (PVA solution in methanol/water ($PVA$) $=$ 0.04 g/ml) was brushed onto the parts to reduce the surface roughness and create a tight layer surrounding the 3D-printed parts. Prior to the coating, remaining dust from the printing process was removed using pressurized air.

PVA coating was carried out according to the following developed protocol. A layer of coating was applied to the surface with a soft brush (e.g. da Vinci series 304 size 16, da Vinci Künstlerpinselfabrik, Nuremberg, Germany). It was conducted inside a laboratory fume hood to instantly remove all methanol vapors. The parts remained inside the fume hood after coating for 15 min to allow the remaining methanol to vaporize. Then, the parts were placed inside a drying oven (UF 160 plus, Memmert, Schwabach, Germany, 80 °C, 30 min). Eventually, the parts were removed from the oven and place again inside a fume hood to cool down to RT. After another 15 min the next layer was applied. 20 layers ensured sufficient impermeability and a satisfactory surface quality.

**Casting Mold**

Two identical casting molds were manufactured from 10 mm tick aluminum sheets, shown in Figure 5.1. To enhance the surface quality of the polydimethylsiloxane (PDMS) parts, the interior of the casting molds was ground and polished (Planopol-2,

Struers, Detriot, OH, USA) according to following protocol: First, a grinding step with CarbiMet 2 grinding paper and #320 [P400] SiC abrasive in water (Buehler, ITW Test & Measurement, Leinfelden-Echterdingen, Germany, 300 1/min, until even) was performed. Next, two two polishing steps finalized the surface. The first polishing step used UltraPad polishing cloth and 9 µm MetaDi Supreme diamond suspension (also from Buehler, 150 1/min for 5 min). The final polishing step was performed with TriDent polishing cloth and 3 µm MetaDi Supreme diamond suspension (also from Buehler, 150 1/min for 4 min).

Since copper in the aluminum panels could inhibit the curing process, elemental analyses were conducted using a spectrometer (xSORT RFA-Handspektrometer, Spectro Analytical, Kleve, Germany). However, the copper content was found uncritical for the curing process (0.061 % $\pm$ 0.01 %).

**Inlay**

The bottom PDMS part was designed with a recess for the magnetic pump drive. Instead of later cutting out the recess, an inlay was inserted to displace the PDMS in the bottom part, depicted in Figure 5.1 (b). This inlay was manufactured using stereolithography (SLA) and a rigid resin (Grey V4, Formlabs, Berlin, Germany). Since, an even surface for later bonding was essential, the bottom part was cast upside down. The inlay was designed to ensure centered alignment within the casting mold and coaxial with the bottom calcium sulfate part. It featured 12 vertical channels that allowed air to rise from the interspace between the inlay and the bottom flow geometry. The inlay was slightly conical, facilitating later removal after curing.

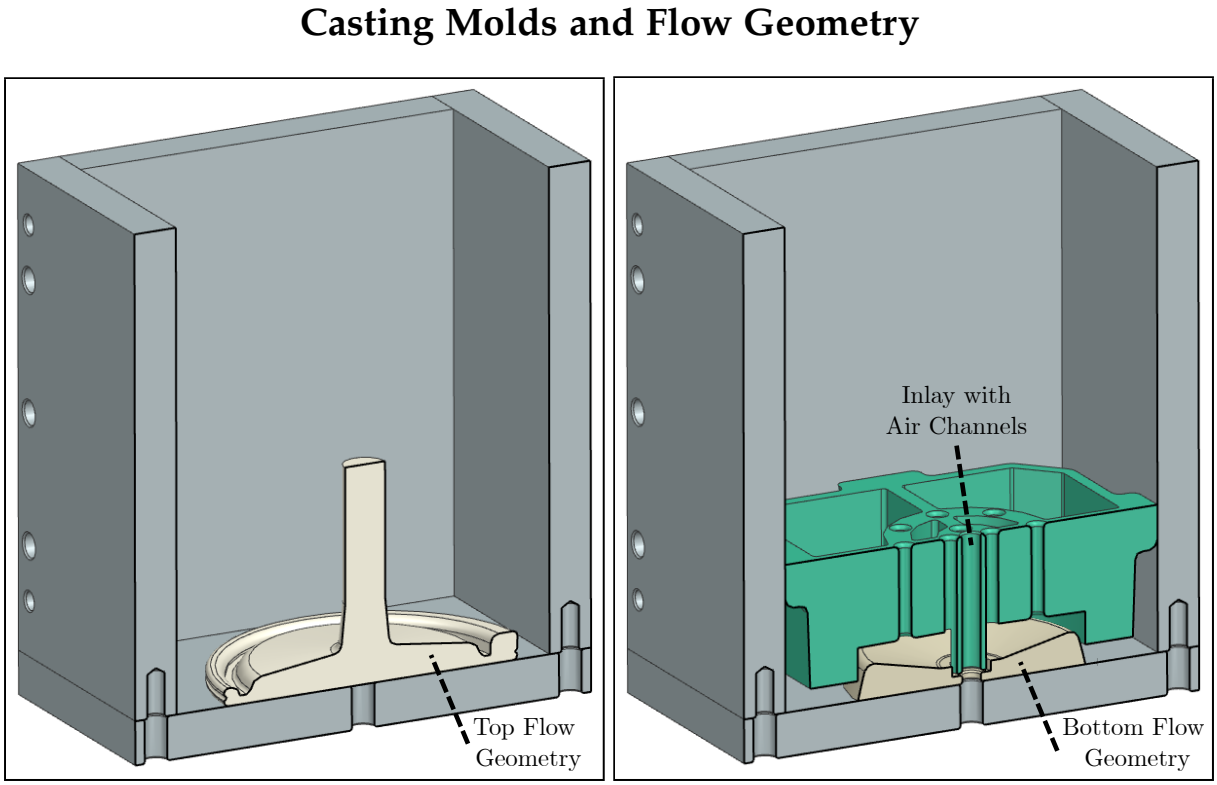


(a) Casting of top flow geometry. (b) Casting of bottom flow geometry.

**Figure 5.1: Aluminum casting Molds with soluble calcium sulfate flow geometries.** (**a**) Top flow geometry of the rotor housing. (**b**) Bottom flow geometry of rotor housing with space for the bearing. An non-soluble inlay with air channels keeps space for the pump drive.

### Silicone Preparation

The casting process started with the preparation of PDMS silicone (Sylgard 184, Dow Chemical, MI, USA).

This material was first degassed in a vacuum chamber for 24 h at 4 °C and 50 mbar to eliminate air bubbles. Performing this step in a cold environment helped extend the pot life once the curing agent was added.

Next, the curing agent was mixed with the PDMS base in a 1:10 mass ratio, as recommended by the manufacturer. The mixture was then extensively stirred using an stirring device (Eurostar 60 control, IKA Werke, Staufen, Germany) with an turbine

stirrer for highly viscous fluids (Visco Jet ® 60 mm, Heidolph Scientific Products, Schwabach, Germany), in two 3 min intervals at 300 1/min rotational speed to ensure uniformity. After the first interval, the mixture was filled into another container. PDMS adherent to the first container's walls was scraped off and added into the second container. This procedure should ensure that the hardener, which may be located on the container wall, has also been mixed. To preserve the mixture's properties and prolong its usability, it was stored again at 4 °C and subjected to a second degassing cycle in a vacuum chamber at 50 mbar for 2 h.

**Mold Preparation**

Before casting, it was essential to ensure that the molds were clean and free of dust or debris. All aluminum sheets of the two mold were cleaned using ethanol and paper towels. Then, three of the four side panels of the casting molds were attached to the bottom plate.

For the top part, a stainless steel bolt (DIN 13 M5 $\times$ 16 mm) was inserted from the bottom through the center drilling of the mold's bottom plate and temporarily held in place. Glue (Pattex Sekundenkleber, Henkel, Düsseldorf, Germany) was applied to the perimeter of the bottom side of the top calcium sulfate part. The calcium sulfate part was slid over the bolt and moderately pressed to the bottom plate. Excess glue was removed instantly. After the glue had fully hardened, the bolt was taken out and the fourth panel of the casting mold was attached.

The bottom part was also glued to the mold's bottom plate. After the removal of the excess glue the inlay was placed on top the calcium sulfate bottom part which automatically centered it. A second stainless steel bolt (DIN 13 M3 $\times$ 70 mm) was inserted through the mold's bottom plate, the calcium sulfate part, and the inlay. It

was fixated with stainless steel nuts (DIN 934 M3 hexagonal nuts) to prevent buoyancy effects of the inlay.

Eventually, aluminum adhesive tape was glued over all seams of the individual plates and screws to ensure the tightness of the molds.

**Silicone Casting**

Prior to casting, a drying oven (UF 160 plus, Memmert GmbH + Co. KG, Schwabach, Germany) was preheated to 50 °C. The prepared PDMS was then carefully poured into the molds, which were slightly tilted to allow a smooth, controlled flow and reduce bubble formation. Any visible bubbles were removed using a single-use 1 ml pipette.

Once filled, the molds were placed under vacuum, where a moderate negative pressure (400 mbar) was applied to eliminate any remaining air bubbles without damaging the intricate 3D geometries. Finally, four disposable cuvettes were filled with the leftover material for later refractive index measurements.

**Silicone Curing**

After the casting process, the filled molds were placed in a drying oven, where the PDMS was cured at 50 °C for approximately 750 min. To ensure complete curing, the process was extended to 14 h. At the beginning of the curing process, the mixture was monitored for a few minutes to check for any rising air bubbles. If air bubbles appeared, they could be carefully removed within the first 30 min. Beyond that point, any further intervention could have damaged the structure due to the increased viscosity of the mixture. Once the curing process was complete, the molds were removed from the oven and allowed to cool to RT.

**Demolding**

Next, the aluminum tape strips were removed, and the screws were gently loosened. To separate the side sections of the mold, one edge was carefully lifted while a small amount of isopropanol was applied into the gap. This facilitated releasing the PDMS from the metal components. This step ensured that the cured PDMS was detached cleanly and precisely from the mold without causing any damage.

To remove the upper section of the geometry, the PDMS was carefully lifted, and isopropanol was applied to help detach it from the 3D-printed structure. Due to the water-soluble nature of the printed material, it could be dissolved using either water or ethanol. The PDMS located beneath the SLA-printed component and above the inlay was then cut away using a scalpel. A long tool was inserted through the opening in the SLA-printed part to push it downward and release it. After demolding, the cast components were placed back into the oven at 70 °C for 4 h (fan set to 30 % and the flap closed) to ensure complete curing and structural stability.

**Pump Rotor**

The native rotor of a non-clinically used Rotaflow RF32 centrifugal pump head as well as its bearing were used in the pump replica. To do so, the pump housing was cut open with a hand saw and the rotor was extracted. Then, the bearing and its surrounding plastic (radius approximately 5 mm around the center of the bearing) were cut out.

Eventually, the bearing was placed in the center of the bottom PDMS part. The required clearance was previously created by the SLA inlay.

**Bonding**

After post-curing, the two halves needed to be bonded. Before doing so, the rotor was placed into the imprint. To achieve this, a bearing was positioned at the opening of the lower part. The impeller's bearing was then set onto this and aligned within the geometry. For proper alignment of the two halves, the lower part was placed on the casting mold and the side panels were mounted. The surface of the PDMS was then carefully coated with curing agent, taking care not to coat the pump imprint to avoid distorting the geometry.

Next, the upper part was positioned on top, and a weight ($\approx$ 300 g) was applied to exert pressure and ensure a bubble-free bond. The bonded assembly was then placed in an oven at 50 °C for 20 h to complete the curing process. After this period, the bonded assembly was removed from the casting mold and cleaned with ethanol.

### 5.2.2 Pump Drive

A pump drive unit for the test rig was developed, depicted in Figure 5.2. The central component was a 12 V DC electric motor (Torpedo 850, MFA/Comodrills, Worth, UK) which was coupled to a aluminum disk with neodymium magnets. Those magnets later introduced the torque to the pump rotor. Two angular contact ball bearings were used that allowed high rotational speed ($>$ 5,000 1/min) with only little vibration. The pump drive was operated was a laboratory power supply (PS 2000 B, Elektro-Automatik, Viersen, Germany) and a speed controller (Drehzahlsteller 10A, H-Tronic, Hirschau, Germany). The PDMS assembly was then placed on top of the pump drive unit with a mounting that enabled proper alignment of the rotation axes.

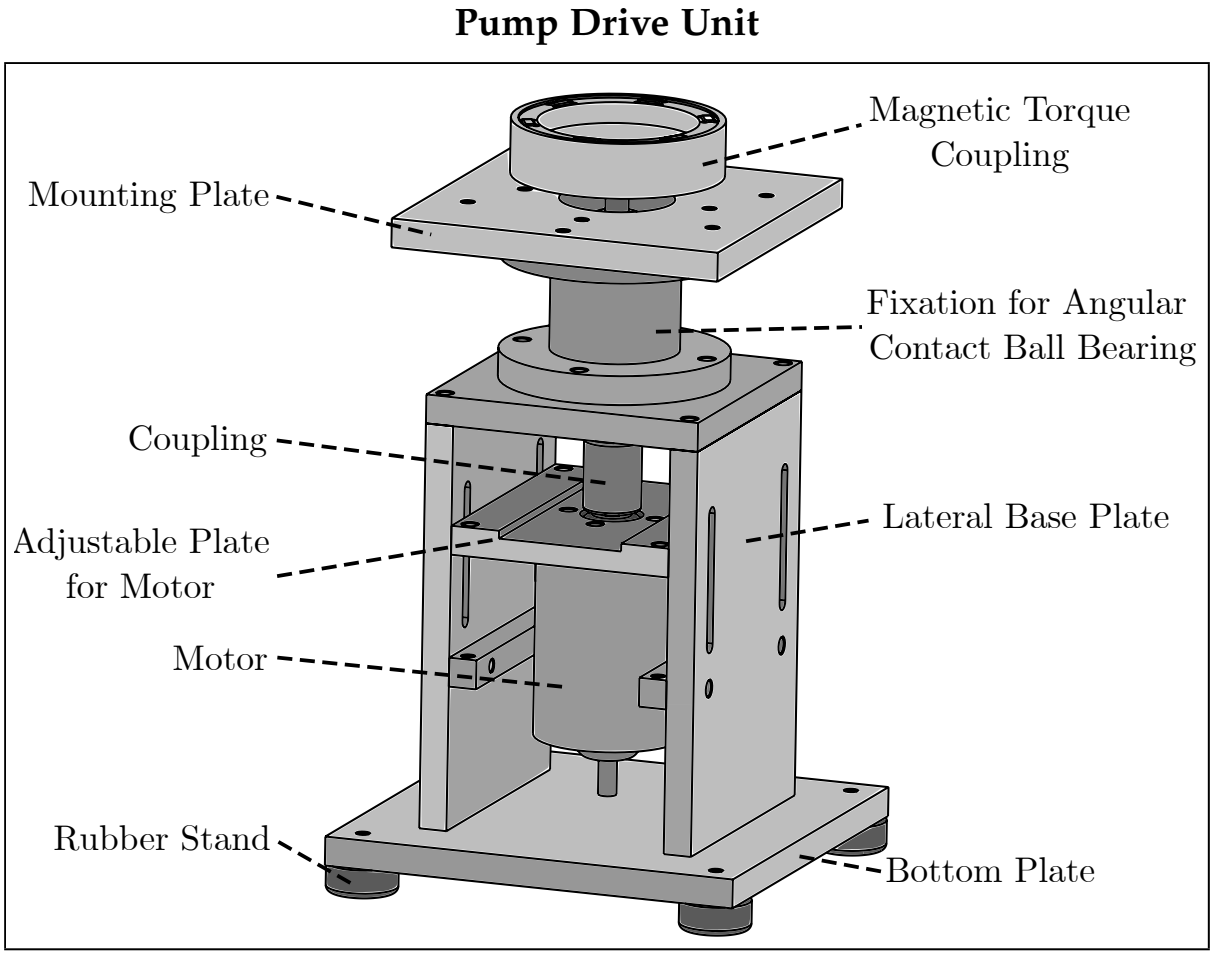


**Figure 5.2: Structure of pump drive unit for non-invasive optical flow measurements.**

### 5.2.3 Measurement Setup

The measurement setup consisted of a two-component LDA system positioned by a traversing unit and the pump replica driven by the pump drive unit submersed in the refractive index matched (RIM) working fluid. The detailed setup is described below and illustrated in Figure 5.3.

#### LDA System

Flow measurements were carried out using the Flow Explorer system (Dantec Dynamics A/S, Skovlunde, Denmark). Prior to data collection, several calibration steps

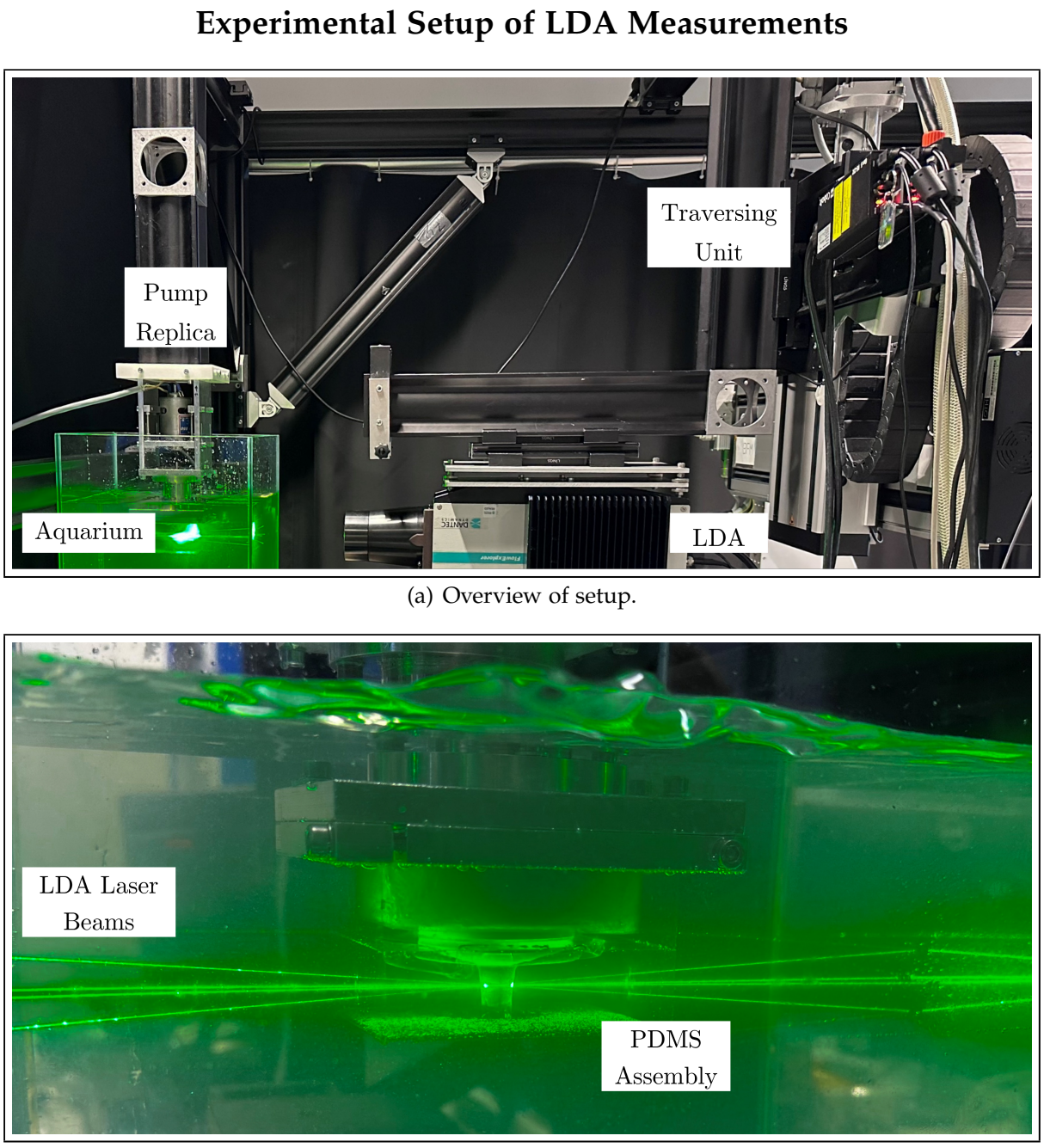


(a) Overview of setup.

(b) Magnification of PDMS assembly.

**Figure 5.3: Setup for non-invasive optical flow measurements in an ECMO pump.** (**a**) Overview of entire experimental setup. It comprised of the pump replica partly immersed in a RIM working fluid inside an aquarium. The LDA system was mounted to a traversing unit allowing precise positioning and automatic capturing of multiple measurement points. (**b**) Magnification of the assembly consisting of two PDMS parts, the original pump rotor as well as its bearing. It was driven by the magnetic pump drive above. The $TiO_2$ particles in the working fluid shown reflections which made the laser beams visible. Velocity data is acquired at the intersecting point of the laser beams.

were undertaken to ensure measurement accuracy. Initially, the fluid's refractive index was adjusted, and titanium oxide particles were introduced as seeding material. The traverse system was calibrated by programming a specific travel distance and verifying it manually, resulting in an optimal setting of 160 pulses/mm for traverse control.

Once calibration was complete, the traverse was moved to its predefined home position. To ensure precise measurements, the laser head was horizontally aligned using an inclinometer to achieve a 0° orientation. Vertical alignment relative to the aquarium was performed manually. After alignment, the laser was activated, and its beam position was visually confirmed. A point at the center of the pump outlet was selected as the reference for scanning and designated as the "parking position" to allow consistent repositioning throughout the experiment.

From this reference point, "Run online acquisitions" were conducted to assess measurement quality. The system displayed the results as a histogram, which confirmed satisfactory performance. The laser was then moved systematically in all directions to observe measurement behavior, helping to distinguish between solid boundaries and fluid regions. This process defined the measurement space, which was used to generate a mesh template via the "Mesh Generator" function.

In total, 210 measurement points were recorded with a sampling rate of 8 kHz. Acquisition parameters included a 15 s acquisition time and a sample size of 50,000. During the measurements, the pump operated at a constant speed of 1400 1/min. After data collection, the results were exported, including both the full data set with time stamps for each point and a summary file containing average velocities and root-mean-square (RMS) values for each coordinate.

### Traversing Unit

The LDA system was positioned using a computer controlled three-axes traversing system (Isel, Eichenzell, Germany). A software interface allowed direct communication between the LDA control software and the traversing unit via G code.

### Measurement Fluid and Refractive Index Matching

Despite the specification of the refractive index in the manufacturer's data sheet, Tauwald et al. [102] found that it deviated slightly from the specified value due to the processing procedure. This was also established during the development of this test stand. An adjustment of the refractive index was therefore absolutely necessary. Two steps were employed to match the refractive index of the PDMS with that of the working fluid.

First, four solid PDMS samples were analyzed using an refractometer (Abbe Refraktometer, Kern und Sohn, Balingen-Frommern, Germany) at RT. To enhance measurement accuracy, bromonaphthalene, chosen for its high refractive index of 1.657, was used as an intermediate medium. The measured refractive indices of the PDMS samples ranged between 1.4140 and 1.4160. To match this range, a water-glycerol mixture was selected as the working fluid due to its blood-like viscosity. Glycerol has a refractive index of approximately 1.4740, while water's is around 1.3381. By adjusting the ratio of these two components, the refractive index of the mixture can be tuned to align with that of the PDMS. This adjustment was verified using a digital refractometer (Refraktometer ORM RS1, Kern und Sohn, Balingen-Frommern, Germany) at RT.

Second, once the mixture's refractive index was close to that of the PDMS, a fine-tuning process was carried out. The RIM fluid was poured into an aquarium (300 mm $\times$ 300 mm $\times$ 300 mm) , and a cross-line laser was directed through the RIM fluid

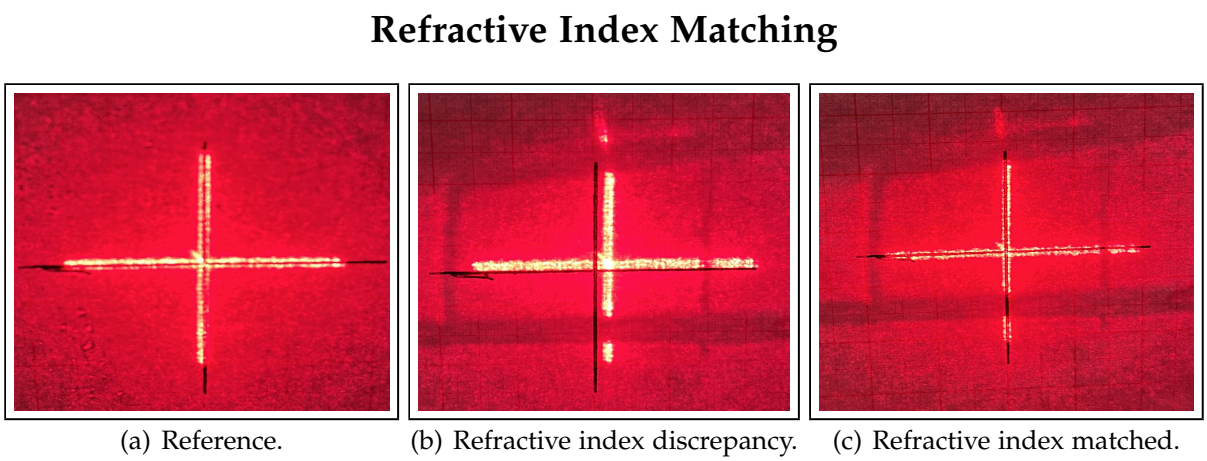


(a) Reference. (b) Refractive index discrepancy. (c) Refractive index matched.

**Figure 5.4: Inline refractive index matching using a cross-line laser.** (**a**) Reference measurement with laser crossing the aquarium without the silicone pump model. Position of the laser cross marked on a graph paper. (**b**) Silicone model placed in the aquarium with the cross-line laser passing through. Discrepancies due to an unmatched refractive index result in a horizontal and vertical shift of the laser cross. (**c**) The refractive index of the fluid matches the one of the silicone model, resulting in an alignment of the marker and the laser cross.

towards the back of the tank, where millimeter paper was attached. A reference line was marked at the laser's intersection point, illustrated in Figure 5.4

Next, the pump replica was positioned in the tank so that the rotor was immersed. The laser was then aligned to pass through the PDMS pump replica. Any deviation between the laser's reflection and the reference line meant a discrepancy of the refractive indices.

To minimize this discrepancy, small amounts of glycerol or water were incrementally added to the mixture. A stirrer (Visco Jet ® 60 mm) continuously mixed the solution to prevent the denser glycerol from settling at the bottom of the tank.

### Laser Beam Correction

LDA uses oblique laser beams for flow measurements. However, in this certain experimental setup internal flow regimes are captured which results in the laser beams permeating different media with individual optical properties. This is relevant for the determination of the measurement point of the LDA. By applying the Snell's Law

(Equation (5.1)) with $n$ being the individual refractive indices and $\Theta$ being the angle of the permeating laser beam, a displacement correction factor was calculated.

**Angle of Laser Beam in RIM Fluid**

$$n_{air} \times \sin(\theta_{air}) = n_{fluid} \times \sin(\theta_{fluid}) \tag{5.1}$$

For this experimental setup, the half-angle between the oblique laser beams is calculated with Equation (5.2):

$$\theta_{air} = \arctan(\frac{d/2}{L}) \approx \boxed{5.71°} \tag{5.2}$$

with $d = 60$ mm as the beam separation and $L = 300$ mm as the focal length in air.

With Equations (5.1) and (5.2), the corresponding half-angle in the RIM fluid was calculated in Equation (5.3).

$$\begin{aligned} \sin(\theta_{fluid}) &= \frac{n_{air}}{n_{fluid}} \times \sin(\theta_{air}) \\ &= \frac{1.000}{1.415} \times \sin(5.71) \\ \theta_{fluid} &\approx \boxed{4.03°} \end{aligned} \tag{5.3}$$

**Displacement Ratio Along Optical Axis**

During the measurements, the LDA system can be move towards or away from the ECMO pump replica along the optical axis ($\Delta Y_{air}$). The corresponding measurement point in the RIM fluid ($\Delta Y_{fluid}$) was determined with Equation (5.4):

$$\begin{aligned} \frac{\Delta Y_{fluid}}{\Delta Y_{air}} &= \frac{\tan(\theta_{air})}{\tan(\theta_{fluid})} \\ &= \frac{\tan(5.71)}{\tan(4.03)} \\ &\approx \frac{0.1001}{0.0704} \approx \boxed{1.422} \end{aligned} \tag{5.4}$$

This means that a shift of 1 mm of the LDA system results in a displacement of the measurement point of 1.422 mm within the RIM fluid.

### 5.2.4 Reynolds Scaling

It is vital to ensure similar flow characteristics in the experiment compared to the clinical use of the ECMO pump. For this reason, Reynolds similarity was applied.

Following fluid mechanical parameters were used for Reynolds scaling: For the RIM fluid: Density of $\rho_{fluid} = 1150\,\mathrm{kg/m^3}$ [102] and a viscosity of $\eta_{fluid} = 0.00944$ Pas and for blood: Density of $\rho_{blood} = 1050\,\mathrm{kg/m^3}$ [103] and a viscosity of $\eta_{blood} = 0.0045$ Pas [37].

The dynamic viscosity of the fluid was derived from the RIM process and the specific ratio of the two fluid components (water and gylcerol) .

In order to achieve realistic flow characteristics, the model and the ECMO pump in the clinical setting must have matching Reynolds numbers, according to Equation (5.5).

$$Re_{fluid} \stackrel{!}{=} Re_{pump} \tag{5.5}$$

Since the Reynolds number is defined as ratio between the inertia forces and the viscous forces inside a fluid, Equation (5.5) can be rewritten as shown in Equation (5.6):

$$\frac{\rho_{fluid} \times v_{fluid} \times d}{\eta_{fluid}} \stackrel{!}{=} \frac{\rho_{blood} \times v_{blood} \times d}{\eta_{blood}} \tag{5.6}$$

With $d$ as the characteristic diameter. However, since the geometry of the pump replica was the same size as the original pump, no geometrical scaling was necessary which allows for a simplification of Equation (5.6) according to Equation (5.7).

$$\begin{aligned} v_{fluid} &= v_{blood} \times \frac{\rho_{blood}}{\rho_{fluid}} \times \frac{\eta_{fluid}}{\eta_{blood}} \\ &= v_{blood} \times 0.913 \times 2.098 \\ &= \boxed{v_{blood} \times 1.916} \end{aligned} \tag{5.7}$$

To ensure comparable flow conditions between the working fluid and blood, the velocity of the working fluid ($v_{fluid}$) must be 1.916 times higher than that of blood ($v_{blood}$) in order to achieve the same Reynolds number. This adjustment allows the flow characteristics observed in the pump using the working fluid to be reliably translated to those expected with blood, thereby ensuring the validity of the LDA measurements.

### 5.2.5 Calculation of the Turbulence Intensity

The turbulence intensity (TI) is a commonly used parameter to characterize the level of turbulence in a flowing fluid. It is defined as the ratio of the RMS ($u'$, $v'$, Equations (5.8),

(5.9)) of the velocity fluctuations to the mean velocity ($\bar{u}$), provided as a percentage (Equations (5.10), (5.11)) [104, 105].

$$u' = \sqrt{\frac{1}{n} \times (u_1^2 + u_2^2 + \cdots + u_n^2)} \tag{5.8}$$

$$v' = \sqrt{\frac{1}{n} \times (v_1^2 + v_2^2 + \cdots + v_n^2)} \tag{5.9}$$

$$TI_u = \frac{u'}{\bar{u}} \tag{5.10}$$

$$TI_v = \frac{v'}{\bar{v}} \tag{5.11}$$

Since this LDA system is capable of measuring two orthogonal velocity vectors, the magnitude of both velocities can be determined using the Pythagorean sum. This is shown in Equation (5.12).

$$TI = \sqrt{TI_u^2 + TI_v^2} \tag{5.12}$$

### 5.2.6 Pumping Performance

A maximum flow rate of $\dot{V} = 5.5$ l/min was measured in preliminary tests, which meets the requirements for the intended experiments. This result is consistent with clinically relevant conditions, where typical treatment flow rates range from 0.5 l/min to 5.0 l/min [106].

### 5.2.7 Data Processing

Data processing was conducted with the BSA-F80 Flow Processor and the BSA Flow Software (both Dantec Dynamics A/S, Skovlunde, Denmark). The visualization of the results for the absolute velocity and the TI was performed with MATLAB (R2024b, MathWorks, Natick, MA, USA).

## 5.3 Results

The results on the reconstruction process, the pump's performance as well as the fluid mechanical results are presented below.

### 5.3.1 Velocity and Turbulence Intensity

The feasibility of the experimental setup was proved with a velocity and TI measurements at an exemplary position marked with a coordinate system in Figure 5.5. The absolute velocity distribution in the exemplary area across numerous measurements points is depicted in Figure 5.6. The measured absolute velocity in this area ranged between 2.7-4.7 m/s with special focus on the areas farther away from the rotor.

The TI within the marked area is illustrated in Figure 5.7. It ranged between 12-30 % and was particularly high (30 %) in the middle of the channel near the rotor. In vicinity of the outlet port, the TI was clearly lower with 12-16 %.

The power spectrum diagram in Figure 5.8 illustrates the energy distribution across frequencies for a measurement point, calculated using Fast Fourier Transformation. Three distinct regions characterize the spectrum: The energy-containing range at low frequencies dominated by large-scale structures, the inertial subrange at medium frequencies, and the dissipation range at high frequencies. Peaks in the spectrum indicate

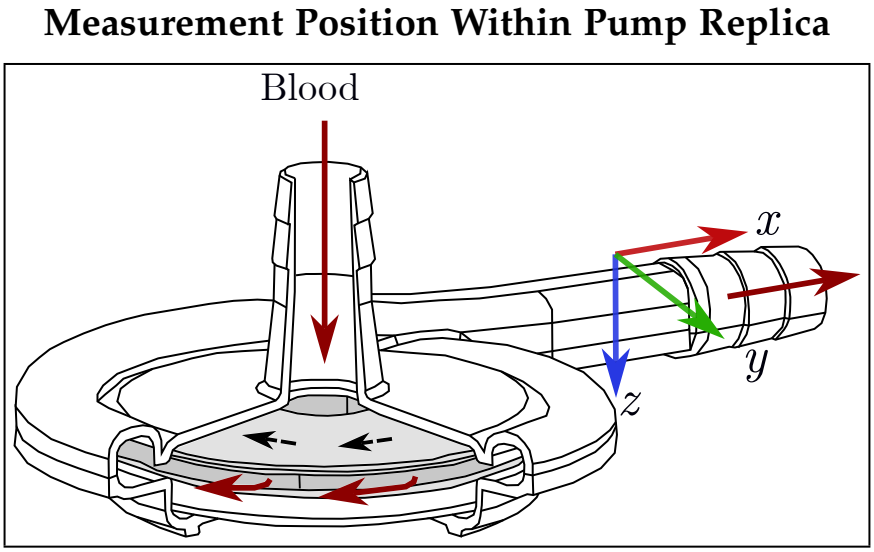


**Figure 5.5: Position of LDA measurement within pump replica close to the outlet port.** Pump flow in $x$-direction.

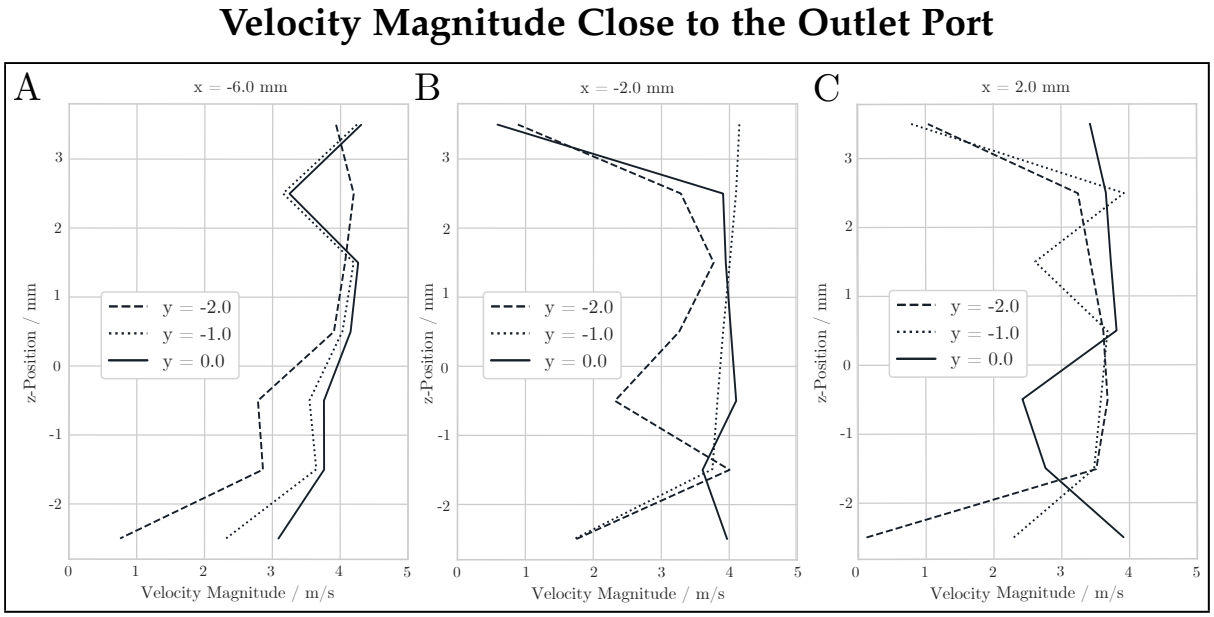


**Figure 5.6: Absolute velocity in the pump channel close to the outlet port.** Illustrated at (**A**) x-position -6 mm, (**B**) x-position -2 mm, and (**C**) x-position 2 mm.

dominant periodic structures in the flow. Comparing spectra across measurement locations reveals spatial turbulence development patterns, providing critical insights into flow behavior and mixing characteristics.

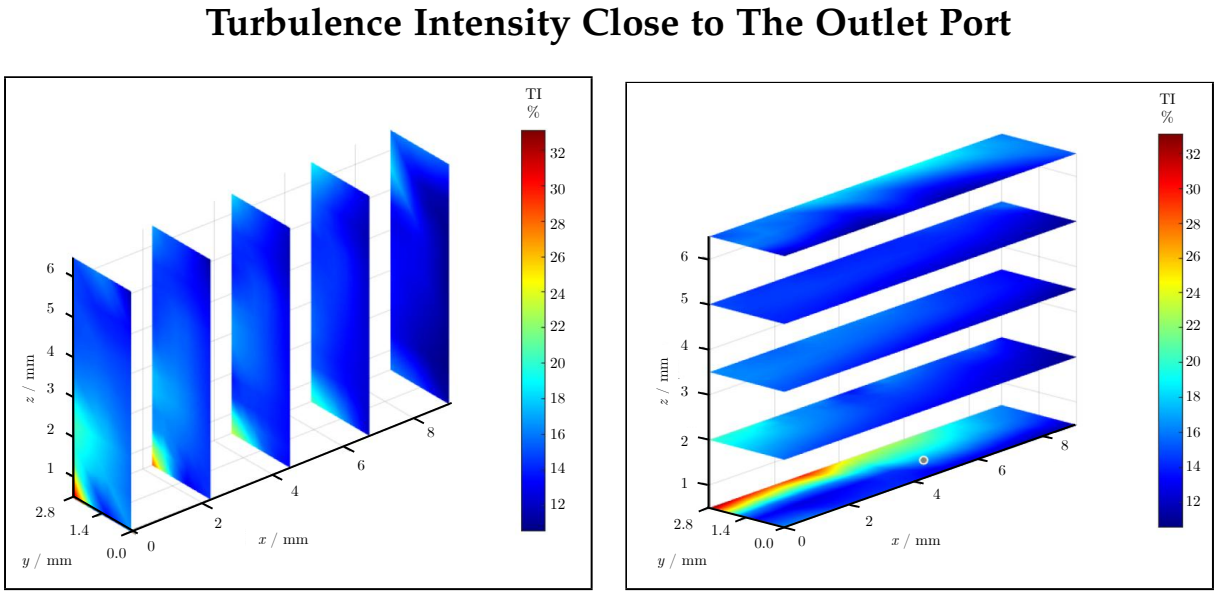


(a) Vertical Planes. (b) Horizontal Planes.

**Figure 5.7: Visualization of the TI close to the outlet port.** Display withing the (**a**) $y$-$z$-plane and withing the (**b**) $x$-$y$-plane.

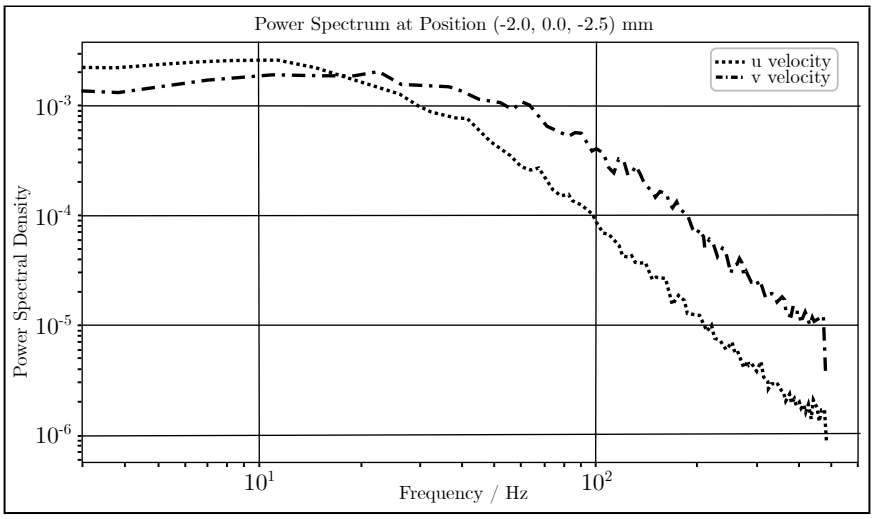


**Figure 5.8: Power spectrum illustration for detection of spatial turbulence development patterns using Fast Fourier Transformation.**

### 5.3.2 Quality of Pump Reconstruction

By following the preparation method for PDMS outlined in Section 5.2.1, a bubble-free and clear mixture was obtained. Any residual air bubbles were manually extracted using a single use pipette. Immediately after pouring, the filled molds were placed in a vacuum chamber and exposed to moderate negative pressure to remove any trapped air without compromising the integrity of the three-dimensional structures.

The surface of the casting material began to solidify after 1 h at 55 °C, at which point further bubble removal was no longer possible. After a total curing time of 15 h in the drying oven, the casting was fully hardened and ready for demolding. To facilitate smooth removal, isopropanol was poured over the mold during demolding, resulting in a clean outer surface. Thanks to the prior application of PVA coating, the three-dimensional geometries were released cleanly without leaving any residue.

The cured PDMS demonstrated sufficient stability to accommodate the original sapphire bearing within the structure. The final dimensions of the upper and lower halves of the transparent pump head housing closely matched those of the original design. Some areas along the inner edges of the upper part were not fully hardened initially but achieved complete stability during the bonding process. This procedure produced a strong, seamless bond between the two cast components that did not show any distortions with regard to light refraction.

### 5.3.3 Refractive Index Matching

To reduce optical distortions during LDA measurements, the refractive index of the working fluid was matched to that of the PDMS. This was achieved by preparing a glycerol-water mixture and systematically adjusting its composition to optimize the refractive index alignment (refractive index $n = 1.4150$). This method proved to

be a promising approach due to its simple handling and the use of non-hazardous substances. However, it was observed that the glycerol tends to settle at the bottom of the aquarium which must be considered to ensure adequate refractive index matching. With means of a stirring device, this issue was effectively overcome. Evaporation of the water was occurring as long as the aquarium was not covered, leading to an increase in the working fluid's refractive index.

## 5.4 Discussion

This study successfully replicated the Rotaflow RF-32 pump using PDMS as the casting material. By adhering to the established manufacturing protocol, a high-quality replica was produced, free from visible air bubbles or casting defects. The achieved transparency is essential for enabling non-invasive optical measurements, which are not feasible with the original pump housing.

### 5.4.1 Velocity and Turbulence Intensity

The results from the exemplary area close to the outlet port that flow velocities up to 4 m/s occur in a realistic pump setting. Lower velocities prevail at the upper and lower boundary of the channel and the highest velocity was measured in the center of the channel. Turbulent flow in the vicinity of the rotor were observable with a TI up to 32 %. The TI decreases along the channel with low TI close to the outlet port. This is expected to be a consequence of the rotor's high number of revolutions. Even though the LDA measurements focused only a small section of the entire pump replica, it indicated that turbulent flow was prevailing as seen in CFD studies [75–79]. The experiment proved the feasibility of conducting non-invasive optical flow measurements in a realistic

ECMO pump model made of PDMS. However, a systematic flow study still needs to be carried out in the future for providing full scale data.

### 5.4.2 Reconstruction of Pump Replica

Despite the overall success of the casting process, certain manufacturing challenges were encountered. Incomplete curing observed at the inner edges of the upper casting component suggests a possible interaction between the adhesive used to secure the 3D-printed parts and the silicone material. However, these areas fully cured during the subsequent second curing step without the inlay and the calcium sulfate parts.

To address this issue, using an alternative adhesive may prevent such interactions. Additionally, replacing the 3D-printed geometry with a metal counterpart, mechanically fixed to the base plate, could further reduce the risk of interference between the adhesive and the casting material. Although the complex geometry of the upper pump half makes metal fabrication impractical for that section, implementing a metal structure for the lower half could significantly minimize casting errors. This hybrid approach would preserve the benefits of the current method while mitigating its limitations, particularly in the lower section, which is more prone to air bubble entrapment due to the inlay.

### 5.4.3 Refractive Index Matching

A water-glycerol mixture was successfully adjusted to match the refractive index of the transparent pump head housing. Measurements across four silicone samples yielded varying refractive indices, averaging at $\bar{n} = 1.4150$. Fine-tuning of the mixture was achieved using the cross-line laser method, allowing precise alignment of the working fluid's optical properties with those of the PDMS material.

However, due to extended time intervals between fluid preparation and use, combined with the large surface area of the aquarium, water evaporation occurred—leading to an increase in the refractive index over time. This issue could be mitigated by implementing a closed aquarium system to reduce evaporation. Especially for experimental setups utilizing larger aquariums, an enclosure is recommended, to maintain an undistorted refractive index.

To ensure reproducibility, it is essential to adjust the refractive index before each measurement. For this purpose, a reference measurement of the adjusted fluid was recorded. This allows for the preparation of a mixture with nearly identical optical properties prior to each experiment, thereby minimizing optical distortions and enhancing the accuracy of subsequent flow measurements.

### 5.4.4 Performance Comparability

The original rotor, integrated into the silicone replica, demonstrated stable and reliable performance across a range of rotational speeds, maintaining consistent behavior even at high rotational velocities. In terms of pumping efficiency, the replicated pump head showed slightly reduced performance compared to the original Rotaflow RF-32, with the most noticeable differences in pumping performance occurring at higher flow rates. However, in the low to medium flow range, the replica performed comparably to the original.

Volume flow tests confirmed flow rates of up to 5.5 l/min, aligning well with the operational requirements of ECMO systems, which typically operate between 0.5 l/min and 5 l/min [103]. These findings indicate that the replicated pump is capable of adequately mimicking the performance characteristics of centrifugal pumps used in ECMO circuits.

The performance gap observed at higher flow rates can be attributed to several factors. Minor deviations in the volute geometry may have affected flow efficiency. Additionally, the interface between the magnetic drive and the impeller in the replica may exhibit slightly different coupling behavior. Measurement setup limitations also played a role. Unlike the original Rotaflow RF-32, the replica's external geometry did not support standard connection mechanisms, likely introducing additional flow resistance and minor inefficiencies.

Despite these differences, the close performance match within the clinically relevant flow range suggests that the internal flow patterns and shear stress distributions are likely similar to those in the original device. This supports the use of the replicated pump for investigating flow-related phenomena such as hemocompatibility, shear-induced platelet activation, and potential clot formation sites in ECMO systems.

### 5.4.5 Experimental Setup

The experimental setup developed for this study proved highly effective for conducting LDA measurements within a centrifugal pump. An alternative measuring technique would be tomographic particle image velocimetry (tomo-PIV) which directly provides three-dimensional flow field information. This technique is gold standard in experimental flow investigations. However, with high rotational speeds as in the pump replica, a high speed tomo-PIV system would be required which was not available. Nonetheless, the LDA system used provided high spatial resolution in the measurement point with a sampling rate of 8 kHz.

A key feature enabling the investigation of various flow phenomena at different rotational speeds was the integration of a stepless speed control system. This capability is particularly valuable, as ECMO devices operate across a wide range of flow rates

[103], each associated with distinct shear stress profiles. The precise control of pump speed allows for a comprehensive analysis of these varying flow regimes.

The setup also demonstrated excellent adaptability, as shown by its seamless integration with the cross-line laser method for refractive index matching. This feature enables real-time detection of refractive index changes during measurements, helping to prevent deviations and ensure data accuracy. Furthermore, the successful incorporation of the original impeller components into the transparent pump housing confirmed the setup's ability to replicate clinically relevant flow conditions. The pump operated reliably throughout the experiments without any noticeable issues.

In terms of performance, the setup delivered high-quality data acquisition. The LDA measurements produced a high data rate, supporting robust statistical analysis of the observed flow phenomena. Although the dataset collected was relatively limited, the results are promising and provide a solid foundation for future research. More extensive data collection will be necessary to draw definitive conclusions.

Overall, the experimental setup effectively addresses the technical challenges associated with non-invasive flow measurements in centrifugal blood pumps. The combination of the test rig and the RIM working fluid establishes a reliable and reproducible platform for ongoing and future flow investigations.

## 5.5 Conclusion

In conclusion, the presented experimental setup successfully replicates conditions comparable to those found in clinical ECMO pumps. With appropriate flow rates and Reynolds number scaling, the results can be meaningfully extrapolated to the original ECMO pump.

The refractive index matching technique proved effective in aligning the optical properties of the PDMS model with those of the working fluid, enabling precise flow measurements through the transparent pump housing. The LDA measurements yielded promising results, demonstrating the setup's capability for detailed flow analysis. For future improvements, integrating the trigger system directly into the LDA measurement software would allow synchronization with impeller rotation. This enhancement could help identify regions prone to clot formation by capturing flow dynamics at specific rotor positions. Overall, this approach effectively replicates the ECMO centrifugal pump and provides a robust platform for investigating clinically relevant flow dynamics.

The pump drive was designed to include different pump heads for investigating other types of ECMO pumps. This will provide reliable experimental data throughout the commonly used centrifugal pumps. Furthermore, future studies could include exploring different rotational speeds and examining specific regions within the pump to gain deeper insights into flow behavior and identify potential thrombogenic zones. A relationship to previously surveyed regions with predominant clot formation, like the area around the rotor bearing point [107], could be the subject of further studies.

# 6. Polymer Embedding of ECMO Pump Heads

First histological examinations of blood clots retrieved from clinically used ECMO pump heads were conducted, providing a major advance towards understanding underlying clot phenomena [107, 108]. However, the retrieved clots disrupted and lost their native three-dimensional shape.

The motivation was to transfer the already established polymer embedding for clinically used MLs from Chapter 3 to ECMO pump heads and later apply the developed histological protocols. This provides clot integrity after removal which again allows for precise statements on the geometry and composition of the clots.

## 6.1 Introduction

Clot progression in ECMO pump heads is a serious complication in the clinical practice of ECMO that may negatively affect its function [4]. Previously, L. Köster observed in clinically used Rotaflow pump heads that clots deposed predominantly around the bearing, the lateral housing, and inside the outlet channel [107, 108].

This chapter highlights the application of polymer embedding to ECMO pumps, how to extract the clots initially attached to the pump's housing or rotor, and how to perform microtome sections. The histological protocols are not presented as they are provided in Chapter 3.

## 6.2 Materials and Methods

Similar to the polymer embedding of MLs in Chapter 3, HistoCURE 8100 liquid polymer solution was used for mechanically stabilizing blood clots within clinically used ECMO pump heads. The embedded pump head were extracted after termination of ECMO support or after a system exchange.

### 6.2.1 Preparation of Pump Heads

The preparation of the pumps followed the same protocol used for MLs. Briefly,the pump head were rinsed with 10 l of isotonic saline solution and adherent deposits were then fixed using a formol solution (4 % m/v paraformaldehyde in 0.1 M PBS (1.15 % m/v $Na_2HPO_4$, 0.20 % m/v KCl, 0.20 % m/v $KH_2PO_4$, 8 % m/v NaCl in distilled water), pH 7.3, + 10 % v/v methanol, 1 l). Afterwards, the pump heads were stored at 4 °C until embedding [31, 61, 62].

### 6.2.2 Pre-Infiltration

Prior to the actual embedding process, a pre-infiltration step was conducted. This was necessary to ensure that the blood clots were internally stabilized and not just encapsulated by the polymer. To do so, the pre-infiltration solution was prepared with 100 ml of HistoCURE 8100 base solution and one package of hardener 1 (0.6 g). The components were filled into a 250 ml flask and stirred for 30 min at 400 1/min. This was conducted inside a cooling room with an ambient temperature of 4 °C. Following this, 10 ml of the mixture were filled into the pump head which was then pivoted to remove residual air. The remaining solution was stored at 4 °C for later processing. The pump head was then fixed to a mounting in a tilted position with both ports facing upwards, allowing air to rise. After 72 h the pre-infiltration process was finished.

### 6.2.3 Embedding

After the pre-infiltration, the hardening solution was prepared. For this, 15 ml (including 5 ml as a reserve) of the remaining pre-infiltration solution was used with the addition of 0.5 ml of hardener 2. This was mixed for about 7 min until a green discoloration was visible. The pre-infiltration solution was removed and the hardening solution was carefully filled in to prevent the formation of air bubbles. The pump head was then again pivoted to remove remaining air bubbles. After 24 h at 4 °C the hardening process was complete. The hardened pump head was removed from the cooling room and warmed to RT for specimen creation.

### 6.2.4 Creation of Specimen

In the step, relevant sections with a visible clot deposition were cut out of the hardened pump head and processed into specimen block for microtome sectioning.

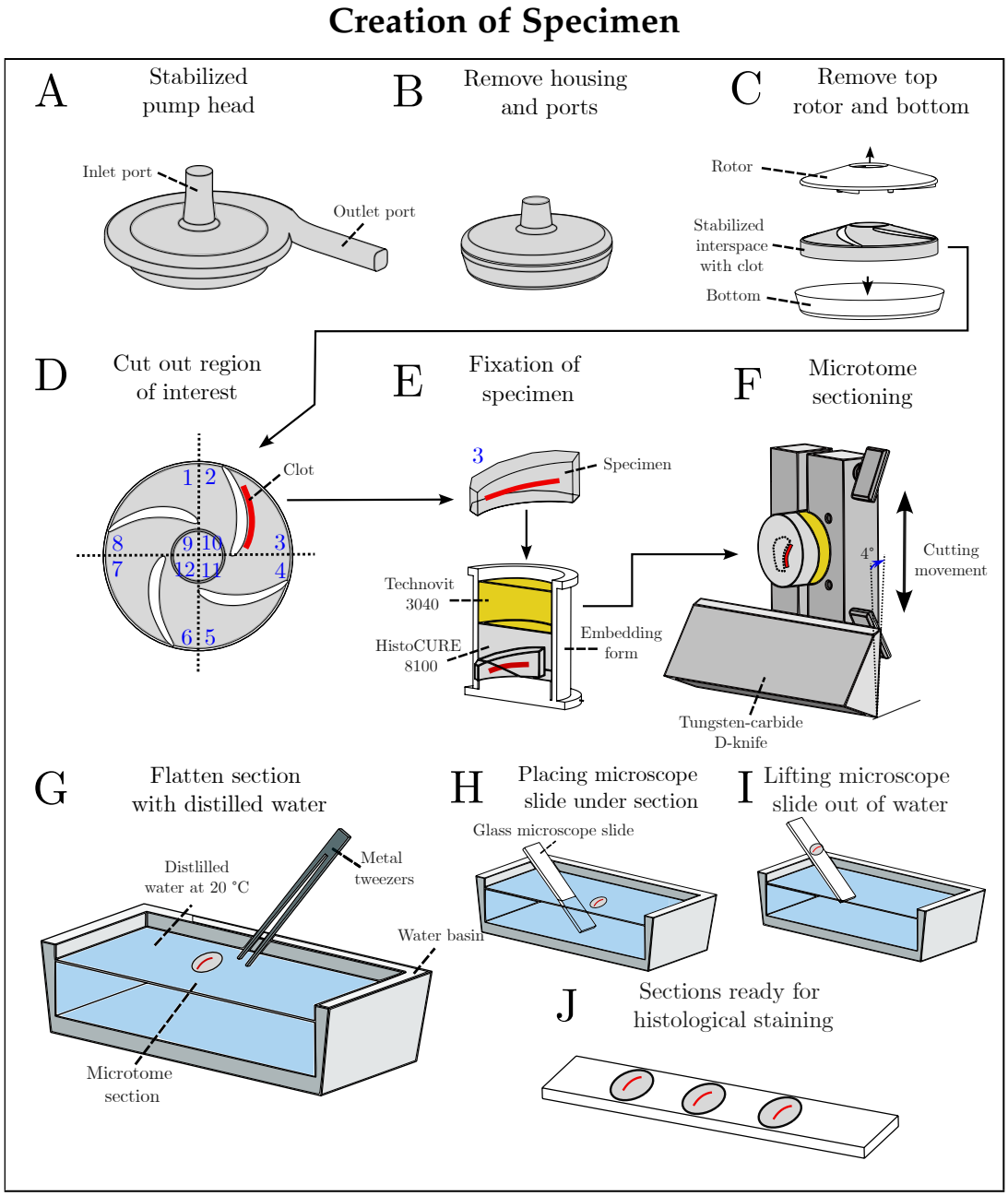


**Figure 6.1: Creation of specimen from embedded ECMO pump head.** (**A**) Hardened pump head with ports and housing. (**B**) Removal of the housing. Cutting off the ports and the surrounding channel. (**C**) Removal of the hardened polymer around the rotor and sawing along the top edge of the bottom rotor part. Then lifting the top rotor part to gain access to the stabilized rotor interspace. (**D**) Assigning numerals to twelve regions inside the stabilized interspace with 1 located closest to the former outlet port. (**E**) Embedding the cut out region including the clot in a block using a combination of HistoCURE 8100 and Technovit® 3040. Removing specimen block from embedding mold. (**F**) Performing microtome sections with a cylindrical mounting and a tungsten-carbide D-knife transferring the section to a water basin with metal tweezers. (**G**) Flattening the section by carefully placing it on the water surface of tempered (20 °C) distilled water. (**H**) Placing a glass microscope slide diagonally under the flattened section. (**I**) Lifting up the glass slide; the section adheres to the slide. (**J**) Multiple sections can be placed on one slide for later histological staining.

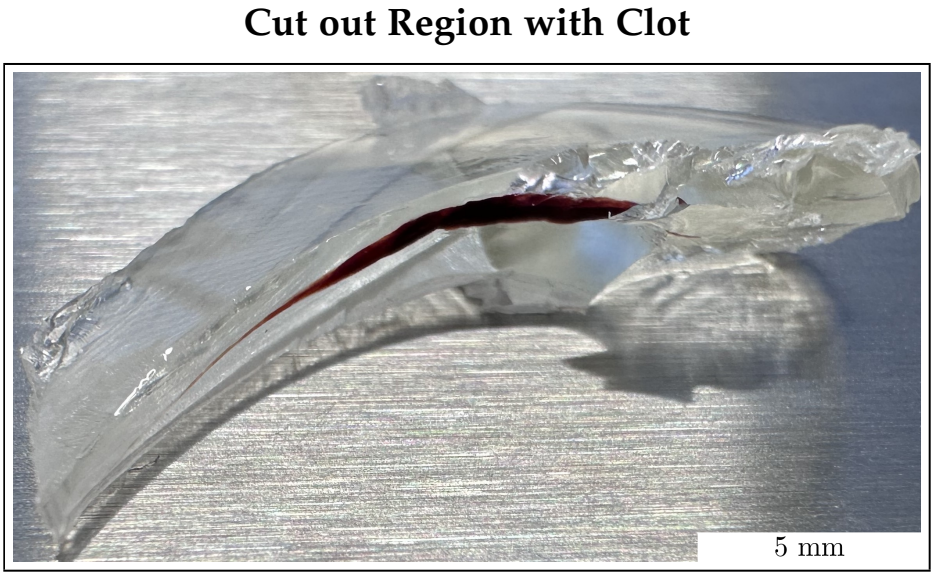


**Figure 6.2: Polymer embedded clot structure after removal from centrifugal pump.** Clot previously adherent to the outer side of the rotor blade as shown in Figure 6.1 (E). The clot was stabilized with polymer prior to removal from rotor blade. Transparent/Gray: HistoCURE 8100; red: clot structure.

First, the housing of the pump head was removed with a hand saw cutting around the perimeter of the pump head. With this, the housing was separated into two halves which were removed since HistoCURE 8100 did not form a chemical binding with the PC from the pump housing. The resulting structure is illustrated in Figure 6.1 (A). Second, the surrounding channel was cut off (Figure 6.1 (B)). If clots deposed within in channel these areas were cut to about 15 mm sections, analogous to Figure 6.1 (E). If clots were attached to the rotor blades or the bearing, the hardened interspace between the rotor top and its bottom part had to be extracted, shown in Figure 6.1 (C). This was performed by cutting along the upper edge of the rotor's bottom part. The rotor top was then deducted upwards. The hardened interspace was then subdivided into 12 regions which were cut out along the marked lines, as illustrated in Figures 6.1 (D) and 6.2. The position 1 was assigned to be the closest region to the outlet port. Position 9 to 12 describe the center of the interspace close to the bearing of the rotor.

The cut out regions were then placed into cylindrical 25 mm embedding molds (same molds as in ML embedding) with the standard flat insert, shown in Figure 6.1 (E). The molds were prior labeled according to the region number. Subsequently, the molds were placed in a sealable container and filled with HistoCURE 8100 hardening solution (about 5 ml per mold, solution prepared as described before). $CO_2$ was flushed into the container for 30 s to remove any $O_2$ which facilitated the hardening at the top boundary layer of the HistoCURE 8100 before sealing the container. In the following, the container was placed in the cooling room for 24 h at 4 °C until fully hardened.

After that, the molds were removed from the cooling room and warmed to RT in a laboratory fume hood. After reaching RT, a second layer of polymer was added. Technovit® 3040 was mixed with a volume ratio of 2 parts of powder and 1 part of liquid (10 ml powder and 5 ml for each mold) and poured into the embedding molds. After 30 min the Technovit® 3040 was fully hardened. The specimen blocks were removed from the molds (Figure 6.3) and microtome sectioning was performed.

### 6.2.5 Microtome Sectioning

Microtome sectioning used the same equipment as the sectioning of embedded ML specimen blocks. Briefly, it was performed with a tungsten-carbide d-knife and a rotary microtome. The specimen block was clamped to microtome mounting for 25 mm cylindrical block and 5-10 µm thick sections were performed with the microtome's manual drive at a high cutting velocity (Figure 6.1 (F)). The knife was tilted 4° towards the specimen block (different angle than used for embedded ML specimen (12°)). The sections were then transferred with pointed metal tweezers to a basin filled with distilled water (water at RT) to flatten the sections (Figure 6.1 (F)). A microscope glass slide was place diagonally beneath the section (Figure 6.1 (H)) and carefully

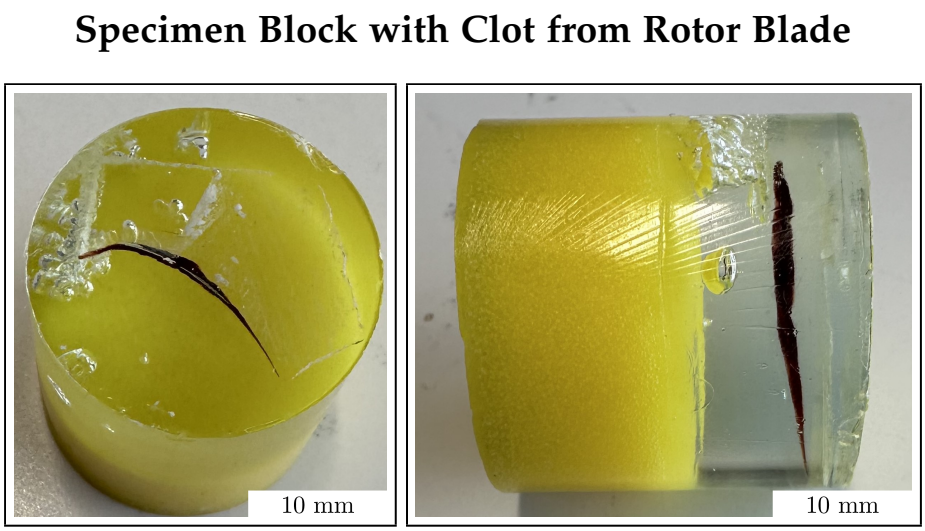


(a) Front view (b) Lateral view

**Figure 6.3: Polymer embedded pump head clot after blocking process.** Previously embedded pump head clot was further included into a polymer block by casting in the polymer fragment with additional HistoCURE 8100 (transparent polymer) in a cylindrical embedding form. To further stabilize the block, Technovit® 3040 (yellow polymer) was used. (**a**) Front view and (**b**) lateral view of specimen block.

lifted (Figure 6.1 (I)). The section then adhered to the glass slide and was ready for histological examination (Figure 6.1 (J)).

### 6.2.6 Microscopy

Transmitting light microscopy and fluorescence microscopy followed the established protocols for sections from embedded ML specimens from Chapter 3. Briefly, an inverse microscope equipped with a grayscale and a RGB camera was used for imaging. Since the sections were sometimes slightly uneven, z-stacks were performed. A z-stack image is a composite image derived from a sequence of individual images, each taken with the camera in a different z-position (vertical position). Overview images were acquired with 100 fold magnification and detailed images with 400 fold magnification.

## 6.3 Results

This chapter presented the transfer of the established polymer embedding for MLs for histological clot characterization to stabilize clots within clinically used ECMO pump head. A two step embedding process was established that first stabilized the clots in their native position and geometry followed by a second embedding step which provided standardized specimen blocks for microtome sectioning. The polymer created a scaffold that sufficiently stabilized the clots.

This method allowed the retrieval of clots adherent to the rotor blades (Figure 6.2). These clots were incorporated inside the hardened polymer allowing for a complete separation from the rotor blade without any manipulation of their geometry or integrity.

These clots were encapsulated with HistoCURE 8100 and Technovit® 3040 to create standardized specimen blocks similar to the creation for embedded ML specimens. This allowed performing reproducible and high quality microtome sections. The knife angle was slightly adapted from 12° for ML specimens to 4° for pump head specimens, as this improved the handling of cylindrical sections compared to the hexagonal ML sections.

Established protocols for histological, IHC, and immunohistofluorescence (IHF) staining as presented in Chapter 3 were applicable.

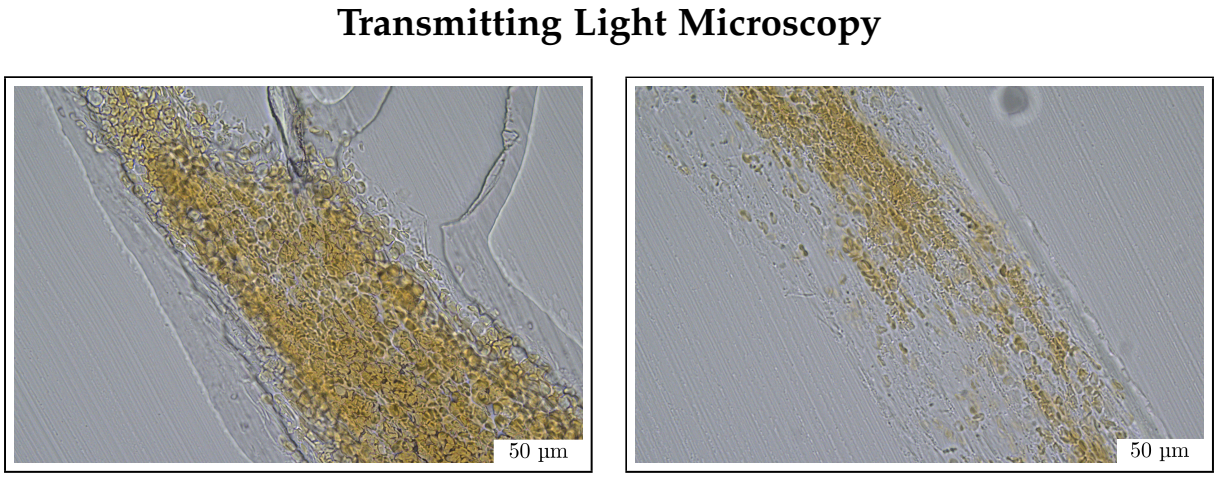


(a) High RBC count (b) Low RBC count

**Figure 6.4: Example of embedded blood clot deposed on rotor blade extracted from a Rotaflow centrifugal pump.** (**a**) High and (**b**) low RBCs count visualized with 400 fold magnification. Gray: HistoCURE 8100 polymer; yellow/red: RBCs within the clot structure.

## 6.4 Discussion

This chapter describes the successful transfer of the polymer embedding protocol for clinically used MLs from Chapter 3 to the application in clinically used ECMO pump heads.

The procedure was largely identical, apart from specific adaptations to the protocol. The volume of polymer used for this application was significantly lower. For this reason, the complexity of the procedure was also considerably reduced. For example, the low polymer volume only resulted in low heat generation due to the exothermic polymerization. In addition, the pump housing was transparent, which meant that air bubbles could be detected and removed immediately.

The hardened polymer solution stabilized the blood clots sufficiently while maintaining their native geometry. It was observed that clots adherent to the housing or the rotor

blades were reliably incorporated in the polymer. This enabled the removal of the hardened polymer including the clot from the pump rotor or housing (Figure 6.2).

Microtome sectioning according to the existing protocol for polymer-embedded specimens also proved to be a reliable and reproducible process. It was found that the cutting behavior and quality were even better than that of the embedded ML. This was attributed to the use of only one material. In contrast to the ML specimens, no polymer composite (PMP and HistoCURE 8100) was used here, only HistoCURE 8100. As the clots were also infused with HistoCURE 8100 from the inside, there was no change in the material hardness here either, which had a positive effect on the sectioning behavior.

Histological examination with the established protocols was possible with a high staining quality. As it was the case with the embedded ML specimens, only the surface of the sections could be stained since the polymer was not capable of deplastification. Consequently, a lower intensity of the fluorescence signal was detected. This was compensated by increasing the concentration of the staining agent, as presented in Chapter 3.

## 6.5 Conclusion

In conclusion, the protocol of polymer embedding using HistoCURE 8100 proves to be transferable to other blood transporting medical devices. With moderate and manageable adaptations to the original protocol for MLs, clot structures from clinically used ECMO pump heads were successfully extracted with their native geometry. Microtome sectioning proved to be reliable and reproducible with a high sectioning quality. The established histological protocols previously described in Chapter 3 were

applicable. The method proves to be a promising approach for clot characterization in native size and shape and builds the foundation for subsequent studies.

# 7. Computer Based NETosis Detection

The formation of NETs is currently discussed to be a potential trigger for clot formation in ECMO [100]. NETs are part of the human immune response of neutrophil granulocytes [100, 109]. A relation between NETs and the formation of clots was previously proved in different studies [110–114]. The process of NET formation (NETosis) can be described as a significant decondensation of the nucleus ultimately followed by an ejection of the DNA-protein complex forming string-like structures [100]. The extent to which NETosis contributes to clotting in MLs is not yet known. In order to gain a deeper insight into NETosis mechanisms, in-vitro experiments were carried out at the UKR. This chapter describes the development and functionality of a software solution specifically designed to evaluate the results of those experiments.

## 7.1 Introduction

In-vitro examinations showed that elevated shear rates ($\dot{\gamma} > 1000\ 1/s$) can trigger the formation of NETs [115]. Whether elevated shear rates are the predominant trigger NETosis in an ECMO circuit remains unknown. To gain deeper insights in shear rate induced NETosis, the researchers from the Department of Anesthesiology and the Department of Cardiothoracic Surgery of the UKR perform in-vitro experiments in which the DNA-protein ejection can be triggered, visualized, and evaluated. The aim in this work in particular was to increase the evaluation speed of their experiments by applying systematic and automated image processing. This chapter presents a brief overview of the experiment, the images acquired, the processing and its mathematical concepts as well as the results for one exemplary data set to demonstrate the data visualization.

## 7.2 Experimental Setup

The experimental setup is illustrated in Figure 7.1. It consisted of a pump system (Fluidic Unit, ibidi, Gräfelfing, Germany) that applied a positive pressure ($+\ \Delta\, p$) on a working fluid containing cells and a fluorescent nuclei dye (SYTOX™ Green, S-7020, Thermo Fisher, Waltham, MA, USA). By this, the working fluid flows continuously through a microfluidic flow chamber with a height of 400 µm respectively 800 µm (Micro slide 0.4 µm and micro slide 0.8 µm, Gräfelfing, Germany). A ML hollow-fiber was perpendicularly placed within the flow chamber on which NETosis was later occurring. With a fluorescence microscope, images were acquired automatically every 9 s for about 2 h running time. The NET formation at exemplary moments is depicted in Figure 7.2.

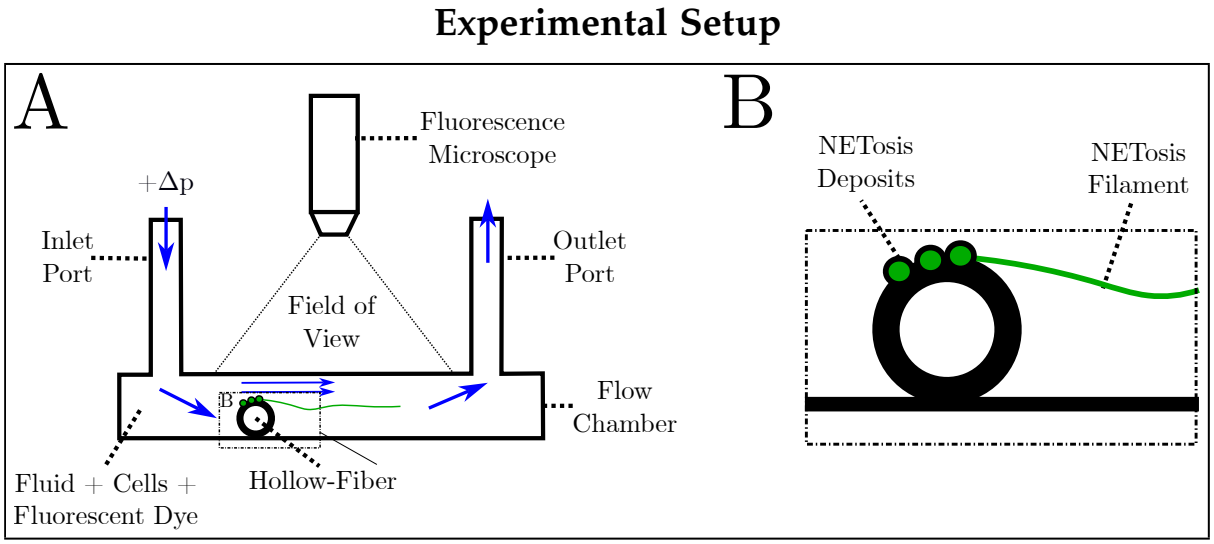


**Figure 7.1: Experimental setup for triggering and visualizing NETosis on ML hollow-fibers.** A fluid with cells is transported through a microfluidic channel with a hollow-fiber orthogonal to the flow field. A fluorescence microscope acquires images in the FITC channel every 9 s. NETotic cells and extracellular DNA is visualized using Sytox™ Green. (**A**) Overview of the experimental setup. (**B**) Magnification of hollow-fiber and adherent NET deposits and NET filaments.

## 7.3 Function of Software

The software uses a procedural structure which processes one image at the time. It is based on Python 3.12 which mainly uses `OpenCV` with `Numba` to accelerate the processing speed. The user can interact with the software via a graphical user interface (GUI).

The position of hollow-fiber is automatically captured during the calibration, shown in Figure 7.3 (a). For this method, only the first image ($I(0)$) is used, as the hollow-fiber remains in the same position relative to the camera. Furthermore, the first image does not show any NET structures which ensures adequate calibration. During the calibration process, the size and area of the image pixels is determined. This allows for a reliable measurement of NET covered area and the length of NET filaments.

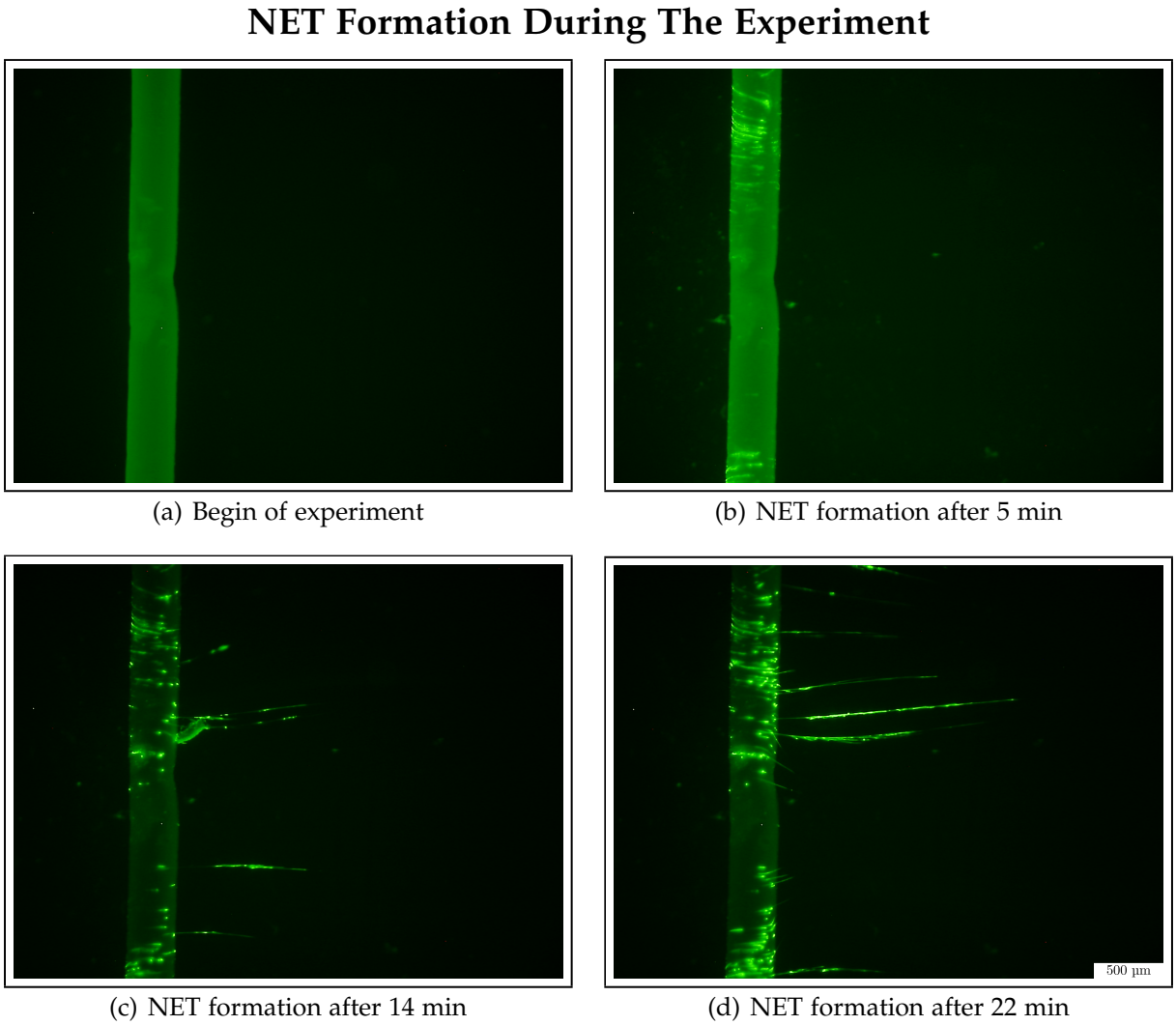


(a) Begin of experiment

(b) NET formation after 5 min

(c) NET formation after 14 min

(d) NET formation after 22 min

**Figure 7.2: Progression of NETosis during experiment.** (**a**) Image of the beginning of the experiment showing only the hollow-fiber. It was visible due to autofluorescence of the PMP material. (**b**) After several minutes, the first cells deposed on the surface of the hollow-fiber. (**c**) Next, DNA filaments were ejected. (**d**) The formation of DNA filaments constantly progressed throughout the acquisition time until they were torn from the holllow-fiber.

The software was bundled as an executable file to run on computers with Windows 10 or later. A detailed description of the working principle of the software is provided below.

### 7.3.1 Importing Images

A data set of images is comprised of about $n \approx 800$ images. All images must have the same image height $h$ and image width $w$. Further, images are referred as $I(n)$ with $n$ being the index of the image in the entire data set. To reduce memory requirements, only the directories to the images $I(n)$ are stored. Only a single image $I(n)$ is evaluated at once. The images are processed in ascending order, depending on the image file name.

### 7.3.2 Processing Calibration Image

Prior to the evaluation of NET structures, the exact location of the hollow-fiber must be known. For this reason, a calibration image is required which only depicts the hollow-fiber. Due to autofluorescence effects of the PMP polymer, the hollow-fiber can be visualized with the fluorescence microscope.

The calibration image $I(0)$ is the first image of the data set (index $n$ = 0). It is converted from the RGB to the hue-saturation-value (HSV) definition. A HSV mask is then used to extract the light green image information (hollow-fiber) from the dark green background with a mask only including the range of (36, 25, 25) to (70, 255, 255). The image is then transferred to a gray scale image, followed by a conversion to a 2-bit binary image (pixel values either 0 or 1) with a binary threshold of 1). In order to remove small pixel structures (artifacts from microscope camera), morphological filtering (opening) with a ones matrix ($H$) as kernel of size $5 \times 5$ pixels is conducted (Equation (7.1)).

$$I_{open}(0) = I(0) \circ H = (I(0) \ominus H) \oplus H \tag{7.1}$$

The result image shows only the hollow-fiber in white (pixel value 1) and all other areas in black (pixel value 0). The coordinates of the left and right edge of the hollow-fiber are then determined (edges of detected fiber marked in Figure 7.3 (a)). The width of the hollow-fiber is derived according to Equation (7.2) from the mean of the fiber width in the first and the last row of $I_{open}(0)$.

$$\bar{w}_{fiber}\ [\text{pix}] = \frac{1}{2} \times ((I_{open}(0)(0, x_3) - I_{open}(0)(0, x_2)) + (I_{open}(0)(h, x_3) - I_{open}(0)(h, x_2)) \tag{7.2}$$

Since the width of the hollow-fiber ($w_{fiber}$ = 0.38 $mm$) is known, the width $w_{pixel}\ [mm]$ and subsequently the area $A_{pixel}\ [mm^2]$ of one pixel is calculated according to Equations (7.3) and (7.4).

$$w_{pixel}\ [\text{mm}] = \frac{w_{fiber}[\text{mm}]}{\bar{w}_{fiber}[\text{pix}]} = \frac{0.38[\text{mm}]}{\bar{w}_{fiber}[\text{pix}]} \tag{7.3}$$

Since pixels are square, the pixel area can also be calculated on the basis of the edge length by squaring it, shown in Equation (7.4).

$$A_{pixel}[\text{mm}^2] = w^2_{pixel}[\text{mm}]^2 \tag{7.4}$$

### 7.3.3 Evaluation of Deposits Area and Count

The area of the hollow-fiber covered by cellular deposits is calculated in two steps. First, the ROI is masked. This means that only the pixel structures in the area of the hollow-fiber is taken into account. This is implemented by matrix multiplication of the binary image $I(n)$ and a constant filtering mask $F_{fiber}$ according to Equation (7.5).

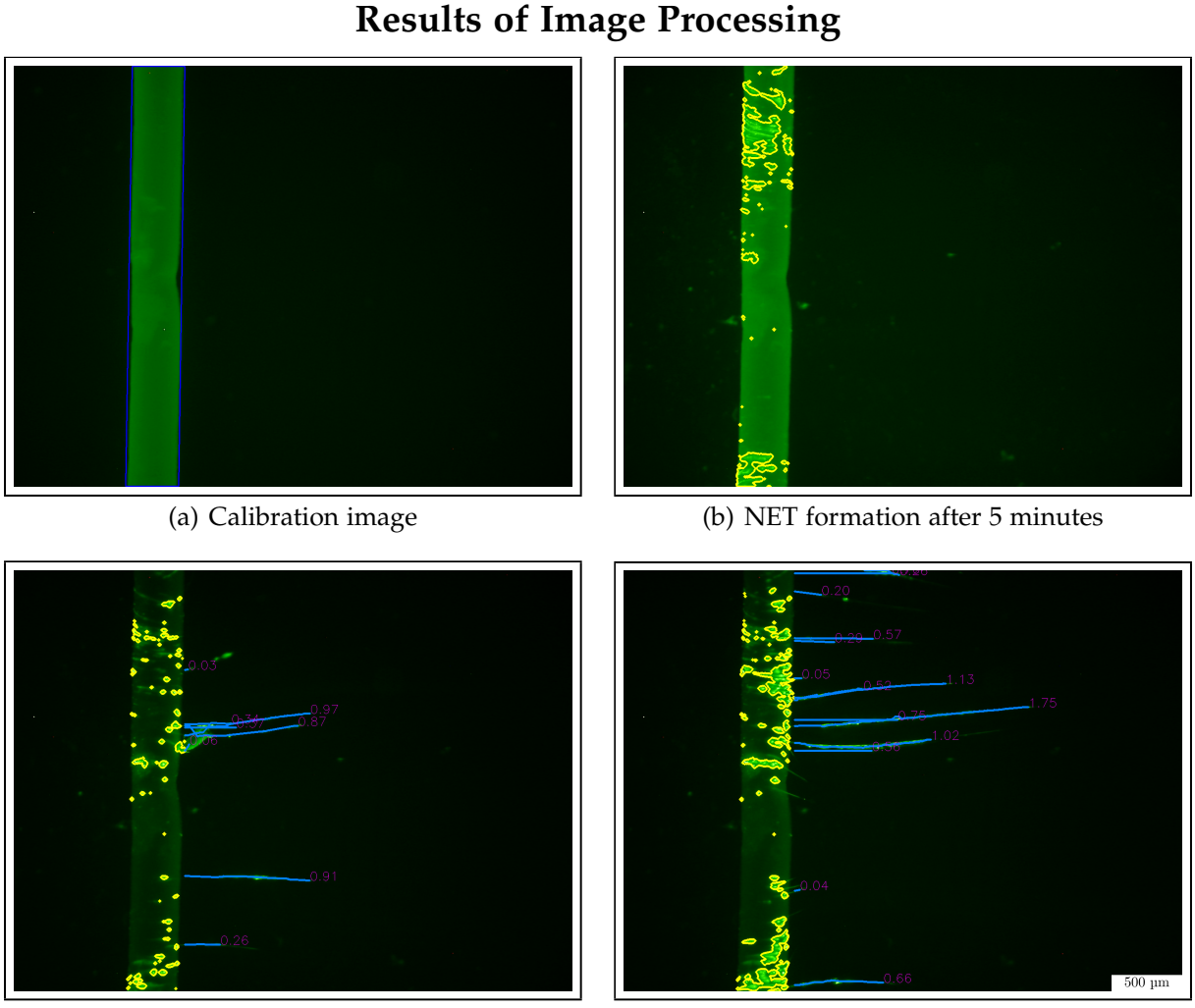


(a) Calibration image

(b) NET formation after 5 minutes

(c) NET formation after 14 minutes

(d) NET formation after 22 minutes

**Figure 7.3: Calibration image and NET formation during experiment.** (**a**) Calibration image $I(0)$ with automatically detected hollow-fiber (blue). (**b**) NET formation after 5 minutes: Accumulation of deposit structures on the hollow-fiber surface. The deposits are automatically detected and marked (yellow). (**c, d**) NET formation after 14 and 22 minutes: Filament structures form and are detected by the software while the number of deposits increases. The filament length (in mm) is calculated and provided next to the detected filament.

$$I_{fiber}(n) = I(n) \times F_{fiber} \tag{7.5}$$

The filtering mask is defined as a binary matrix with values of 1 in the ROI and 0 at all other elements shown in Equation (7.6). The horizontal section of the matrix between $x_2$ and $x_3$ marks the contours of the hollow-fiber. The exact values of $x_2$ and $x_3$ are derived from the calibration process. Since the hollow-fiber could possibly be inserted at a slight angle, $x_2$ is assigned the smallest x-value of the left fiber edge and $x_3$ the largest x-value of the right hollow-fiber edge. For reasons of efficiency and robustness, only the x-coordinates of the hollow-fiber in the first and last line are considered here.

$$F_{fiber} = \begin{array}{c} \begin{matrix} 0 & \dots & x_1 & x_2 & \dots & x_3 & x_4 & \dots & w \end{matrix} \\ \begin{pmatrix} 0 & \dots & 0 & 1 & \dots & 1 & 0 & \dots & 0 \\ \vdots & \ddots & 0 & 1 & \ddots & 1 & 0 & \ddots & 0 \\ 0 & \dots & 0 & 1 & \dots & 1 & 0 & \dots & 0 \end{pmatrix} \begin{matrix} 0 \\ \vdots \\ h \end{matrix} \end{array} \tag{7.6}$$

The area and number of the deposits was calculated using the `cv2.findContours` function. Redundant points of the contour are discarded with the `cv2.CHAIN_APPROX_SIMPLE` flag and the contour hierarchy is defined with the `cv2.RETR_EXTERNAL` flag. A number of $m$ contours is then provided in every image $I_{fiber}(n)$. Finally, the `cv2.contourArea` function returns the number of pixels $N_{pixels_{contour(m)}}(n)$ within every detected contour which is then multiplied with the area of a pixel $A_{pixel}$ (Equation (7.7)).

$$A_{deposits}(n) = \sum_{0}^{m} N_{pixels_{contour(m)}}(n) \times A_{pixel} \tag{7.7}$$

### 7.3.4 Evaluation of Filaments Area

The evaluation of the area covered by filaments follows the same algorithm but with a different filtering mask $F_{filaments}$ according to Equation (7.8).

$$I_{filaments}(n) = I(n) \times F_{filaments} \tag{7.8}$$

However, since only the area to the right of the fiber should be evaluated, a filtering mask with values of 1 right of the hollow-fiber ($\geq x_2$) is used as shown in Equation (7.9). Similar to $F_{fiber}$ the value of $x_2$ is also derived from the calibration process (largest x-value of right hollow-fiber edge).

$$F_{filaments} = \begin{matrix} 0 & \dots & x_1 & x_2 & \dots & w \end{matrix} \begin{matrix} \\ \\ \\ \end{matrix} \begin{pmatrix} 0 & \dots & 0 & 1 & \dots & 1 \\ \vdots & \ddots & 0 & 1 & \ddots & 1 \\ 0 & \dots & 0 & 1 & \dots & 1 \end{pmatrix} \begin{matrix} 0 \\ \vdots \\ h \end{matrix} \tag{7.9}$$

Determination of the total area covered by the filaments follows the same procedure as for the calculation of the area of the cellular deposits. The total area of filament structures in the filtered image ($I_{filaments}(n)$) is calculated by the sum over all rows and columns of the image multiplied by the previously defined area of a single pixel $A_{pixel}$ (Equation (7.10)).

$$A_{filaments}(n) = \sum_{0}^{w} \sum_{0}^{h} I_{fiber}(n) \times A_{pixel} \tag{7.10}$$

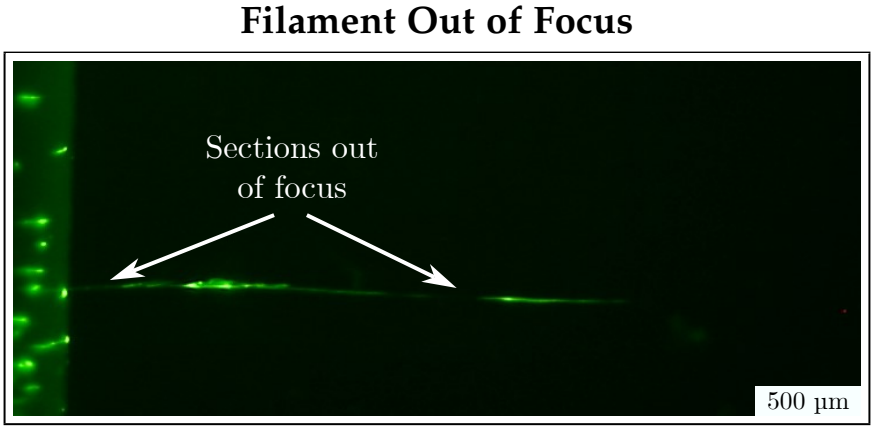


**Figure 7.4: NETosis filament out of focus plane during experiment.**

### 7.3.5 Evaluation of Filaments Length

The filament length is an important piece of information for the investigation of NETosis in this experimental setup. However, its detection proved to be a major challenge in the development of the algorithm, as some parts of the filaments did not remain in the focal plane during the experiment. This means that only sections of them can be seen in the images, as shown in Figure 7.4. In the images, it was observed that even if no connection between the filament and the hollow-fiber was visible, these sections remained in position and did not flow downstream. For this reason, there must be a connection to the hollow-fiber, which means that the sections must be part of a single filament. Consequently, the algorithm must recognize all sections of a filament and combine them to reconstruct the entire original filament. Only then can the filament length be determined.

The filament reconstructions used two different mathematical approaches. The detected skeleton structures were approximated with (1) a linear function or (2) with cubic splines. The linear function proved to require less computational effort while the spline fit was more accurate. The gradient vector of the function at the maximum $x$-value of

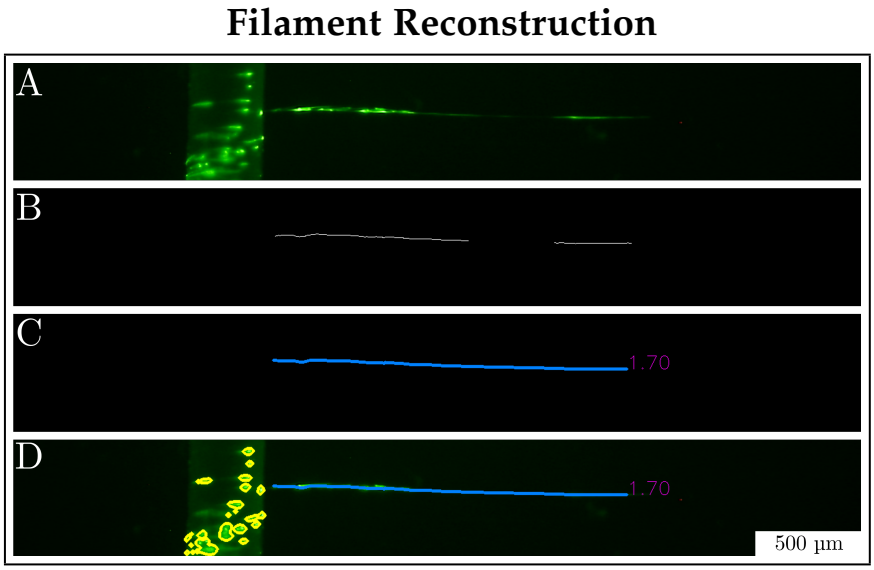


**Figure 7.5: Process of filament reconstruction.** (**A**) Input of raw image from microscope. (**B**) Skeletonizing of filament to receive to longest connected pixel structure. (**C**) Reconstruction of original filament by extrapolation of detected filament sections and calculation of its length (in mm) by performing a spline approximation. (**D**) Result image with marked deposits and filaments.

the skeleton was calculated. If another skeleton was found in a range $\pm$ 10° close to the right end of the left skeleton, both skeletons were connected.

### 7.3.6 Export Results

After completion of the image processing, the results can be exported as CSV and XLSX files for further statistical analysis. Furthermore, a report summarizing the results of the image processing and documenting its meta data and settings is generated as PDF file. If the setting 'Auxiliary Files' is checked, all result images, skeleton images, deposit images, filament section images, and the calibration image with indicated hollow-fiber edges that are generated during the image processing can be saved. The detected filament contours are also automatically exported as JSON file structured in Common Object in Context (COCO) format.

### 7.3.7 Export Contour Data for Deep Learning

The filament contours stored in a COCO structured file can be used for labeling in annotation software like Computer Vision Annotation Tool (CVAT). On this basis they can be used for training a Deep Learning (DL) model.

### 7.3.8 Validation

Validation was conducted with defined test images including the hollow-fiber and various filament structures with known dimensions. It was observed whether relevant deviations due to the opening process exists and if the filament length was correct. In addition, with 20 randomly selected images from provided data sets the lengths of the filaments were manually measured and compared with the automatic evaluation from the software. No significant differences were detected.

## 7.4 Results

Figure 7.6 presents the results for one example data set to demonstrate the algorithm's functionality and the data representation. The area covered by deposits and filaments and their number were of particular interest. Moreover, the mean length of the filaments is presented.

### 7.4.1 NET Filaments

A total number of images $n = 842$ were analyzed. The first minor filament structures occurred after 279.0 $s$. The area covered by the filaments shows an irregular progression with its peak at $A_{filaments} = 0.4$ mm$^2$ after $t = 85$ min, shown in Figure 7.6 (a). Especially relevant are the top region followed by the bottom region, while the middle

region presented the lowest filament covered area. 772 of 842 images (92 %) in the middle region, 739 of 842 images (88 %) in the top region and also 739 of 842 images (88 %) in the bottom region included filament structures.

The number of detected filaments during the experiment is depicted in Figure 7.6 (b). It can be seen that a strong formation of filaments begins after approximately 10 min. The number of filaments increases steadily until it levels off at approximately 70 min and then remains relatively constant in the range between $n_{filaments} = 35 - 42$. The mean filament length rises rapidly, particularly at the beginning, up to a length of 0.5 mm and then also falls rapidly again. After 60 min, the mean length rises again to approximately 0.37 mm and falls again at the end of the experiment.

### 7.4.2 NET Deposits

The area of the hollow-fiber covered by NET deposits during the experiment is depicted in Figure 7.6 (d). After approximately 5 min the first cell depositions were visible on the hollow-fiber surface when a bolus of Sytox™ Green staining was added. The staining bolus resulted in a short term peak. Thereafter, a steady incline of the area was prominent. After 65 min a constant state was reached.

The NET deposit count in Figure 7.6 (e) showed a rapid increase with its peak of $n_{deposits} = 69$ at $t = 17$ min followed by a steady decline. After 60 min, it reached a constant state between $n_{deposits} = 37 - 43$. As the deposits agglomerate to larger confluent structures, the NET deposits count decreased during the experiment. However, the area covered by NET deposits steadily increased until the entire hollow-fiber area was covered after about $t = 70$ min

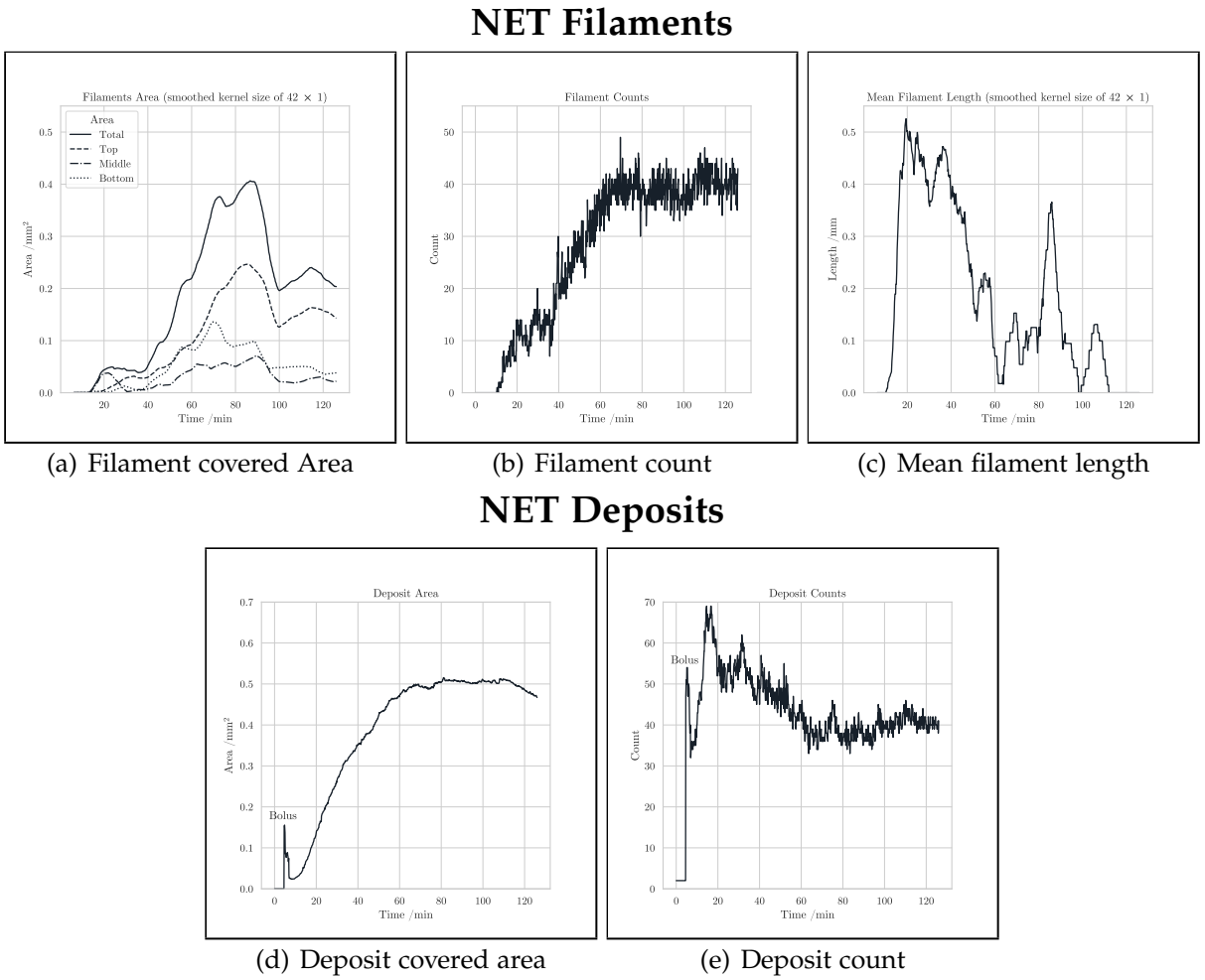


(a) Filament covered Area (b) Filament count (c) Mean filament length

(d) Deposit covered area (e) Deposit count

**Figure 7.6: Exemplary results from NETosis detection software.** (**a**) Display of area covered by deposits. (**b**) Absolute number of detected filaments. (**c**) Mean filament length; for better readability a smoothing was performed with a window width of 5 % of the total number of images evaluated. (**d**) Display of area covered by deposits. (**e**) Absolute number of detected deposits.

## 7.5 Discussion

The presented image processing software automatically detects NET structures, such as deposed DNA aggregates or fragments of nuclei and DNA filaments in images captured during a flow channel experiment. It provides specific information on the area and occurrence of the NET structures as well as the length of detected DNA filaments.

### 7.5.1 Evaluation Performance

The software significantly reduces the evaluation time and effort compared to the previous manual measurements. It uses packages with a C code backend such as `OpenCV` or `Numba` and filtering with matrix multiplication to significantly decrease the evaluation time. The internal Python code is structures into two major steps: The detection of deposits followed by the detection of filaments. Especially the filament reconstruction requires a high computational effort. For this reason, an intermediate check was implemented. If a minimum amount of pixel structures (threshold given by user to increase code robustness) is detected, the reconstruction process is initiated. Otherwise, the reconstruction step is skipped. This occurs predominantly in the early phase of the evaluation as no filaments have been formed.

A calibration based on the known width of the inserted hollow-fiber ($w_{fiber}$ = 0.38 $mm$) is automatically conducted in the beginning of the image processing. With this, reliable measurements of NET covered areas and filament lengths are possible.

### 7.5.2 Usability

The software is equipped with a GUI to enable interactions with the user. The user is guided step-by-step through the software by the GUI. Standard evaluation settings are set tuned to the microscope's parameters. In addition, a digital user manual is included to the software.

### 7.5.3 Limitations

Despite the overall satisfactory detection quality and speed, the software has its limitations. First, when encountering overlapping filaments, it occurs that filament sections are mistakenly connected. Overlapping filaments represent one single connected pixel

structure are likely interpreted as one single filament. The adaptation of internal threshold during the development of the software reduced this effect but still it cannot be prevented completely. in contrast the area calculation of the filaments is less susceptible, since all pixel structures are captured. Furthermore, the software assumes that the origin of the filaments is the right edge of the hollow-fiber. Consequently, if filaments originate left from the right hollow-fiber edge, the first parts are interpreted as deposits and the filament will be slightly reduced. The application of DL may solve these problems. Since an export of the filament contours as a COCO formatted file is implemented, the labeling effort is significantly reduced thus allowing the training of a DL model and better prediction of filament structures.

The deposit area is assumed to be a plane. However, they deposed on a cylindrical surface. This optical distortion is not yet currently considered.

For reliable detection, the brightness of the input images must be similar as the binarization is based on a static threshold throughout the image processing. Therefore, varying image brightness and quality may significantly affect the results.

## 7.6 Conclusion

In conclusion, the presented software fulfills the requirements for reliable detection of NET structures in the flow channel experiments. The number and area of filament and deposit structures are automatically captured. Furthermore, a comprehensive reconstruction algorithm allows the length measurement of filaments that migrated out of the microscope's focus plane.

This software solution significantly reduces the evaluation time for the NETosis examination setup. It yields essential information on NET formation and contributes to future insight into shear induced NETosis.

# 8. Conclusion and Outlook

This work highlighted different approaches to investigate shear-induced coagulation in MLs.

Initially, the clot volume in seven clinically used PLS MLs was recorded and critically analyzed using three different state-of-the-art imaging techniques. A newly established method for polymer embedding of MLs was presented, which enables histological analyses of cross-sectioned ML hollow-fibers and thus expands the repertoire of histological examinations. Furthermore, CFD calculations were performed on a generic and native ML model to investigate the influence of the hollow-fiber arrangement on the flow field and the shear rate. Next, the successful development of an experimental setup for non-invasive optical flow measurements within a realistic ECMO pump head using LDA was presented. The work was concluded with the presentation of a polymer embedding protocol for ECMO pumps and a computerized evaluation of NETosis.

## 8.1 Clot Formation is Location-Dependent

There was a clear trend towards a higher clotting volume in the inlet chamber of the investigated MLs. One possible explanation is the presence of TPU hollow-fibers, which may promote the formation of blood clots. However, the current study situation does not allow a clear statement in this regard, as the majority of the studies focused exclusively on histological examinations of gas exchanging hollow-fibers. The future investigation of the influence of TPU hollow-fibers on the clot formation in MLs is therefore endorsed.

A second possible explanation is different density of hollow-fiber packing in the inlet and outlet chamber of the ML. Since the derived correction factors prove a fiber mat packing with a higher density in the outlet chamber, the fiber mat interspace is clearly smaller compared to it the inlet chamber. It is expected to result in a geometrically limitation of clot formation which results in a higher clot volume per fiber mat in the inlet chamber. Also this approach has not been discussed in the literature. A future investigation of the influence of fiber mat packing on clot formation is also recommended.

## 8.2 Cross-Sectional ML Investigations as New Standard

Top view microscopic examinations of immunological deposits on ML fiber mats resembles the standard method for various studies. However, elongated vWF is expected to align with the blood flow which is orthogonal to the viewing plane. Therefore it is hardly visible with this state-of-the-art method. As a solution, a cross-sections perspective can provide this piece of information. Since the hollow-fiber are porous and delicate, microtome sections failed in preliminary tests. It was concluded

that the mechanical stability must be increased to allow reproducible sections. As paraffin showed a distinct lower hardness than the hollow-fibers, a polymer was chosen. Polymer embedding of clinically used MLs was introduced as a new method. Standard histological and IHC staining protocol were established and tested.

## 8.3 No vWF Elongation Due to Irregular Fiber Arrangement

This work presets highly resolved CFD results from a generic and a native ML model. The generic model comprised of a symmetrical and the native model of an asymmetrical hollow-fiber arrangement. It was found that the irregular fiber arrangement of the native model resulted in a clearly higher flow velocity and higher shear rates. Still, the shear rates were not sufficient to induce a vWF elongation.

## 8.4 Successful Development of Realistic Pump Model for Non-Invasive Optical Flow Investigations

Even though only the flow within the outlet channel and not the area close to the rotor was captured, it clearly indicated that a highly turbulent flow regime prevailed under realistic conditions inside an ECMO pump. The feasibility of non-invasive optical flow investigations in a realistic ECMO pump replica was proven. The experimental setup was practical and functional and allows for systematic LDA measurements in the future as a basis for reliable flow data.

## 8.5 NETosis as Possible Clotting Pathway

The influence of NETosis in intra-device clot formation in MLs is currently discussed in the literature. However, it is not yet sufficiently understood. In-vitro investigations might provide deeper insights. The developed image processing and evaluation software represents a reliable tool to efficiently extract important data from the acquired microscopic images. With the help of this software solution, experiments can be evaluated more reliably and precisely and new insights into shear induce NET formation can be gained.

## 8.6 Summary

Clot formation within MLs remains a complex phenomenon. However, relevant subsections of the ML were isolated. Especially the inlet chamber shows a special affinity for the deposition of blood clots. Whether it is due to the use of TPU hollow-fibers or due to the lower fiber mat packing density and the increased space available, should be subject of future investigations. CFD in a native ML geometry proved that the fiber mat arrangement has significant influence on the flow field and therefore on the shear stress. Yet, no pathological flow regime was found with regard to vWF elongation. However, the CFD calculations were based on a hollow-fiber model which excluded all other components but the fiber mats. As seen with the FMI, these certain areas show a constant clot volume. Whereas, FMI indicated that the distributor plate, the diving wall, the collector plate, significantly affect the clot volume deposed on the fiber mats in their vicinity. It certainly recommends focusing on the distributor plate, partition wall and collection plate areas in future CFD calculations. High shear rates in these areas might induce a vWF elongation. Subsequently, the elongated vWF

flows downstream and remains in the interspace between the hollow-fibers which again triggers local clot formation. In conclusion, solely the arrangement of the gas exchanging hollow-fibers is unlikely to be the effector of clot formation within the ML.

It was indicated that a turbulent flow regime prevailed in the ECMO pump. However, only a small section of the pump was evaluated to demonstrate the feasibility of the experimental setup. It is endorsed to perform LDA at various measurement point of the pump replica to provide sufficient data. Nevertheless, the foundation for such studies has been successfully established.

A polymer embedding protocol for clinically used MLs was successfully developed which resembled a new state-of-the-art technique for the investigation of intra-device clot formation. Furthermore, its capability of transfer the embedding protocol to ECMO pumps was successfully tested.

The influence of NETosis to the clotting phenomena in ECMO is not yet understood. However, the presented image processing software helps researchers with the visualization and evaluation of NET formation on PMP hollow-fibers.

In conclusion, clot formation in MLs remains a complex phenomenon. However, it seems plausible that the centrifugal pump plays a key role in intra-device clot formation in ECMO.

# Bibliography

[1] M. Arlt, A. Philipp, S. Voelkel, L. Rupprecht, T. Mueller, M. Hilker, B. M. Graf, and C. Schmid. "Extracorporeal Membrane Oxygenation in Severe Trauma Patients with Bleeding Shock". In: *Resuscitation* 81.7 (July 1, 2010), pp. 804–809. ISSN: 0300-9572. DOI: 10.1016/j.resuscitation.2010.02.020. https://www.sciencedirect.com/science/article/pii/S0300957210001243 (visited on 06/09/2023).

[2] G. Makdisi and I.-W. Wang. "Extra Corporeal Membrane Oxygenation (ECMO) Review of a Lifesaving Technology". In: *J Thorac Dis* 7.7 (July 2015), E166–176. ISSN: 2072-1439. DOI: 10.3978/j.issn.2072-1439.2015.07.17. PMID: 26380745.

[3] S. M. Hastings, D. N. Ku, S. Wagoner, K. O. Maher, and S. Deshpande. "Sources of Circuit Thrombosis in Pediatric Extracorporeal Membrane Oxygenation". In: *ASAIO Journal* 63.1 (Jan. 2017), pp. 86–92. ISSN: 1058-2916. DOI: 10.1097/MAT.0000000000000444. https://journals.lww.com/00002480-201701000-00015 (visited on 06/09/2023).

[4] M. Lubnow, A. Philipp, M. Foltan, T. Bull Enger, D. Lunz, T. Bein, A. Haneya, C. Schmid, G. Riegger, T. Müller, and K. Lehle. "Technical Complications during Veno-Venous Extracorporeal Membrane Oxygenation and Their Relevance Predicting a System-Exchange – Retrospective Analysis of 265 Cases". In: *PLoS ONE* 9.12 (Dec. 2, 2014). Ed. by A. Schäfer, e112316. ISSN: 1932-6203. DOI: 10.1371/journal.pone.0112316. https://dx.plos.org/10.1371/journal.pone.0112316 (visited on 12/12/2023).

[5] H. J. Dalton, P. Garcia-Filion, R. Holubkov, F. W. Moler, T. Shanley, S. Heidemann, K. Meert, R. A. Berg, J. Berger, J. Carcillo, C. Newth, R. Harrison, A.

Doctor, P. Rycus, J. M. Dean, T. Jenkins, and C. Nicholson. "Association of Bleeding and Thrombosis With Outcome in Extracorporeal Life Support*:" in: *Pediatric Critical Care Medicine* 16.2 (Feb. 2015), pp. 167–174. ISSN: 1529-7535. DOI: 10.1097/PCC.0000000000000317.
http://journals.lww.com/00130478-201502000-00011 (visited on 06/12/2025).

[6] J. H. Gibbon and J. D. Hill. "Part I. The Development of the First Successful Heart-Lung Machine". In: *The Annals of Thoracic Surgery* 34.3 (Sept. 1982), pp. 337–341. ISSN: 00034975. DOI: 10.1016/S0003-4975(10)62507-6.
https://linkinghub.elsevier.com/retrieve/pii/S0003497510625076 (visited on 03/24/2025).

[7] W. Böttcher and H. Woysch. "Die erste erfolgreiche herzchirurgische Operation mit Hilfe der Herz-Lungen-Maschine [The first successful heart surgery using the heart-lung machine]". In: *Z Herz- Thorax- Gefäßchir* 20.6 (Dec. 2006), pp. 248–260. ISSN: 0930-9225, 1435-1277. DOI: 10.1007/s00398-006-0551-3.
http://link.springer.com/10.1007/s00398-006-0551-3 (visited on 03/24/2025).

[8] M. Krane, R. Bauernschmitt, and R. Lange. "Die Herz-Lungen-Maschine [The Heart-Lung-Machine]". In: *Medizintechnik: Life Science Engineering*. Ed. by E. Wintermantel and S.-W. Ha. Springer Berlin Heidelberg, 2009, pp. 1373–1386. ISBN: 978-3-540-93936-8.

[9] R. H. Bartlett. "The Story of ECMO". In: *Anesthesiology* 140.3 (Mar. 2024), pp. 578–584. ISSN: 0003-3022, 1528-1175. DOI: 10.1097/ALN.0000000000004843.
https://journals.lww.com/10.1097/ALN.0000000000004843 (visited on 03/24/2025).

[10] ELSO. *ECLS Registry Report*. 2021.
https://www.elso.org/registry.aspx (visited on 02/18/2024).

[11] *PubMed*. PubMed.
https://pubmed.ncbi.nlm.nih.gov/?term=ECMO+Clotting (visited on 01/23/2025).

[12] J. D. Hill, T. G. O'Brien, J. J. Murray, L. Dontigny, M. L. Bramson, J. J. Osborn, and F. Gerbode. "Prolonged Extracorporeal Oxygenation for Acute Post-Traumatic Respiratory Failure (Shock-Lung Syndrome): Use of the Bramson Membrane Lung". In: *N Engl J Med* 286.12 (Mar. 23, 1972), pp. 629–634. ISSN: 0028-4793, 1533-4406. DOI: 10.1056/NEJM197203232861204.
http://www.nejm.org/doi/10.1056/NEJM197203232861204 (visited on 03/24/2025).

[13] H. Jakob, G. Hafner, C. Thelemann, A. Stürer, W. Prellwitz, and H. Oelert. "Routine Extracorporeal Circulation with a Centrifugal or Roller Pump". In: *ASAIO Transactions* 37.3 (July 1991), pp. M487–M489.

[14] G. J. Peek, M. Mugford, R. Tiruvoipati, A. Wilson, E. Allen, M. M. Thalanany, C. L. Hibbert, A. Truesdale, F. Clemens, N. Cooper, R. K. Firmin, and D. Elbourne. "Efficacy and Economic Assessment of Conventional Ventilatory Support versus Extracorporeal Membrane Oxygenation for Severe Adult Respiratory Failure (CESAR): A Multicentre Randomised Controlled Trial". In: 374 (2009).

[15] Y. Iwashita. "The History of Extracorporeal Membrane Oxygenation and Its Role in Coronavirus Disease 2019". In: *Shimane Journal of Medical Science* 37.2 (2020), pp. 57–60. DOI: 10.51010/sjms.37.2_57.
https://doi.org/10.51010/sjms.37.2_57 (visited on 03/24/2025).

[16] S. A. Conrad, L. M. Broman, F. S. Taccone, R. Lorusso, M. V. Malfertheiner, F. Pappalardo, M. Di Nardo, M. Belliato, L. Grazioli, R. P. Barbaro, M. M. McMullan, V. Pellegrino, D. Brodie, M. M. Bembea, E. Fan, M. H. Mendonca, R. Diaz, and R. H. Bartlett. "The ELSO Maastricht Treaty for ECLS Nomenclature: Abbreviations for Cannulation Configuration in Extracorporeal Life Support - a Position Paper of the Extracorporeal Life Support Organization". In: *Critical Care* 23.1 (Feb. 8, 2019), p. 36. ISSN: 1364-8535. DOI: 10.1186/s13054-019-2334-8.
https://doi.org/10.1186/s13054-019-2334-8 (visited on 01/19/2024).

[17] A. Combes, D. Hajage, G. Capellier, A. Demoule, S. Lavoué, C. Guervilly, D. Da Silva, L. Zafrani, P. Tirot, B. Veber, E. Maury, B. Levy, Y. Cohen, C. Richard, P. Kalfon, L. Bouadma, H. Mehdaoui, G. Beduneau, G. Lebreton, L. Brochard, N. D. Ferguson, E. Fan, A. S. Slutsky, D. Brodie, and A. Mercat. "Extracorporeal Membrane Oxygenation for Severe Acute Respiratory Distress Syndrome". In: *N Engl J Med* 378.21 (May 24, 2018), pp. 1965–1975. ISSN: 0028-4793, 1533-4406. DOI: 10.1056/NEJMoa1800385.
http://www.nejm.org/doi/10.1056/NEJMoa1800385 (visited on 03/24/2025).

[18] K. Ramanathan, D. Antognini, A. Combes, M. Paden, B. Zakhary, M. Ogino, G. MacLaren, D. Brodie, and K. Shekar. "Planning and Provision of ECMO Services for Severe ARDS during the COVID-19 Pandemic and Other Outbreaks of Emerging Infectious Diseases". In: *The Lancet Respiratory Medicine* 8.5 (May 2020), pp. 518–526. ISSN: 22132600. DOI: 10.1016/S2213-2600(20)30121-1.

https://linkinghub.elsevier.com/retrieve/pii/S2213260020301211 (visited on 03/24/2025).

[19] J. E. Tonna, P. S. Boonstra, G. MacLaren, M. Paden, D. Brodie, M. Anders, A. Hoskote, K. Ramanathan, R. Hyslop, J. J. Fanning, P. Rycus, C. Stead, N. A. Barrett, T. Mueller, R. D. Gómez, P. Malhotra Kapoor, J. F. Fraser, R. H. Bartlett, P. M. A. Alexander, R. P. Barbaro, and on behalf of the Extracorporeal Life Support Organization (ELSO) Member Centers Group. "Extracorporeal Life Support Organization Registry International Report 2022: 100,000 Survivors". In: *ASAIO Journal* 70.2 (Feb. 2024), p. 131. ISSN: 1058-2916. DOI: 10.1097/MAT.0000000000002128.
https://journals.lww.com/asaiojournal/fulltext/2024/02000/extracorporeal_life_support_organization_registry.9.aspx#ej-article-sam-container (visited on 03/15/2024).

[20] K. Lehle, A. Philipp, M. Foltan, F. Schettler, M. Ritzka, T. Müller, and M. Lubnow. "Coagulation Abnormalities in Patients with COVID-19 on Venovenous ECLS Increased Risk for Technical Complications and Support Times but Had No Impact on Survival". In: *Artificial Organs* 46.8 (Aug. 2022), pp. 1669–1681. ISSN: 0160-564X, 1525-1594. DOI: 10.1111/aor.14218.
https://onlinelibrary.wiley.com/doi/10.1111/aor.14218 (visited on 12/14/2023).

[21] A. Dorken-Gallastegi, Y. Lee, G. Li, H. Li, L. Naar, X. Li, T. Ye, E. Van Cott, R. Rosovsky, D. Gregory, R. Tompkins, G. Karniadakis, H. M. Kaafarani, G. C. Velmahos, J. Lee, and G. H. Frydman. "Circulating Cellular Clusters Are Associated with Thrombotic Complications and Clinical Outcomes in COVID-19". In: *iScience* 26.7 (July 2023), p. 107202. ISSN: 25890042. DOI: 10.1016/j.isci.2023.107202.
https://linkinghub.elsevier.com/retrieve/pii/S2589004223012798 (visited on 12/14/2023).

[22] J. Helms, C. Tacquard, F. Severac, I. Leonard-Lorant, M. Ohana, X. Delabranche, H. Merdji, R. Clere-Jehl, M. Schenck, F. Fagot Gandet, S. Fafi-Kremer, V. Castelain, F. Schneider, L. Grunebaum, E. Anglés-Cano, L. Sattler, P.-M. Mertes, F. Meziani, and CRICS TRIGGERSEP Group (Clinical Research in Intensive Care and Sepsis Trial Group for Global Evaluation and Research in Sepsis). "High Risk of Thrombosis in Patients with Severe SARS-CoV-2 Infection: A Multicenter Prospective Cohort Study". In: *Intensive Care Med* 46.6 (June 2020),

pp. 1089–1098. ISSN: 0342-4642, 1432-1238. DOI: 10.1007/s00134-020-06062-x. https://link.springer.com/10.1007/s00134-020-06062-x (visited on 03/28/2025).

[23] M. Kranz, D. Pointner, M. S. Wagner, M. Lubnow, K. Lehle, and L. Krenkel. "High-Resolution Flow Investigations in Membrane Lungs for Understanding Shear-Induced Blood Clot Formation". In: *New Results in Numerical and Experimental Fluid Mechanics XV*. Ed. by A. Dillmann, G. Heller, E. Krämer, C. Breitsamter, C. Wagner, and L. Krenkel. Vol. 156. Notes on Numerical Fluid Dynamics and Multidisciplinary Desing. Regensburg: Springer Nature Switzerland, 2026, pp. 1–10. ISBN: 978-3-032-11114-2. DOI: 10.1007/978-3-032-11115-9_12.

[24] H.-H. Chang, Y.-C. Chen, C.-J. Huang, C.-C. Kuo, Y.-M. Wang, and C.-W. Sun. "Optimization of Extracorporeal Membrane Oxygenation Therapy Using Near-infrared Spectroscopy to Assess Changes in Peripheral Circulation: A Pilot Study". In: *Journal of Biophotonics* 13.10 (Oct. 2020), e202000116. ISSN: 1864-063X, 1864-0648. DOI: 10.1002/jbio.202000116. https://onlinelibrary.wiley.com/doi/10.1002/jbio.202000116 (visited on 03/24/2025).

[25] M. Foltan, D. Dinh, M. Gruber, T. Müller, C. Hart, L. Krenkel, C. Schmid, and K. Lehle. "Incidence of Neutrophil Extracellular Traps (NETs) in Different Membrane Oxygenators: Pilot in Vitro Experiments in Commercially Available Coated Membranes". In: *J Artif Organs* (Jan. 8, 2025). ISSN: 1619-0904. DOI: 10.1007/s10047-024-01486-4. https://doi.org/10.1007/s10047-024-01486-4 (visited on 07/01/2025).

[26] Maquet. *Extracorporeal Life Support PLS System Data Sheet MCP_BR_10066_EN_1*. Mar. 2015.

[27] Xenios. *ECLS Treatment Options with Xenios*. Xenios AG. https://www.xenios-ag.com/therapeutic-application/ecls/ (visited on 07/04/2025).

[28] Medtronic. *Nautilus™ ECMO Oxygenator with Balance™ Biosurface | Medtronic*. https://www.medtronic.com/en-ie/healthcare-professionals/products/cardiovascular/extracorporeal-membrane-oxygenation/nautilus-ecmo-oxygenator-balance-biosurface.html (visited on 07/04/2025).

[29] LivaNova. *EOS ECMO | LivaNova Europe*. https://www.livanova.com/cardiopulmonary/en-gb/oxygenators/eos-ecmo (visited on 07/04/2025).

[30] U. Boeken, A. Assmann, S. Klotz, F. Born, A. Rieth, and C. Schmid, eds. *Mechanische Unterstützung im akuten Kreislaufversagen [Mechanical Support in Acute*

*Circulatory Failure]*. Berlin, Heidelberg: Springer Berlin Heidelberg, 2020. ISBN: 978-3-662-59900-6. DOI: 10.1007/978-3-662-59901-3.
http://link.springer.com/10.1007/978-3-662-59901-3 (visited on 07/08/2024).

[31] M. S. Wagner, M. Kranz, L. Krenkel, D. Pointner, M. Foltan, M. Lubnow, and K. Lehle. "Computer Based Visualization of Clot Structures in Extracorporeal Membrane Oxygenation and Histological Clot Investigations for Understanding Thrombosis in Membrane Lungs". In: *Front. Med.* 11 (June 19, 2024). ISSN: 2296-858X. DOI: 10.3389/fmed.2024.1416319.
https://www.frontiersin.org/articles/10.3389/fmed.2024.1416319 (visited on 06/19/2024).

[32] H. Appelt, A. Philipp, T. Mueller, M. Foltan, M. Lubnow, D. Lunz, F. Zeman, and K. Lehle. "Factors Associated with Hemolysis during Extracorporeal Membrane Oxygenation (ECMO)—Comparison of VA- versus VV ECMO". In: *PLoS ONE* 15.1 (Jan. 27, 2020). Ed. by A. Ballotta, e0227793. ISSN: 1932-6203. DOI: 10.1371/journal.pone.0227793.
https://dx.plos.org/10.1371/journal.pone.0227793 (visited on 06/09/2023).

[33] E. Wintermantel and S.-W. Ha. *Medizintechnik Life Science Engineering: Interdisziplinarität · Biokompatibilität · Technologien · Implantate · Diagnostik · Werkstoffe · Business [Medical Technology Life Science Engineering: Interdisciplinarity · Biocompatibility · Technologies · Implants · Diagnostics · Materials · Business]*. Berlin, Heidelberg: Springer Berlin Heidelberg, 2008. ISBN: 978-3-540-74924-0. DOI: 10.1007/978-3-540-74925-7.
http://link.springer.com/10.1007/978-3-540-74925-7 (visited on 02/20/2024).

[34] N. Herring and D. J. Paterson. *Levick's Introduction to Cardiovascular Physiology, Sixth Edition*. 6th ed. Boca Raton: CRC Press, Apr. 17, 2018. 448 pp. ISBN: 978-1-351-10775-4. DOI: 10.1201/9781351107754.
https://www.taylorfrancis.com/books/9781351107754 (visited on 03/20/2025).

[35] D. A. Fedosov, W. Pan, B. Caswell, G. Gompper, and G. E. Karniadakis. "Predicting Human Blood Viscosity in Silico". In: *Proc. Natl. Acad. Sci. U.S.A.* 108.29 (July 19, 2011), pp. 11772–11777. ISSN: 0027-8424, 1091-6490. DOI: 10.1073/pnas.1101210108.
https://pnas.org/doi/full/10.1073/pnas.1101210108 (visited on 09/04/2023).

[36] R. E. Klabunde. *Cardiovascular Physiology Concepts*. Philadelphia : Lippincott Williams & Wilkins, 2005. 254 pp. ISBN: 978-0-7817-5030-1.
http://archive.org/details/cardiovascularph0000klab (visited on 11/05/2024).

[37] R. Brandes, F. Lang, and R. F. Schmidt, eds. *Physiologie des Menschen: mit Pathophysiologie [Human Physiology: with Pathophysiology]*. Springer-Lehrbuch. Berlin, Heidelberg: Springer Berlin Heidelberg, 2019. ISBN: 978-3-662-56467-7. DOI: 10.1007/978-3-662-56468-4.
http://link.springer.com/10.1007/978-3-662-56468-4 (visited on 02/26/2024).

[38] R. Fåhræus and T. Lindqvist. "The Viscosity of the Blood in Narrow Capillary Tubes". In: *American Journal of Physiology-Legacy Content* 96.3 (Mar. 1, 1931), pp. 562–568. ISSN: 0002-9513. DOI: 10.1152/ajplegacy.1931.96.3.562.
https://www.physiology.org/doi/10.1152/ajplegacy.1931.96.3.562 (visited on 07/02/2023).

[39] R. J. Roselli and K. R. Diller. *Biotransport: Principles and Applications*. New York, NY: Springer New York, 2011. ISBN: 978-1-4419-8118-9. DOI: 10.1007/978-1-4419-8119-6.
http://link.springer.com/10.1007/978-1-4419-8119-6 (visited on 06/03/2025).

[40] C. Birkenmaier. "A Hybrid Computational Approach for Non-Newtonian Blood Flows Using Euler-Euler Modelling and Deep Regression". Regensburg: University Regensburg, 2020.

[41] T. A. Springer. "Von Willebrand Factor, Jedi Knight of the Bloodstream". In: *Blood* 124.9 (Aug. 28, 2014), pp. 1412–1425. ISSN: 0006-4971, 1528-0020. DOI: 10.1182/blood-2014-05-378638.
https://ashpublications.org/blood/article/124/9/1412/73072/von-Willebrand-factor-Jedi-knight-of-the (visited on 12/12/2023).

[42] M. Hayakawa, K. Takano, M. Kayashima, K. Kasahara, H. Fukushima, and M. Matsumoto. "Management of a COVID-19 Patient during ECMO: Paying Attention to Acquired von Willebrand Syndrome". In: *JAT* 28.4 (Apr. 1, 2021), pp. 396–401. ISSN: 1340-3478, 1880-3873. DOI: 10.5551/jat.58362.
https://www.jstage.jst.go.jp/article/jat/28/4/28_58362/_article (visited on 06/09/2023).

[43] C. Valladolid, A. Yee, and M. A. Cruz. "Von Willebrand Factor, Free Hemoglobin and Thrombosis in ECMO". In: *Front. Med.* 5 (Aug. 17, 2018), p. 228. ISSN: 2296-858X. DOI: 10.3389/fmed.2018.00228.

https://www.frontiersin.org/article/10.3389/fmed.2018.00228/full (visited on 07/08/2024).

[44] T. Tamura, H. Horiuchi, Y. Obayashi, M. Fuki, M. Imanaka, M. Kuroda, S. Nishimura, M. Amano, J. Sakamoto, Y. Tamaki, S. Enomoto, M. Miyake, H. Kondo, C. Izumi, and Y. Nakagawa. "Acquired von Willebrand Syndrome in Patients Treated with Veno-Arterial Extracorporeal Membrane Oxygenation". In: *Cardiovasc Interv and Ther* 34.4 (Oct. 2019), pp. 358–363. ISSN: 1868-4300, 1868-4297. DOI: 10.1007/s12928-019-00568-y.
http://link.springer.com/10.1007/s12928-019-00568-y (visited on 07/08/2024).

[45] H. Tauber, H. Ott, W. Streif, G. Weigel, L. Loacker, J. Fritz, A. Heinz, and C. Velik-Salchner. "Extracorporeal Membrane Oxygenation Induces Short-Term Loss of High-Molecular-Weight von Willebrand Factor Multimers". In: *Anesthesia & Analgesia* 120.4 (Apr. 2015), pp. 730–736. ISSN: 0003-2999. DOI: 10.1213/ANE.0000000000000554.
https://journals.lww.com/00000539-201504000-00011 (visited on 06/09/2023).

[46] A. Schlagenhauf, J. Kalbhenn, U. Geisen, F. Beyersdorf, and B. Zieger. "Acquired von Willebrand Syndrome and Platelet Function Defects during Extracorporeal Life Support (Mechanical Circulatory Support)". In: *Hamostaseologie* 40.02 (May 2020), pp. 221–225. ISSN: 0720-9355, 2567-5761. DOI: 10.1055/a-1150-2016.
http://www.thieme-connect.de/DOI/DOI?10.1055/a-1150-2016 (visited on 06/09/2023).

[47] B. Samuelson Bannow, M. Recht, C. Négrier, C. Hermans, E. Berntorp, H. Eichler, M. E. Mancuso, R. Klamroth, J. O'Hara, E. Santagostino, T. Matsushita, and C. Kessler. "Factor VIII: Long-established Role in Haemophilia A and Emerging Evidence beyond Haemostasis". In: *Blood Reviews* 35 (May 2019), pp. 43–50. ISSN: 0268960X. DOI: 10.1016/j.blre.2019.03.002.
https://linkinghub.elsevier.com/retrieve/pii/S0268960X18301292 (visited on 05/13/2025).

[48] J.-f. Dong, J. L. Moake, L. Nolasco, A. Bernardo, W. Arceneaux, C. N. Shrimpton, A. J. Schade, L. V. McIntire, K. Fujikawa, and J. A. López. "ADAMTS-13 Rapidly Cleaves Newly Secreted Ultralarge von Willebrand Factor Multimers on the Endothelial Surface under Flowing Conditions". In: *Blood* 100.12 (Dec. 1, 2002), pp. 4033–4039. ISSN: 1528-0020, 0006-4971. DOI: 10.1182/blood-2002-05-1401.
https://ashpublications.org/blood/article/100/12/4033/88314/ADAMTS13-rapidly-cleaves-newly-secreted-ultralarge (visited on 06/15/2025).

[49] C. Aponte-Santamaría, V. Huck, S. Posch, A. K. Bronowska, S. Grässle, M. A. Brehm, T. Obser, R. Schneppenheim, P. Hinterdorfer, S. W. Schneider, C. Baldauf, and F. Gräter. "Force-Sensitive Autoinhibition of the von Willebrand Factor Is Mediated by Interdomain Interactions". In: *Biophysical Journal* 108.9 (May 2015), pp. 2312–2321. ISSN: 00063495. DOI: 10.1016/j.bpj.2015.03.041.
https://linkinghub.elsevier.com/retrieve/pii/S0006349515003021 (visited on 07/08/2024).

[50] E. Di Stasio and R. De Cristofaro. "The Effect of Shear Stress on Protein Conformation". In: *Biophysical Chemistry* 153.1 (Dec. 2010), pp. 1–8. ISSN: 03014622. DOI: 10.1016/j.bpc.2010.07.002.
https://linkinghub.elsevier.com/retrieve/pii/S0301462210001900 (visited on 12/20/2023).

[51] S. Pasala, R. T. Fiser, K. C. Stine, C. J. Swearingen, and P. Prodhan. "Von Willebrand Factor Multimers in Pediatric Extracorporeal Membrane Oxygenation Support". In: *ASAIO Journal* 60.4 (July 2014), pp. 419–423. ISSN: 1058-2916. DOI: 10.1097/MAT.0000000000000084.
https://journals.lww.com/00002480-201407000-00011 (visited on 07/08/2024).

[52] G. Rosenberg, C. A. Siedlecki, C.-S. Jhun, W. J. Weiss, K. Manning, S. Deutsch, and W. Pierce. "Acquired Von Willebrand Syndrome and Blood Pump Design". In: *Artificial Organs* 42.12 (Dec. 2018), pp. 1119–1124. ISSN: 0160-564X, 1525-1594. DOI: 10.1111/aor.13291.
https://onlinelibrary.wiley.com/doi/10.1111/aor.13291 (visited on 07/08/2024).

[53] B. A. Herbig, X. Yu, and S. L. Diamond. "Using Microfluidic Devices to Study Thrombosis in Pathological Blood Flows". In: *Biomicrofluidics* 12.4 (July 1, 2018), p. 042201. ISSN: 1932-1058. DOI: 10.1063/1.5021769.
https://pubs.aip.org/bmf/article/12/4/042201/1059778/Using-microfluidic-devices-to-study-thrombosis-in (visited on 12/14/2023).

[54] T. Steiger, M. Foltan, A. Philipp, T. Mueller, M. Gruber, A. Bredthauer, L. Krenkel, C. Birkenmaier, and K. Lehle. "Accumulations of von Willebrand Factor within ECMO Oxygenators: Potential Indicator of Coagulation Abnormalities in Critically Ill Patients?" In: *Artif Organs* 43.11 (Nov. 2019), pp. 1065–1076. ISSN: 0160-564X, 1525-1594. DOI: 10.1111/aor.13513.
https://onlinelibrary.wiley.com/doi/10.1111/aor.13513 (visited on 06/09/2023).

[55] C. Dornia, A. Philipp, S. Bauer, P. Hoffstetter, K. Lehle, C. Schmid, M. Lubnow, C. Stroszczynski, and A. G. Schreyer. "Visualization of Thrombotic Deposits in Extracorporeal Membrane Oxygenation Devices Using Multidetector Computed Tomography: A Feasibility Study". In: *ASAIO Journal* 59.4 (July 2013), pp. 439–441. ISSN: 1058-2916. DOI: 10.1097/MAT.0b013e3182976eff.
https://journals.lww.com/00002480-201307000-00015 (visited on 06/09/2023).

[56] M. Panigada, C. L'Acqua, S. M. Passamonti, C. Mietto, A. Protti, R. Riva, and L. Gattinoni. "Comparison between Clinical Indicators of Transmembrane Oxygenator Thrombosis and Multidetector Computed Tomographic Analysis". In: *Journal of Critical Care* 30.2 (Apr. 2015), 441.e7–441.e13. ISSN: 08839441. DOI: 10.1016/j.jcrc.2014.12.005.
https://linkinghub.elsevier.com/retrieve/pii/S088394411400495X (visited on 09/04/2023).

[57] C. Birkenmaier, C. Dornia, K. Lehle, T. Müller, M. Gruber, A. Philipp, and L. Krenkel. "Analysis of Thrombotic Deposits in Extracorporeal Membrane Oxygenators by High-resolution Microcomputed Tomography: A Feasibility Study". In: *ASAIO Journal* 66.8 (Aug. 2020), pp. 922–928. ISSN: 1058-2916. DOI: 10.1097/MAT.0000000000001089.
https://journals.lww.com/10.1097/MAT.0000000000001089 (visited on 12/14/2023).

[58] S. Callaghan, T. Cai, C. McCafferty, S. Van Den Helm, S. Horton, G. MacLaren, P. Monagle, and V. Ignjatovic. "Adsorption of Blood Components to Extracorporeal Membrane Oxygenation (ECMO) Surfaces in Humans: A Systematic Review". In: *JCM* 9.10 (Oct. 12, 2020), p. 3272. ISSN: 2077-0383. DOI: 10.3390/jcm9103272.
https://www.mdpi.com/2077-0383/9/10/3272 (visited on 12/14/2023).

[59] K. Lehle, A. Philipp, O. Gleich, A. Holzamer, T. Müller, T. Bein, and C. Schmid. "Efficiency in Extracorporeal Membrane Oxygenation—Cellular Deposits on Polymethypentene Membranes Increase Resistance to Blood Flow and Reduce Gas Exchange Capacity". In: *ASAIO Journal* 54.6 (Nov. 2008), pp. 612–617. ISSN: 1058-2916. DOI: 10.1097/MAT.0b013e318186a807.
https://journals.lww.com/00002480-200811000-00010 (visited on 06/09/2023).

[60] K. Lehle, L. Friedl, J. Wilm, A. Philipp, T. Müller, M. Lubnow, and C. Schmid. "Accumulation of Multipotent Progenitor Cells on Polymethylpentene Membranes During Extracorporeal Membrane Oxygenation: Immunophenotyping

of Progenitor Cells after ECMO Therapy". In: *Artificial Organs* 40.6 (June 2016), pp. 577–585. ISSN: 0160564X. DOI: 10.1111/aor.12599. https://onlinelibrary.wiley.com/doi/10.1111/aor.12599 (visited on 06/09/2023).

[61] J. Wilm, A. Philipp, T. Müller, A. Bredthauer, O. Gleich, C. Schmid, and K. Lehle. "Leukocyte Adhesion as an Indicator of Oxygenator Thrombosis During Extracorporeal Membrane Oxygenation Therapy?" In: *ASAIO Journal* 64.1 (Jan. 2018), pp. 24–30. ISSN: 1058-2916. DOI: 10.1097/MAT.0000000000000586. https://journals.lww.com/00002480-201801000-00004 (visited on 06/09/2023).

[62] I. Dropco, A. Philipp, M. Foltan, D. Lunz, M. Lubnow, and K. Lehle. "Extended Cellular Deposits on Gas Exchange Capillaries Are Not an Indicator of Clot Formation: Analysis of Different Membrane Oxygenators". In: *ASAIO Journal* 69.4 (Apr. 2023), e134–e141. ISSN: 1058-2916. DOI: 10.1097/MAT.0000000000001892. https://journals.lww.com/10.1097/MAT.0000000000001892 (visited on 12/12/2023).

[63] X. Fu, Z. Su, Y. Wang, A. Sun, L. Wang, X. Deng, Z. Chen, and Y. Fan. "Comparison of Hemodynamic Features and Thrombosis Risk of Membrane Oxygenators with Different Structures: A Numerical Study". In: *Computers in Biology and Medicine* 159 (June 2023), p. 106907. ISSN: 00104825. DOI: 10.1016/j.compbiomed.2023.106907. https://linkinghub.elsevier.com/retrieve/pii/S0010482523003724 (visited on 09/08/2023).

[64] M. Hormes, R. Borchardt, I. Mager, T. Schmitz-Rode, M. Behr, and U. Steinseifer. "A Validated Cfd Model to Predict O $_2$ and Co $_2$ Transfer Within Hollow Fiber Membrane Oxygenators". In: *Int J Artif Organs* 34.3 (Mar. 2011), pp. 317–325. ISSN: 0391-3988, 1724-6040. DOI: 10.5301/IJAO.2011.6494. http://journals.sagepub.com/doi/10.5301/IJAO.2011.6494 (visited on 09/04/2023).

[65] B. Lukitsch, R. Koller, P. Ecker, M. Elenkov, C. Janeczek, M. Pekovits, B. Haddadi, C. Jordan, M. Gfoehler, and M. Harasek. "Water as a Blood Model for Determination of CO2 Removal Performance of Membrane Oxygenators". In: *Membranes* 11.5 (May 12, 2021), p. 356. ISSN: 2077-0375. DOI: 10.3390/membranes11050356. https://www.mdpi.com/2077-0375/11/5/356 (visited on 09/04/2023).

[66] G. Fragomeni, M. V. Caruso, and M. Rossi. "Flow Analysis in VA ECMO Support: A CFD Study". In: *2020 IEEE International Conference on Bioinformatics and Biomedicine (BIBM)*. 2020 IEEE International Conference on Bioinformatics

and Biomedicine (BIBM). Seoul, Korea (South): IEEE, Dec. 16, 2020, pp. 1440–1441. ISBN: 978-1-7281-6215-7. DOI: 10.1109/BIBM49941.2020.9313370. https://ieeexplore.ieee.org/document/9313370/ (visited on 09/04/2023).

[67] D. Dipresa, P. Kalozoumis, M. Pflaum, A. Peredo, B. Wiegmann, A. Haverich, and S. Korossis. "Hemodynamic Assessment of Hollow-Fiber Membrane Oxygenators Using Computational Fluid Dynamics in Heterogeneous Membrane Models". In: *Journal of Biomechanical Engineering* 143.5 (May 1, 2021), p. 051010. ISSN: 0148-0731, 1528-8951. DOI: 10.1115/1.4049808. https://asmedigitalcollection.asme.org/biomechanical/article/doi/10.1115/1.4049808/1096598/Hemodynamic-Assessment-of-Hollow-Fiber-Membrane (visited on 09/11/2023).

[68] K. L. Gage, M. J. Gartner, G. W. Burgreen, and W. R. Wagner. "Predicting Membrane Oxygenator Pressure Drop Using Computational Fluid Dynamics". In: *Artificial Organs* 26.7 (July 2002), pp. 600–607. ISSN: 0160-564X, 1525-1594. DOI: 10.1046/j.1525-1594.2002.07082.x. http://doi.wiley.com/10.1046/j.1525-1594.2002.07082.x (visited on 09/04/2023).

[69] F. R. Nezami, F. Khodaee, E. R. Edelman, and S. P. Keller. "A Computational Fluid Dynamics Study of the Extracorporeal Membrane Oxygenation-Failing Heart Circulation". In: *ASAIO Journal* 67.3 (Mar. 2021), pp. 276–283. ISSN: 1058-2916. DOI: 10.1097/MAT.0000000000001221. https://journals.lww.com/10.1097/MAT.0000000000001221 (visited on 09/08/2023).

[70] J. Zhang, T. D. Nolan, T. Zhang, B. P. Griffith, and Z. J. Wu. "Characterization of Membrane Blood Oxygenation Devices Using Computational Fluid Dynamics". In: *Journal of Membrane Science* 288.1–2 (Feb. 2007), pp. 268–279. ISSN: 03767388. DOI: 10.1016/j.memsci.2006.11.041. https://linkinghub.elsevier.com/retrieve/pii/S0376738806007654 (visited on 05/09/2023).

[71] N. Cancilla, L. Gurreri, G. Marotta, M. Ciofalo, A. Cipollina, A. Tamburini, and G. Micale. "Performance Comparison of Alternative Hollow-Fiber Modules for Hemodialysis by Means of a CFD-Based Model". In: *Membranes* 12.2 (Jan. 20, 2022), p. 118. ISSN: 2077-0375. DOI: 10.3390/membranes12020118. https://www.mdpi.com/2077-0375/12/2/118 (visited on 09/04/2023).

[72] R. Graefe, R. Borchardt, J. Arens, P. Schlanstein, T. Schmitz-Rode, and U. Steinseifer. "Improving Oxygenator Performance Using Computational Simulation

and Flow Field-Based Parameters: IMPROVING OXYGENATOR PERFORMANCE USING CFD AND PARAMETERIZATION". In: *Artificial Organs* 34.11 (Nov. 2010), pp. 930–936. ISSN: 0160564X. DOI: 10.1111/j.1525-1594.2010.01157.x.
https://onlinelibrary.wiley.com/doi/10.1111/j.1525-1594.2010.01157.x (visited on 05/09/2023).

[73] K. Gu, Y. Zhang, B. Gao, Y. Chang, and Y. Zeng. "Hemodynamic Differences Between Central ECMO and Peripheral ECMO: A Primary CFD Study". In: *Med Sci Monit* 22 (Mar. 3, 2016), pp. 717–726. ISSN: 1643-3750. DOI: 10.12659/MSM.895831.
http://www.medscimonit.com/abstract/index/idArt/895831 (visited on 09/04/2023).

[74] M. Harasek, L. Benjamin, E. Paul, J. Christoph, E. Martin, K. Thomas, H. Bahram, J. Christian, N. Susanna, K. Claus, U. Roman, and G. Margit. "Fully Resolved Computational (CFD) and Experimental Analysis of Pressure Drop and Blood Gas Transport in a Hollow Fibre Membrane Oxygenator Module". In: *Chemical Engineering Transactions* 76 (Oct. 2019), pp. 193–198. DOI: 10.3303/CET1976033.
https://doi.org/10.3303/CET1976033 (visited on 09/04/2023).

[75] D. Han, J. L. Leibowitz, L. Han, S. Wang, G. He, B. P. Griffith, and Z. J. Wu. "Computational Fluid Dynamics Analysis and Experimental Hemolytic Performance of Three Clinical Centrifugal Blood Pumps: Revolution, Rotaflow and CentriMag". In: *Medicine in Novel Technology and Devices* 15 (Sept. 2022), p. 100153. ISSN: 25900935. DOI: 10.1016/j.medntd.2022.100153.
https://linkinghub.elsevier.com/retrieve/pii/S2590093522000406 (visited on 09/08/2023).

[76] F. Fiusco. *Hemodynamics of Artificial Devices Used in Extracorporeal Life Support*. Stockholm: KTH Royal Institute of Technology, 2021. ISBN: 978-91-7873-982-0.

[77] N. Berg, L. Fuchs, and L. Prahl Wittberg. "Flow Characteristics and Coherent Structures in a Centrifugal Blood Pump". In: *Flow Turbulence Combust* 102.2 (Feb. 2019), pp. 469–483. ISSN: 1386-6184, 1573-1987. DOI: 10.1007/s10494-018-9994-3.
http://link.springer.com/10.1007/s10494-018-9994-3 (visited on 07/08/2024).

[78] G. Fuchs, N. Berg, L. M. Broman, and L. Prahl Wittberg. "Flow-Induced Platelet Activation in Components of the Extracorporeal Membrane Oxygenation Circuit". In: *Sci Rep* 8.1 (Sept. 18, 2018), p. 13985. ISSN: 2045-2322. DOI: 10.1038/

s41598-018-32247-y.
https://www.nature.com/articles/s41598-018-32247-y (visited on 07/08/2024).

[79] G. He, J. Zhang, A. Shah, Z. B. Berk, L. Han, H. Dong, B. P. Griffith, and Z. J. Wu. "Flow Characteristics and Hemolytic Performance of the New Breethe Centrifugal Blood Pump in Comparison with the CentriMag and Rotaflow Pumps". In: *Int J Artif Organs* 44.11 (Nov. 1, 2021), pp. 829–837. ISSN: 0391-3988. DOI: 10.1177/03913988211041635.
https://doi.org/10.1177/03913988211041635 (visited on 02/18/2024).

[80] C. Birkenmaier, T. Steiger, A. Philipp, K. Lehle, and L. Krenkel. "Flow-Induced Accumulations of Von Willebrand Factor Inside Oxygenators During Extracorporeal Life Support Therapy". In: *2018 International Conference BIOMDLORE*. 2018 International Conference BIOMDLORE. June 2018, pp. 1–3. DOI: 10.1109/BIOMDLORE.2018.8467205.

[81] M. V. Caruso, A. Renzulli, and G. Fragomeni. "Influence of IABP-Induced Abdominal Occlusions on Aortic Hemodynamics: A Patient-Specific Computational Evaluation". In: *ASAIO J* 63.2 (2017), pp. 161–167. ISSN: 1538-943X. DOI: 10.1097/MAT.0000000000000479. PMID: 27861423.

[82] H. Liu, L. Lan, J. Abrigo, H. L. Ip, Y. Soo, D. Zheng, K. S. Wong, D. Wang, L. Shi, T. W. Leung, and X. Leng. "Comparison of Newtonian and Non-newtonian Fluid Models in Blood Flow Simulation in Patients With Intracranial Arterial Stenosis". In: *Front. Physiol.* 12 (Sept. 6, 2021). ISSN: 1664-042X. DOI: 10.3389/fphys.2021.718540.
https://www.frontiersin.org/journals/physiology/articles/10.3389/fphys.2021.718540/full (visited on 09/26/2024).

[83] C. Birkenmaier and L. Krenkel. "Convolutional Neural Networks for Approximation of Blood Flow in Artificial Lungs". In: *New Results in Numerical and Experimental Fluid Mechanics XIII*. Ed. by A. Dillmann, G. Heller, E. Krämer, and C. Wagner. Vol. 151. Cham: Springer International Publishing, 2021, pp. 451–460. ISBN: 978-3-030-79560-3. DOI: 10.1007/978-3-030-79561-0_43.
https://link.springer.com/10.1007/978-3-030-79561-0_43 (visited on 03/09/2024).

[84] J. I. Nunez, A. F. Gosling, B. O'Gara, K. F. Kennedy, P. Rycus, D. Abrams, D. Brodie, S. Shaefi, A. R. Garan, and E. W. Grandin. "Bleeding and Thrombotic Events in Adults Supported with Venovenous Extracorporeal Membrane Oxygenation: An ELSO Registry Analysis". In: *Intensive Care Med* 48.2 (Feb. 2022),

pp. 213–224. ISSN: 0342-4642, 1432-1238. DOI: 10.1007/s00134-021-06593-x. https://link.springer.com/10.1007/s00134-021-06593-x (visited on 05/19/2025).

[85] S. Baumgartner, M. Lubnow, M. V. Malfertheiner, A. Philipp, M. Foltan, D. Lunz, T. Müller, and C. Fisser. "Major Bleeding and Thromboembolic Events in Veno-Venous Extracorporeal Membrane Oxygenation-Patients With Isolated Respiratory Failure". In: *ASAIO Journal* 68.12 (Dec. 2022), pp. 1529–1535. ISSN: 1058-2916. DOI: 10.1097/MAT.0000000000001698. https://journals.lww.com/10.1097/MAT.0000000000001698 (visited on 05/19/2025).

[86] J. Thomas, V. Kostousov, and J. Teruya. "Bleeding and Thrombotic Complications in the Use of Extracorporeal Membrane Oxygenation". In: *Semin Thromb Hemost* 44.01 (Feb. 2018), pp. 020–029. ISSN: 0094-6176, 1098-9064. DOI: 10.1055/s-0037-1606179. http://www.thieme-connect.de/DOI/DOI?10.1055/s-0037-1606179 (visited on 05/19/2025).

[87] C. Wiest, T. Müller, M. Lubnow, C. Fisser, A. Philipp, M. Foltan, R. Schneckenpointner, and M. V. Malfertheiner. "Intracranial Hemorrhage in a Large Cohort of Patients Supported with Veno-Venous ECMO. A Retrospective Single-Center Analysis". In: *Perfusion* 39.8 (Nov. 2024), pp. 1667–1675. ISSN: 0267-6591, 1477-111X. DOI: 10.1177/02676591231213514. https://journals.sagepub.com/doi/10.1177/02676591231213514 (visited on 05/19/2025).

[88] M. Kranz, M. S. Wagner, L. Krenkel, T. Müller, M. Lubnow, A. Philipp, K. Lehle, and ECMO Research Group Regensburg. "Clot Localization within Membrane Lungs Using Different Imaging Methods and Histological Clot Characterization as a Way to Prevent Thrombosis in Extracorporeal Membrane Oxygenation". In: *Perfusion* 38 (1_suppl May 2023), p. 160. ISSN: 0267-6591, 1477-111X. DOI: 10.1177/02676591231162023. https://journals.sagepub.com/doi/10.1177/02676591231162023 (visited on 01/07/2025).

[89] A. Kaesler, F. Hesselmann, M. O. Zander, P. C. Schlanstein, G. Wagner, P. Bruners, T. Schmitz-Rode, U. Steinseifer, and J. Arens. "Technical Indicators to Evaluate the Degree of Large Clot Formation Inside the Membrane Fiber Bundle of an Oxygenator in an In Vitro Setup". In: *Artificial Organs* 43.2 (Feb. 2019), pp. 159–166. ISSN: 0160-564X, 1525-1594. DOI: 10.1111/aor.13343. https://onlinelibrary.wiley.com/doi/10.1111/aor.13343 (visited on 01/19/2024).

[90] M. Kranz, M. S. Wagner, D. Pointner, M. Haus, M. Lubnow, K. Lehle, and L. Krenkel. "Polymer Embedding of Membrane Lungs for Histological Investigations of Intra-Device Clot Formation". In: *Front. Cardiovasc. Med.* 13 (Feb. 4, 2026). ISSN: 2297-055X. DOI: 10.3389/fcvm.2026.1650978.
https://www.frontiersin.org/journals/cardiovascular-medicine/articles/10.3389/fcvm.2026.1650978/full (visited on 02/04/2026).

[91] M. Kranz, M. S. Wagner, D. Pointner, S. Waldbauer, T. Müller, M. Lubnow, M. Foltan, L. Krenkel, and K. Lehle. "Polymeric Embedding of Membrane Lungs: A Novel Method for Histological Investigations of Intra-Device Clot Formation". In: *Perfusion* 39 (1_suppl Apr. 2024), p. 140. ISSN: 0267-6591, 1477-111X. DOI: 10.1177/02676591241239138.
https://journals.sagepub.com/doi/10.1177/02676591241239138 (visited on 01/07/2025).

[92] S. Rousselle and J. Wicks. "Preparation of Medical Devices for Evaluation". In: *Toxicol Pathol* 36.1 (Jan. 2008), pp. 81–84. ISSN: 0192-6233, 1533-1601. DOI: 10.1177/0192623307310962.
http://journals.sagepub.com/doi/10.1177/0192623307310962 (visited on 12/12/2023).

[93] N. Malik, J. Gunn, C. M. Holt, L. Shepherd, S. E. Francis, C. M. H. Newman, D. C. Crossman, and D. C. Cumberland. "Intravascular Stents: A New Technique for Tissue Processing for Histology, Immunohistochemistry, and Transmission Electron Microscopy". In: *Heart* 80.5 (Nov. 1, 1998), pp. 509–516. ISSN: 1355-6037. DOI: 10.1136/hrt.80.5.509.
https://heart.bmj.com/lookup/doi/10.1136/hrt.80.5.509 (visited on 12/12/2023).

[94] H. W. De Jonge, M. A. De Bakker, F. J. Verbeek, and W. A. Weijs. "Embedding of Large Specimens in Glycol Methacrylate: Prerequisites for Multi-signal Detection and High-resolution Imaging". In: *Microscopy Res & Technique* 66.1 (Jan. 2005), pp. 25–30. ISSN: 1059-910X, 1097-0029. DOI: 10.1002/jemt.20139.
https://analyticalsciencejournals.onlinelibrary.wiley.com/doi/10.1002/jemt.20139 (visited on 12/12/2023).

[95] T. L. Ponsioen, R. J. Van Der Worp, M. J. Van Luyn, J. M. Hooymans, and L. I. Los. "Packages of Vitreous Collagen (Type II) in the Human Retina: An Indication of Postnatal Collagen Turnover?" In: *Experimental Eye Research* 80.5 (May 2005), pp. 643–650. ISSN: 00144835. DOI: 10.1016/j.exer.2004.11.014.
https://linkinghub.elsevier.com/retrieve/pii/S001448350400346X (visited on 07/22/2024).

[96] T. V. Colace and S. L. Diamond. "Direct Observation of von Willebrand Factor Elongation and Fiber Formation on Collagen During Acute Whole Blood Exposure to Pathological Flow". In: *ATVB* 33.1 (Jan. 2013), pp. 105–113. ISSN: 1079-5642, 1524-4636. DOI: 10.1161/ATVBAHA.112.300522. https://www.ahajournals.org/doi/10.1161/ATVBAHA.112.300522 (visited on 09/04/2023).

[97] C. Wagner, A. Dillmann, G. Heller, and E. Krämer. *Proceedings of the 24th STAB-Symposium 2024 in Regensburg Und STAB-Jahresbericht 2024*. Oct. 2024. https://www.dlr.de/de/as/aktuelles/veranstaltungen/stab/2024/stab-jahresbericht_2024.pdf.

[98] M. O. Bernabeu, R. W. Nash, D. Groen, H. B. Carver, J. Hetherington, T. Krüger, and P. V. Coveney. "Impact of Blood Rheology on Wall Shear Stress in a Model of the Middle Cerebral Artery". In: *Interface Focus* 3.2 (Apr. 6, 2013), p. 20120094. ISSN: 2042-8898. DOI: 10.1098/rsfs.2012.0094. PMID: 24427534. https://www.ncbi.nlm.nih.gov/pmc/articles/PMC3638489/ (visited on 02/07/2025).

[99] X. Yu and S. Diamond. "Fibrin Modulates Shear-Induced NETosis in Sterile Occlusive Thrombi Formed under Haemodynamic Flow". In: *Thromb Haemost* 119.04 (Apr. 2019), pp. 586–593. ISSN: 0340-6245, 2567-689X. DOI: 10.1055/s-0039-1678529. http://www.thieme-connect.de/DOI/DOI?10.1055/s-0039-1678529 (visited on 04/08/2025).

[100] M. Haus, M. Foltan, A. Philipp, T. Mueller, M. Gruber, M. P. Lingel, L. Krenkel, and K. Lehle. "Neutrophil Extracellular Traps - a Potential Trigger for the Development of Thrombocytopenia during Extracorporeal Membrane Oxygenation". In: *Front. Immunol.* 15 (Feb. 21, 2024), p. 1339235. ISSN: 1664-3224. DOI: 10.3389/fimmu.2024.1339235. https://www.frontiersin.org/articles/10.3389/fimmu.2024.1339235/full (visited on 04/03/2024).

[101] N. Sultanova, S. Kasarova, and I. Nikolov. "Dispersion Properties of Optical Polymers". In: *Acta Phys. Pol. A* 116.4 (Oct. 2009), pp. 585–587. ISSN: 0587-4246, 1898-794X. DOI: 10.12693/APhysPolA.116.585. http://przyrbwn.icm.edu.pl/APP/PDF/116/a116z442.pdf (visited on 05/29/2025).

[102] S. M. Tauwald, F. Erzinger, M. Quadrio, M. Rütten, C. Stemmer, and L. Krenkel. "Tomo-PIV in a Patient-Specific Model of Human Nasal Cavities: A Methodological Approach". In: *Meas. Sci. Technol.* (Feb. 9, 2024). ISSN: 0957-0233, 1361-6501.

DOI: 10.1088/1361-6501/ad282c.
https://iopscience.iop.org/article/10.1088/1361-6501/ad282c (visited on 02/13/2024).

[103] C. Vlachopoulos, M. O'Rourke, and W. W. Nichols. *McDonald's Blood Flow in Arteries: Theoretical, Experimental and Clinical Principles*. 0th ed. CRC Press, July 29, 2011. ISBN: 978-0-429-16692-1. DOI: 10.1201/b13568.
https://www.taylorfrancis.com/books/9781444128789 (visited on 06/14/2025).

[104] C. Tropea, A. L. Yarin, and J. F. Foss, eds. *Springer Handbook of Experimental Fluid Mechanics*. Berlin, Heidelberg: Springer, 2007. ISBN: 978-3-540-25141-5. DOI: 10.1007/978-3-540-30299-5.
http://link.springer.com/10.1007/978-3-540-30299-5 (visited on 05/28/2025).

[105] A. Corbetta, V. Menkovski, R. Benzi, and F. Toschi. "Deep Learning Velocity Signals Allow Quantifying Turbulence Intensity". In: *Sci Adv* 7.12 (Mar. 17, 2021), eaba7281. ISSN: 2375-2548. DOI: 10.1126/sciadv.aba7281. PMID: 33731341.
https://www.ncbi.nlm.nih.gov/pmc/articles/PMC7968843/ (visited on 05/28/2025).

[106] A. Badheka, S. E. Stucker, J. W. Turek, and M. L. Raghavan. "Efficacy of Flow Monitoring during ECMO". In: *ASAIO J* 63.4 (2017), pp. 496–500. ISSN: 1058-2916. DOI: 10.1097/MAT.0000000000000538. PMID: 28169848.
https://www.ncbi.nlm.nih.gov/pmc/articles/PMC5736305/ (visited on 06/14/2025).

[107] L. Köster. "Histologische Aufarbeitung von Pumpenkopfthrombosen Nach Extrakorporaler Membranoxygenierung (ECMO) [Histologic Analysis of Pump Head Thrombosis after Extracorporeal Membrane Oxygenation (ECMO)]". Regensburg: University Regensburg, 2025.

[108] L. Köster, M. Kranz, M. S. Wagner, M. Foltan, T. Müller, M. Lubnow, L. Krenkel, and K. Lehle. "Histological Investigations of Intra-Device Clot Formation in ECMO Pumps". In: *Perfusion* 39 (1_suppl Apr. 2024), p. 105. ISSN: 0267-6591, 1477-111X. DOI: 10.1177/02676591241239138.
https://journals.sagepub.com/doi/10.1177/02676591241239138 (visited on 01/07/2025).

[109] V. Brinkmann, U. Reichard, C. Goosmann, B. Fauler, Y. Uhlemann, D. S. Weiss, Y. Weinrauch, and A. Zychlinsky. "Neutrophil Extracellular Traps Kill Bacteria". In: *Science* 303.5663 (Mar. 5, 2004), pp. 1532–1535. ISSN: 0036-8075, 1095-9203. DOI: 10.1126/science.1092385.
https://www.science.org/doi/10.1126/science.1092385 (visited on 05/07/2025).

[110] T. A. Fuchs, A. Brill, D. Duerschmied, D. Schatzberg, M. Monestier, D. D. Myers, S. K. Wrobleski, T. W. Wakefield, J. H. Hartwig, and D. D. Wagner. "Extracellular DNA Traps Promote Thrombosis". In: *Proc. Natl. Acad. Sci. U.S.A.* 107.36 (Sept. 7, 2010), pp. 15880–15885. ISSN: 0027-8424, 1091-6490. DOI: 10.1073/pnas.1005743107.
https://pnas.org/doi/full/10.1073/pnas.1005743107 (visited on 12/20/2023).

[111] A. Brill, T. Fuchs, A. Savchenko, G. Thomas, K. Martinod, S. De Meyer, A. Bhandari, and D. Wagner. "Neutrophil Extracellular Traps Promote Deep Vein Thrombosis in Mice". In: *Journal of Thrombosis and Haemostasis* 10.1 (Jan. 2012), pp. 136–144. ISSN: 15387836. DOI: 10.1111/j.1538-7836.2011.04544.x.
https://linkinghub.elsevier.com/retrieve/pii/S1538783622061293 (visited on 05/07/2025).

[112] K. Martinod and D. D. Wagner. "Thrombosis: Tangled up in NETs". In: *Blood* 123.18 (May 1, 2014), pp. 2768–2776. ISSN: 0006-4971, 1528-0020. DOI: 10.1182/blood-2013-10-463646.
https://ashpublications.org/blood/article/123/18/2768/32513/Thrombosis-tangled-up-in-NETs (visited on 05/07/2025).

[113] E. A. Middleton, X.-Y. He, F. Denorme, R. A. Campbell, D. Ng, S. P. Salvatore, M. Mostyka, A. Baxter-Stoltzfus, A. C. Borczuk, M. Loda, M. J. Cody, B. K. Manne, I. Portier, E. S. Harris, A. C. Petrey, E. J. Beswick, A. F. Caulin, A. Iovino, L. M. Abegglen, A. S. Weyrich, M. T. Rondina, M. Egeblad, J. D. Schiffman, and C. C. Yost. "Neutrophil Extracellular Traps Contribute to Immunothrombosis in COVID-19 Acute Respiratory Distress Syndrome". In: *Blood* 136.10 (Sept. 3, 2020), pp. 1169–1179. ISSN: 0006-4971, 1528-0020. DOI: 10.1182/blood.2020007008.
https://ashpublications.org/blood/article/136/10/1169/461219/Neutrophil-extracellular-traps-contribute-to (visited on 05/07/2025).

[114] Y. Zhang, R. Peng, S. Pei, S. Gao, Y. Sun, G. Cheng, D. Yu, X. Wang, Z. Gao, B. Ji, and Z. Zhou. "Neutrophil Extracellular Traps Are Increased after Extracorporeal Membrane Oxygenation Support Initiation and Present in Thrombus: A Preclinical Study Using Sheep as an Animal Model". In: *Thrombosis Research* 221 (Jan. 2023), pp. 173–182. ISSN: 00493848. DOI: 10.1016/j.thromres.2022.10.019.
https://linkinghub.elsevier.com/retrieve/pii/S004938482200439X (visited on 12/20/2023).

[115] X. Yu, J. Tan, and S. Diamond. "Hemodynamic Force Triggers Rapid NETosis within Sterile Thrombotic Occlusions". In: *Journal of Thrombosis and Haemostasis* 16.2 (Feb. 2018), pp. 316–329. ISSN: 15387836. DOI: 10.1111/jth.13907. https://linkinghub.elsevier.com/retrieve/pii/S1538783622009308 (visited on 12/20/2023).

# List of Figures

1.1 Relevance of ECMO application and research worldwide. . . . . 3
1.2 Overview of ECMO components . . . . . 6
1.3 Cannulation of VV and VA ECMO . . . . . 7
1.4 Overview of blood components and their function . . . . . 9
1.5 Rheological properties of human blood . . . . . 10
1.6 Role of the vWF within the coagulation cascade . . . . . 12
1.7 Configuration of the von Willebrand protein after exposure to shear stress 12
1.8 Concept of vWF deposition as initiator for clotting . . . . . 18

2.1 Definition of region of interest for clot calculation. . . . . 21
2.2 Setup for image acquisition of FMI . . . . . 24
2.3 Automatic selection of statistical test . . . . . 26
2.4 Explanation of wrongfully detected clot volume with MDCT . . . . . 28
2.5 Display of the blood compartment of ML . . . . . 29
2.6 Concept of correction factor for MDCT clot calculation . . . . . 29
2.7 Setup for measuring blood filled volume of ML . . . . . 33
2.8 Total clot volume of investigated MLs . . . . . 36
2.9 Total clot volume in the investigated MLs . . . . . 38
2.10 Clot volume in the investigated MLs . . . . . 40
2.11 Clot volume per fiber mat in seven investigated MLs. . . . . 44
2.12 Clot progression along the ML . . . . . 49
2.13 Comparison of clot volume in VV ECMO and VA ECMO . . . . . 50
2.14 Clot volume in seven investigated MLs . . . . . 51
2.15 Comet shaped clot structures . . . . . 52
2.16 Qualitative display of key criteria of used imaging modalities . . . . . 55

3.1 Limitations of top view microscopy and concept of cross-sections . . . . 60
3.2 Preliminary embedding tests with Technovit® 9100 . . . . . 61
3.3 Visual summary of embedding process . . . . . 66
3.4 Setup for ML embedding . . . . . 67
3.5 Creation of specimen from embedded MLs . . . . . 70
3.6 Microtome mounting for cylindrical specimen . . . . . 74
3.7 Clot structures in sections from embedding MLs . . . . . 75
3.8 Warp threads in sections from embedding MLs . . . . . 76
3.9 Established histological and IHC stainings for transmitting light microscopy . . . . . 77
3.10 Established IHF protocols . . . . . 83
3.11 Identification of distinct biological clot components . . . . . 88
3.12 Embedding of PMP and TPU hollow-fibers . . . . . 89
3.13 Visualization of cytoplasm with MPO using IHF . . . . . 90
3.14 Differentiation of MPO signal intensity in IHC and IHF stainings . . . . 93
3.15 Visualization of vWF structures using the TRITC-channel and digital image subtraction . . . . . 95

4.1 Generic model of ML for CFD . . . . . 106
4.2 Geometry and mesh of native ML model for CFD . . . . . 107
4.3 Velocity magnitude and WSS within the generic model . . . . . 110
4.4 Velocity magnitude and WSS within the native model . . . . . 112

5.1 Aluminum casting Molds with soluble flow geometries . . . . . 121
5.2 Structure of pump drive unit for non-invasive optical flow measurements 126
5.3 Setup for non-invasive optical flow measurements in an ECMO pump . 127
5.4 Inline refractive index matching . . . . . 130
5.5 Position of LDA measurement within pump replica . . . . . 136
5.6 Absolute velocity in the pump channel close to the outlet port . . . . . 136
5.7 Visualization of the turbulence intensity close to the outlet port . . . . . 137
5.8 Power spectrum illustration . . . . . 137

6.1 Creation of specimen from embedded ECMO pump head . . . . . 148
6.2 Polymer embedded clot structure after removal from centrifugal pump 149
6.3 Polymer embedded pump head clot after blocking process . . . . . 151

6.4 Example of embedded blood clot deposed on rotor blade . . . . . 153

7.1 Experimental setup for triggering and visualizing NETosis on ML hollow-fibers . . . . . 158
7.2 Progression of NETosis during experiment . . . . . 159
7.3 Calibration image and NET formation during experiment . . . . . 162
7.4 NETosis filament out of focus plane . . . . . 165
7.5 Process of filament reconstruction . . . . . 166
7.6 Exemplary results from NETosis detection software . . . . . 169

# List of Tables

1.1 Commonly used ML designs and specifications . . . . . 8
1.2 Commonly used ECMO pumps and specifications . . . . . 8

2.1 Operation data of investigated MLs . . . . . 22
2.2 Blood volume of ML subsections . . . . . 35

3.1 Required equipment and tools . . . . . 63
3.2 Required reagents . . . . . 64

# Acknowledgments

This PhD thesis was written during my time as research assistant at the Department of Biofluid Mechanics at the Technical University of Applied Sciences (OTH) Regensburg in close cooperation with the University Regensburg and the University Hospital Regensburg. I look back positively on the last years at this institution and would like to thank many people who helped me to cope with this project.

I would especially like to thank Prof. Dr. -Ing. Lars Krenkel for supervising my research project and for supporting me over the time at the Regensburg Center of Biomedical Engineering (RCBE). I would like to thank my mentors Prof. Dr. rer. nat. Karla Lehle, Prof. Dr. med. Christof Schmid, and Prof. Dr. med. Matthias Lubnow for their support during the doctoral period. Thanks to Dipl. Ing. Maik Foltan, M.Sc. for introducing me to the interesting world of cardiovascular perfusion in 2018. Without him, I would not have worked in this exciting subject area. Thanks to Lisa and my family who gave me important support in my private life during the doctoral period. I would like to thank my dear friend and colleague Dr. med. Maria Stella Wagner as well as my three former students Magdalena Tinwald, M.Sc., Daniel Pointner, M.Sc., and Steffen Rabenstein, B.Sc. very much for the instructive time and cooperation. My former collegues at the department Dr. -Ing. Sandra Melina Malescha, Dr. rer. nat. Lea Huber, Vera Stelzer, M.Sc., Johanna Michel, M.Sc., and Florian Erzinger, M.Sc. deserve special thanks for their support within the university as well as in private life.

This work was supported by the German Research Foundation (DFG) with the "Towards an Implantable Lung" priority program SPP 2014 (project number: 447721607). Final funding for the completion of the PhD program was granted by the Regensburg Center of Health Sciences and Technology (RCHST) and the UKR. Furthermore, equipment was funded by institutional grants from the RCBE, the RCHST, the OTH

Regensburg, and from the Bavarian Ministry of Science and Arts in the framework of the Bavarian Academic Forum (Bayerisches Wissenschaftsforum) (BayWISS) - doctoral consortium "Health Sciences".

# Selbstständigkeitserklärung / Affidavit

Ich, Michael Kranz, geboren am 22.11.1995 in Regensburg erkläre hiermit, dass ich die vorliegende Arbeit ohne unzulässige Hilfe Dritter und ohne Benutzung anderer als der angegebenen Hilfsmittel angefertigt habe. Die aus anderen Quellen direkt oder indirekt übernommenen Daten und Konzepte sind unter Angabe der Quelle gekennzeichnet. Insbesondere habe ich nicht die entgeltliche Hilfe von Vermittlungs- bzw. Beratungsdiensten (Promotionsberater*in oder andere Personen) in Anspruch genommen. Die Arbeit wurde bisher weder im In- noch im Ausland in gleicher oder ähnlicher Form einer anderen Prüfungsbehörde vorgelegt.

I, Michael Kranz, born on 22$^{nd}$ November 1995 in Regensburg, Germany hereby declare that I have written this thesis without the unauthorized assistance of third parties and without the use of aids other than those specified. The data and concepts taken directly or indirectly from other sources are marked with the reference to the source. In particular, I have not used the paid assistance from mediation or advisory services (doctoral advisor or other persons). The thesis has not been submitted in the same or a similar form to any other examining authority in Germany or abroad.

Regensburg, der 11.07.2025

Michael Kranz, M.Sc.